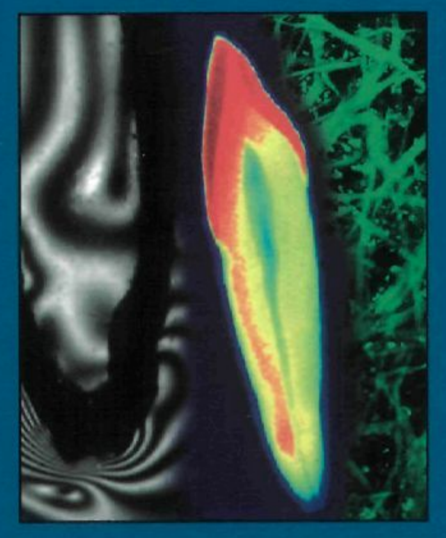


Vol. 4

Series on Biomaterials and Bioengineering

Fundamentals and Applications of Biophotonics in Dentistry

Anil Kishen
Anand Asundi

Imperial College Press

Vol. 4

Series on Biomaterials and Bioengineering

Fundamentals and Applications of Biophotonics in Dentistry

SERIES ON BIOMATERIALS AND BIOENGINEERING

Series Editors: **A W Batchelor** (Monash Univ. Sunway Campus Malaysia Sdn Bhd)
J R Batchelor (UK)
Margam Chandrasekaran (Singapore Institute of Manufacturing Technology, Singapore)

Vol. 1: An Introduction to Biocomposites
by Seeram Ramakrishna *(National University of Singapore, Singapore),*
Zheng-Ming Huang *(Tongji University, China),*
Ganesh V Kumar *(National University of Singapore, Singapore),*
A W Batchelor *(Monash University Malaysia, Malaysia)*
Joerg Mayer *(TECIM, Switzerland)*

Vol. 2: Life-Enhancing Plastics: Plastics and Other Materials in Medical Applications
by Anthony Holmes-Walker *(BioInteractions Ltd, UK)*

Vol. 3: Service Characteristics of Biomedical Materials and Implants
by Andrew W Batchelor *(Monash University Malaysia, Malaysia)* and
Margam Chandrasekaran *(Singapore Institute of Manufacturing Technology, Singapore)*

Vol. 4

Series on Biomaterials and Bioengineering

Fundamentals and Applications of Biophotonics in Dentistry

Anil Kishen

National University of Singapore, Singapore

Anand Asundi

Nanyang Technological University, Singapore

ICP Imperial College Press

Published by

Imperial College Press
57 Shelton Street
Covent Garden
London WC2H 9HE

Distributed by

World Scientific Publishing Co. Pte. Ltd.
5 Toh Tuck Link, Singapore 596224
USA office: 27 Warren Street, Suite 401-402, Hackensack, NJ 07601
UK office: 57 Shelton Street, Covent Garden, London WC2H 9HE

British Library Cataloguing-in-Publication Data
A catalogue record for this book is available from the British Library.

FUNDAMENTALS AND APPLICATIONS OF BIOPHOTONICS IN DENTISTRY
Series on Biomaterials and Bioengineering — Vol. 4

Copyright © 2007 by Imperial College Press

All rights reserved. This book, or parts thereof, may not be reproduced in any form or by any means, electronic or mechanical, including photocopying, recording or any information storage and retrieval system now known or to be invented, without written permission from the Publisher.

For photocopying of material in this volume, please pay a copying fee through the Copyright Clearance Center, Inc., 222 Rosewood Drive, Danvers, MA 01923, USA. In this case permission to photocopy is not required from the publisher.

ISBN 1-86094-704-2

Printed by FuIsland Offset Printing (S) Pte Ltd, Singapore

PREFACE

Biophotonics is revolutionizing the field of medicine, biology and chemistry and creating a new breed of medical engineers while at the same time getting engineers a taste of medicine. From an engineer's perspective, biophotonics is the application of photonics – the technology of generating and harnessing packet of light energy called photons – to image, detect and manipulate biological materials. In biology the understanding of molecular mechanisms, function of proteins and molecules has seen great new advances. In biomedical engineering detection, diagnoses and treatment targeting both macro-objects like the teeth or bone as well as micro-objects such as bacteria have seen better understanding through the development of new tools. There is another school of thought, albeit much smaller that defines biophotons as a quantum of light that is permanently and continuously emitted by all living systems. For example, humans emit radiation similar to a blackbody with maximum power being emitted at a wavelength of about 10 μm.

Regardless of definition, biophotonics is a multi-disciplinary field that bridges engineering, the sciences and medical fields. This diversity of sciences and technologies usually makes for challenging and interesting projects – that could be driven by engineers and clinicians alike. However, there is still the need that clinicians understand some concepts in photonics while engineers get a feel for medical and bio-chemical sciences. Towards this end, this book is written by persons from different fields such as engineering, sciences and medical field.

The book is roughly divided into two sections – the first introduces the readers to some basic concepts in the field of biophotomechanics. As the name suggests, this topic looks at the use of optical methods (photo) for the study of mechanical behaviour (mechanics) of biological objects

in the macro-scale such as teeth and bone. The next chapter introduces some recent techniques on bioimaging such as fluorescence microscopy and optical coherence tomography amongst others. Chapter 4 introduces spectroscopy – a erstwhile tool in biophotonics while chapter five deals with lasers and laser tissue interaction. Finally Chapter 6 provides an introduction to Photodynamic therapy a growing technology for targeted application of photonic radiations.

The second half of the book applies some of these basic concepts to the field of dentistry to highlight some of the features and adaptation of photonics in this area. Dental photomechanics provides an understanding of mechanical and thermal characteristics of dentine and permits a better understanding of the causes of damage and failure of certain treatments. Chapter 8 uses spectroscopic methods specifically Micro-Raman spectroscopy for a better understanding of the materials aspects of dentine and adhesives. The next chapter on Dental and Oral Optics describes tools and techniques for imaging and optical properties of dentine and enamel. The final chapter on fiber optic sensors explores new sensor development for effective and fast ways of detecting and diagnosing oral bacteria.

We, as editors, feel that the book would be just as informative for final year undergraduate, graduate students in bioengineering as it would to clinicians and dental surgeons to gain a better understanding of a process or treatment.

Anil Kishen and Anand Asundi

CONTENTS

APPLICATIONS

CHAPTER 1

INTRODUCTION

Anil Kishen

Biophotonics Laboratory, Faculty of Dentistry Laboratory,
National University of Singapore, Republic of Singapore
E-mail: rsdak@nus.edu.sg

1.1 Introduction

Photonics is a light based optical technology that is considered as the leading technology for the new millennium. During the last 50 years, there has been many breakthroughs in photonics which laid foundation for its wide range of applications in health care. Most applications of photonics in health care were based on various types of light and different types of photon-tissue interactions. Application of photonics based techniques offer several specific advantages such as rapidity, sensitivity, specificity, inexpensive and non-invasive (needle less). It has been observed that many diseases of the mouth are accompanied by characteristic changes in the tissue structure. Some of the typical examples include dental caries, non-carious lesions in teeth, gingivitis, periodontitis, precancerous lesions and tumors of the oral tissues. Dentistry has traditionally depended on contemporary science and technology for improvement in diagnostic tools and advancement in treatment options. However, the impact of photonics in clinical Dentistry has been significantly less than in clinical Medicine and Surgery.

Current dental practice has been emphasizing more on (1) early diagnosis and preventions of common oral diseases and (2) to conserve tooth structure as much as possible during restorative procedures. Thus Atraumatic and Non Invasive Treatment (ANIT) modalities have been the key thrust in Dentistry today. Keeping in mind the tremendous

potential of optical technology to provide high sensitive tissue information non-invasively, and the ability to induce localized and specific tissue changes, this should be the foremost technology to embrace for advancement in dentistry. In addition, research has highlighted saliva as a potential source of diagnostic markers to monitor the health status of the whole body. Saliva is increasingly used as an investigational aid in the diagnosis of diseases, such as dental caries, HIV, diabetes mellitus, oral cancer and breast cancer. Saliva meets all the requirements for a non-invasive, accessible and highly efficient diagnostic medium. When compared with the procedures for collecting blood, the use of saliva is less invasive and less traumatic to the patients. The most important benefit of light based diagnostic methods is their capability to detect clinically relevant information much early before actual clinical signs and symptoms appear in the patient. This allows photonics based techniques not only to be non-invasive during application but also detect disease associated tissue changes very early. Early detection of disease process will enable clinicians to carry out preventive treatment measures or minimally invasive treatment procedures that are less traumatic and cost effective.

1.2 Definition and Significance

Photonics include all light-based (optical) technology that is hailed as the dominant technology of this millennium. Biophotonics is a multidisciplinary category under photonics, which involves the fusion of photonics and biomedical sciences. **Biophotonics** defined as the science of generating and harnessing light (photons) to image, detect and manipulate biological materials. It is applied in Medicine and Dentistry to understand, diagnosis and treatment of diseases. Biophotonics mainly involves the interaction between light with biological tissues, and is used to study biological tissues and biological processes at different scales that ranges from micro to nano-levels. Biophotonics integrates lasers, photonics, nanotechnology and biotechnology. This integrated approach provides new dimension for diagnostics and therapeutics. This rapidly growing new discipline will have a major impact on health care.

Light has been used as a therapeutic agent and experimental approach for many centuries. The major use of light for therapeutic applications in health care sciences was noticeably initiated after the development of lasers in 1960. Invention of lasers, a concentrated source of monochromatic light has revolutionized photonics. Most of the earlier clinical studies in dentistry were conducted with high energy lasers such as Ruby laser ((1963), CO2 (1968), YAG (1974), Argon (1977), Nd:YAG (1977) and Q-switched YAG (1980).

Last decade saw the advent of semiconductor diode lasers which are referred to as soft lasers. These lasers are compact, low cost device which have very high electrical and optical efficiency. In Dentistry the soft lasers have been used for acceleration of wound healing, enhanced remodelling and repair of bone, restoration of normal neural function following injury, normalization of abnormal hormonal function and modulation of the immune system. Although low-level light offers many potential advantages in Dentistry, further research is warranted before serious clinical applications.

1.3 Classification of Biophotonics in Dentistry

Biophotonics in Dentistry is crucial for the early detection of diseases, to carry out more effective minimally-invasive targeted-therapies and to restore diseased tissues functionally and esthetically. Different applications of biophotonics in health care are shown in Fig. 1.1. Biophotonics in Dentistry can be broadly categorized into (1) research and (2) clinical applications (see Fig. 1.2). Under clinical application they can be further subdivided into (2A) diagnostics and (2B) therapeutics.

1.3.1 *Diagnostic*

Low-energy light interacting with tissue gives rise to a characteristic luminescence, which provides information on different clinically useful parameters such as blood flow, pH and oxygen content. In addition, it

may also provide information on the physiologically and pathologically induced biochemical changes.

1.3.2 *Therapeutic*

Thermal interaction: In this process heat generated by the high-energy laser light is used to disrupt tissues. This process will mechanically induce coagulation, vaporization, carbonization and melting. Ruptured blood vessels are sealed by the laser induced coagulation of blood. The heat generated by laser beam on the focused tissue can be also used to weld tissue segments instead of using sutures. Further, high energy lasers are also used to cut-through tissues.

Photodynamic Therapy: This method uses light to trigger chemical reactions in the body for therapeutic applications. A photosensitizing agent is utilized to achieve the photodynamic effect. Photodynamic therapy is also called as photoradiation therapy, phototherapy, or photochemotherapy.

Photo-biostimulation: In this method extremely low-power light is used to induce photochemical effects on tissues. A low-powered laser procedure does not produce heat and therefore does not damage biological tissues; it stimulates the tissues and promotes healing by penetrating deep into the tissues initializing the process of photochemical effect. Photo-biostimulation is applied in Dentistry for many applications such as post extraction edema, sensitive teeth, gums and benign mouth lesions.

Bioimaging: Optical and x-ray imaging has influenced the practice of dentistry dramatically. Reconstruction of images in both two and three-dimensions has allowed better visualization of models and disease processes, allowing quantification of disease changes over time, thus assisting the treatment planning decisions and improving patient care. Some of these innovations are in the research and development stage. Bioimaging finds application in oncology, inflammatory processes, wound healing, pharmacokinetics, pharmacodynamics, toxicology,

infectious disease, gene expression and more. Furthermore, new concepts of non-invasive imaging (optical biopsy) rely on better understanding of the signal's origin, both "native" and exogenous.

1.3.3 *Research*

Photomechanics: Much research in dentistry is directed to understand the stress-strain states in biological and artificial structures (restorations and prosthesis). Photomechanical experiments are optics based experiments used to study the material property gradients in biological materials and the stress-strain distribution in tooth and supporting bone structures. These high sensitive experimental techniques are used to extrapolate clinically relevant material properties within dental structures and within biological interfaces. Photoelasticity, Moiré interferometry and Electronic Speckle pattern interferometry are some of the most commonly employed optical techniques in dental biomechanics. In the past analyzing optical fringes to deduce clinically useful experimental data was considered tedious and time consuming. However, with the recent advances in digital image processing systems, analysis of optical fringes has been robust and efficient.

Spectroscopy: A spectrum is a representation of the electromagnetic radiation which is absorbed or emitted by a sample. The qualitative applications of absorption spectrometry depends on the fact that a given molecular species absorbs light only in the specific region of the spectrum, and in varying degrees, characteristic of that particular species. Such a display is called an absorption spectrum of that molecular species and serves as a fingerprint for identification purpose. UV-Visible spectroscopy monitors the electronic states of the molecules, while an infrared spectroscopy determines changes in the vibrational states of the molecules. These techniques are very valuable for the non-invasive testing (without needles) of biochemical substances for diagnostic and therapeutic purposes. Raman spectroscopy, which is based on Raman scattering, measures the inelastic scattering when high-energy photon interact with a molecule (or crystal lattice). This analytical technique is finding significant application in pharmaceutical industry. There is a

growing interest in single cell, tissue, organ level measurements as applied to basic physiology, non-invasive diagnostics, and in vivo studies.

Fiber-optic sensors: Optical fibers in health care sciences have come a long way; however, they still need further improvements. Fiber optics offers the advantage of flexibility of beam manipulation. In the past fiber optics was used mostly as an optical conduit to illuminate inaccessible regions and to conduct high-energy lasers to specific tissue site for cutting. Recently, many fiber optic based sensors are being developed with intentions to provide a safe, rapid and non-invasive testing of clinically relevant physiological variables. The fiber optic based sensor offers advantages such as electrical isolation, physical flexibility and needless of electrical power for driving the sensor unit. Additionally, they find application in designing customized probes that are tailored for specific applications. These probes combine the advantage of spectroscopic techniques with fiber optics.

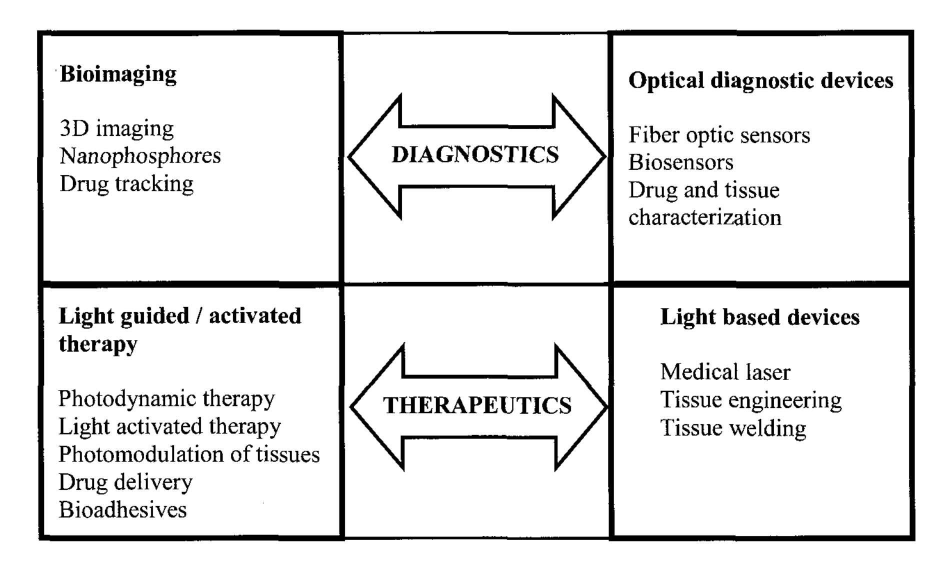


Fig. 1.1. Applications of biophotonics for health care.

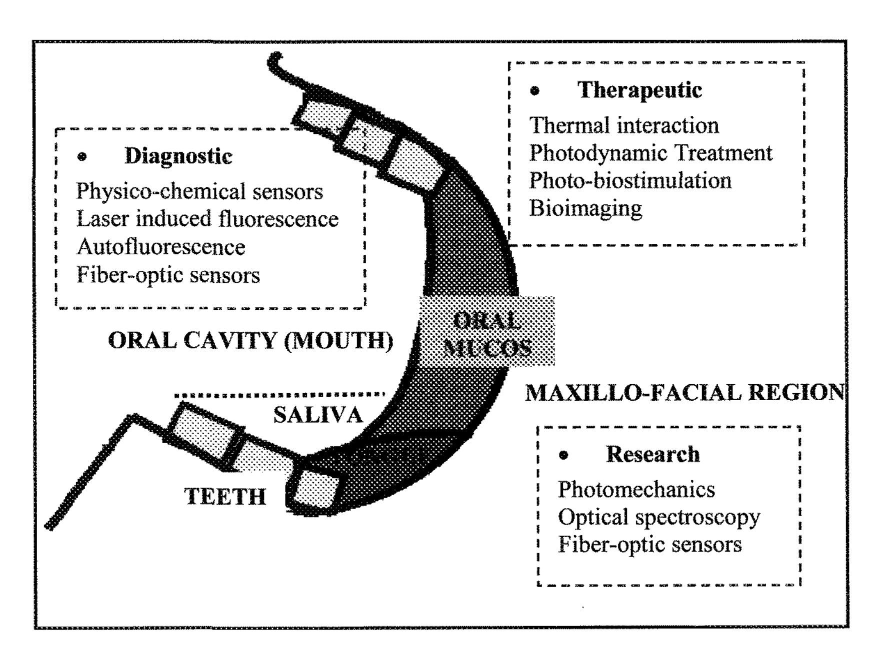


Fig. 1.2. The comprehensive multidisciplinary scope of biophotonics in dentistry.

1.4 Future Opportunities

Dental practitioners have been traditionally plagued with different problems pertaining to the diagnosis and treatment of oral diseases. Biophotonics is an emerging technology that promises to have a broad and significant impact on health care. In the past decade, key technologies such as (a) compact lasers, (b) CCD detectors, (c) volume holographic elements and (d) easy-to-use computing platforms combined with fiber-optic coupled instrumentation has developed many diagnostic and therapeutic instruments in health care. Rapid detection and non-invasive tissue modulation are the most important advantages of photonics based methods. These methods allow early detection of diseases and implementation of preventative or minimally invasive treatment regimes that avert drastic tissue damage. Currently, biophotonics is entering a new era of rigorous clinical testing and evaluation. As photonics find major application in health care, it is particularly important that the basic principles and potential pitfalls of technology is also understood. Although optical spectroscopy may one

day replace some of the conventional clinical techniques, it is important to combine the advantages of photonics with lessons learned by the clinicians in the past. This approach will enable us to develop clinically useful technologies for better health care management.

Biophotonics offers remarkable prospectus for both clinical applications and fundamental research. In the future biophotonics is anticipated to play a major role in creating new technologies for significant health care benefits and immense commercial potential for different biomedical industries. Future opportunities with biophotonics are: development and testing of multiple-analyte based nano-probes, optical biosensors for infections and cancers, in vivo optical biopsy, tissue welding, tissue contouring and regeneration, in vivo imaging of human subjects, real-time monitoring of drug delivery and action. All these technological aids should be supported by long-term clinical evaluations.

1.5 Scope of this Book

The aim of this book is to provide a basic understanding of broad range of topics for individuals from different backgrounds to acquire minimum knowledge for research and development in biophotonics. The chapters in this book is sorted under two major categories, the first category describes the fundamental aspects of photonics such as Photomechanics, Biomedical Imaging, Lasers and laser-tissue interaction, spectroscopy and Photodynamic therapy. The second category describes the applications of biophotonic, especially with relevance to dentistry. Dental Photobiomechanics, Raman Spectroscopy, dental tissue optics and fiber optic diagnostic sensors are dealt under this category.

References

1. G.A. Catone, C.C. Alling, Laser applications in Oral and Maxillofacial Surgery, WB Saunders Company: London (1997).
2. A. Katzir. Lasers and optical fibers in medicine, Academic Press, Inc: New York (1993).
3. P.N. Prasad. Introduction to Biophotonics. Wiley Interscience Inc., New Jersey (2003).

CHAPTER 2

PHOTOMECHANICS

Anand Asundi

School of Mechanical and Aerospace Engineering,
Nanyang Technological University
Nanyang Avenue, Singapore 639798
E-mail: masundi@ntu.edu.sg

Photomechanics is the application of optical methods (Photo) to solve problems in mechanics. This field has been growing steadily over the past couple of decades especially with the advent of low cost light sources, detectors and CCD cameras and image processing methodology. This chapter has been divided into 8 sections starting with introduction to the field of mechanics and optics. A good understanding of the basic principles of the two pillars of photomechanics would enable easy application in a wide variety of situations. Following this introduction, specific techniques such as Moiré and Grating methods, Photoelasticity, Speckle and Holography are highlighted. The final section looks at the recent advances in Digital Photomechanics, which has made enormous strides in the last decade and has all but made obsolete the ubiquitous photographic film.

2.1 Introduction to Mechanics

In this chapter, the emphasis is primarily on solid mechanics, which is the area that deals with the response of objects to external stimuli such as force, temperature, etc. Furthermore, the treatment is based on the more practice-based strength of materials approach. In the strength of materials approach, the starting point is the entire structure under the action of external forces. The various components of the structure are then broken down into sub-systems while maintaining the overall equilibrium of the

object. Hence there are few standard geometric and loading conditions which form the basis of all complex objects and loading systems.

2.1.1 *Force and Stress*

External forces acting on a body may be due to mechanical loads or as support reactions. Under the action of these forces, the body is said to be in equilibrium if the sum of forces and sum of moments are equal to zero. For a general three-dimensional case, using the standard Cartesian coordinates, this will give rise to 6 equilibrium conditions. These equilibrium conditions allow determination of the unknown support reactions in *statically determinate* problems. If the entire structure is in equilibrium under the action of the external forces, then any part of the structure should also be in equilibrium. Hence, if a part of the structure is isolated, the external forces on that part need to be balanced by internal forces at the cut-section. While there are will be many possible combinations of internal force distribution on the cut section which satisfies equilibrium, the correct one is that which also ensures consistency of displacement and strain distribution; i.e. compatibility equations. The internal force is not always uniformly distributed over the cut cross-section. Hence instead of internal force, the concept of stress was introduced. Stress is an abstract quantity, whose basis is more mathematical than physical.

Stress is defined as the force per unit area. If the force is acting normal to the cross-sectional area, the stress is termed normal stress and will be denoted as σ (Fig. 2.1(a)). Subscripts are attached to this symbol to denote the direction of stress and the direction of the normal to the surface on which the force acts. Thus σ_{xx} or simply σ_x denotes normal stress acting in the x-direction on a surface whose normal is parallel to the x-direction. Shear stresses, on the other hand are the tangential component of the force divided by the cross-sectional area (Fig. 2.1(b)). Shear stress is denoted by the symbol τ, with subscripts as before to signify the direction of stress and the normal to surface on which the stress acts. Thus τ_{xy} signifies shear stress acting on a plane whose normal is the x-direction and the stress is directed in the y-direction. Thus for an

3-D element as shown in Fig. 2.2, there will be a total of nine stress components – three normal stresses and six shear stresses. To satisfy moment equilibrium, the shear stresses ($\tau_{xy} = \tau_{yx}$, $\tau_{xz} = \tau_{zx}$ and $\tau_{xz} = \tau_{zx}$) are not all independent.

By convention tensile normal stresses which pull the element apart are positive and the shear stress which causes the element to rotate in the counterclockwise direction is positive. The above definition provides what is referred to as *local stress*. There is also the *average normal stress* – which is the total force acting normal to a surface divided by the area on which it is acting. A similar definition follows for the *average shear stress*, in which case the total force is tangential to the same area. If the internal forces are distributed uniformly over the cross-section, then the average stress is equal to the local stress.

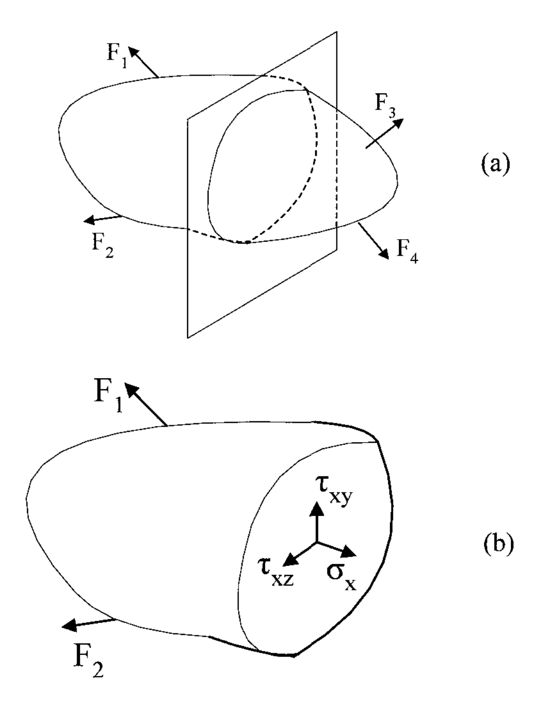


Fig. 2.1. Concept of stress.

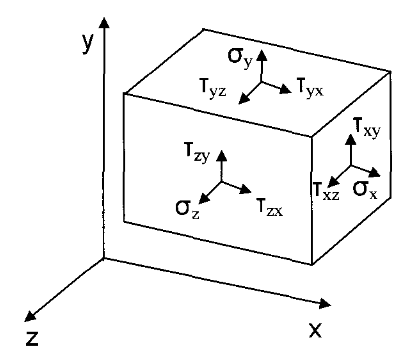


Fig. 2.2. 3-D stress components.

A complex loading system can be simplified into four basic sub-systems and the resultant stress is then calculated based on the superposition of the stresses determined from each of these basic sub-systems. The four subsystems are: axial loading, shear loading, transverse loading or bending and torsion. The corresponding stresses for each of the cases can be written as:

Axial or longitudinal Loads (P) gives rise to normal stress if the load is applied perpendicular to the cross-section area and can be written as

$$\sigma = \frac{P}{A} \tag{2.1}$$

The axial stress can be tensile or compressive depending on the external loads. Shear loading similarly gives shear stress which is the load applied tangentially (V) to an area divided by the cross-section area

$$\tau = \frac{V}{A} \tag{2.2}$$

A load applied transverse to the long axis of a beam gives rise to a bending moment (M) and shear force (V) and these in turn result in normal and shear stresses which are given as:

$$\sigma = \frac{My}{I}$$
$$\tau = \frac{VQ}{Ib} \tag{2.3}$$

where y is the distance from the neutral or centroidal axis of the beam. Q is the moment of the area above the section of interest about the neutral axis at which the shear stress is desired and b is the width of cross-section. The normal stress is tensile on one side of the neutral axis and compressive on the other.

Finally, a twisting moment (T) or torque gives rise to shear stresses at any cross-section which can be written as

$$\tau = \frac{Tr}{J} \tag{2.4}$$

where r is the distance from the centre and J is the polar moment of inertia. This expression is only valid for beams with circular cross-section.

2.1.2 *Deformation and Strain*

Consider a two dimensional square element ABCD as shown in Fig. 2.3. After loading the element displaces and distorts to A′B′C′D′. The displacements in the 'x' and 'y' directions are 'u' and 'v' respectively. Also the lengths of AB and AC have changed as has the angle BAC. Normal strains are defined as the change in length. Normal strain is defined as the change in length divided by the original length. Normal strains are denoted by the symbol ε. To distinguish the strain components, subscripts as for the stress are added – thus ε_{xx} or ε_x is the normal strain in the x-direction. Similarly shear strain is the change in the angle between two lines which were initially at right angles to each other. Shear strains are represented by the symbol γ with subscripts defining the plane of the angle.

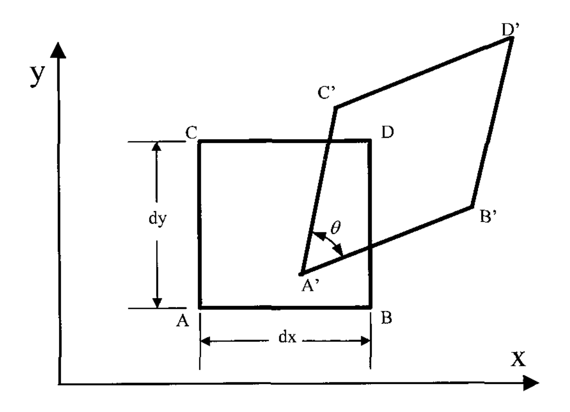


Fig. 2.3. Displacement and strain.

Thus from Fig. 2.3, we have two normal strains and one shear strain which can be written as:

$$\varepsilon_x = \frac{A'B' - AB}{AB}$$

$$\varepsilon_y = \frac{A'C' - AC}{AC} \tag{2.5}$$

$$\gamma_{xy} = 90 - \angle BAC$$

Note that the displacements 'u' and 'v' do not enter into the equations and are called the rigid body displacements. Incidentally these definitions provide the average strain, analogous to the average stress, over the gauge length AB or AC.

More rigorously, strains are defined as the change in length over the initial length as the initial length tends to zero. Hence in terms of incremental displacement, if the displacement of point A was (u. v) and the displacement of points B and C was (u + du, dv) and (du, v + dv), then eqn. (2.5) can be re-written as

$$\varepsilon_x = \frac{du}{dx}$$
$$\varepsilon_y = \frac{dv}{dy} \qquad (2.6)$$
$$\gamma_{xy} = \frac{du}{dy} + \frac{dv}{dx}$$

where dx and dy are the elemental lengths of AB and AC.

Some important notes in the derivation of eqn. (2.6),

(i) Incremental displacements are assumed to be small such that A′B′ is approximated with the projection A′B′ on the x-axis and the change in angles are small. If large deformations are encountered, then there would be a need to use the correct length of A′B′.

(ii) The displacement and deformation in the third ('z') direction are ignored. For small deformation, it would not influence the terms in eqn. (2.7). There would three additional strain components that arise namely the normal strain in the z-direction and two other shear strain components.

(iii) The strains are measured with respect to the initial length. These are referred to as the Lagrangian strains. In some experimental methods, measurements require that strains be referred to final length – this is the so-called Eulerian strain. For small strains both are equal.

The strains follow much the same rules as for stress in that there are principal planes in which the normal strains, referred to as principal strains, are maximum (minimum) and the shear strain is zero. Also we can locate planes where the shear strain is a maximum and on these planes the normal strain is the mean strain. Each of the stress components described in the previous section is associated with one or more strain components.

For axial loads, there is change in length in both the longitudinal and transverse directions. Hence axial loads give rise to normal strains in the three directions. Along the direction of the load, the normal strain is tensile or compressive depending on the applied load. However, in the

transverse directions for isotropic and homogenous materials, the strain is opposite to the axial strain. The ratio of the transverse strain to the axial strain is termed as the Poisson's ratio of the material.

In case of shear load, there is only one shear strain, which as described earlier can be determined by the change from the initial right angle. Bending loads give rise to both axial and shear strains while torsion is a case of pure shear.

2.1.3 *Stress-Strain Equations*

For isotropic homogeneous materials, normal stresses give rise to normal strains and shear stresses give rise to shear strain. The relation between stress and strain is referred to as the Hooke's law and in the most general form can be written as

$$\begin{aligned} \varepsilon_i &= \frac{\sigma_i}{E} - \frac{\nu}{E}(\sigma_j + \sigma_k) \\ \tau_{ij} &= \frac{E}{(1+\nu)}\gamma_{ij} \end{aligned} \tag{2.7}$$

where E, ν and G are mechanical properties of the material – namely the Young's Modulus, Poisson's ratio respectively and the subscripts i, j, k correspond to the Cartesian axes x, y, and z.

All the equations used so far are valid for isotropic, homogeneous and elastic cases. This means that the specimen has the same mechanical properties in all directions (isotropic) and at all points (homogeneous) and the loads are such that the specimen returns to its original state on removal of load (elastic).

2.2 Basic Optical Engineering

There are three main divisions in optics – geometrical optics, physical optics and photonics. These divisions have evolved historically and although the three areas are part of the same set, each one has independently grown and practiced. Typically, geometrical optics is

widely adopted by lens and optical systems (such as microscope) designers, physical optics by people working in precision measurement and photonics deals with optical devices such as lasers and detectors and light matter interaction. In this section, a brief review of these three areas will be given.

2.2.1 *Geometrical Optics*

Fermat's law is the basis for all aspects of geometrical optics. Fermat's law states that light takes the path with the shortest time between two points. Since the velocity of light depends on the medium in which it is traveling, it is the shortest time rather than the shortest distance (straight line) between two points, which is the path that light will take. The velocity of light (v) in any medium is given by

$$v = \frac{c}{n} \tag{2.8}$$

where 'c' is the velocity of light in vacuum ($\sim 3 \times 10^8$ m/s) and 'n' is the refractive index of the material.

In geometrical optics, light propagation is drawn as rays and when the ray encounters an interface, part of the ray is reflected and part is refracted as shown in Fig. 2.4. The law of reflection and the law of refraction can be derived from Fermat's law and can be stated as:

Law of reflection: For a specular object the angle of incidence is equal to the angle of reflection and both rays lie in the same plane as the normal.

Law of refraction: When light propagates from one medium to another, the ray bends either towards the normal or away from the normal and satisfies the following relation:

$$n_1 \sin\theta_1 = n_2 \sin\theta_2 \tag{2.9}$$

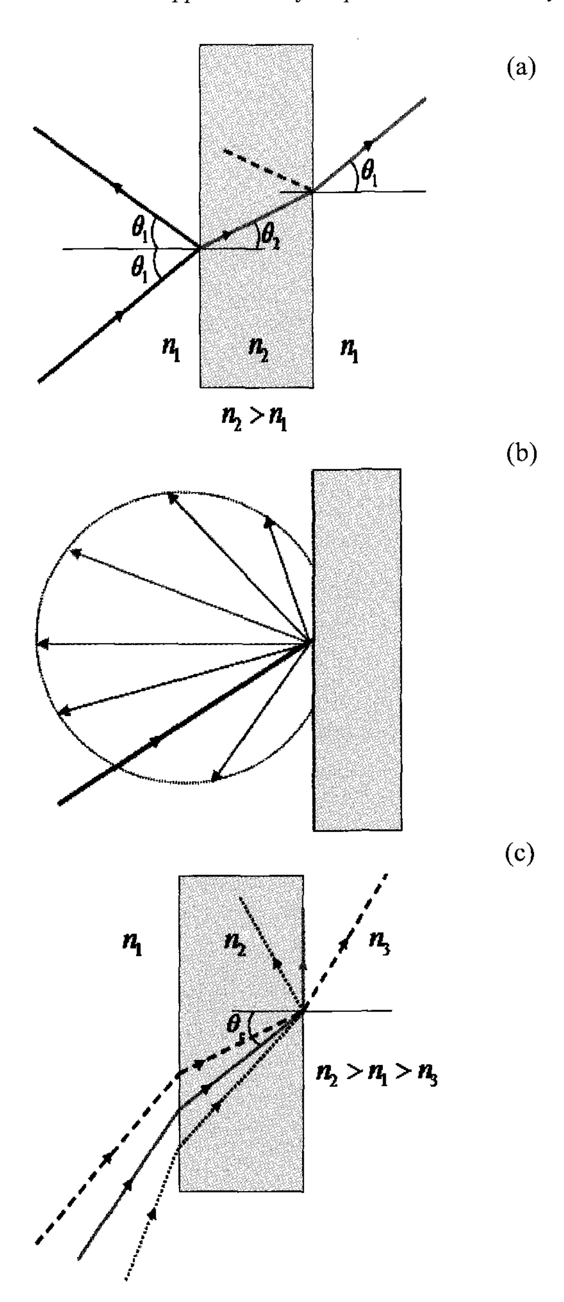


Fig. 2.4. (a) Reflection and refraction of light at interface. (b) Lambertian reflection. (c) Total Internal Reflection of light.

In addition, if the surface of the object is diffuse, light is scattered in all directions. Indeed for Lambertian surfaces, the light scatter is a function of the angle as shown in Fig. 2.4(b). Also as can be seen in Fig. 2.4(a), when light propagates from a medium of high refractive index to a medium with lower refractive index, the refracted ray bends away from the normal. As the angle of incidence increases, a 'critical angle' is reached at which the refracted beam is parallel to the interface (Fig. 2.4(c)). If the angle on incidence becomes greater than the critical angle then the ray is reflected back into the same medium. This phenomenon is called Total Internal Reflection and is the basis of light propagation in optical fibers.

2.2.2 *Physical (Wave) Optics*

In this aspect of optics, light is a transverse electro-magnetic wave, with a wavelength (λ) and a frequency (f) which are related as:

$$\lambda f = c \tag{2.10}$$

As with water waves, the electric (or magnetic) field which describes the light wave, oscillates perpendicular to the direction of propagation (Fig. 2.5). Thus the light wave propagates a distance λ in the time it takes the electric field to cycle through one period ($T = 1/f$) and hence eqn. 2.10. The electric field can be written as:

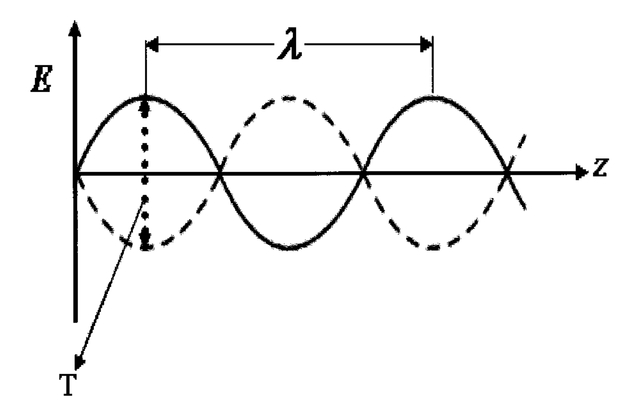


Fig. 2.5. Characteristic of light as a wave.

$$E = A \exp i(kz - \omega t) \tag{2.11}$$

where A is the amplitude of the wave, term in the brackets is called the phase, $k = 2\pi/\lambda$ is the wave vector and $\omega = 2\pi f$ is the angular frequency.

All detectors respond to the square of the amplitude and hence the intensity of the light field is: $I = |E|^2 = EE^* = A^2$, where * denotes the complex conjugate.

Three phenomena mark the wave nature of light which cannot be explained by the geometrical optics formulation. These are interference, diffraction and polarization. These phenomena can be explained based on the Huygen's principle, according to which, each point on the propagating wave is the source of a new spherical wave as shown in Fig. 2.6. The tangent to the new waves provides the new wavefront and is the basis of wave propagation.

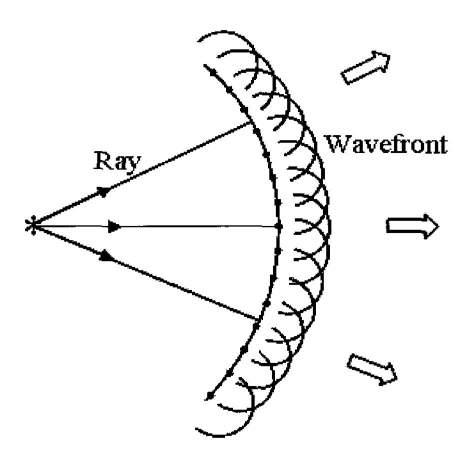


Fig. 2.6. Huygen's principle of light propagation.

2.2.2.1 *Interference*

Consider the experimental schematic shown in Fig. 2.7. Light of a single frequency, from a source is split by a beam splitter and each of the waves travel different paths to mirrors M_1 and M_2 and are recombined on reflection from the mirrors. Assume that the light-travels distances z_1 and

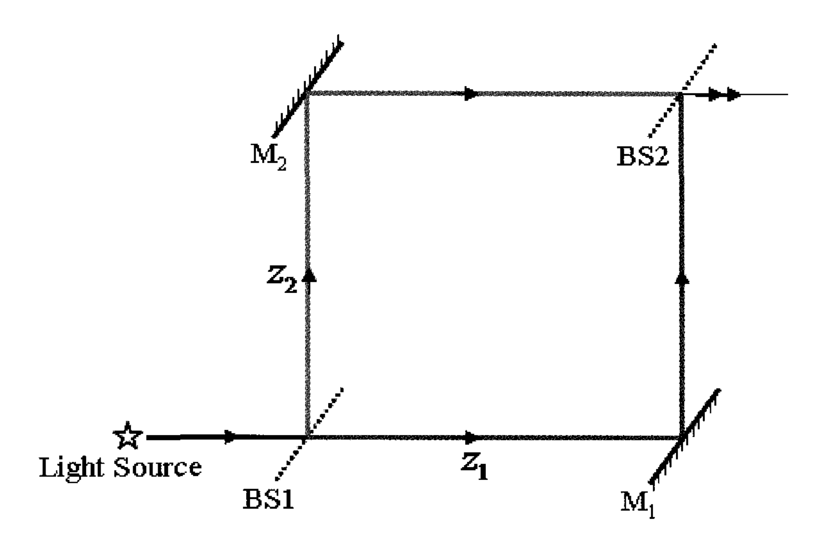


Fig. 2.7. Mach-Zhender interferometer for demonstrating interference of light by amplitude division.

z_2 from the beam splitter to mirrors M1 and M2 respectively and back to the beam splitter. The electrical field for the two waves can be written as:

$$\begin{aligned} E_1 &= A_1 \exp i(kz_1 - \omega t) \\ E_2 &= A_1 \exp i(kz_2 - \omega t) \end{aligned} \tag{2.12}$$

The resultant electrical field when the two waves recombine is thus:

$$E_r = (E_1 + E_2) \tag{2.13}$$

and the resulting intensity is

$$\begin{aligned} I_r &= (E_1 + E_2)(E_1^* + E_2^*) \\ &= A_1^2 \{1 + \cos k(z_1 - z_2)\} \end{aligned} \tag{2.14}$$

The term $(z_1 - z_2)$ is called the optical path difference (OPD). Hence the interference equation can be re-written as

$$I_r = A_1^2\{1 + \cos\frac{2\pi}{\lambda}(OPD)\} \tag{2.15}$$

Thus when the OPD is a multiple of the wavelength of light, the resulting intensity is a maximum and this is called Constructive Interference. On the other hand when the OPD is odd multiples of half the wavelength of light, we get Destructive Interference. Interference thus provides us with a very sensitive (sub-micrometer) method for deformation or displacement measurement. Usually in interferometers, one of the arms has the reference beam and the other has the object beam. Various configurations for interferometers have been developed and in wide use for precision metrology.

In the previous example, the light amplitude was divided by the beam splitter to generate the two beams. Alternately, the wavefront could be split up as shown in Fig. 2.8. In this set-up, which is known as the familiar Young's experiment, a parallel beam of light is incident on two small apertures separated by a distance'd'. Based on Huygen's principle, light from each of these apertures can be treated as a source of new wavefront which propagates to the screen. This wavefronts can interfere and the phenomenon is very similar to water flowing from two orifices. Using the same formulation as eqns (2.12 to 2.14), interference fringes will be seen at a screen placed at a distance 'L' from the apertures. The interference pattern is given by eqn. 2.15 and the phase difference or OPD for the two beams at any point on the screen can be readily determined.

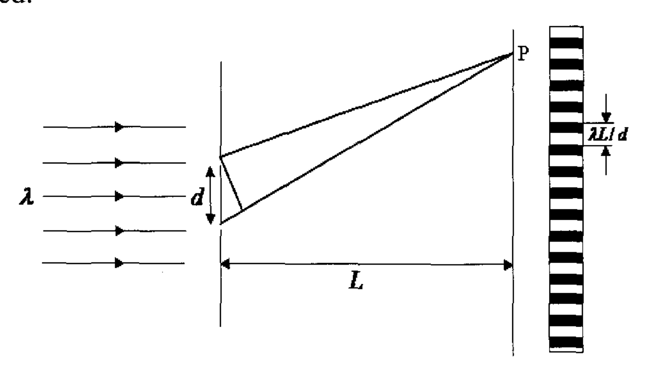


Fig. 2.8. Young's experiment for interference by wavefront division.

2.2.2.2 *Diffraction*

Consider the case of light passing through a small aperture of length'd'. According to Huygen's principle each point in the aperture plane is the source of a new wavefront. Hence in order to calculate the total intensity received at any point on the screen, we need to add the light fields emerging from every point on the aperture. Consider two waves emerging at an angle θ, *as* shown in Fig. 2.9. For the on-axis beam, the electric field can be written as

$$dE = dA \exp i(kz - \omega t) \tag{2.16}$$

While for an off-axis beam, as shown in Fig. 2.14, the electric field is

$$dE = dA \exp i(k(z + \Delta d \sin\theta) - \omega t) \tag{2.17}$$

where Δd sinθ is the additional path the off-axis beam has to propagate to the same point as the on-axis beam.

Integrating over the size of the aperture and squaring we get the intensity as

$$I = A^2 \sin c^2 (\frac{\pi d \sin\theta}{\lambda})$$

where (2.18)

$$\sin c\phi = \frac{\sin\phi}{\phi}$$

Destructive interference occurs when dsinθ = λ. A diffraction pattern as shown in Fig. 2.9 is seen on the screen. Unlike the interference patter, given by eqn. (2.15), the sinc function in the diffraction pattern means that the intensity of the diffraction maxima reduces for higher orders (Fig. 2.9). As an exercise, consider the case where you have two slits each one of width 'd' and separated by a distance 'a'. Each slit provides a diffraction pattern and the two slits gives rise to an interference pattern.

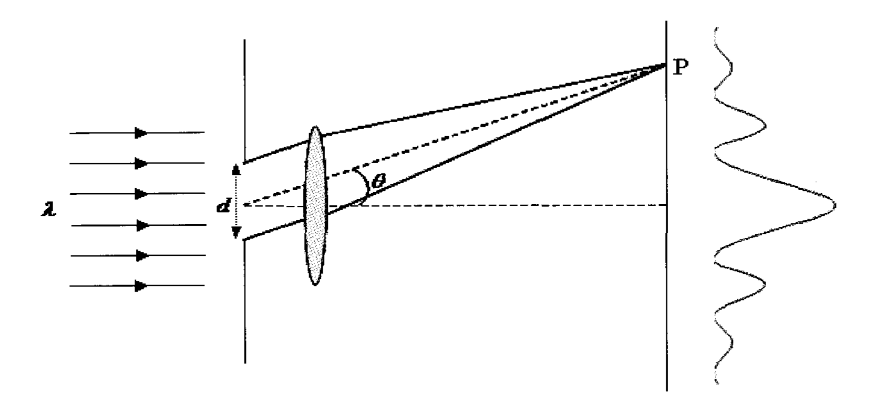


Fig. 2.9. Diffraction from a slit.

While diffraction limits the resolution for an optical imaging and non-imaging systems, diffraction by a grating, which can be thought of as multiple slits, has been used for measurement. As the number of slits increase, the regions of constructive interference narrow to very sharp peaks (Fig. 2.10). A grating can be thought of multiple slits with equal width and spacing. The spacing between the slits is the pitch of the diffraction grating and its inverse is the frequency ('f') of the grating.

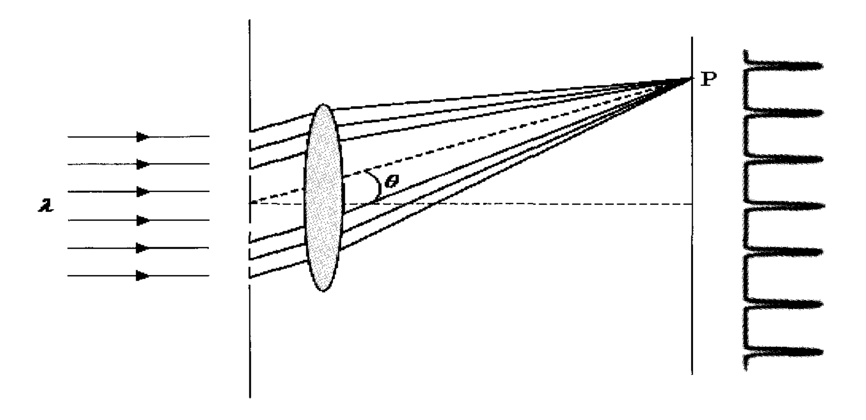


Fig. 2.10. Diffraction from multiple slits.

The diffraction equation (Fig. 2.11) which governs the spacing between the peaks of constructive interference can be written as:

$$\sin\beta = \sin\alpha \pm m\lambda f \tag{2.19}$$

where α is the angle of incidence, β is the diffraction angle and m is an integer which is referred to as the diffraction order. The spectrometer is a widely used instrument which uses diffraction to distinguish the spectral content with very high resolution.

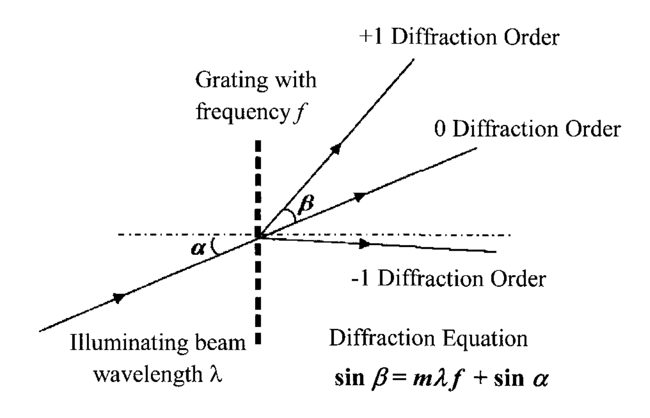


Fig. 2.11. Diffraction equation for a grating.

2.2.2.3 *Polarisation*

The electric field vector 'E' which describes the electromagnetic wave oscillates in a plane perpendicular to the propagation direction. If the direction of oscillation in the plane is in one direction, then the wave is said to be plane polarized (Fig. 2.12(a)). On the other hand if the oscillation of the light vector is random over time, the wave is said to be randomly polarized (Fig. 2.12(b)). Alternately, plane polarized light can be thought of light vector having two components along the two Cartesian axes which remains the same, while for randomly polarized light, the two components change randomly.

Polarized light can thus be written as:

$$\begin{aligned} E_x &= A_x \exp i(kz - \omega t + \phi_x) \\ E_y &= A_y \exp i(kz - \omega t + \phi_y) \end{aligned} \tag{2.20}$$

where E_x and E_y are the components of light vector along the x and y directions with amplitudes A_x and A_y and additional phases φ_x and φ_y respectively.

The resultant magnitude of the light vector is

$$E^2 = E_x^2 + E_y^2 = \frac{E_x^2}{A_x^2} - 2\frac{E_x E_y}{A_x A_y}\cos(\phi_y - \phi_x) + \frac{E_y^2}{A_y^2} = \sin^2(\phi_y - \phi_x) \quad (2.21)$$

Thus for plane polarized light $\varphi_y - \varphi_x = 0$, while for $\varphi_y - \varphi_x \neq 0$, we get elliptically polarized light, which becomes circularly polarized if $\varphi_y - \varphi_x = \pi/2$ and $A_x = A_y$. For randomly polarized light there is no relation between φ_x and φ_y which fluctuate randomly.

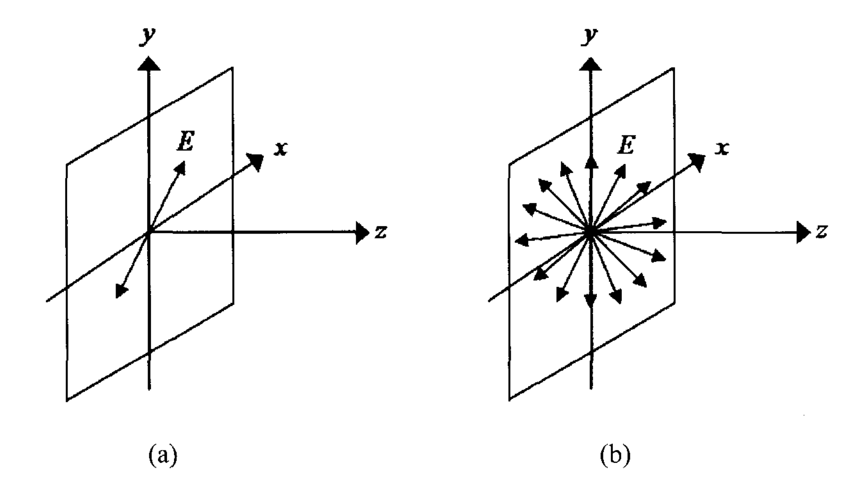


Fig. 2.12. (a) Plane polarized light. (b) Randomly polarized.

Light can be polarized in various ways – the most common being through the use of a Polarizer. Consider the schematic shown in Fig. 2.13. Randomly polarized light is incident on a polarizer whose polarization axis is vertical. The light vector emerging from the polarizer is parallel to the polarization axis. If a second polarizer is placed behind the first one with its polarization axes at an angle θ to that of the first one, the electrical field emerging from the second polarizer will be $E_0 \cos\theta$ and the intensity is $I = I_0 \cos^2\theta$ where E_0 and I_0 are the magnitude of

the electric field and intensity after the first polarizer. This is the Malus' law. If an optically active material (one that changes the polarization of the light) is placed between the two polarisers, the output intensity can be related to the optical activity of the material. This principle is used in Photoelastic method of stress analysis.

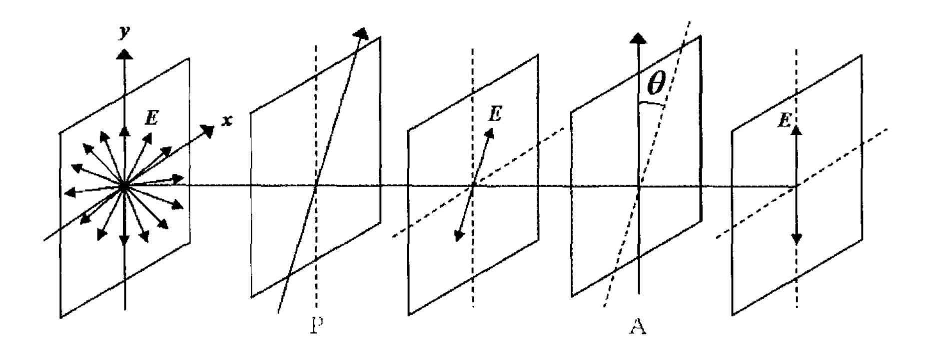


Fig. 2.13. Malus's law.

2.2.3 *Photonics*

Photonics has its basis on two phenomena – the absorption and emission of energy in discrete quantities leading to concept of a photon and the emission of electrons from the surface of materials depends on the photon frequency rather than the intensity of light – called the photoelectric effect. The first effect led to the development of novel light sources like the laser and LEDs while the second led to development of detectors and the now ubiquitous Charge Coupled Device (CCD) camera. Additionally, the first phenomenon is finding greater use in laser-material interaction such as Photodynamic Therapy (PDT) while the second phenomenon has shown application in Confocal and Multi-photon microscopy.

To explain these new observations, the concept of the photon as a quantum unit of the electric field was introduced in the early part of the last century. The photon is a packet of energy with both particle and wave characteristics. The energy of a photon is:

$$E_{ph} = h\nu \tag{2.22a}$$

where h is the Planck's constant.

Also the photon with zero rest mass has a momentum (p) associated with it given as:

$$p = \frac{h}{\lambda} \tag{2.22b}$$

The interaction of photon with matter can be explained by the Bohr's model. This model is similar to the planetary model of our solar system. The Neutrons and Protons of an atom form a dense mass at the centre of the atom similar to the Sun. The electrons orbit around this 'sun' like the planets. However, the electrons cannot take any orbit and also the orbits are quantized (discrete) rather than continuous. Each atom has its own discrete energy levels and the atom would thus absorb and emit light with specific frequencies seen by their absorption or emission spectra. Consider the schematic in Fig.2.14. An electron at energy level E_1 can absorb a photon and raise itself to E_2 provided the energy of the photon is:

$$E_{ph} = E_2 - E_1 = h\nu = \frac{hc}{\lambda} \tag{2.23}$$

Similarly as shown in Fig. 2.14(b), the electron at E_2 will drop down spontaneously to E_1 and emit a photon with a wavelength given by the same eqn. 2.23. Hence the absorption and emission frequencies are the same for a particular atom and helps distinguish it from other atoms. It was also proposed by Einstein, that there is a third kind of emission – called stimulated emission. In this case as shown in Fig. 2.14(c), an electron at a higher energy level can be stimulated by a photon to drop and in so doing emits a photon which is identical to the stimulating photon. Based on the energy conservation principle, it can be shown that the probability of absorption and stimulated emission of photons are equal and much smaller than the probability of spontaneous emission. The stimulated emission observation led to the development of the LASER, which is an acronym for Light Amplification by Stimulated Emission of Radiation. The early lasers were primarily gas lasers and

their efficiency (output power/input power) was very low. With the advent of solid state laser diodes, where the principle of operation is based on recombination of electrons and holes in a semi-conductor, the efficiency can be significantly raised. Furthermore, these laser diodes can efficiently provide the right input power to make the new generation Diode Pumped Solid State Lasers (DPSSL) more efficient, compact and powerful. While gas lasers still provide a very narrow bandwidth and large coherence, DPSS lasers are gradually replacing them in many applications. Lasers and their applications are discussed in more detail in a later chapter.

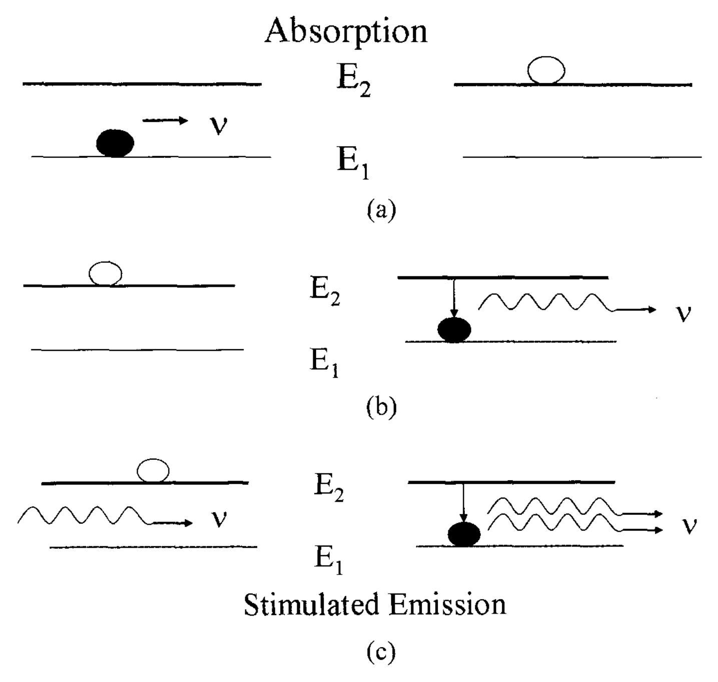


Fig. 2.14. Absorption, emission and stimulated emission of photons.

The photoelectric effect has led to the development of the CCD camera which have made great strides in recent years and all but antiquated the film. With the added advantage that the images are now available in digital form for processing and quantification of information that is required. The CCD is made up of rectangular elements called pixels, whose size and number determine the resolution and size of

image. The rectangular array of pixels necessitated by the readout scheme of the CCD, causes artifacts such as aliasing or moiré if the structured being imaged has a periodic pattern with a frequency (called the Nyquist frequency) greater than twice that of the CCD array. The smallest pixel size currently available is about 3 μm square while the size of the CCD array can range from 1/3 inch to 1 inch. The spatial frequency of the CCD camera is at best about 200 lines/mm, which is still much smaller than high resolution films used for x-ray and holography which have spatial frequencies of over 2000 lines/mm. However, the advantages gained by having the image in digital format can overcome some of these problems of digital cameras and they have also been used for holographic imaging.

2.3 Photomechanics

Photomechanics is thus the merging of two fields of optics and mechanics for measurement applications. As has been indicated from a mechanics point of view the stress, strain and displacement/deformation are quantities that would be of interest to scientists. All these three quantities are inter-dependent and hence measuring one of them in principle should permit the deduction of the other two. However stress and strain are abstract mathematically quantities and cannot be directly measured. Furthermore, to get strains from displacement/deformation, there is a need to differentiate the data. While digital methods are able to provide whole-field deformation map with great accuracy and sensitivity, numerical differentiation is still error-prone. Hence techniques have been developed to measure strain and stress indirectly. The most common method for strain measurement is the electrical resistance strain gauges. These gauges have been in use for more than 100 years and provide sensitive and accurate measurement of in-plane strain components on the surface of objects. They are based on the principle of a change in resistance due to a change in length (or strain). However the strain gauge is a point-wise method and can be cumbersome if whole-field strain determination is required. Also it is a contact method and not suitable for all applications. Optical methods are thus finding greater applications specifically in areas of micro, nano and

bio technology where electrical resistance gauges are either too big or cannot be used. In this section, some of the methods currently in used for optical strain analysis or photomechanics will be discussed. Some applications of this will come through in subsequent chapter which would if require go into more details of the subject.

As discussed in section 2.1, for a general 3-D problem there are 3 unknown deformation components from which the six independent strain components can be deduced and correspondingly the 6 independent stress quantities for an isotropic, homogeneous material. However most problems are simplified and traditionally, techniques are divided into in-plane and out-of-plane displacement measurement methods. For in-plane methods, generally the two displacement components 'u' and 'v' along the two Cartesian coordinates (x, y) are required. Since optical methods give whole-field deformation patterns, these displacement patterns are called the 'u-field' and 'v-field' patterns. Alternately for the in-plane measurement, there is a need to measure the three strain components and three stress components. For out-of-plane displacement, generally the parameters of interest are the out-of-plane displacement (w), the slope of the surface (dw/dx, dw/dy) and the curvatures which are the second derivatives of the displacement and have three components similar to strain and stress.

2.3.1 *Moiré and Grid Methods*

Moiré/Grid methods are a versatile set of techniques which can be adapted for in-plane and out-of-plane displacement, strain, slope and curvature measurement. One of the advantages is that this method provides a specific component independent of the others and thus makes interpretation easy. This depends on how the grid is created on the specimen to be measured. If the grid is directly imprinted on the surface of the specimen, in-plane components result, while if the grid is projected or reflected off the surface, out-of-plane components are obtained. Since, the components that are not to be measured, do not affect, the measured component, noise is also minimal. Finally moiré/grid methods can be explained by means of geometric optic concepts, physical/wave optics theory and also digitally using the aliasing effect alluded to earlier.

2.3.1.1 *Gratings and Moiré*

The moiré/grid methods utilize rectangular/square grids or gratings as displacement gauging elements. As was discussed in sec. 2.1, strains are defined as changes in length and changes in angle of a square element and hence moiré/grid methods can directly measure strain. For most metrological applications the gratings are primarily an array of equi-spaced dark and bright lines (line gratings) or a set of crossed lines or dots (cross gratings). Radial and circular gratings have occasionally been used as have colour gratings. The pitch, **(p)**, of a grating is the spacing between lines. The direction perpendicular to the grating lines is the Principal Direction of the grating. Sometimes the frequency, **f**, which is the inverse of the pitch, is used to identify gratings. The width of the dark and bright lines is also an important parameter. These are generally the same with their sum is equal to the pitch of the grating. Finally, while the preferred intensity along the principal direction of the grating is sinusoidal, binary gratings as well as other profiles have also been used.

Metrological applications generally utilize two initially identical gratings. One of them follows the deformation of the object or is in some way distorted by the specimen and is the specimen or deformed grating; while the other remains unchanged and is the reference grating. The two gratings need not be two physically different gratings but could be a record of the same grating before and after loading. In the moiré grid methods for deformation measurement, it is required to determine the changes in the grating pitch and relate these to the deformation causing these changes. This can be done by either looking at each element of the grating and monitoring the change in pitch and the angle between the lines as in the definition of strain. This is termed as the grid method and is only suitable if the pitch of the grating is large and there are only a few points to monitor. If whole field deformation map is needed, the moiré effect is invoked.

Moiré, referred to as aliasing in the computer vision community, is the pattern resulting from the superposition of two nearly similar gratings. Physically, consider two identical gratings which are superposed with the black lines of one grating exactly over the black lines of the second grating. The transmitted light intensity average over

one pitch is a maximum. If one of the gratings (deformed grating) is shifted in the principal direction by half the pitch, the resulting intensity is a minimum. This cycle is repeated. Thus the intensity is a maximum if the deformed grating displaces by Np where N is an integer. This is similar to the interference equation, where the wavelength of light is replaced by the pitch of the grating. Mathematically, consider the intensity transmitted by a sinusoidal grating of frequency f_1 which can be written as:

$$I_1 = A\{1+\sin(2\pi f_1 x)\} \tag{2.24a}$$

When the specimen deforms the frequency changes to f_2 and hence eqn. 2.24(a) becomes

$$I_2 = A\{1+\sin(2\pi f_1(x+u(x))\} \tag{2.24b}$$

where u(x) is the displacement of the grating from its original position.
Superposing, these two gratings, give the resultant intensity as

$$I = I_1 + I_2 = 2A\{1+\sin(2\pi f_1 x)\cos(\pi f_1 u(x)\} \tag{2.25}$$

If the frequency of the grating is high, such that it cannot be resolved by the imaging system then the resulting intensity can be simplified to

$$\begin{aligned} I &= 2A\{1+\frac{1}{2}\cos(\pi f_1 u(x))\} \\ &= 2A\{1+\frac{1}{2}\cos(\frac{\pi u(x)}{p_1})\} \end{aligned} \tag{2.26}$$

It is noted that the equations are vary similar to that obtained in interferometry (eqn. 2.15), where the pitch of the grating replaces the wavelength (λ) and the OPD is replaced by the displacement u(x). Hence bright and dark fringes follow similarly and the from the phase term we get the moiré equation:

$$u(x) = Np_1 \qquad \text{N} = 0, 1, \ldots \tag{2.27}$$

Note the grating is sensitive to displacement only in the principal direction, i.e. direction perpendicular to grating lines. Also, the sensitivity of the moiré method depends on the pitch of the grating – smaller the pitch, higher the sensitivity. Based on the pitch, optical moiré methods have been historically classified into – grid methods, moiré methods and moiré interferometry. For the grid methods, the pitch of the grating is greater than 1 mm. Moiré methods utilize gratings with a pitch in the range of 0.01 mm to 1 mm; while in moiré interferometry the grating pitch is smaller than 0.01 mm, with the smallest value of half the wavelength of light. Currently, it is possible to make gratings with pitch smaller than the wavelength of light. Indeed the naturally occurring periodic structures of crystals are gratings as well. In these cases we use the aliasing features of the scanning microscopes as a means to generate so-called nano-moiré methods. The difference between these methods is the way in which the information is delineated and displayed. In the grid method, the individual gratings are analyzed separately and their differences obtained. No moiré is visually displayed although the difference between the two gratings when displayed would correspond to a moiré pattern. In the moiré method, geometrical optics formulation in the form of obstruction of light is used to explain the formation of the moiré fringe pattern. In moiré interferometry, diffraction and interference form the basis of fringe formation. Regardless of these differences in explanation of fringe formation all the techniques provide the same information; i.e. contour maps of object deformation following eqn. (2.27).

A slew of moiré methods are available and broadly classed under in-plane and out-of plane methods. For in-plane deformation and strain analysis, the specimen grating is printed on or bonded to the specimen and deforms in unison with the underlying specimen. In the out-of-plane methods, a grating is 'projected' onto the specimen, whose profile, slope or curvature distorts the grating to form the specimen grating. These specimen gratings are interrogated with a reference grating to show the moiré patterns of deformation. Typically, for in-plane displacements, high frequency gratings (>100 lines/mm) are required while for out-of-plane displacements, coarser gratings (<100 lines/mm) suffice.

2.3.1.2 *In-plane Deformation Measurement*

For in-plane deformation measurement, creating the specimen grating is a critical and important task. The easiest and most widely used approach is to transfer the grating from a film or glass mold onto the specimen via epoxy. For high frequency gratings, a simple yet elegant replication approach using low viscosity adhesives has been developed. Lithography offers an alternative to creating very high frequency gratings as does ion-beam etching. Gratings for in-plane deformation and strain measurement are cross gratings with grating lines in two perpendicular directions since there is a need to get the two in-plane displacement components. The reference grating can either be a physical grating placed in close proximity to the specimen grating, or a virtual grating created by the interference of two plane waves incident at equal and opposite angles to the specimen grating, or it could be the sampling period of the imaging system. The first approach is applied for gratings which are relatively coarse, the second method is suitable for optical moiré interferometry, while the third approach preferred for nano-moiré.

Fig. 2.15(a) shows the schematic of a typical set-up for a moiré interferometer. Both the u and v fields can be recorded sequentially. Fig. 2.15 (b, c) shows a typical moiré pattern recorded on a dentine sample subject to compression. The displacement components along the horizontal (u-field) and vertical (v-field) directions are shown. The relative displacement between two adjacent fringes is equal to the pitch of the reference grating, which in this case is 0.417 μm. Note that it is not possible to get the absolute displacement unless the displacement at one point is known. Also the sign of displacement is not apparent from these patterns; i.e. from the fringe pattern we cannot tell whether the specimen is subject to tension or compression. However, as discussed earlier, strains are more important for in-plane cases. Strains can be readily obtained at any point by measuring the spacing between adjacent fringes and since the relative displacement between these fringes is known to be the pitch of the reference grating, the strain, gradient of displacement is given as:

$$\varepsilon_x = \frac{\partial u}{\partial x} = \frac{p}{S_x^u}$$
$$\varepsilon_y = \frac{\partial v}{\partial y} = \frac{p}{S_y^v} \tag{2.28}$$
$$\gamma_{xy} = \frac{\partial u}{\partial y} + \frac{\partial v}{\partial x} = \frac{p}{S_y^u} + \frac{p}{S_x^v}$$

where S is the fringe spacing in the x or y direction from the u- or v-field fringe patterns.

Of course this process might be tedious if a whole-field distribution is preferred but as will be discussed later image processing algorithms can help in this regard.

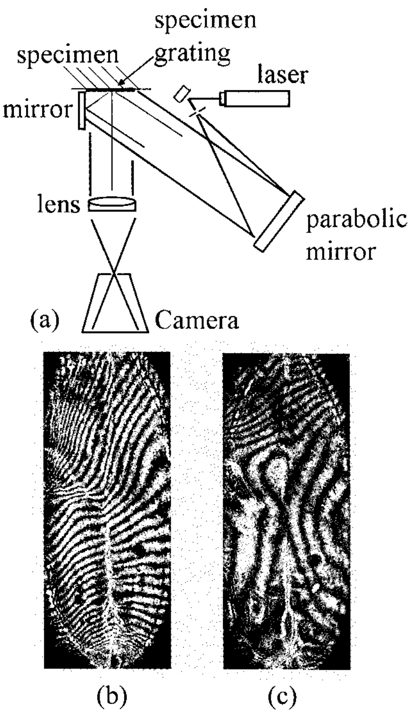


Fig. 2.15. (a) Schematic of moiré interferometer. Moiré interferometric fringes for deformation of dentine subject to mechanical load (b) u-field and (c) v-field fringe patterns.

2.3.1.3 *Out-of-plane Displacement Measurement*

For out-of-plane measurement, the grating is 'projected' on to the specimen whose surface profile distorts the grating to create the specimen grating. This is interrogated with a reference grating to give contours of out-of-plane displacement component. The straightforward way would be to project a grating on to the specimen using a projector. With the availability of digital projectors, it is now easy to create the grating in the computer and manipulate it as desired for a specific application. Indeed the possibility of using colour gratings becomes easy and provides an added dimension to the moiré method. The distorted image is recorded at an angle (α) to the projection direction (Fig. 2.16). As can be seen from the schematic in Fig. 2.16, a depth variation (Δz) causes a shift in the grating image (Δx) on the image plane. From simple triangulation it can be shown that for a grating of pitch 'p',

$$\Delta x = \Delta z \tan\alpha = Np \qquad where\ N = 0, \pm 1, \pm 2.... \tag{2.29}$$

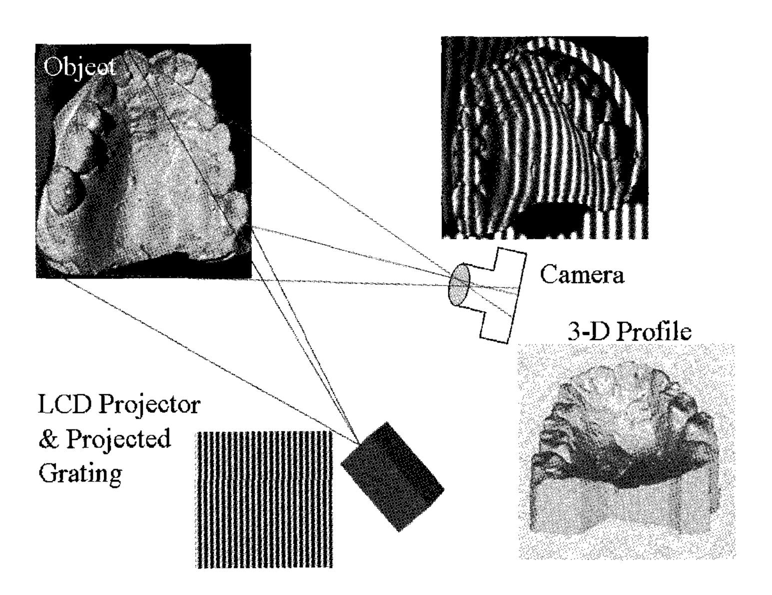


Fig. 2.16. Projection grating principle.

Fig. 2.17(a) shows a typical distorted image recorded of dental cast. The distorted image when superposed with a reference grating (Fig. 2.17(b)) generates the moiré pattern shown in Fig. 2.17(c). These fringes are contours of out-of-plane displacement with the relative out-of-plane displacement of p/tan α between adjacent fringes. For out-of-plane deformation, it is generally necessary to know the absolute displacement. Hence, there is a need to find a point where the displacement is known or equal to zero from which the fringes could be numbered sequentially. Of course, it is also important to know the sign of the fringes to distinguish a hill from a valley. Use of computer generated gratings has the added benefit that it is amenable to manipulation with no moving parts which makes data processing and analysis simpler and easier to implement.

Other out-of-plane sensing methods using gratings are the shadow moiré method and the reflection moiré method. In the shadow moiré method, the shadow of a grating is distorted by the surface profile of the object. This distorted shadow (specimen) grating when viewed through the original grating creates a moiré pattern which provides the surface profile of the object. Fig. 2.18(a) is an example of the shadow moiré fringe pattern showing the pressure distribution under the foot over a typical step. Shadow moiré has also been used as alternative for scoliosis detection in children. Another method is the reflection moiré method. As its name suggests, it is only applicable to reflecting objects. A grating when viewed through the specular object is distorted due to variations in the slope of the surface. Reflections on glass windows of high rise buildings show this kind of distorted images of the neighbouring building. Fig. 2.18(b) is the reflection moiré pattern showing warpage of a Si wafer due to thin film stress. Indeed moiré patterns are all around us and it would be educational to try to interpret a moiré pattern seen in our daily lives (Fig. 2.18(c)).

2.3.2 *Speckle Methods*

While moiré utilizes periodic patterns called gratings, speckle methods use random patterns for displacement sensing. Hence while in

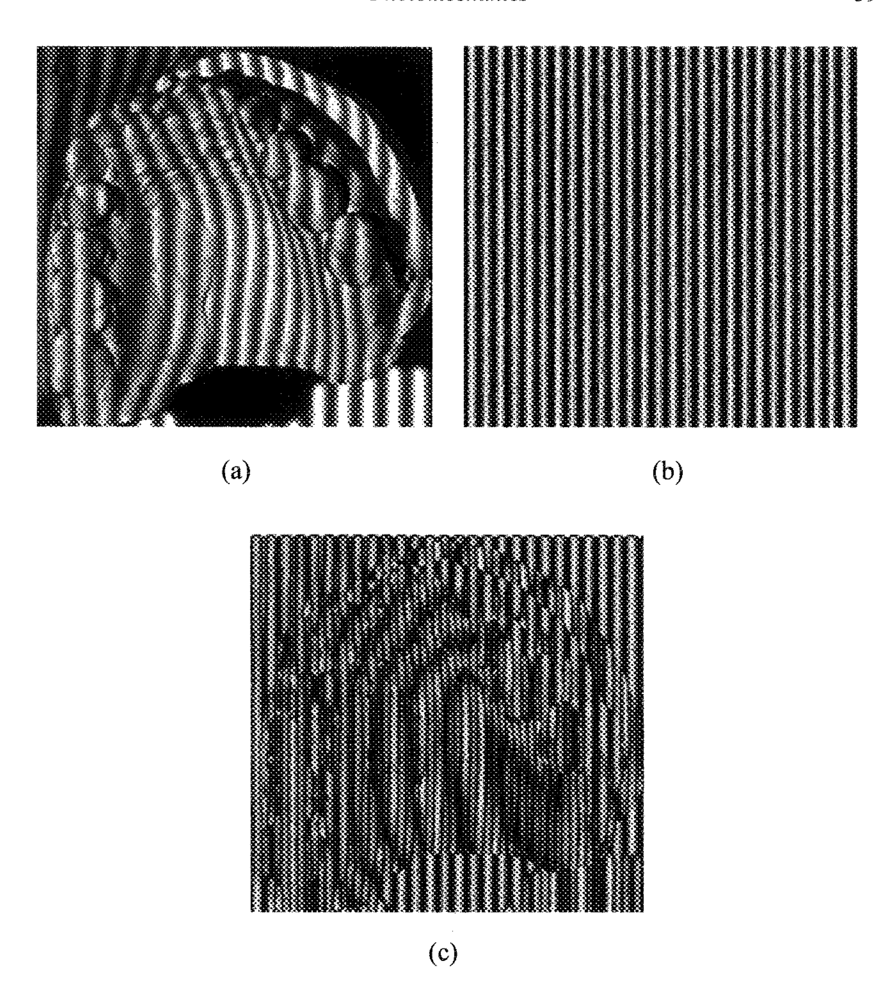


Fig. 2.17. (a) Projected grating distorted by shape of dental cast. (b) Reference grating. (c) Moiré fringes formed by superposition of projected and reference grating.

the moiré method, the displacement component are readily visualized, speckles being a random distribution of dark and white spots does not always exhibit this kind of fringe pattern. There are cases when the random pattern does show some specific moiré-like patterns. Nevertheless for quantification, there is a need for optical or numerical filtering. However, for speckle methods, surface preparation is minimal and straightforward. Hence while the moiré method requires good

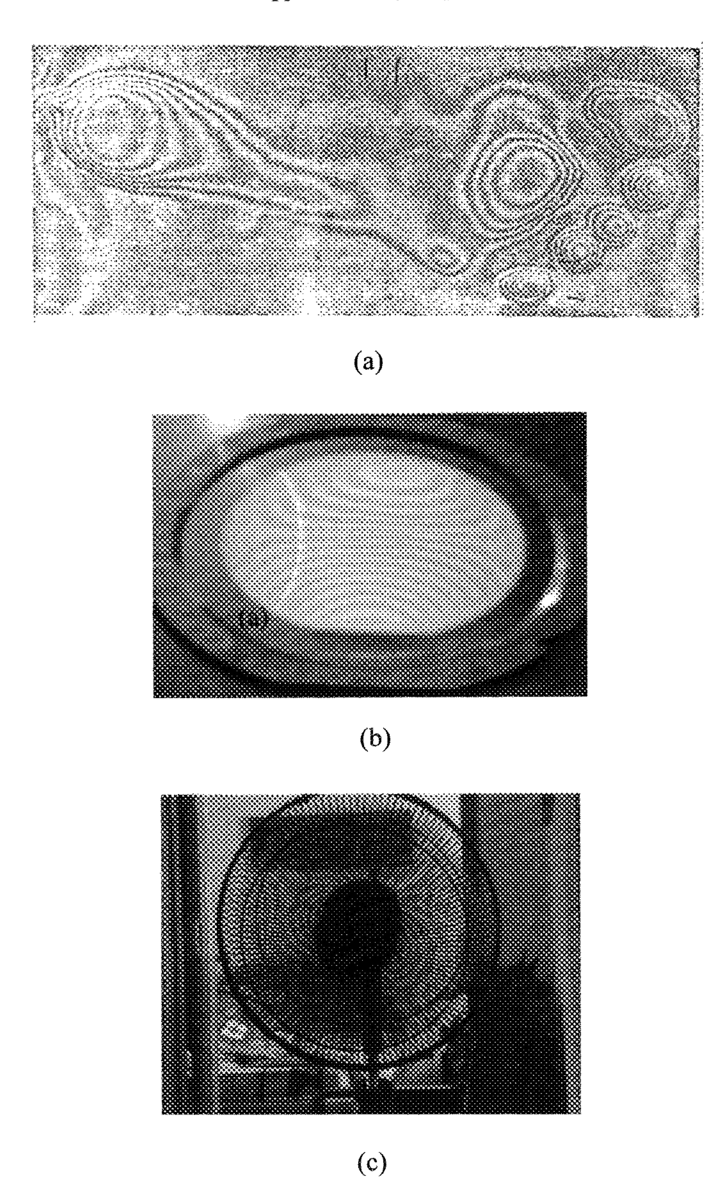


Fig. 2.18. (a) Shadow moiré fringes depicting pressure distribution for a complete gait cycle. (b) Reflection moiré fringes showing warpage of Silicon wafer. (c) Moiré fringes in nature.

specimen preparation, the fringes seen are easily interpreted, while in speckle methods, surface preparation is minimal but at the cost of increased image processing computation. Speckles come in three flavours–laser speckles, white light speckles and sampled speckles. Laser speckles are due to multiple interference of coherent laser light scattered from a diffuse object. White light speckles are physically created random pattern on the object. These could be due to surface preparation, example, painting the surface with black and white spots or could be due to the natural texture of the surface. Finally sampled speckles are due to the sampling nature of current imaging systems. The sensitivity of the speckle method depends on the size of the speckles which depends on the type of speckle, the recording method and resolution of recoding media. For laser speckles the speckle size (σ) is given as

$$\sigma = \frac{\lambda}{2NA} \tag{2.30}$$

where NA is the effective numerical aperture. If a lens is used to record the speckle pattern then the numerical aperture is inversely proportional to the F/# of the lens (Fig.2.19(a)), while if no lens is used to record the objective speckle, NA = 2L/D where L is the distance from the object to screen and D is the size of the object (Fig 2.19(b)).

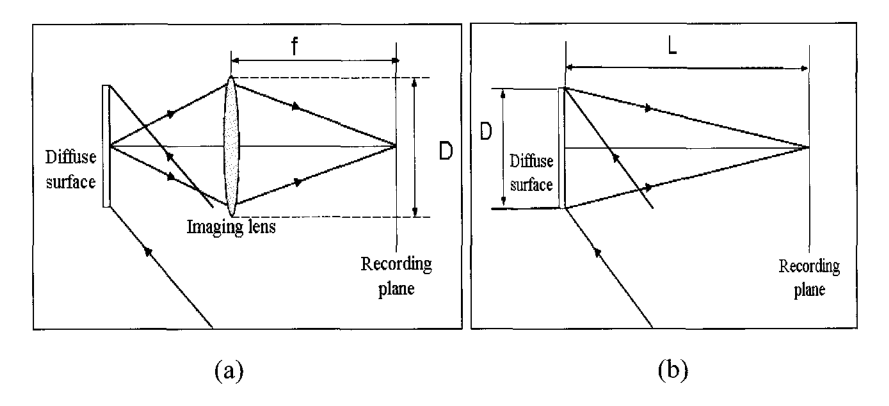


Fig. 2.19. (a) Subjective speckles (b) Objective speckles.

For white light speckles, the speckle size is first dependent on the size of speckles created on the object surface and then limited by the recording system as for laser speckles. Finally for sampled speckle, the speckle size is governed by the pixel size of the recording system. In speckle methods for deformation measurement, two exposures of the object before and after deformation are recorded, Depending on how the speckle patterns are recorded, as with the moiré method, speckle methods can be applied to wide variety of measurements from in-plane to out-of plane for static and dynamic cases. The difference as mentioned earlier is in the extraction of the information from the speckle pattern. This will be explained below for the in-plane and out-of-plane displacement measurements as they follow slightly different approaches.

2.3.2.1 *Speckle Photography*

In speckle photography two speckle patterns are recorded before and after deformation. This so-called double exposed specklegram can be interrogated in two ways to determine the displacement components in two perpendicular directions. The first is the pointwise filtering method. As the name suggest, a laser beam illuminates a point on the specklegram. The speckle before and after deformation can be thought of as two apertures, which when illuminated by a beam of light, generate an interference pattern (Young's fringes) whose spacing and orientation gives the displacement components as:

$$u = \frac{\lambda L}{S_x} \qquad v = \frac{\lambda L}{S_y} \tag{2.31}$$

where u, v are the displacement components and S_x and S_y are the fringe spacing in the x and y direction respectively, L is the distance from the specklegram to the screen. Interrogating the speckle pattern over the entire film provides the displacement components at all points from which the strain can be deduced as discussed earlier. Alternately, the specklegram can be placed in an optical filtering set-up to provide

whole-field fringes similar to the moiré fringe pattern. An aperture placed at a distance 'r' from the optical axis at the Fourier plane filters a specific frequency from the speckle pattern. Effectively, this corresponds to having a specimen with a grating with an effective pitch (p_{eff}) given by

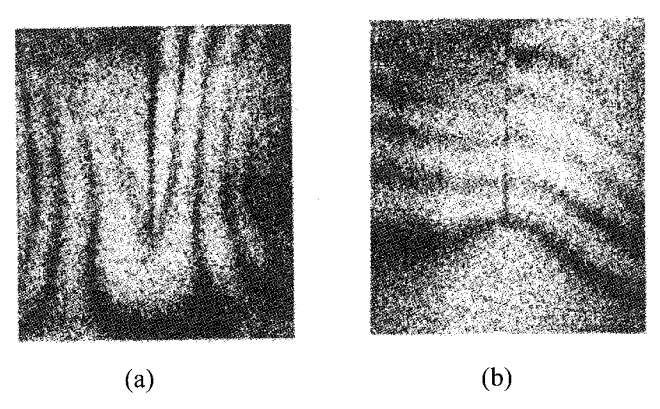
$$p_{eff} = \frac{\lambda f}{r} \tag{2.32}$$

where f is the focal length of the Fourier lens.

The pattern seen through this gives a fringe pattern which provides contours of displacement component in the 'r' direction. Thus if the speckle pattern is filtered along the x and y direction at distances r_x and r_y, the u and v displacement components can be written as

$$u = n\frac{\lambda f}{r_x} \qquad n = 0, \pm 1, \pm 2.... \qquad v = n\frac{\lambda f}{r_y} \tag{2.33}$$

A typical u and v field fringe pattern is shown in Fig. 2.20. The speckle method has the advantage that the effective grating pitch can be selected after recording, while in the moiré method the sensitivity, i.e. the pitch is pre-selected. However, the speckle fringe pattern is noisier than the moiré pattern since the unwanted frequencies are also present.



(a) (b)

Fig. 2.20. (a) u and (b) v field deformation fringes from wholefield filtering.

2.3.2.2 *Speckle Interferometry*

Speckle interferometry is only possible with laser speckles since we need a coherent light source for interferometry. The experimental set-up is similar to the Michelson interferometer, except that the specimen is a diffuse surface. The reference beam could also be speckled or can be a plane beam reflected off the mirror. As with conventional two beam interferometer, we can write the intensity of the interference pattern between the speckled object beam and the reference beam as:

$$I_1 = A_1^2 + A_2^2 + 2A_1A_2\cos\phi \tag{2.34a}$$

where A_1 and A_2 are the amplitudes of the object and reference beam and φ is the random phase difference between the speckled object beam and the reference beam.

When the object is deformed an additional phase difference δ is introduced and hence the interference intensity becomes:

$$I_2 = A_1^2 + A_2^2 + 2A_1A_2\cos(\phi + \delta) \tag{2.34b}$$

These two patterns are recorded digitally and stored in a computer. The absolute difference between the two patterns gives:

$$I_r = 4A_1A_2\left|\sin(\phi + \frac{\delta}{2})\sin\frac{\delta}{2}\right| \tag{2.34c}$$

This expression is very similar to that obtained for the moiré superposition of two gratings. The intensity will be zero if $\delta = n\pi$.

Figure 2.21 (a) and (b) show the two speckle patterns before and after loading and Fig. 2.21(c) shows their difference. As with the interferometer configuration, the phase difference δ is related to the out-of-plane displacement (w) as

$$\delta = \frac{2\pi}{\lambda} w = n\pi$$

or (2.34d)

$$w = \frac{n\lambda}{2}$$

Indeed, if the illuminating beam were not incident at normal incidence, the method would be sensitive to both the in-plane and out-of-plane displacement components. This will be exemplified in the discussion in the next section on holographic interferometry. Furthermore as with the moiré methods, by shearing two object beams, the derivative of displacements can be measured. Indeed due to its similarities with the moiré method, essentially all set-ups realized in the moiré method can be duplicated. However, since the data reduction is not straightforward, shadow speckle and reflection speckle may not yield quantitative results as simply as their counterparts in the moiré method.

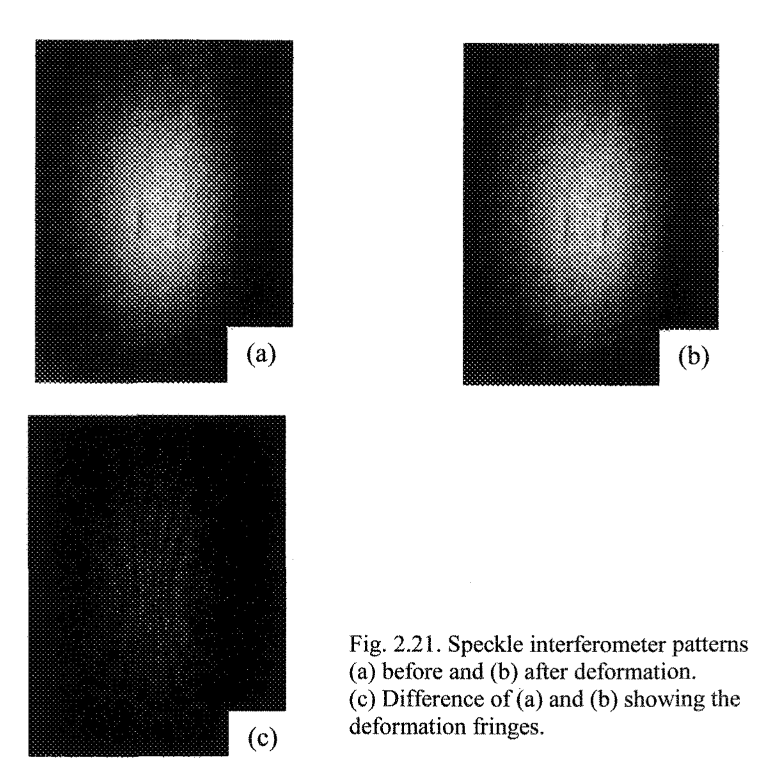


Fig. 2.21. Speckle interferometer patterns (a) before and (b) after deformation. (c) Difference of (a) and (b) showing the deformation fringes.

2.3.3 *Photoelasticity*

Photoelasticity uses the birefringent (or double refraction) property of some materials to visualize and quantify the principal stress difference. When polarized light is incident on a birefringent material, the light is split into two components along two perpendicular directions which have different refractive index. Some materials such as quartz and mica exhibit this phenomenon in their natural state (permanent birefringence), while other materials such as epoxy and glass become birefringent under stress (temporary birefringence). If the birefringence is due to load or stress, the two axes along which the light propagates coincide with the principal stress directions and the refractive index is proportional to the stress intensity in these two directions.

2.3.3.1 *Stress Optic Law*

Thus in the unstressed state, the index of refraction (n) is the same value throughout the material. While in the stressed state, the index of refraction in the direction of principal stress σ_1, σ_2 are different, n_1 and n_2. Thus according to the Stress Optic Law, which has similarities with the stress-strain law described earlier,

$$\begin{aligned} n_1 - n &= C_1\sigma_1 + C_2\sigma_2 \\ n_2 - n &= C_1\sigma_2 + C_2\sigma_1 \end{aligned} \tag{2.35a}$$

where C_1, C_2 are the Absolute Stress Optic Coefficients. Combining the two equations gives

$$n_1 - n_2 = (C_1 - C_2)(\sigma_1 - \sigma_2) = C(\sigma_1 - \sigma_2) \tag{2.35b}$$

where C is the Relative Stress Optic Coefficient

The phase difference between the two beams can be written as:

$$\delta = \delta_1 - \delta_2 = \frac{2\pi d}{\lambda}(n_1 - n_2) \tag{2.35c}$$

where d is the thickness of the specimen

The Relative Retardation between the two beams is defined as

$$\frac{\delta}{2\pi} = \frac{d}{\lambda}(n_1 - n_2) = \frac{dC}{\lambda}(\sigma_1 - \sigma_2)$$

or (2.35d)

$$(\sigma_1 - \sigma_2) = \frac{\phi}{2\pi}\frac{\lambda}{C}\frac{1}{d}$$

This leads to the Relative Stress Optic Law:

$$(\sigma_1 - \sigma_2) = \frac{Nf_\sigma}{d} \tag{2.36a}$$

where N = $\alpha/2\pi$, is the fringe order, $f_\sigma = \lambda/C$ is the material fringe constant.

Since the principle stress difference is one half the maximum shear stress, the Stress Optic Law in shear becomes

$$\tau_{\max} = \frac{(\sigma_1 - \sigma_2)}{2} = \frac{Nf_\tau}{d} \tag{2.36b}$$

where f_τ is the material fringe value in shear.

Similarly using the stress-strain equations, the Strain Optic law is:

$$(\varepsilon_1 - \varepsilon_2) = \frac{Nf_\varepsilon}{d} \tag{2.36c}$$

where $f_\varepsilon = f_\sigma(1 + \nu)/E$ is the material fringe value for strain.

2.3.3.2 *Plane Polariscope*

In order to visualize the fringe pattern due to the phase difference between the two mutually perpendicular beams propagating through the specimen, the simplest set-up is a plane polariscope as shown in Fig. 2.22. Randomly polarized light is incident on the polarizer. The light

exiting the polarizer is polarized in the direction of the polarization axis, P. It then impinges on the birefringent specimen in which it is split into two components along the principal stress direction and propagates with different velocities due to the difference in refractive index. The analyzer then recombines the two beams to show the interference pattern depicting the phase difference between the two beams. The intensity of light emerging from the analyzer whose polarization axis is oriented at an angle, β to the polarization axis of the polarizer can be written as:

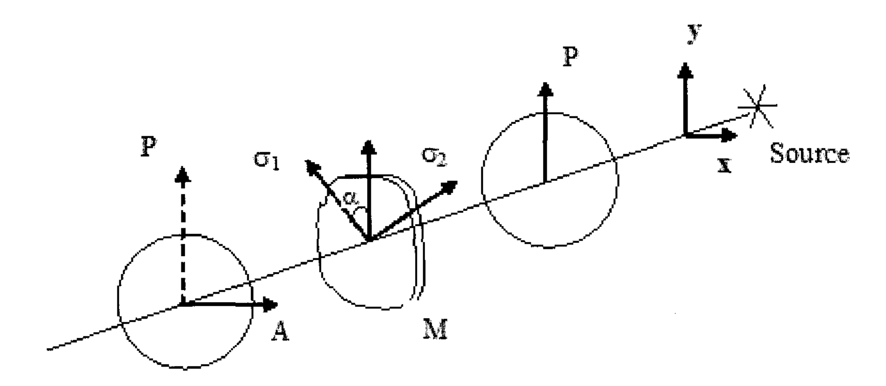


Fig. 2.22. Schematics of plane polariscope.

$$I = I_0\left(\sin^2\beta\cos^2{\delta/2} + \sin^2(2\theta-\beta)\sin^2{\delta/2}\right) \tag{2.37}$$

where θ is the angle between the polarization axis of the polarizer and the principal stress direction.

For stress analysis, two configurations are commonly used. In the dark field arrangement, the axes of the polarizer and analyzer are crossed, i.e. β = 0

$$I = I_0\left(\sin^2 2\theta\sin^2{\delta/2}\right)$$

The intensity, I will be zero if

$$\sin 2\theta = 0 \Rightarrow 2\theta = 2\pi \Rightarrow \theta = {n\pi}/{2}$$

This will occur at points where the principal stress direction coincides with the axis of the polarizer. These dark lines are called ISOCLINICS, i.e. loci of points with the same inclination of principal stress.

The resultant can also be zero if

$$\sin {\delta}/{2} = 0 \Rightarrow {\delta}/{2} = n\pi \qquad n = 0, 1, 2 \cdots$$

$${\delta}/{2\pi} = n = N = {d}/{f_\sigma} (\sigma_1 - \sigma_2)$$

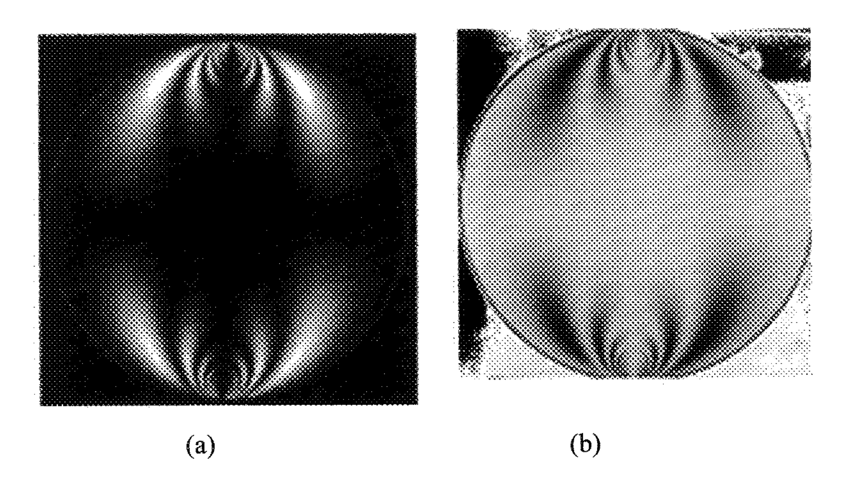
These correspond to points where the principal stress difference magnitude is such that the resultant intensity is zero. These fringes are the ISOCHROMATICS.

The other set-up has the axis of the polariser and analyzer parallel to each other and is called the light-field arrangement or parallel polariscope. Substituting ($\beta = \pi/2$) into eqn. (2.37) gives

$$I = I_0 \left(\cos^2 \frac{\delta}{2} - \cos^2 2\theta \sin^2 {\delta}/{2} \right)$$

The distinction between the two sets of fringes is not so distinct in this case, except if the term involving the isoclinic angle is zero. In this case, this pattern gives the complement of the dark field fringe pattern. Thus at dark fringes in the dark-field pattern become bright fringes here. Figure 2.23 (a) and (b) show the photoelastic fringes for a disk under compression for the dark field and light field polariscopes. For the dark field polariscopes two sets of fringes corresponding to the isoclinics and isochromatics are clearly seen. While both sets are required for a full stress analysis, it would be desirable if they could be obtained separately. To obtain the isoclinics only, one possible way is to apply a very small load. Since the directions of principal stresses are independent of the load, they would appear the same. However, the number of isochromatics would be substantially smaller. On the other hand to

observe only the isochromatics, use is made of a crosses circular polariscope described below. It is possible to obtain a fringe pattern from two plane polariscope pictures but how it can be done is left to the interested reader.



(a) (b)

Fig. 2.23. (a) Dark field fringe pattern showing isochromatics and isoclinics. (b) Bright field fringe pattern.

2.3.3.3 *Circular Polariscope*

In the crossed circular polariscope shown in Fig. 2.24, two additional elements are added before and after the specimen. These are the circular polarisers or quarter wave plates. As discussed earlier, these wave-plates convert the plane polarized light to circularly polarized light. The two circular polarizes are placed in opposite sense such that the first converts the plane polarized wave to circularly polarized and the second converts circularly polarized to plane polarized. They effectively cancel out each other. However, the specimen sees circularly polarized light incident on it and hence is unable to obtain a reference direction for the isoclinics. Thus the isoclinics are eliminated.

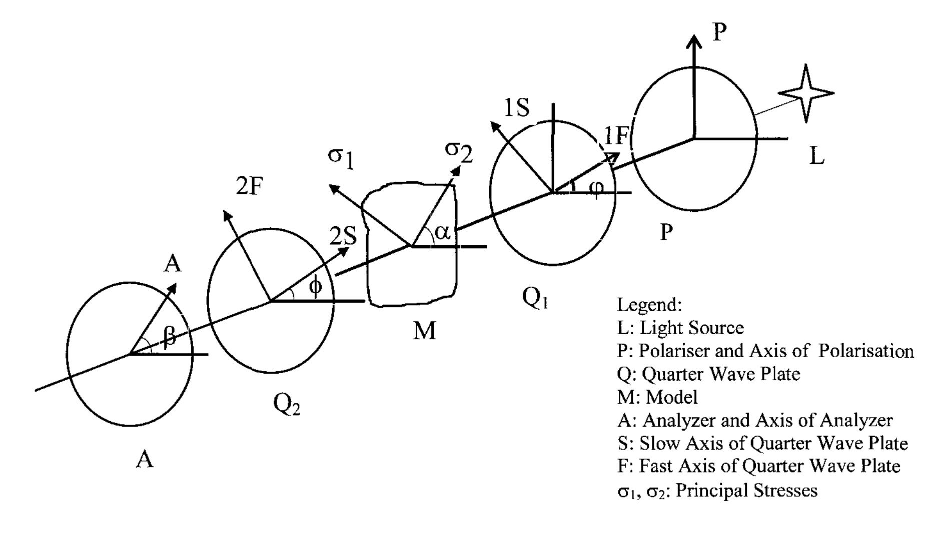


Fig. 2.24. Schematic of circular polariscope.

For an arbitrary orientation of the analyzer, the final intensity emerging from the analyzer can be written as:

$$I = I_0\{1 - \cos 2\gamma \cos\delta - \cos 2\theta \sin 2\gamma \sin\delta\} \tag{2.38}$$

where (γ + 90) is the angle between the analyzer direction and the polarizer axis.

Thus for the dark field arrangement, $\gamma = 0^0$ and hence the intensity is

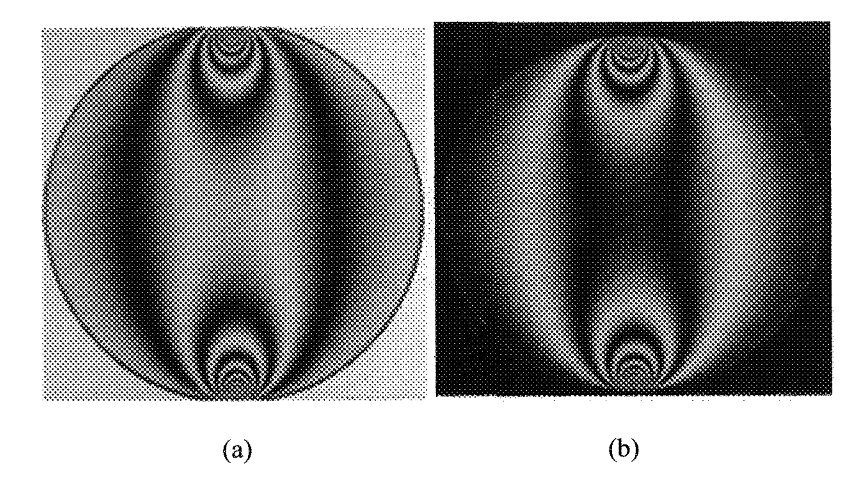
$$I = I_0(1 - \cos\delta) = \frac{I_0}{2}\sin^2\frac{\delta}{2}$$

Hence only the isochromatics are seen with the same equation as for the plane polariscope and dark fringes are seen for $\delta/2 = n\pi$, where n takes integer values

For the bright field arrangement, $\gamma = 90^0$, and hence the intensity of light emerging from the analyzer becomes

$$I = I_0(1 + \cos\delta) = \frac{I_0}{2}\cos^2\frac{\delta}{2}$$

In this case dark fringes are seen when $\delta/2 = (n + 1/2)\pi$. This shows that the bright fringes in the dark field set-up become dark in the bright field set-up as shown in Fig. 2.25. Before the advent of digital image processing methods, only the dark fringes were used for analysis and hence the dark field and bright field fringes gave fringe orders in increments of 0.5 instead of 1 if only the dark fringes were used. The Tardy method along with eqn (2.38), was subsequently developed to obtain fractional fringe orders with much higher sensitivity could be determined. Current digital photoelastic methods attempt to solve eqn. (2.38) to obtain both the isoclinic and isochromatics over the whole field.



(a) (b)

Fig. 2.25. (a) Dark and (b) Bright field fringe patterns of a disk under compression.

2.3.3.4 *Fringe Analysis and Interpretation*

Prior to using photoelasticity for stress analysis, the material needs to be calibrated, i.e. the value of f_σ needs to be determined. This is done by using a calibrating specimen, which is one where the stress at a point in known from theory. One of these specimens is a disk under compression, similar to the one shown in Fig. 2.25. The principal stress difference along the horizontal diameter is given as:

Typically in the calibration process, the fringe order v/s the principal stress difference is plotted and the slope of the line is proportional to the material fringe value f_σ, once f_σ is determined, the next step is to determine the principal stress difference for the specimen under stress. Generally, for most stress analysis problems, the maximum stress areas are of interest. These correspond to regions where the fringe density is high. Also, generally the maximum stress is found at the boundaries of the specimen. At a boundary, it is known that the principal stress directions are parallel and perpendicular to the normal at the boundary. This can be verified by observing the intercept of the isoclincs with the boundary. Hence the principal stress directions are known and the isoclinics are not required. A crossed circular polariscope can be used to determine the principal stress difference if the fringe order can be determined. Determination of fringe orders is not straightforward for general stress analysis problems. However, in many cases this can be done quite readily. One of the first issues is to find the zero fringe order. For this, generally white light illumination is used. Phase difference depends on the wavelength of light and except for the case when the phase difference is zero, this is a function of the wavelength of light. Hence the zero order fringe will be black, while the other fringes will be colored (Fig. 2.26).

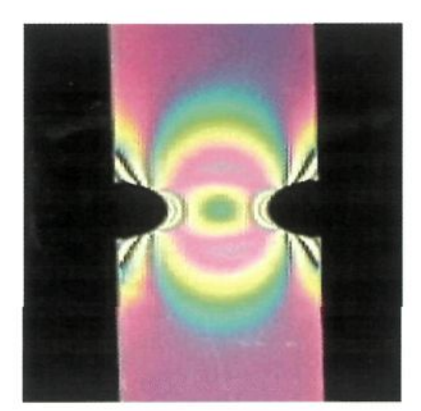


Fig. 2.26. Colour photoelastic fringes depicting isochromatics around a notch. The black fringe indicates the zero order fringe.

This is a simple method for determination of the zero fringe order. Once the zero fringe order is determined, light of one wavelength is used to get a gray scale image for other fringe order determination. While it is possible to use the color image itself to determine the fringe order, the technique is still not adopted due to lack of quantitative objective color measurement schemes for whole-field processing. Fringe orders increase/decrease monotonically. Hence once the zero order fringe has been determined, the next dark fringe has fringe order 1 and so on. Fringe orders are positive which means that $\sigma_1 \geq \sigma_2$. This means that the fringe orders cannot distinguish tensile stress from compressive stress. One suggested approach to determining the sign of the boundary stress is to apply a compressive stress at the point on the boundary a sharp object point. If the stress within the sample is tensile, the compressive stress would add on to it resulting in an increase in fringe order. In the case of Fig. 2.26, using symmetry and the knowledge that the stress increases as we approach the notch enables one to order the fringes increasing from the zero order fringe to the point of maximum stress. The fringes provide the principal stress difference or the maximum shear stress and the orientation of the principal stress. To separate the stress components, numerical or other experimental methods have been proposed. As mentioned earlier, the stress on the boundaries is usually the highest and at the boundary, the principal stress normal to the boundary is zero. Hence it is relatively simple to get the unknown principal stress.

2.3.4 *Holography*

Holography uses interference to store the object wave, i.e. the amplitude and the phase and diffraction to play back the object wave as if it were emanating from the object itself. Since the reconstruction is done after the recording process, there is no need for an imaging lens. This was the motivation behind the Nobel prize winning development of holography by Gabor who found the aberration of lenses are the limiting factor in electron microscopy. As has been shown earlier, interference enables recording of the phase difference between the object beam and a reference beam. Hence if the reference beam was used to reconstruct the interference pattern, the object amplitude and phase would be

reconstructed by diffraction. This is exemplified in Fig. 2.27, which shows that interference between two plane waves gives a fringe pattern whose spacing depends on the angle between the two interfering beams. If this interference pattern is illuminated by one of the reference beam, the diffraction equation shows that the angle of diffraction (Fig. 2.27) is in the same direction as the original object beam. Mathematically, we can write the interference equation between the object and reference beam as:

$$H(x,y) = O^2(x,y) + R^2(x.y) + O(x,y)R^*(x,y) + O^*(x,y)R(x,y) \quad (2.39)$$

where H(x,y) is the recorded hologram, O(x,y), is the object wave, R(x,y) is the reference wave and * indicates complex conjugate.

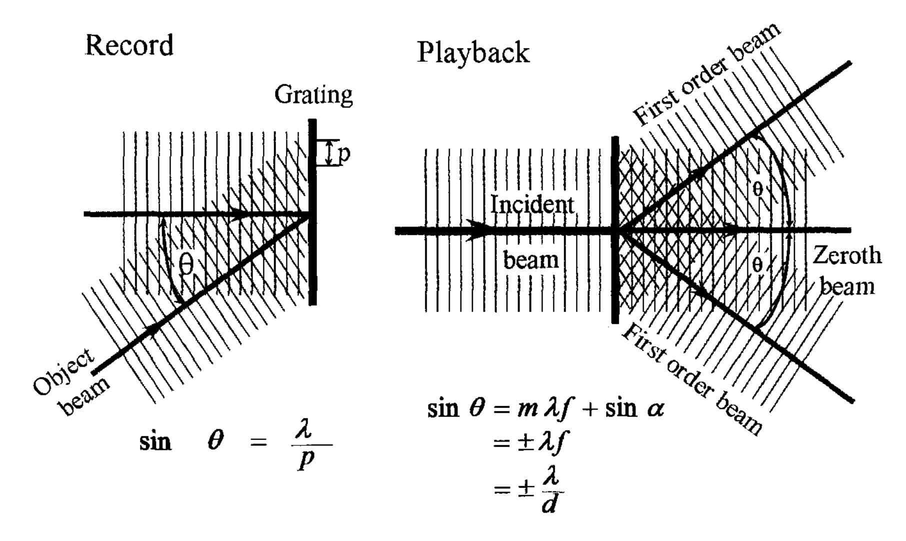


Fig. 2.27. Interference and diffraction for recording and reconstruction of holograms.

If the hologram is illuminated by the reference beam, the resultant wave (Ur) emerging from the hologram is

$$\begin{aligned} Ur &= (O^2 + R^2)\,R + OR^*R + O^*RR \\ &= (O^2 + R^2)\,R + OR^2 + O^*RR \end{aligned} \quad (2.40)$$

Here the first term replays the reference wave, which is also the undiffracted wave. The second term gives the object wave, while the third term is the conjugate of the object wave. Thus we see that the object wave stored in the hologram is reconstructed in its entirety by illuminating the hologram with the reference beam. This means that it is possible to see the object as if it was actually there in its full 3-D glory. Holography has thus found tremendous commercial applications for 3-D display. Other applications include data storage and Interferometric measurement.

2.3.4.1 *Holographic Interferometry*

As with other photomechanics methods discussed earlier, holographic interferometry needs to record two holograms – one before deformation and the other after deformation. Consider the holographic set-up shown in Fig. 2.28(a). Let the object wave before and after deformation be $O_1(x,y) = A\exp(i\varphi_1(x,y))$ $O_2(x,y) = A\exp(i\varphi_2(x,y))$, and where A is the amplitude and φ is the phase. The interference of these two object waves when the double exposed hologram is reconstructed gives the familiar interference fringes whose intensity is given by

$$I = 2A^2\{1+\cos(\phi_1-\phi_2)\} \tag{2.41}$$

The phase difference $(\varphi_1 - \varphi_2)$ is related to the deformation of the object. To understand this relationship, consider a point, P on the object which after deformation moves to P' as shown enlarged in Fig. 2.28 (b). The optical path difference is thus related to the phase difference and can be derived as

$$(\phi_1-\phi_2) = \frac{2\pi}{\lambda}\mathbf{d}(\cos\alpha+\cos\beta) = \frac{2\pi}{\lambda}2\mathbf{d}\cos\gamma\cos(\frac{\alpha+\beta}{2}) \tag{2.42}$$

where α and β are the angles of incidence and observation and γ is the angle between the bisector of these angles and the direction of deformation and **d** is the deformation vector. As before bright fringes will be seen when the phase difference is a multiple of 2π. Thus we get:

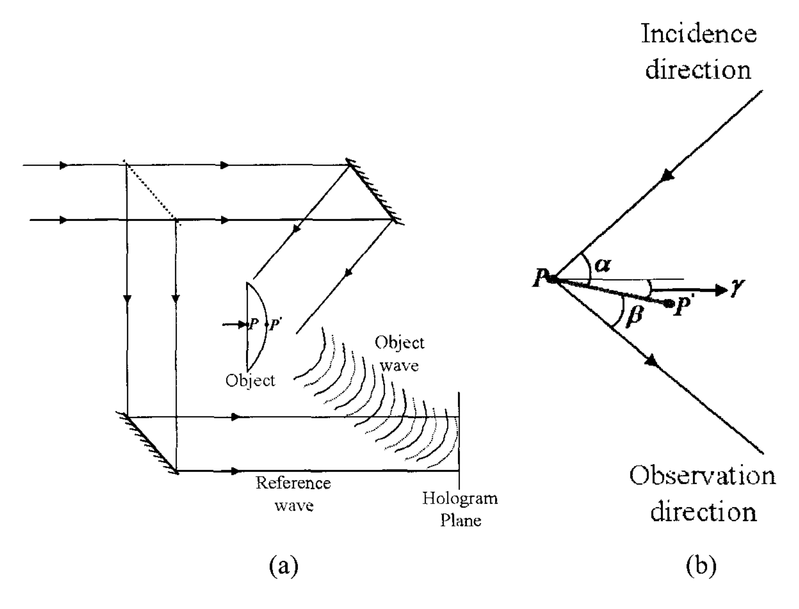


Fig. 2.28. (a) Schematic of a holographic Interferometric set-up. (b) Relation between phase difference and deformation of specimen.

$$\mathbf{d}\cos\gamma = \frac{n\lambda}{2\{\cos(\frac{\alpha+\beta}{2})\}} \tag{2.43}$$

Thus holography provides the component of displacement vector along the direction of the perpendicular bisector of the illumination and receiving directions with a sensitivity of $\lambda/2 \cos(\alpha + \beta)/2$. It is impossible to separate the three displacement components using just the one fringe pattern. Hence depending on the problem, the illumination and observation directions are so arranged as to measure only one component. Typically this is the out-of-plane displacement, for which the set-up is so arranged that $\alpha = \beta$. Figure 2.29 shows a typical holographic fringe pattern for a plate subject to pressure. Only part of the entire plate is seen and the clarity of fringes is similar to that for the moiré method. The maximum displacement can be determined by counting the fringe orders to the centre of the plate and multiplying by half the wavelength of light.

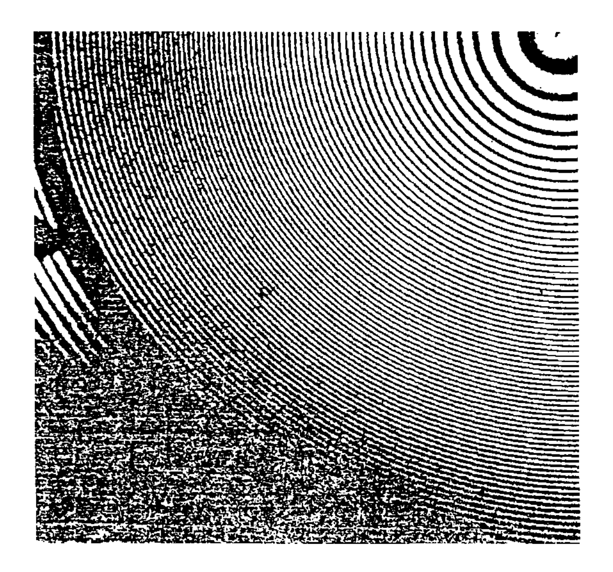


Fig. 2.29.

2.3.5 *Digital Photomechanics*

The intensity of a fringe pattern can be expressed as

$$I(x,y) = I_b(x,y) + I_m(x,y)\cos 2\pi N(x,y) \tag{2.44}$$

where $I(x,y)$ is the intensity at any point (x,y). $I_b(x,y)$ is the background intensity and equal to $(I_{max} + I_{min})/2$, $I_m(x,y)$ is the fringe modulation intensity and equal to $(I_{max} - I_{min})/2$ and N(x,y) is the desired fringe order. I_{max} and I_{min} are the maximum and minimum intensities in the fringe pattern. For manual fringe processing, the maximum or minimum intensity points were investigated as it was easier to identify. The advent of digital image processing techniques now enables us to identify fractional fringe orders at every point on the fringe pattern using eqn. (2.44). For an ideal fringe pattern $I_b\,(x,y) = I_m\,(x,y) = I_{max}/2$, and is uniform throughout the fringe pattern. In this case, if the intensity of the fringe pattern is digitized either by a digital camera or a scanner, the fringe pattern at each point can be readily determined from a single pattern. Of course even the best fringe pattern when digitized does not

show a uniform maximum and minimum distribution over the entire field. Thus in a general case, there are three unknowns, $I_b(x,y)$, $I_m(x,y)$ and $N(x,y)$ and only one intensity equation. Three major approaches have been suggested for fringe pattern analysis – namely the Fractional Fringe Method (FFM), the Fourier Transform Method (FTM) and the Phase Shift Method (PSM).While the first two require only one fringe pattern for processing, they are unable to provide the sign of the fringes. The PSM requires a minimum of three fringe patterns and provides the sign of fringes but may not be easily amenable for dynamic fringe analysis. Furthermore the FFM is better suited if there only a few fringes for the FFTM more the fringes the better.

2.3.5.1 *Fractional Fringe Method*

As indicated by eqn (2.44), the fringe pattern has a sinusoidal distribution. However, due to the variations in intensity and contrast, I_b and I_m are also functions of the coordinates (x, y). The approach in FFM is to determine I_b and I_m for each half of a fringe and interpolate the phase, between the minimum and maximum of this fringe, via the cosine function. Thus eqn. (2.44) can be rearranged as

$$N(x,y) = \frac{1}{2\pi}\cos^{-1}\left[\frac{\left(I(x,y) - I_b\right)}{I_m}\right] \tag{2.45}$$

2.3.5.2 *Fourier Transform Method*

The Fourier Transform Method (FTM) generally requires a high density of fringes. If the fringe density is low, a so-called carrier pattern can be added. This can be done by tilting the reference beam in interferometers or using a reference grating with different pitch than the initial specimen grating. A Fourier transform of the fringe pattern is first obtained using the Fast Fourier Transform (FFT) algorithm. The Fourier transform of a quasi-periodic fringe pattern will have two lobes centered on the central fringe frequency and the zero order central lobe. The side lobes have the information of the phase term. Thus the side lobe can be

delineated from the rest of the pattern and the data Fourier transformed again. Since the data selected in the Fourier domain is not symmetric, the Fourier transform yields a real and an imaginary component. The desired phase can then be determined as:

$$N(x,y) = \frac{1}{2\pi}\tan^{-1}\frac{\mathrm{Im}}{\mathrm{Re}} \tag{2.46}$$

where Im and Re are the Imaginary and Real parts of the inverse transform.

This phase is wrapped in the region (−π to +π). Phase unwrapping is needed to make the distribution of phase continuous. Unwrapping requires knowledge of the fringe sign and the phase of the starting point. This feature is not available for the FTM, using a single fringe pattern. Proposals have been made to use more than one fringe pattern. However, if more than one fringe pattern is to be used the Phase Shift Method (PSM) is preferable.

2.3.5.3 *Phase Shift Method*

It can be seen from eqn. (2.44) that a minimum of three images are necessary to solve for the three unknowns, I_b, I_m and N(x,y). The three independent images can be obtained by adding a known incremental phase α to the fringe pattern. One possibility is to provide four phase steps of 0, π/2, π, and 3π/2. The required fringe order N(x,y) can then be deduced as:

$$N(x,y) = \frac{1}{2\pi}\tan^{-1}\left[\frac{I_4 - I_2}{I_1 - I_3}\right] \tag{2.47}$$

Phase unwrapping as before is performed to obtain a continuous map of the phase distribution.

2.4 Concluding Remarks

Photomechanics is an established field and is finding a wider spread of applications with bio-engineering and micro and nano mechanics experiencing greater thrusts. Being essentially a non-contact and remote

method, it provides a novel alternative to conventional electrical sensors. The field is a combination of mechanics and optics and with the advent of digital imaging; a third discipline needs to be incorporated as well. From the mechanics viewpoint, stress, strain and deformation are parameters of interest. While they are inter-related, it is always best to find a method which can directly measure a desired quantity. Stress and strain being abstract quantities thus cannot be directly measured and hence most of the techniques developed are for displacement and deformation measurement. Optically, three major fields have historically evolved – geometric optics, wave optics and photonics. Photonics primarily deals with light sources, detectors and light matter interaction and hence its role in photomechanics is more from the point of view of novel sources and detectors which can be incorporated. Geometric optics based methods are generally more rugged than wave optics based system. However the sensitivity of the latter is higher than that of the former. Most of these techniques have been established over the last century but due to the ease of use of the electrical based sensors, widespread use has been limited. With the current boom in bio-engineering and micro and nano-system measurement, photomechanics methods offer the only solution to problems of interest. Furthermore with digital imaging and image processing being readily available, processing of fringe patterns has now become commonplace so interpretation of fringe patterns can be accomplished by most users.

References

Mechanics

1. Hearn, E.J. *Mechanics of Materials,* Pergamon Press, Oxford (1985).
2. Gere, J.M., Timoshenko, S.P. *Mechanics of materials*, PWS-KENT, Boston, Mass (1990).
3. Popov, E.P. *Introduction to Mechanics of Solids*, Prentice-Hall, Englewood Cliffs (1968).
4. Timoshenko S.P., Goodier J.N. *Theory of elasticity*, McGraw-Hill, New York (1970).

Optics

5. Hecht, E. Optics, Addision Wesley, *San Francisco* (2002).

6. Walker, B.H. *Optical Engineering - Fundamental*, McGraw Hill (1995).
7. Yu, F.T.S. *Optical Engineering*, Cambridge University Press (1997).
8. Lauterborn, W. *Coherent optics: fundamentals and applications*, Springer Verlag (1995).
9. Born, M. and E. Wolf. *Principles of optics,* Pergamon, Oxford (1970).
10. Goodman, J.W. *Introduction to Fourier Optics*, McGraw Hill, New York (1968).
11. Ghatak, A.K. *Introduction to modern optics*, McGraw Hill, New York (1971).

Photomechanics

12. Guild, J. *Diffraction gratings as measuring scales, practical guide to metrological use of moiré fringes*, Oxford University Press, Oxford (1960).
13. Durelli A.J. and V.J. Parks. *Moiré analysis of strain*, Prentice-Hall, New Jersey. (1969).
14. Beeston, B.E.P., Horne R.W. and R. Markham. *Electron diffraction and optical diffraction techniques*, North Holland, Amsterdam (1972).
15. Kafri, O. and I. Glatt. The *physics of moiré metrology*, Wiley, New York (1990).
16. Dally, J.W. and W.F. Riley. *Experimental Stress Analysis*, McGraw Hill, New York (1991).
17. Sirohi, R.S. Speckle Metrology, Marcel Dekker, *New York* (1993).
18. Robinson D.W. and G.T. Reid (eds.).,*Interferogram analysis: Digital fringe pattern measurement techniques*, Institute of Physics, London (1993).
19. Gasvik, G. Optical Metrology, Wiley, *New York* (1994).
20. Post, D., Han, B.T. and P. Ifju. High Sensitivity Moiré, Springer Verlag, *New York* (1994).
21. Rastogi, P.K. (ed.). *Optical Measurement Techniques and Applications*, Artech House, Massachusetts (1997).
22. Cloud. G. *Optical Methods of Engineering Analysis*, Cambridge University Press, New York (1998).
23. Sirohi R.S. and F.S. Chau. *Optical methods of measurement: wholefield techniques*, Marcel Dekker, New York (1999).
24. Rastogi P. (ed). *Photomechanics, Topics in Applied Physics*, Vol. 77, Springer Verlag, Berlin (2000).
25. Ramesh, K. *Digital Photoelasticity*, Springer Verlag, Berlin (2000).
26. Amidror, I. *The theory of moiré phenomenon*, Kluwer Academic, Dordecht (2000).
27. Asundi, A. *MATLAB® for Photomechanics – A Primer*, Elsevier Science Ltd., Oxford (2002).
28. Hariharan, P. *Basics of Holography*, Cambridge University Press, Cambridge (2002).
29. Steinchen, W. and Lianxiang Yang. *Digital Shearography*, SPIE Press, Bellingham (2003).
30. Schnars, U. and W. Jueptner. *Digital Holography*, Springer, Berlin. (2005).

CHAPTER 3

BIOMEDICAL IMAGING

Tatiana B. Krasieva, Petra Wilder-Smith

Beckman Laser Institute, University of California at Irvine
1002 Health Sciences road, Irvine, California, 92617, USA
E-mail: tkrasiev@uci.edu

The medical community has a strong interest in new, more sophisticated methods for non- or minimally invasive diagnostic or treatment purpose. Biophotonics is one of the most rapidly changing and promising fields of biomedical imaging undergoing transformation from pure research applications to a clinical setting including studies in oncology, inflammatory processes, wound healing, pharmacokinetics and pharmacodynamics, toxicology, infectious disease, gene expression and more. More reliable, varied and economical light sources (from miniature diode to femto-second tunable lasers), more sensitive and fast detectors (CCD chips, avalanche photodiodes, photomultiplier tubes), and novel interfaces to computers and computational methods, drives the technology development. New concepts of non-invasive imaging ("optical biopsy", "molecular imaging") rely on better understanding of the signal's origin, both "native" and exogenous. New reporters (fluorescent proteins, quantum dots) are used for brighter, better-localized, non-bleaching fluorescence imaging. Dynamic assays for oxy- and deoxyhemoglobin ratios, lipid and water content in benign and malignant tissues are being developed using concepts of photon migration and used in cancer research. Multi-modality approaches where different optical imaging modalities synergize with and compliment each other are gaining in momentum and may bring forward many new advantages in biology and medicine in the very near future.

3.1 Introduction

Visual information aided physicians from the earliest days of medical practice. Nowadays, modern practitioners have at their disposal a vast arsenal of extremely potent imaging techniques: ultrasound, X-ray, MRI, CT scan to name just a few. However, the need for high-resolution imaging at a tissue and cellular level cannot be comprehensively addressed by any of these modalities. Current medical imaging technologies allow visualization of tissue anatomy in the human body at resolutions no better then a few hundred micrometers. This resolution is insufficient for the detection of early-stage tissue abnormalities associated with diseases such as cancer and atherosclerosis, which require sub-micron scale visualization.

Biophotonics offers the means to achieve high-resolution imaging goals. New imaging concepts – both coming to maturity and newly emerging – may address the needs of non- or minimally invasive diagnostics and treatment modalities. The last two decades have broadened the technical base of optical imaging instrumentation with improved light sources (super luminescent diodes, super-fast and tunable lasers), and more sensitive detectors. This is a by-product of the recent boom in telecommunications, which has provided a wide selection of rather inexpensive and well-developed fibers, and a strong drive for miniaturization, leading to the incorporation of micro electrical mechanical systems (MEMS) and adaptive optics into optical devices design. Developments in computer technologies provide ever increasing computation speed, storage capacity, and data transfer rate and support specialized imaging software for real-time, high dynamic range, large area or 3-D data reconstruction and visualization. The "cross-pollination" between biology, medicine and engineering disciplines sometimes brings quite unexpected developments, for example, coated "quantum dots" – semiconductor nanocrystals – which may become the next big development after GFP in fluorescence contrast improvement.

The increasing visibility of biophotonics – of which a considerable portion is dedicated to imaging – over the last decade is best illustrated by the commencement of a specialized Journal of Biomedical Optics (JBO), which began publication in 1996 and is published by SPIE in

cooperation with the International Biomedical Optics Society. Notably, JBO increased its publication frequency from quarterly to bimonthly in 2004 and is now covered in MEDLINE from the January 2000 issue onwards.

What are the requirements for an ideal optical imaging modality? Probably, it would be the ability for deep tissue (tens of millimeters) non-contact examination with high (sub-micron) resolution in real-time utilizing "native" tissue properties (no exogenous contrast enhancers) with a flexible (fiber-based) probe for the quantitative measurement of tissue constituents and microstructure. Parts of this dream instrument are already in existence. Some are being developed. Some offer an alternative approach. This chapter provides an overview, somewhat limited by the restricted chapter's length, of what has happened in the field over the last few years.

3.2 Non-Linear Optical Microscopy (NLOM): Multiphoton Excited Fluorescence (MPEF) and Second Harmonic Generation (SHG)

The importance of optical microscopy in biology and medicine is unquestionable. It is indispensable in biomedical research, as a tool for the visualization and analysis of cellular structure, physiology and function. Conventional light microscopy deals with both living cells and tissues, providing a means of observing and analyzing dynamic processes and fixed materials.

Microscopy is a gold standard when it comes to histological evaluations and the field is too wide and well established to be discussed here. "Traditional" objects for light microscopy in biology and medicine are cellular monolayers or thin tissue slices in native state or, very often, treated with specific chemicals, dyes and/or fluorescent labels.

Confocal fluorescence microscopy made possible the addition of a third axis (depth) in otherwise mainly two-dimensional imaging, bringing research models closer to the reality of three-dimensional organisms. The main problem of conventional (including confocal) microscopy is a rather shallow depth of penetration of the probing light, which usually resides in the UV and visible portion of the light spectrum.

Animal forms living under the light of our sun are usually well equipped to block the penetration of light irradiation into the body (scales, skin, etc) with the exception of the eye, which is protected by an external shield – an eyelid. Generally, internal tissues are not transparent either, with different light scattering and absorption properties.

This may explain why non-linear optical microscopy (NLOM) needed less then 15 years to evolve from the first proof-of-principle to commercially available systems (BioRad Microscience in 1996, later Zeiss, Leika), to hundreds of research papers concerning the method, to the ultimate development of applications for clinical diagnosis and treatment.[1] In-depth discussion, history of development and applications, and extensive list of NLOM relevant papers may be found in a number of excellent reviews.[2-5]

3.2.1 *Principles of NLOM*

Multiphoton excitation of molecules is a nonlinear process involving either the absorption of multiple photons with combined energy sufficient for driving a molecular transition to an excited electronic state (MPEF- multiphoton excited fluorescence) or the non-absorptive process of frequency doubling by a highly polarizable substance with a noncentrosymmetric molecular organization (HG – harmonic generation) (See Fig 3.1). In both processes two lower energy (near-infrared, NIR) photons are converted into one emerging visible (or UV) photon, with precisely twice the energy (and half the wavelength) of incoming light (SHG), or slightly less then double due to the loss of energy during relaxation of the excited state (MPEF), as in any fluorescence process.

These phenomena may occur when two photons interact with the suitable (i.e. fluorescent or harmonic generating) molecule simultaneously, and because of a very low probability of such interaction, there should be a huge temporal and spatial photon density. For continuous wave (CW) lasers this translates into a very high power producing highly destructive consequences.

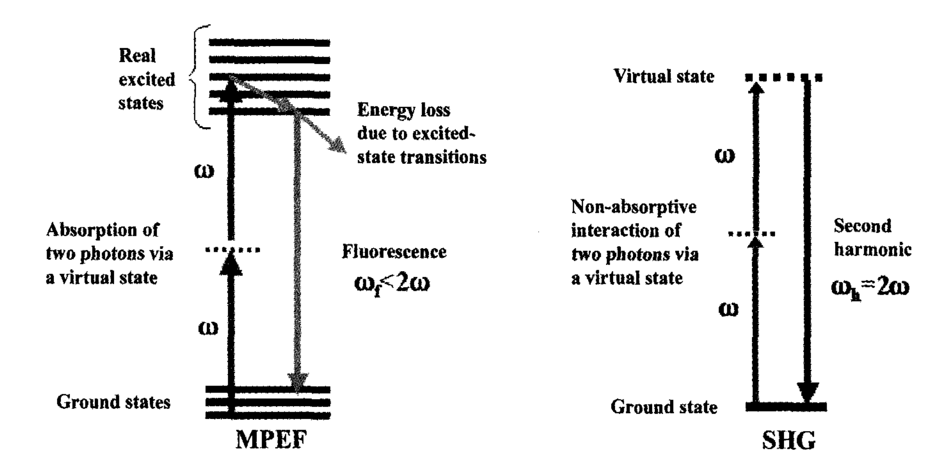


Fig. 3.1. Jablonski diagram illustrating the photophysical processes for the multi-photon excited fluorescence (left) and second harmonic generation (right). Note that in second-harmonic generation no actual electronic excitation takes place. For clarity only a two-photon case is depicted.

These adverse effects are avoided by the use of femtosecond pulsed lasers delivering high peak energy light burst in the shortest time now possible (femtosecond), achieving low average powers whilst avoiding (most of the time) unwanted side effects. This non-linearity also explains the tomographic properties of NLOM. Nonlinear processes occur only within the focal volume of the objective (see Fig 3.2), where photon density suffices to drive non-linear interactions. This gives rise to another advantage of NLOM over conventional excitation: reduced photo damage to a specimen (or none at all in case of non-absorptive SHG). Another advantage is improved depth of penetration due to lower scattering of longer wavelengths by tissues. Also, because most commercially available femtosecond lasers (Ti-Sapphire mostly) are tunable, excitation is not limited to the few laser lines available for conventional confocal scanning, providing a continuous range of excitation that may cover an extended range of fluorophores including UV-excitable markers without requiring the use of a UV source.

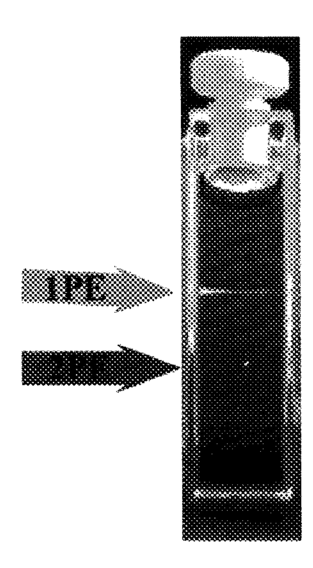


Fig. 3.2. One- and two-photon excitation profiles. Fluorescence excited by one-photon is visible throughout the path of the laser beam exiting from microscope objective (1PE). Two-photon excited fluorescence arises only in the focal volume of the identical objective (2PE).

The multiphoton process can effectively excite almost all relevant fluorophores, both "intravital" and synthetic. SHG in tissues is restricted mostly to collagen, which is an extremely important molecule for biomedical research. It is one of the most important components of extracellular matrices (ECM) and the SHG signal provides a unique signature for its identification. SHG for imaging purposes began to attract attention later then MPEF in spite of its similar instrumentation platform. The main reason for this is that harmonic generation is a coherent process (scattered photons maintain phase information), producing highly directed radiation (most of the signal wave propagates with the laser) rather then isotropic emission as in fluorescence.[5] Thus, transmitted light is the most favorable geometry for collecting SHG with the associated disadvantages this brings for thick tissue and *in-vivo* applications.[6] However, the ratio of the forward to backward signal depends on sample characteristics, notably scattering

properties. Higher sample turbidity facilitates secondary scattering of SHG, improving signal acquisition in backscattering (*epi-*) geometry and enabling co-registration of both MPEF and SHG signals.[7] A well-organized, comprehensive description and on-line tutorial on multiphoton microscopy can be accessed on-line at http://micro.magnet.fsu.edu/primer/techniques/fluorescence/multiphoton/multiphotonintro.html

3.2.2 *Development and Applications of NLOM*

An interesting analysis of literature referencing NLOM authored by Zipfel *et al.*[5] shows that more than half of all publications in this topic, despite the proclaimed maturity of the method are still devoted to technique and instrumentation development. Of the studies investigating biology-relevant questions, about two-thirds made use of non-commercial, laboratory-built systems, and over 80% of publications come from just a dozen research groups, indication that NLOM is an extremely powerful methodology requiring complimentary expertise (engineering/physics/biology-medicine) for its successful application. Moreover, this information seems to indicate that this modality is not yet at the level of routine use of confocal microscopy. However, the scope of successful applications of NLOM is very impressive.

NLOM technology is perfectly suited for the development of non- or minimally invasive biopsy. Tissue histological and pathological analysis relies on morphological information and requires sub-micron resolution to render sub-cellular details visible. Traditionally, this information is extracted from histological sections of the excised tissues. NLOM can provide such information *in-situ*. Optical biopsy does not require surgical excision and fixation, thus preserving structural and biochemical information; can utilize intrinsic ("auto") fluorescence and SHG rendering exogenous labels unnecessary; and it can provide 3-dimensional information due to the inherent tomographic ability of the method. Two-photon ex-vivo imaging of mouse dermal and subcutaneous structured was demonstrated by So *et al.* in 1998.[8]

Combination of MPEF with SHG imaging provides reliable identification of cellular and extracellular components (Fig. 3.3) for the visualization and analysis of complex processes that involve cell-ECM interactions and ECM remodeling. Examples of such processes include structural development, wound healing, and carcinogenesis. The research in this area involves investigation of the origin of the signal[9-10] and biomedical questions such as single cell behavior in metastatic breast cancer tumors[11] or dynamic imaging of collagen and its modulation during cancer progression.[12] Examples of 3-D imaging of different tissue types and organs utilizing NLOM are quite numerous and all share the constraint of a limited field of view (FOV), which is a trade mark of microscopy: the higher the resolution, the smaller the area of interrogation. Advances in both hardware and software may resolve this issue by utilizing "tiling" where large areas are imaged by "gluing" together an array of images taken sequentially (See Fig 3.3).[13-14] This approach, however, requires extended data collection time.

Aside from optical biopsy, a new hot topic in NLOM is redox fluorometry.[15] Redox fluorometry is based on the analysis of intrinsic fluorescence of reduced pyridine nucleotides (NADH and NADPH) and oxidized flavoproteins, which can be used to characterize cellular metabolic state. This approach, with the use of traditional excitation sources (flash photolysis), was pioneered by Britton Chance more then 40 years ago.[16-17] It was limited by photobleaching of fluorophores, photodamage to biological samples (especially due to need in UV excitation), inner filter effect, and shallow penetration depth in turbid environments. With almost all those limitations overcome by the application of MPEF, redox fluorescence imaging combined with imaging capabilities have attracted renewed interest and may provide a powerful tool for research on cellular metabolic activity.[18] Other recent promising variations of NLOM include two-photon fluorescence correlation microscopy. This approach was applied to measuring spatially resolved transport parameters that are crucial for evaluating the access rate of drugs in tumors *in vivo*.[19]

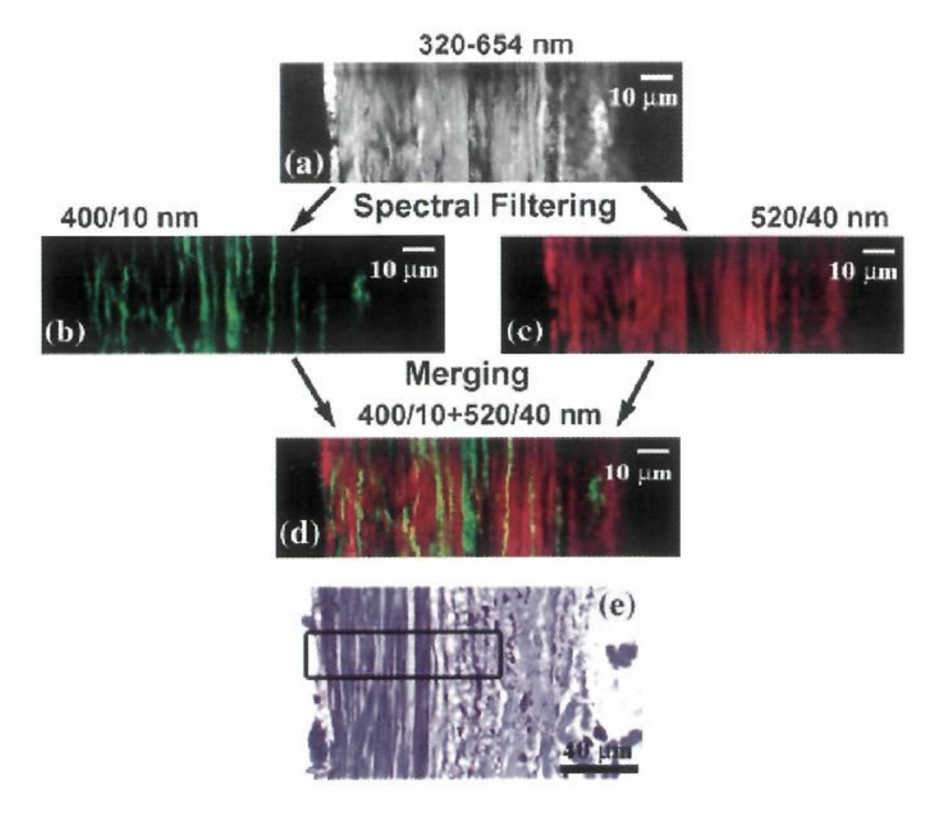


Fig. 3.3. Selective imaging of arteries over large areas. Composite images of several adjacent frames of optical sections showing the SHG (b), TPF (c), and combined SHG/TPF (a and d) intensities of the matrix fibers in the left anterior descending coronary artery cross-section ring from the intima (left) to the adventitia (right). MPM images were obtained using various emission filters: an SBG39 emission filter (320–654 nm) (a), a 400/10-nm filter (b), and a 520/40- nm band-pass emission filter (c). Overlay image of b and c is shown in d. Histology section is shown in e for comparison. The area marked with the black box corresponds to the area shown in a-d (reprinted with permission from Zoumi *et al.*[14]).

To bring NLOM from "the bench to the bedside" some improvements are absolutely necessary. Like all microscopy methods relying on laser light scanning, NLOM is rather slow. Even video-rate systems are rare and these trade the increased speed of acquisition

for sensitivity and/or resolution.[20] Quite encouraging is a recent communication from Dombeck and co-workers[21] reporting use of SHG microscopy for recording action potentials in neurons in culture with 0.833 msec temporal and 0.6 μm spatial resolution. Leichleiter and co-workers[22] developed a multi-photon scanning microscope using acoustic optical detector capable of rapid imaging of physiological events (30–120 frames/s). However, this system requires slow detection for weakly fluorescent biological samples.

Another improvement that would facilitate translational research is a development of a multi-photon microendoscope. A major obstacle in the development of such a flexible probe is the need to transmit an ultra-short light pulse through a length of fiber without losing pulse properties, and then to collect the weak emitted signal. So far the reported successful designs for multiphoton endoscopy utilized gradient-index (GRIN) rod lenses. Both proposed systems suffer some shortcomings. Bird and Gu[23] coupled a GRIN lens to a single-mode fiber creating a flexible probe, however, the reported achieved axial resolution was below 3 μm. The system developed by Jung *et al* yielded high-resolution images (axial resolution 0.85 μm) but lacks flexibility due to free-space optical coupling of the microendoscope to the microscope objective.[24] In both experimental systems, the signal was registered from bright exogenous fluorescent probes.

3.2.3 *NLOM in Dentistry*

Use of multi-photon techniques in dentistry is very rare to date, probably due to the specialized equipment and expertise required, as well as the lack of an existing flexible probe capability. Not surprisingly, the first two publications utilizing NLOM for *in vivo* studies in oral malignancy, which appeared almost simultaneously in 2004 used the same hamster cheek pouch model.[25-26] This model is well documented and requires minimum engineering to accommodate it for use with the microscope stage. Both groups analyzed cellular content and extra-cellular morphology data from intrinsic fluorescence and SHG, and

extensive statistical analysis to show excellent agreement with histological evaluations in all stages of carcinogenesis.

In 2005, additional studies were published in cancer research, which concentrates solely on fluorescence imaging and analysis of morphological and fluorescence features of punch biopsies (same hamster model).[27] The authors put forward several variables as possible diagnostic tools for cancer progression. The complimentary fluorescence intensity measures were consistent with the results of many other publications showing lower levels of autofluorescence attributed to NADH for different cancer types, including oral cancer in the human oral cavity. Combining the strength of different approaches on one platform may bring new advantages. Fluorescence and SHG imaging, fluorescence imaging and redox fluorometry already proved this concept. Wilder-Smith and co-workers, in an attempt to further improve sensitivity and specificity of diagnosis based on optical biopsy, combined MPEF and SHG microscopy with another powerful technique, optical coherence tomography.[28] As expected, both sensitivity (79–91%) and specificity (67–90%) were a few percent higher then either one of methods could achieve alone.

3.3 Optical Coherence Tomography (OCT)

The wide scientific community was introduced to the principles of optical coherence tomography (OCT) in 1991, when a group of researchers from Boston published their seminal "Optical coherence tomography" paper.[29] Recent advances in OCT technology have permitted the application of this modality to a broad range of medical diagnostics. Appealing characteristics of OCT include its micron-scale resolution (1–15 μm), a relatively good depth of penetration (a few mm), depth resolution decoupled from transverse resolution, contact-free and non-invasive operation, and the possibility of creating various function dependent image-contrasting methods.[30] The compatibility of OCT systems with the fiber optical components used in telecommunications permits relatively inexpensive design and excellent portability. Fiber optic systems can be incorporated into catheters or endoscopes, allowing high-resolution images of biological tissue microstructure.

OCT is an optical imaging technique that allows cross-sectional imaging of biological tissues in both transparent and highly turbid media. OCT uses the partial coherence properties of a light source and is somewhat analogous to ultrasound B-mode imaging except that infrared light waves rather than acoustic waves are used, thus providing superior resolution. However, the echo delay time of backscattered light returning to the OCT instrument from the sample cannot be measured directly by electronic methods, as in the case of an ultrasound pulse, due to the high propagation speed of light. To achieve effective detection, a technique known as interferometry is utilized.

3.3.1 *Principles of OCT*

The principles of OCT have been described in detail by Huang *et al.*[29] A schematic of the Michelson interferometer that permits measurements of precise depth and magnitude of low-coherent light reflection is shown in Fig 3.4. Light from the source is split equally with one half directed to the reference arm and another half to the sample arm of the interferometer. The optical path length in the reference arm supplies a gate on the detection. The scanning reference arm mirror determines the depth at which backscatter will be measured and induces a known Doppler-shift in the returning light. The sample is positioned at the apex of the sample arm and the optical beam is focused into the tissue. The portion of light reflected or backscattered by the internal microstructure of a specimen is combined with undeviated reflected light from the reference arm and sent to a detector, and electronically filtered around the Doppler-shifted frequency. Interference fringes are formed only if both optical path lengths are matched to within the coherence length of the source. The coherence length L is given approximately by $L = \lambda^2/(n\ \Delta\lambda)$, where λ is the central wavelength of the source, n is the refractive index in a medium and $\Delta\lambda$ is a spectral width of the light source. The axial resolution (Z) is determined by the coherence length of a source. The transverse resolution (X-Z or Y-Z) is determined by the spot size of the incident beam within the tissue.

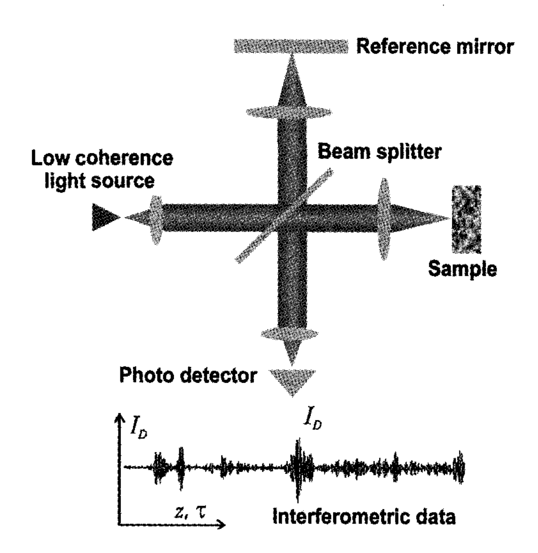


Fig. 3.4. The light source (low-coherent SLD or broadband laser source) is coupled into a Michelson-type interferometer. The resulting interferogram contains spectroscopic information about the reflected or backscattered light. The envelope of interferometric data is used in OCT imaging to detect the intensity of the reflected/backscattered light.

Images are formed by performing repeated axial measurements at different transverse positions as the optical beam is scanned across the tissue. The resulting data constitute a two-dimensional map of the backscattering or reflectance from internal architectural morphology and cellular structures in the sample. OCT contrast is determined by transitions between layers with different indices of refraction (for example, fatty or muscle tissue) and differences in reflectivity of cellular components (i.e. membranes and nuclei). Thus no exogenous contrast-forming agents (stains, fluorophores) are necessary.

3.3.2 *Developments and Applications of OCT*

Due to the transparency of ocular structures, ophthalmology was one of the first successful medical imaging applications of OCT, and it still remains one of the main fields of OCT instrumentation development. In

1993 Swanson *et al.*[31] reported the first *in vivo* measurements of human retinal structure with optical coherence tomography. Not surprisingly, the first commercial application of this technology was released by Humphrey Instruments (presently Zeiss Humphrey Systems) in 1995, as an optical coherence tomography scanner for imaging and measuring posterior ocular structures. Second and third generation scanners have been produced, providing real-time cross-sectional images of the retina with an axial resolution of ten microns or less and greater depth resolution permitting the direct measurement of the optic nerve head, retinal nerve fiber layer and macula.

Initially, OCT systems utilized superluminescent diodes (SLDs) with a bandwidth of a few tens of nanometers as light sources achieving a resolution of approximately 15 μm, which is not sufficient to image individual cells and structures within cells. The usual milliwatt power level of SLDs was not sufficient for high imaging speed. With the advent of alternative light source such as solid-state broad bandwidth femtosecond mode-locked lasers, high-resolution and high-speed OCT imaging became possible. This was demonstrated in 1998 by *in-vivo* imaging of *Xenopus laevis* (African frog) tadpole, a common developmental biology model.[32] Axial resolution achieved in this study was on the order of 4–5 μm and OCT images were compared to histological preparations, showing different stages of mitotic activity, cell migration as well as resolved cellular membranes and nuclei.

In the following year, the same group pushed "the resolution envelope" even further, reporting the development of *in-vivo* ultrahigh-resolution OCT system.[33] Images of *Xenopus laevis,* consisting of 1200 x 1000 pixels, were recorded over 0.54 mm x 0.5 mm with 1 μm x 3 μm (longitudinal x transverse) resolution. The use of a state of the art broad-bandwidth femtosecond Kerr-lens mode-locked Ti: Sapphire laser with double-chirped mirrors emitting sub-two cycle pulses with bandwidths of up to 350 nm, centered at 800 nm was seminal to this achievement. However, the trade-off for such unique imaging abilities is a highly complex and sophisticated system requiring a number of specially designed optical and electronic elements.

Use of advanced near-infrared light sources opened the path for OCT imaging in strongly scattering tissues.[34-35] In most medical applications, imaging depth is an important issue. Light penetration depth in biological tissues is dependent on absorption and scattering properties. The amount of absorption and scattering is highly dependent on the wavelength of probing light and reaches a relative minimum near 1300 nm. Due to the high sensitivity and dynamic range of OCT, the possibility of light source optimization, rapid data acquisition, small inexpensive catheter/endoscope design (current size is 1 mm in diameter and can be reduced further), a compact portable structure, and resolution approaching that of standard histopathology (i.e. optical microscopy), OCT demonstrates its greatest potential as an alternative to excision biopsy. However, further developments to overcome current limitations (inadequate penetration depth, resolution, acquisition rate, and lack of large-scale clinical trials) are needed for bringing OCT to mainstream medical practice.

An OCT system that can image up to the video rate was described by Rollins *et al* in 1998.[36] The system utilizes a high power broadband source centered at 1300 nm and real time image acquisition hardware. Real time imaging was demonstrated in vivo in tissues relevant to early human disease diagnosis (skin, eye) and in *Xenopus laevis* embryo. The images were free of motion artifacts and allowed clear visualization and measurement of the anatomical structures. One of the main limiting factors for the development of a high-speed acquisition system is the need to scan rapidly the length of the reference arm in the interferometer over the distance corresponding to the imaging depth range. Implementation of an alternative method known as Fourier domain OCT or spectral domain OCT (SD-OCT) may be an answer to this problem. In SD-OCT, no mechanical scanning of the reference arm is required. Instead, the cross-spectral density at the detection arm of the interferometer is measured by means of a spectrometer.[37] Implementation of this approach[38] resulted in an ultrahigh-speed SD-OCT system that achieves acquisition rates of 29,300 depth profiles per second. *In vivo* SD-OCT image of the human retina around the optic nerve head, consisting of 1000 depth profiles acquired in 34 ms was presented. Dimensions are 6.4 mm wide by 1.7 mm deep.

Spectroscopic OCT is an extension of conventional OCT for performing both cross-sectional tomographic and spectroscopic imaging.[39] This method allows the spectrum of backscattered light to be measured over the entire available optical bandwidth simultaneously in a single measurement. The spectral region between 650 to 1000 nm is favored because it overlaps absorption features in oxyhemoglobin and deoxyhemoglobin and may permit the functional imaging of hemoglobin oxygen saturation. Spectroscopic OCT can also be used to enhance image contrast, permitting the observation of differentiation of tissue microstructure and pathologies through their spectroscopic properties or functional states.

Image contrast improvement is another area of major effort. For example, polarization sensitive (PS) OCT capitalizes on the birefringent properties of highly turbid media such as bovine tendon.[40] PS-OCT may find its utility in dentistry by providing information on the mineralization status and/or the scattering properties of dental hard tissues, specifically dentin and enamel.[41-42] More recently, highly successful use of second harmonic generation (SHG) by collagen in biological tissues in MPEM imaging has attracted the interest of the OCT community. Jiang *et al.* have presented a second harmonic OCT system (SH OCT), which combined the structural sensitivity of SHG with the coherence gating of OCT.[43] SH OCT efficiency, contrast and resolution enhancement was demonstrated on a simple model (two collagen layers sandwiched between glass slides). In the future, this technique may be extended to third-harmonic generation and other possible coherent nonlinear processes for tomographic imaging.

Optical Doppler tomography (ODT) is an imaging modality that adds measurements of flow dynamics (speed of blood flow, almost exclusively) to imaging of tissue structure simultaneously.[44] ODT combines Laser Doppler Flowmetry (LDF) with OCT to obtain high-resolution tomographic images of static and moving constituents simultaneously in highly scattering biological tissues. Morphology and blood circulation were imaged *in vivo* in *Xenopus laeves* tadpoles[44] (See Fig 3.5). Aortic location and morphology are evident in the structural image (See Fig 3.5(A)), while a high-contrast image of aortic blood flow velocity is seen in the correspondent Fig 3.5(B).

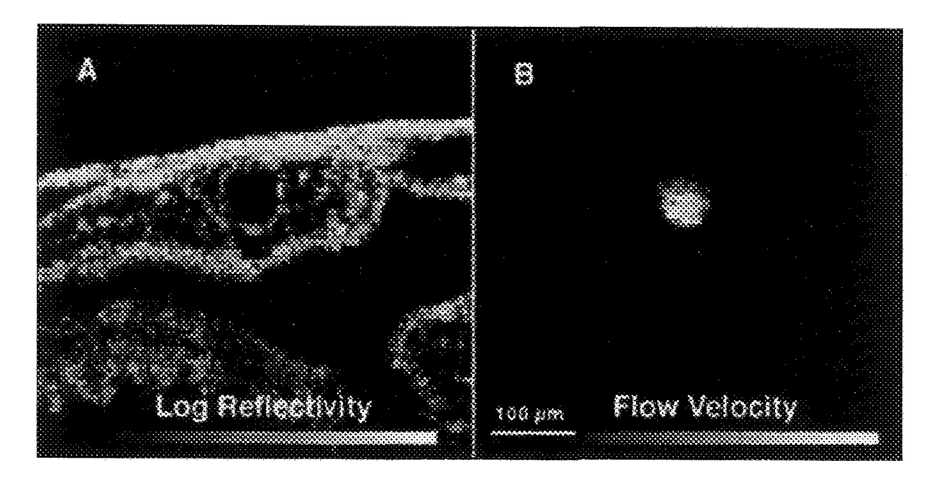


Fig. 3.5. ODT structural (A) and velocity (B) images of aortic blood flow in *Xenopus laeves* (reprinted with permission from [44]).

These results demonstrate that ODT can image tissue structure and blood flow simultaneously with high spatial resolution and speed sensitivity.

The first phase-resolved OCT/ODT images of blood flow in human skin with fast scanning speed and high velocity sensitivity were reported by Zhao *et al.* [45] This approach leads to an increase in imaging speed by more than 2 orders of magnitude without compromising spatial resolution or velocity sensitivity. The minimum flow velocity that can be detected is as low as 10 μm/s, while a spatial resolution of 10 μm is maintained.

Results from *in vitro* and *in vivo* model studies have demonstrated that ODT can map the blood flow velocity profile with high spatial resolution in scattering medium. Techniques currently used for blood flow velocity determination are based on the Doppler effect, and utilize a low-power near-IR (650–780 nm) laser (Laser Doppler Flowmetry (LDF)), or ultrasound (Doppler Ultrasound (DUS)) as probing sources. However, the relatively long acoustic wavelengths required for deep tissue penetration limit the spatial resolution of DUS to approximately 200 μm. Given its better resolution, simple hardware requirements, and relatively compact size, ODT is a promising technique for both basic research and clinical medicine.

3.3.3 *OCT in Dentistry*

Application of OCT in dentistry till date has been limited to intra-oral applications.[27, 40-41, 45-53] Early studies focused mainly on the topics of periodontal disease and hard tissue pathology. In 1998 Colston and co-workers demonstrated the potential of OCT for noninvasively imaging periodontal tissues in the porcine model.[47] Later that year the first *in vivo* optical coherence tomography (OCT) images of human dental tissue were presented.[48] Authors presented a dental optical coherence tomography system with a very promising feature – the incorporation of the interferometer sample arm and transverse scanning optics into a handpiece suitable for intraoral use. Examples of use of this imaging system for dentistry illustrated its potential for diagnosis of periodontal disease, detection of caries, and evaluation of dental restorations. The average imaging depth of this system varied from 3 mm in hard tissues to 1.5 mm in soft tissues. Axial resolution was 15 μm. The system had a lateral resolution of 50 μm and an average total lateral scan distance of 12 mm. The total scan time for each image was approximately 45 seconds. However, active work in the area of endoscopic OCT may soon provide better solutions for dental applications. For example, Pan and co-workers[53] reported an endoscopic OCT system utilizing MEMS that achieved scanning speed of 5 frames per second for 2.9 mm X 2.8 mm area with transverse and axial resolution of 20 and 10 μm respectively.

As was mentioned earlier, birefringence of dentin and enamel provided PS-OCT with a contrast agent useful in indicating pre-carious or carious lesions.[42] PS-OCT can provide additional information related to the mineralization status and/or the scattering properties of the dental materials.[41] More recently, intra-oral applications of OCT were expanded to the diagnosis of oral malignancy and pre-malignancy.[51, 54] Wilder-Smith *et al.* evaluated the use of OCT to characterize epithelial and sub-epithelial changes during carcinogenesis in the hamster cheek pouch model, comparing the diagnostic capabilities of OCT with conventional histopathological diagnosis and staging (See Fig 3.6).[54] The results for diagnosis show good agreement within scorers, between scorers and between modalities (histopathology and OCT), assessed using kappa-statistics. Sensitivity was excellent for the diagnosis of SCC, and

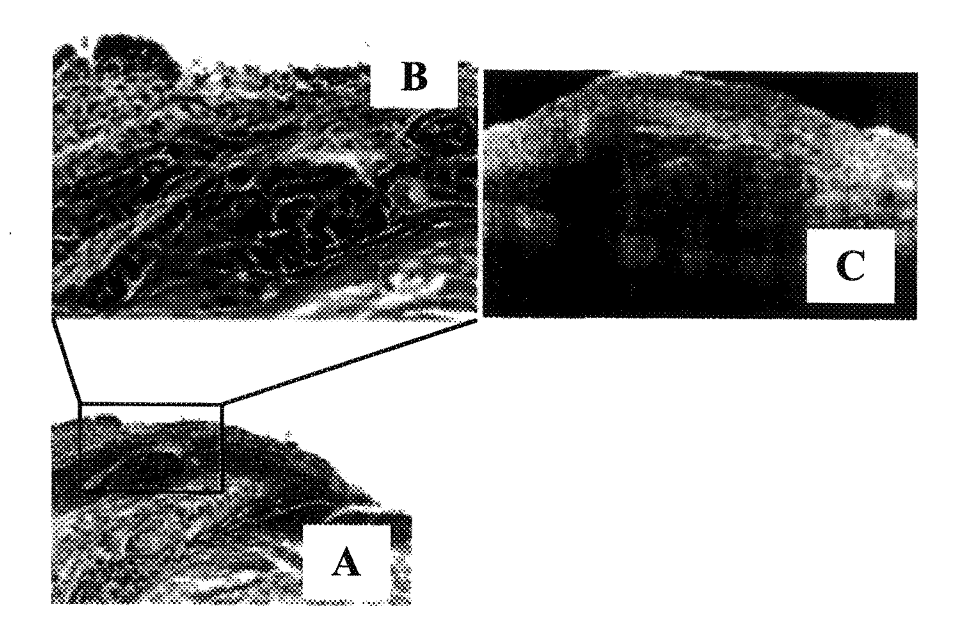


Fig. 3.6. Malignant cheek pouch H&E stained image (A, 20x; B, 40x) and in vivo OCT (C) of same cheek pouch with squamous cell carcinoma. In H&E, epithelial pearls are invading the connective tissue. Individual cancer cells exhibit pleomorphism, increase nuclear to cytoplasm ratio, and hyperchromatism. In OCT, see the loss of normal epithelial stratification and basement membrane. Image definition from site with SCC was consistently much poorer than from other sites, due to reduced penetration by light into malignant tissues (reprinted with permission from Wilder-Smith *et al.*[54]).

somewhat reduced for differentiating between different types of dysplasia. As the resolution capabilities of OCT technology are rapidly improving, the ability to differentiate between different stages of dysplasia should also improve.

In summary, OCT is today one of the most rapidly developing biomedical optical modalities. Optical *in vivo* biopsy is one of the most appealing and challenging fields of biophotonic application. The high resolution, significant penetration depth, and the potential for functional imaging, provide more information than that was gained from "traditional" biopsy, without the need for invasive sampling. New broad-bandwidth light sources, the use of photonic crystal fibers and

superfluorescent fiber sources, new contrasting techniques, and full 3-D data restoration represent just a few of the areas of rapid and ongoing innovation. Further details on OCT with relevance to dentistry can be found in chapter 9 (Section 9.11) of this book. Detailed review of this topic can be found in the following references.[29, 54-56]

3.4 Coherent Anti-Stokes Raman Scattering (CARS) and Modulated Imaging (MI)

There are several other emerging or established but rapidly evolving methods in biomedical imaging, which should however briefly also be mentioned in this overview.

In microscopy, imaging based on Coherent Anti-Stokes Raman Scattering (CARS) for the noninvasive characterization of chemical compounds or components within complex biological systems utilizes intrinsic molecular vibrational properties (stretch or skeletal vibrations of C—H, C—C, O—H bonds).

All Raman spectroscopy is based on the Raman effect, which is the inelastic scattering of photons by molecules. The Raman effect comprises a very small fraction, about 1 in 10^7, of incident photons. In Raman scattering, the energies of the incident and scattered photons is less than the incident radiation for the Stokes line and the energy of the scattered radiation is more than the incident radiation for the anti-Stokes line. The energy increase or decrease from the excitation is related to the vibrational energy spacing in the ground electronic state of the molecule and therefore the corresponding wave number of the Stokes and anti-Stokes lines is a direct measure of the vibrational energies of the molecule. However, spontaneous Raman imaging is often limited by the weak Raman scattering cross section, which dictates high laser powers, and by the presence of strong auto-fluorescence background.

To circumvent the signal-to-background limitations inherent to spontaneous Raman detection, CARS has been combined with optical microscopy. Because of its coherent nature, in which the molecular bonds oscillate in phase and interfere constructively, and its active pumping of the vibrational states, the CARS signal is at least five orders of magnitude more sensitive than spontaneous Raman scattering.

Although it is not possible to detect a single vibrational mode at room temperature, it is feasible to detect a macromolecule with thousands of identical vibrational modes that interfere coherently. Resolution, depth of imaging and speed of data acquisition in CARS microscopy are comparable with fluorescence laser scanning methods. The appeal of CARS microscopy lies in the possibility for chemical mapping of small molecules such as lipids, hormones, and drug molecules whose functions in cells and tissues are likely to be altered by labeling.

Common requirements for CARS and two-photon fluorescence microscopy with regard to excitation source speak for their combination on a same platform, permitting simultaneous vibrational and fluorescence imaging of the same sample.[58] The first attempts to move from *in-vitro* to *ex-vivo* imaging (single live neuron imaging in a spinal cord of a guinea pig) were also reported recently (*ibid*). At the moment, CARS is a highly specialized, technically challenging and rather expensive method enjoying a surge on the method development side, with various schemes including picosecond excitation, epi-detection, and polarization sensitive detection under investigation. Detailed descriptions of theory, instrumentation, and CARS applications can be found in recent review papers.[59-60]

Laser Doppler velocimetry was previously mentioned in comparison with Doppler OCT for blood flow monitoring. Another method proposed for blood perfusion mapping and imaging is laser speckle imaging (LSI).[61] Laser speckle is a random interference effect that gives a grainy appearance to objects illuminated by laser light. If there is a flow of individual moving scatterers (such as blood cells), the speckle pattern fluctuates. Information about the velocity distribution of the scatterers can be derived from these fluctuations. LSI uses readily available off-the-shelf equipment and the software operates in a user-friendly way. It is a single-shot technique, so capture and processing take less than one second. The main disadvantage of LSI is the loss of resolution caused by the need to average over a block of pixels (typically 5 x 5 or 7 x 7) in order to produce the spatial statistics used in the analysis. Laser Doppler imaging has been on the market for some time, whereas LSI is still in the laboratory and will need significant engineering development before it can be commercialized. This may be worth doing to capitalize on truly

real-time operation and the ability to directly observe perfusion changes.[62-63]

For the methods discussed so far, light scattering events would bring a detrimental effect on both resolution and penetration depth. A growing number of experimental approaches and medical applications capitalize on the analysis of tissue scattering properties, expressed as scattering and absorption coefficients, most notably diffuse optical spectroscopy and imaging.[63-65] This approach is based on NIR Frequency-Domain Photon Migration (FDPM) models and technology. The FDPM–based approach lacks the resolution of optical microscopy or OCT but provides a far greater penetration depth (a few centimeters) and direct quantitative measurements of tissue constituents such as oxy- and deoxy-hemoglobin, cytochrome c oxidase redox state, lipid content, water concentration, and tissue "scatter power" dependant on scattering by cells, organelles, and extracellular matrix.[67-70] Diffuse optical methods have been successfully applied in the field of cancer research, most notably in breast cancer management in a clinical environment, and for monitoring chemotherapy, hormonal effects, tumor characterization and risk assessment.[71-73]

Diffuse optical methods provide invaluable complimentary information to other well-established methods like MRI or ultrasound in quantifying physiologic parameters in cancer detection, measuring cerebral blood flow, assessing burn depth, monitoring muscle function, or concentrations of exogenous compounds.[75] Another interesting design combines static light scattering (SLS) with light microscopy.[76] This technique allows the characterization of local light-scattering patterns in thin tissue sections, to classify tissue types with surprisingly high specificity and sensitivity.

Last, but not least, is a newly emerging modulated imaging (MI) approach,[77] which strives "to fill the gap in biological tissue imaging between sub millimeter imaging and diffuse optical tomography". This method is based on spatially modulated illumination, where patterns of various spatial frequencies are projected onto the sample. The analysis of frequency-dependent reflection yields quantitative data on optical properties of the medium, and based on the broadband FDPM approach into time-resolved and spatially resolved measurements.[78] Variations of

spatial frequency of illumination pattern permit control of detection depth sensitivity within the turbid medium. MI is a scan-free method utilizing a high-sensitivity, low-noise, high-dynamic range cooled CCD as a detector. This facilitates a rapid, non-contact wide-field data acquisition, permitting quantitative sample characterization in terms of absorption and scattering properties. So far the reported resolution of images is far from that achieved using microscopy or OCT, but further development of this rapid and possibly inexpensive method could overcome this obstacle.

3.5 Fluorescence Contrast Enhancement

Although modern biomedical applications of optical imaging raise a general interest in the utilization of "internal" contrast agents, the investigation of complex processes in live cells and organisms require readily distinguishable sensor/reporter mechanisms. The idea of fluorescent markers is one of the oldest in molecular and cellular biology continuously in use for almost hundred years. However, even such "old news" has undergone an extreme makeover in the last decade.

The era of Fluorescent Proteins (FP) as sensors for functional imaging from single cells to entire living organisms started in the early 90s, based on a report by Prasher and co-workers[79] describing the cloning and sequencing of both cDNA and genomic clones of green fluorescent protein (GFP) from the jellyfish Aequorea Victoria. In less then three years mutants with improved fluorescence characteristics were developed.[80-81] GFP had become well established as a marker for gene expression and protein targeting in intact cells and organisms by 1998.[82]

The primary advantages of FP-based indicators over "traditional" fluorescent organic dyes are a low rate of photo toxicity and possibility to "tailor" FPs to respond to a great variety of biological events and signals, and targeted to subcellular compartments while minimally perturbing the cell under investigation. Major trends in FP development and applications were recently reviewed in-depth in some articles.[83-84]

The convergence of molecular biology and noninvasive imaging brought forward the idea of "molecular imaging". This concept can best be described as "the visualization of cellular processes in space and time

at a molecular or genetic level of function", where imaging modalities include nuclear, magnetic resonance and optical technologies.[85] Optical molecular imaging utilizes both fluorescent and bioluminescent reporters. For now its applications are mostly concentrated on small animal imaging using a commercially available small animal imager (*ibid*).[86] Not surprisingly, fluorescent reporters include genetically encoded GFP and DsRed, as well as other color variants. However, excitation and emission of FPs generally are limited to the visible part of the light spectrum (400-650 nm). Some dyes that were developed for use *in vivo* microscopy applications (for example the family of AlexaFluors and cyanine dyes by Molecular Probes, Eugene, OR, USA and Indocyanin Green) cover the far red and NIR spectral region (600–885 nm) in "optical molecular imaging" applications.

An alternative to fluorescence could, in some cases, be bioluminescence, depending on biological suitability. Bioluminescent reporters are based on genetically expressed luciferase proteins. Light emission is a result of a chemical reaction involving luciferase, luciferin, oxygen, and ATP. No excitation light is required but (with the exception of bacterial luciferase), in order to initiate the reaction, the injection of luciferin is necessary. Bioluminescence emission usually is not as bright as fluorescence, but the almost complete absence of background emission makes for excellent signal-to-background ratios for bioluminescent imaging. A very appealing feature of existing instrumentation is the absolute calibration that allows analysis of animal images in terms of physical units of radiance, permitting quantitative comparison of data.

Another interesting alternative to conventional fluorophores is semiconducting nanocrystals, known as "quantum dots" (QDs).[87-89] The core of QD consists of a semiconductor nanocrystal, usually CdSe, surrounded by a passivation shell of ZnS, which is in turn coated with polymer for protection from water. Polymer coating also provides reactive chemical groups for protein conjugation and improves solubility in biological media. The advantages of QDs over organic dyes and FPs are superior brightness due to the large extinction coefficients and the relatively high quantum yields, as well as unchallenged photostability. They combine continuous excitation with very narrow emission spectra,

thus permitting well resolved spectrally multi-color imaging with a single excitation wavelength.

Application of QDs in biology and medicine was hindered until recently by problems of biocompatibility, non-specific binding, and aggregation in divalent buffers as well as concerns regarding their potential toxicity. Recent improvements in biocompatibility of nanocrystals, notably use of PEG as a coating material and alternative methods for QD synthesis[90] moved studies utilizing QDs as optical contrast agents from the *in vitro* to the *in vivo* realm. Voura and co-workers[91] successfully employed QDs in tracking metastatic tumor cell extravasation in live mice with specific attention to the problem of toxicity. However, further studies of cumulative effects as well as long-term effects are needed before any QD can reach clinical applications, based on the very limited number of studies to date on living organisms.[92]

3.6 Concluding Remarks

Biomedical imaging is one of the most dynamically developing fields at this time. Combining the efforts of researchers from a multitude of disciplines (biology, engineering, chemistry, physics, mathematics and medicine), impressive advancements in both established and newly emerging technologies have been achieved over the past decade.

Optical *in vivo* biopsy is one of the most appealing and challenging fields of biophotonic development. Its main goal is to match and exceed the information provided by "traditional" excised biopsies regarding tissue and cell function and morphology *in situ* and *in vivo*. High resolution, high penetration depth, potential for functional imaging, portability and affordability all contribute to the ever-increasing interest afforded to light-based technologies. There is yet to be a single platform to meet "all of the above" requirements. In the meantime multi-modality approaches (MPM + OCT, MPM + CARS, endoscopy + OCT and MPM, FDPM + MRI and more), where different optical imaging modalities synergize with and compliment each other, are gaining in momentum and may bring about many new advantages in biology and medicine.

Acknowledgments

This work was supported in part by grant from National Center for Research Resources, NIH # P41RR01192. We would like to thank Drs. Julia Lyubovitsky and Shuo Tang for valuable comments on the early drafts.

References

1. W. Denk, J.H. Strickler, and W.W. Webb, *Science,* 248, 73 (1990).
2. F. Helmchen, and W. Denk, *Current Opinion in Neurobiol.*, 12, 593(2002) and *Nat. Methods*, 2, 932(2005).
3. K. Koenig, *J. of Microscopy,* 200, 83(2000).
4. P. So, C.Y. Dong, B.R. Masters, and K.M. Berland, *Annu .Rev. Biomed. Eng*, 2, 399 (2000).
5. W. Zipfel, R.M. Williams, and W.W. Webb, *Nat. Biotechnology*, 21, 1396 (2003).
6. P.J. Campagnola, and L.M. Loew, *Nat. Biotechnology*, 21, 1356(2003).
7. A. Zoumi, A. Yeh, and B.J. Tromberg, *Proc. Natl. Acad. Sci. USA*, 99, 11014 (2002).
8. P.T.C. So, H. Kim, and I.E. Kochevar, *Opt. Express*, 3, 339 (1998).
9. W. Mohler, A.C. Millard, and P.J. Campagnola, *Nat. Methods,* 29, 97 (2003).
10. R.M. Williams, W.R. Zipfel, and W.W. Webb, *Biophysical J.*, 88, 1377 (2005).
11. W. Wang, J.B. Wyckoff, V.C. Frohlich, Y. Oleynikov, S. Huttelmaier, J. Zavadil, L. Cermak, E.P. Bottinger, RH. Singer, J.G. White, J.E. Segall, and J.S. Condeelis, *Cancer Res.,* 62, 6278 (2002).
12. E. Brown, T. McKee, E. di Tomaso, A. Pluen, B. Seed, Y. Boucher, and R.K. Jain, *Nat. Medicine*, 9, 796 (2003).
13. H.S. Lee, Y. Liu, H.C. Chen, L.L. Chiou, G.T. Huang, W. Lo, and C.Y. Dong, *Opt. Letters*, 29, 2614 (2004).
14. A. Zoumi, X. Lu, G.S. Kassab, and B.J. Tromberg, *Biophysical J.*, 87, 2778 (2004).
15. S. Huang, A.A. Heikal, and W.W. Webb, *Biophys. J,* 82, 2811 (2002).
16. B. Chance, P. Cohen, F. Jobsis, and B. Schoener, *Science,* 137, 499(1962).
17. B. Chance, I.A. Salkovitz, and A.G.B. Kovach, *Am. J. Physiology,* 223, 207(1972).
18. D.W. Piston, B. Masters, and W.W. Webb, *J. Microscopy,* 178, 20(1995).
19. G. Alexandraxis, E.B. Brown, R.T. Tong, T.D. McKee, R.B. Campbell, Y. Boucher, and R.K. Jain, *Nat. Medicine*, 10, 203 (2004).
20. Q.T. Nguyen, N. Callamaras, C. Hsieh, and I. Parker, *Cell Calcium,* 30, 383 (2001).
21. D.A. Dombeck, M. Blanchard-Desce, and W.W. Webb, *J. of Neurosci.*, 24, 999 (2004).
22. J.D. Leichleiter, D.T Lin, and I. Sieneart, *Biophysical J.*, 83, 2292 (2002).

23. D. Bird, and M. Gu, *Opt. Letters*, 28, 1552 (2003).
24. J.J. Jung, A.D. Mrtha, E. Aksay, R. Stepnoski, and M.J. Schnitzer, *J. Neurophysiol.*, 92, 3121(2004).
25. J. Sun, T. Shilagard, B. Bell, M. Motamedi, and G. Vargas, *Opt. Express*, 12, 2478 (2004).
26. P. Wilder-Smith, K. Osann, N. Hanna, N. El Abbadi, M. Brenner, D. Messadi, and T. Krasieva, *Lasers in Surgery and Medicine*, 35, 96 (2004).
27. M.C. Skala, J.M. Squirrell, K.M. Vrotsos, J.C. Eickhoff, A. Gendron-Fitzpatrick, K.W. Eliceiri, and N. Ramanujam, *Cancer Res.*, 65, 1180 (2005).
28. P. Wilder-Smith, T. Krasieva, W.G. Jung, J. Zhang, Z. Chen, K. Osann, and B. Tromberg, *J. of Biomed. Optics*, 10, 051601 (2005).
29. D. Huang, E.A. Swanson, C.P. Lin, J.S. Schuman, W.G. Stinson, W. Chang, M.R. Hee, T. Flotte, K. Gregory, C.A. Puliafito, and J.G. Fujimoto, *Science*, 254, 1178 (1991).
30. A.F. Fercher, W. Drexler, C.K. Hitzenberger, and T. Lasser, *Reports On Progr. In Phys.*, 66, 239 (2003).
31. E.A. Swanson, J.A. Izatt, M.R. Hee, D. Huang, C.P. Lin, J.S. Schuman, C.A. Puliafito, and J.G. Fujimoto, *Opt. Lett.*, 18, 1864 (1993).
32. S.A. Boppart, B.E. Bouma, C. Pitris, J.F. Southern, M.E. Brezinski, and J.G. Fujimoto, *Nature Medicine*, 4, 861 (1998).
33. W. Drexler, U. Morgner, F.X. Kartner, C. Pitris, S.A. Boppart, X.D. Li, E.P. Ippen, and J.G. Fujimoto, *Opt. Letters*, 24, 1221 (1999).
34. M.E. Brezinski, and J.G. Fujimoto, IEEE Journal Of Selected Topics In Quantum Electronics, 5, 1185(1999).
35. G.J. Tearney, M.E, Brezinski, B.E. Bouma, S.A. Boppart, C. Pitris, J.F. Southern, and J.G. Fujimoto, *Science*, 276, 2037 (1997).
36. A.M. Rollins, M.D. Kulkarni, S. Yazdanfar, R. Ung-Arunyawee, and J.A. Izatt, *Opt. Express*, 3, 219 (1998).
37. A.F. Fercher, C.K. Hitzenberger, G. Kamp, and S.Y. El-Zaiat, *Opt. Commun.*, 117, 43(1995).
38. N. Nassif, B. Cense, B.H. Park, S.H. Yun, T.C. Chen, B.E. Bouma, G.J. Tearney, and J.F. de Boer, *Opt. Letters*, 29, 480 (2004).
39. U. Morgner, W. Drexler, F.X. Kartner, X.D. Li, C. Pitris, E.P. Ippen, and J.G. Fujimoto, *Opt. Letters*, 25, 111 (2000).
40. J.F. De Boer, T.E. Milner, M.J.C. van Gemert, and J.S. Nelson, *Opt. Letters*, 22(12), 934 (1997).
41. Baumgartner, A., Dichtl, S., Hitzenberger, C.K., Sattmann H., Robl, B., Moritz, A., Fercher, A.F. and Sperr, W., *Caries Res.*, 34, 59 (2000).
42. X.J. Wang, T.E. Milner, J.F. de Boer, Y. Zhang, D.H. Pashley, and J.S. Nelson, *Appl. Optics*, 38, 2092 (1999).
43. Y. Jiang, I. Tomov, Y. Wang, and Z. Chen, *Opt. Letters*, 29, 1090 (2004).

44. Z. Chen, Y. Zhao, S.M. Srinivas, J.S. Nelson, N. Prakash, and R.D. Frostig, *IEEE J. Of Select. Topics In Quantum Electronics*, 5, 1134 (1999).
45. Y. Zhao, Z. Chen, C. Saxer, S. Xiang, J.F. de Boer, and J.S. Nelson, *Opt. Letters*, 25, 114 (2000).
46. B.T. Amaechi, A.G. Podoleanu, G. Komarov, S.M. Higham, and D.A. Jackson, *Oral Health and Preventive Dentistry,* 4, 377 (2004).
47. B.W. Colston, M.J. Everett, L.B. Da Silva, L.L. Otis, P. Stroeve, and H. Nathel, *Appl. Optics*, 37, 3582 (1998).
48. B.W. Colston, U.S. Sathyam, L.B. DaSilva, M.J. Everett, P. Stroeve, and L.L. Otis, *Opt. Express*, 3, 230 (1998).
49. B.W. Colston, M.J. Everett, U.S. Sathyam, L.B. DaSilva, and L.L. Otis, *Assessment of Oral Health,* Monogr Oral Sci., Faller R.V. (ed), Basel, Karger, 32 (2000).
50. F.I. Feldchtein, V.M. Gelikonov, R.R. Iksanov, G.V. Gelikonov, R.V. Kuranov, A.M. Sergeev, N.D. Gladkova, M.N. Ourutinan, J.A. Warren Jr., and D.H. Reitze, *Opt. Express*, 3, 239 (1998).
51. E.S. Matheny, N. Hanna, R. Mina-Araghi, W.G. Jung, Z. Chen, P. Wilder-Smith, and M. Brenner, *J. Investigat. Medicine,* 51, S78 (2003).
52. L.L. Otis, M.J. Everett, U.S. Sathyam, and B.W. Colston, Jr., *J. Am. Dent. Assoc.*, 131, 511 (2000).
53. Y. Pan, H. Xie, and G. Fedder, *Opt. Letters*, 26, 1966 (2001).
54. P. Wilder-Smith, W.G. Jung, M. Brenner, K. Osann, H. Beydoun, D. Messadi, and Z. Chen, *Lasers in Surg. and Med.,* 35, 269 (2004).
55. J. G. Fujimoto, *Nat. Biotechnol.*, 21, 1361 (2003).
56. J.M. Schmitt, IEEE J. Of Select. Topics In Quantum Electronics, 5, 1205 (1999).
57. C. Yang, *Photochem. and Photobiol.*, 81, 215 (2005).
58. H. Wang, Y. Fu, P. Zickmund, R. Shi, and J.-X. Cheng, *Biophys. J.,* 89, 581 (2005).
59. J.-X. Cheng, and X.S. Xie, *J. Phys. Chem. B,* 108, 827(2004).
60. A. Volkmer, J. *Phys. D: Appl. Phys.*, 38, R59 (2005).
61. J.D. Briers, *Physiol. Meas.*, 22, R35 (2001).
62. Y. Aizu, and T. Asakura, *J. Biomed. Opt.,* 4, 61 (1999).
63. A.K. Dunn, H. Bolay, M.A. Moskowitz, and D.A. Boas, *J. Cereb. Blood Flow Metab.,* 21, 195(2001).
64. D.A. Boas, M.A. O'Leary, B. Chance, and A.G. Yodh, *Proc. Natl. Acad. Sci. USA,* 91, 4887 (1994).
65. B. Chance, N. G. Wang, M. Maris, S. Nioka, and E.M. Sevick, *Adv. Exp. Med. Biol.* 317, 297(1992).
66. J.B. Fishkin, and E. Gratton, *J. Opt. Soc. Am., A,* 10, 127 (1992).
67. B. Beauvoit, T. Kitai, and B. Chance, *Biophys. J.,* 67, 2501 (1994).
68. J. B. Fishkin, O. Coquoz, E.R. Anderson, M. Brenner, and B.J. Tromberg, *Appl. Optics*, 36, 10 (1997).
69. E. Gratton, S. Fantini, M.A. Franceschini, G. Gratton, and M. Fabiani, *Philos. Trans. R. Soc. Lond. B Biol Sci.*, 352, 727(1997).

70. E.M. Sevick, B. Chance, J. Leigh, and S. Nioka, *Anal. Biochem.* 195, 330 (1991).
71. A.E. Cerussi, A.J. Berger, F. Bevilacqua, N. Shah, D. Jakubowski, J. Butler, R.F. Holcombe, and B.J. Tromberg, *Acad. Radiol.* 8, 211(2001).
72. D.B. Jakubowski, A.E. Cerussi, F. Bevliacqua, N. Shah, D. Hsiang, J. Butler, and B.J. Tromberg, *J. Biomed. Opt.,* 9, 230 (2004).
73. B.W. Pogue, S.P. Poplack, T.O. McBride, W.A. Wells, K.S. Osterman, U.L. Osterberg, and K.D. Paulsen, *Radiology,* 218, 261 (2001).
74. N. Shah, A.E. Cerussi, D. Jakubowski, D. Hsiang, J. Butler, and B.J. Tromberg, *J. of Biomed. Optics,* 9, 534 (2004).
75. D.J. Cuccia, F. Bevilacqua, A.J. Durkin, S. Merritt, B.J. Tromberg, G. Gulsen, H. Yu, J. Wang, and O. Nalcioglu, *Appl. Optics*, 42, 2940 (2003).
76. A.K. Popp, M.T. Valentine, P.D. Kaplan, and D.A. Weitz, *Applied Opt.*, 42, 2871 (2003).
77. D.J. Cuccia, F. Bevilacqua, A.J. Durkin, and B.J. Tromberg, *Opt. Letters,* 30, 1354 (2005).
78. T. Pham, O. Coquoz, J. Fishkin, E. Anderson, and B.J. Tromberg, *Rev. Sci. Instrumentat.,* 71, 2500 (2000).
79. D.C. Prasher, V.K. Eckenrode, W.W. Ward, F.G. Prendergast, and M.J. Cormier, *Gene*, 111, 229 (1992).
80. A. Cubitt, R. Heim, S. Adams, A. Boyd, L. Gross, and R. Tsien, *Techniques in Biol. Sci.* (TIBS), 20, 448 (1995).
81. R. Heim, A. Cubitt, and R. Tsien, *Nature,* 373, 663 (1995).
82. R. Tsien, *Annu. Rev. Biochem.*, 67, 509 (1998).
83. O. Griesceck, *Current Opinion in Neurobiol.*, 14, 636 (2004).
84. J. Zhang, R. Campbell, A. Ting, and R. Tsien, *Nature Reviews/ Molec. cell biol.,* 3, 906 (2002).
85. M. Doubrovin, I. Serganova, P. Mayer-Kuckuk, V. Ponomarev, and R. Blasberg, *Bioconjugate Chem.,* 15, 1376 (2004).
86. T. Troy, D. Jekic-McMullen, L. Sambucetti, and B. Rice, *Molec. Imaging,* 3, 9 (2004).
87. D.S. Lidke, and D.J. Arndt-Jovin, *Physiology,* 19, 322 (2004).
88. I.L. Medintz, H.T. Uyeda, E.R. Goldman, and H. Mattoussi, *Nat. Materials,* 4, 435 (2005).
89. O.V. Salata, *J. of Nanobiotechnology* 2(3), (2004). http://www.jnanobiotechnology.com/content/2/1/3.
90. J.M. De la Fuente, M. Fandel, C.C. Berry, M. Riehle, L. Cronin, G. Aitchison, and A.S.G. Curtis, *ChemBioChem.*, 6, 933 (2005).
91. E.B. Voura, J.K. Jaiswal, H. Mattoussi, and S.M. Simon, *Nat. Medicine,* 10, 993 (2004).
92. W. Jiang, E. Papa, H. Fischer, S. Mardyani, and W.C.W. Chan, *Trends in Biotechnol.,* 22, 607(2004).

CHAPTER 4

SPECTROSCOPY

Janaky Narayanan

Department of Physics, National University of Singapore
2 Science Drive 3, Singapore 117542.

The interaction of electromagnetic radiation with matter is governed by the frequency of the radiation and the properties of the absorber and leads to a variety of phenomena such as scattering, absorption and emission. Different regions of the electromagnetic spectrum and various spectroscopic techniques can be used to extract details of the molecular structure, structural changes and molecular environment of materials. In this chapter, the fundamentals of absorption and emission spectroscopy are discussed with particular reference to biological macromolecules.

4.1 Introduction

Apart from the chemical and biological techniques, several physical techniques have contributed to the development of the science of molecular biology. No single technique, except x-ray diffraction of single crystals, can resolve the complete three dimensional structure of a biomacromolecule. X-ray crystallography has several limitations such as difficulties in growing good quality single crystals and acquisition and analysis of data for precise determination of atomic positions. However, by employing spectroscopic techniques one can "look" at small parts of a macromolecule and get details about their stereochemistry, conformation, binding sites and other structural information. Ultraviolet (UV)-visible spectroscopy, fluorescence spectroscopy, circular and linear dichroism (CD and LD), Infrared (IR) and Raman spectroscopies,

Electron Spin Resonance (ESR) and Nuclear Magnetic Resonance (NMR) spectroscopies are some of the techniques that are of great utility in the structural analysis of biological molecules.

The basis of spectroscopy is the interaction between electromagnetic radiation and matter. The charge and spin distributions in a molecule endow it with certain electrical and magnetic properties, which are affected when it is exposed to electromagnetic radiation. As a result, the molecules undergo a change of state and also alter the radiation that emerges from the sample. A wide range of wavelength of electromagnetic radiation can be employed in the spectroscopy of biological molecules – from x-rays ($\sim 10^{-10}$ m) to radio waves (~ 0.1 m) – to probe distinct aspects of molecular structure. This has led to the development of various experimental techniques. The fraction of the incident radiation absorbed or dissipated by the sample is measured in absorption spectroscopy, some modes of NMR spectrometry and various elastic scattering techniques. The radiation emitted by the sample as a result of excitation due to incident radiation is measured in fluorescence, phosphorescence and inelastic scattering techniques. The polarization properties of the radiation are exploited in the circular and linear dichroism and fluorescence polarization measurements.

Any molecule absorbs radiation in some wavelength range and gets excited to a higher energy state. There exist various physical processes by which the molecule can de-excite to its ground state. These processes characterize the structural properties and the molecular environment. As a consequence of the excitation of the molecule, chemical bonds can be broken, new bonds can be formed, the molecule may get oxidized or reduced and its conformation can change. All these processes comprise the topics of photophysics and photochemistry and can be probed by various spectroscopic techniques. In this chapter certain fundamental aspects of these processes and techniques are dealt with.

4.2 Molecular Orbitals and Transitions

Molecules are atoms held together by electrons forming bonds. The molecule as a whole can rotate, and the nuclei can vibrate because the

bonds have some flexibility. A molecule may exist in a number of different stationary states characterized by discrete values of energy and angular momentum, electron density distribution, and equilibrium geometry. The allowed states of the molecule and the mechanisms by which it can change from one state to another are well described by using the principles of quantum mechanics. The stationary states are obtained as the solutions (denoted by the wave functions, Ψ) of time-independent Schrödinger equation of the system.

For an electron in an atom, the term atomic orbital is used to describe its stationary state. The hydrogen atom's lone electron is said to occupy the 1*s* orbital. In the notation 1*s*, the number 1 represents the principal quantum number meaning that the electron occupies the first energy state, the K-shell, and *s* represents the sub-shell that characterizes the orbital angular momentum associated with the orbital motion of the electron around the nucleus. The *s* orbitals have a maximum occupancy of two paired electrons with opposite spins. The *p* orbitals can have six electrons which are paired in each of the p_x, p_y and p_z orbitals, and so on. Electron configuration refers to the arrangement of electrons in various atomic orbitals. The atomic number, *Z*, of fluorine, neon and sodium are, respectively, 9, 10, and 11. The electron configurations of these atoms are, respectively, $1s^2 2s^2 2p^5$, $1s^2 2s^2 2p^6$, and $1s^2 2s^2 2p^6 3s$.

A molecular orbital is obtained by linear superposition of atomic orbitals and can contain no more than two electrons. For example, in the formation of the hydrogen molecule by covalent bonding of two hydrogen atoms, the linear combination of the two 1*s* atomic orbitals leads to the formation of two molecular orbitals denoted by σ and σ^*, as shown in Fig. 4.1. The *bonding orbital* σ is occupied by the two electrons with antiparallel spins. When the molecule is excited, one of the electrons jumps to the *anti-bonding* orbital, σ^*. The anti-bonding state, being of higher energy, is an unstable state and the molecule tends to de-excite to the lower energy bonding state.

Orbitals generated by the fusion of *s* orbitals normally are σ orbitals. The *s* orbitals have a spherical symmetry around the atomic nucleus. The *p* orbitals have a nodal point at the nucleus and have a butterfly like

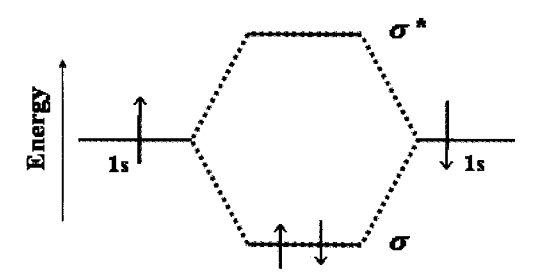
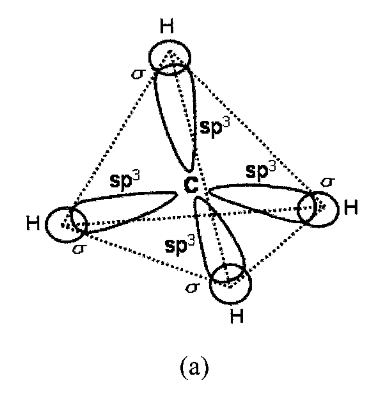


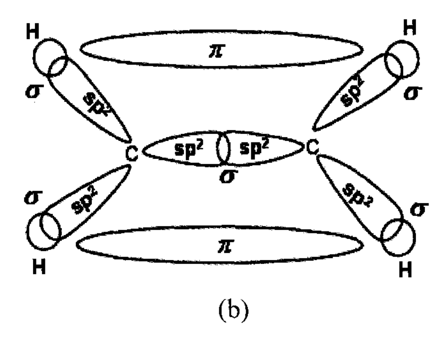
Fig. 4.1. The molecular orbitals σ and σ^* of the hydrogen molecule formed by the superposition of 1*s* atomic orbitals of hydrogen atoms.

configuration (dumb-bell shape). The end-to-end superposition of the *p* orbitals forms σ bonds and the sideway coalescence leads to the formation of π bonds. As in the case of σ orbitals, the π orbitals also have bonding (π) and anti-bonding (π^*) states. In addition to σ and π orbitals in the molecules, there are *n orbitals* (non-bonding orbitals) that resemble atomic orbitals embedded in the molecule. The *n* electron is localized to the neighborhood of one nucleus and interacts only weakly with the other nuclei. If a molecule contains atoms such as oxygen ($1s^2\ 2s^2 2p_x 2p_y 2p_z^2$) or nitrogen ($1s^2 2s^2 2p_x 2p_y 2p_z$), the highest energy state occupied by paired electrons corresponds to the lone pairs which are not involved in bonds, thus retaining their atomic character (non-bonding orbitals). For example, in NH_3 one lone-pair and in H_2O two lone-pair non-bonding orbitals are produced.

In multi-atomic molecules, the atomic orbitals of the same atoms often combine to form *hybrid orbitals* before they form molecular orbitals. The number of hybrid orbitals are equal to the number of atomic orbitals that combine. The electron configuration of carbon is $1s^2 2s^2 2p_x 2p_y$. Since it has two unpaired *p* electrons in the ground state, it is expected to be bivalent. However, in compounds carbon exhibits a valence of four which can be explained by the formation of hybrid orbitals. By promoting one of the 2*s* electrons to $2p_z$ state, it acquires an electron configuration of $1s^2 2s 2p_x 2p_y 2p_z$. The orbitals of the four unpaired electrons combine among themselves to form hybrid orbitals.



(a)



(b)

Fig. 4.2. (a) sp^3 hybridization and formation of CH_4 molecule; (b) sp^2 hybridization and formation of C_2H_4.

When all four orbitals combine, the tetragonal or sp^3 hybridization results in four equivalent hybrid orbitals directed towards the corners of a regular tetrahedron centered on the carbon nucleus. These hybrid orbitals can form four σ molecular orbitals with $1s$ orbitals of four hydrogen atoms leading to the formation of methane (CH_4), as shown in Fig. 4.2(a).

In trigonal, or, sp^2 hybridization, $2s$, $2p_x$ and $2p_y$ orbitals of the carbon atom are mixed, leading to three sp^2 orbitals in the xy plane at an angle of 120° to each other. The fourth atomic orbital, the $2p_z$ of each carbon atom is unchanged by sp^2 hybridization and contains the so-called π electrons. For example, in the formation of ethylene ($H_2C{=}CH_2$) molecule, the three sp^2 hybrids of the two carbon atoms are fused with

each other and with $1s$ orbital of hydrogen atoms to form five localized σ orbitals in the plane of the molecule. The p_z orbitals, which extend above and below the molecular plane, then fuse together to form π orbitals as shown in Fig. 4.2(b). Thus the double bond between the two carbon atoms contains one σ bond and one π bond, whereas the C-H single bonds are σ bonds.

In ground states of organic molecules the following molecular orbitals are generally found: (i) Bonding σ orbitals in single bonds between atoms consisting of almost localized electrons with strong binding. (ii) Bonding π orbitals in multiple bonds between atoms consisting of delocalized electrons which interact easily with their environment. (iii) Non-bonding n orbitals with electrons not involved in bonds and thus retaining their atomic character.

An electron from the ground state orbital can be excited to a higher energy state by absorption of radiation, provided the energy of the photon $h\nu$ is equal to the energy difference between the two states. Here, h is Planck's constant and ν is the frequency of the radiation. $\nu = c/\lambda$, where c is the speed of light and λ is the wavelength. Two types of orbitals are important in excited states – anti-bonding σ^* orbital and anti-bonding π^* orbital which is delocalized. In the ground state, σ orbital corresponds to the lowest energy state and n orbital is the highest energy state. σ^* is the highest excited state. As shown in Fig. 4.3, there are six possible electronic transitions between the ground and excited states, namely, $\sigma \rightarrow \sigma^*$, $\pi \rightarrow \sigma^*$, $n \rightarrow \sigma^*$, $\sigma \rightarrow \pi^*$, $\pi \rightarrow \pi^*$, and $n \rightarrow \pi^*$.

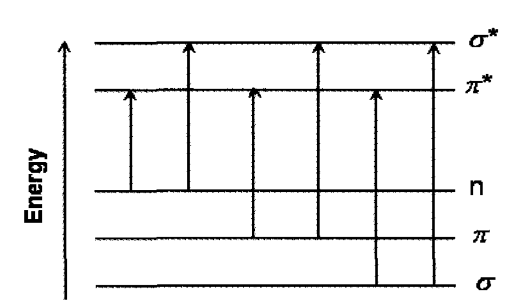


Fig. 4.3. A simple molecular orbital energy level diagram (not to scale) showing the ordering of the orbitals in energy relative to each other.

The energy required for $\sigma \rightarrow \sigma^*$ transition is the highest and $n \rightarrow \pi^*$ transition corresponds to the lowest energy transition. The $\pi \rightarrow \pi^*$ transitions lie in the spectral range $\lambda > 200$ nm to the near infrared. Most biological molecules absorb radiation in this range. The $n \rightarrow \pi^*$ transitions are relatively weak compared to the intense $\pi \rightarrow \pi^*$ transitions. $\pi \rightarrow \pi^*$ transitions shift to longer wavelength side (red-shift) when the solvent polarity changes from non-polar to polar and this is called *bathochromicity*. The $n \rightarrow \pi^*$ transitions are distinguished from $\pi \rightarrow \pi^*$ transitions by the *hypsochromicity* (blue-shift, that is, shift to shorter wavelengths) in going from non-polar to polar solvents. $\pi \rightarrow \sigma^*$, $n \rightarrow \sigma^*$, and $\sigma \rightarrow \pi^*$ transitions are in general blurred by solvent absorptions below 190 nm. The $\sigma \rightarrow \sigma^*$ transitions lie in the range of vacuum UV (~ 100 nm).

4.3 Transition Dipole Moment

A molecule may possess a permanent electric dipole moment (e.g. H_2O) due to the centers of positive and negative charges being non-coincident, or, may have no permanent dipole moment as in the case of benzene (C_6H_6). However, the electric vector of the incident radiation can induce a dipole moment even in molecules with no permanent dipole moment. During electronic transitions when the charge distribution between the ground and excited state changes, the dipole moment of the molecule also changes. Each electronic transition has an associated transition dipole moment which can be determined from the quantum mechanical calculation of the change in the charge distribution in going from the initial state to the final state, taking into account the wave functions of these two states. If the transition dipole moment is large, the probability of the electronic transition is large and hence the absorption intensity will also be large.

The various electronic transitions have very different transition probabilities for absorption. When orbitals involved in the transition do not overlap in space the transition probability is low. The most intense transitions are those in which a strong dipole oscillation (large transition

dipole moment) is involved and where the orbitals have a good spatial overlap. This is the case for $\pi \rightarrow \pi^*$ transitions, which are highly favored and give rise to intense absorption bands. In $\pi \rightarrow \pi^*$ excitation, the excited π^* electron keeps a strong coupling with its partner in the π orbital and the π and π^* orbitals occupy the same region in the molecule. In $n \rightarrow \pi^*$ transition, an electron moves from a localized orbital to a delocalized orbital. The spatial overlap of the two orbitals therefore is poor and the transition probability is considerably low. As a result, the absorption bands of $n \rightarrow \pi^*$ transitions are about a hundred times less intense than those of the $\pi \rightarrow \pi^*$ transitions. The intrinsic lifetime (duration for which the electron stays in the excited state) of $n \rightarrow \pi^*$ state is about a hundred times greater than that for $\pi \rightarrow \pi^*$ state. Hence the molecule becomes very reactive as an electron donor or an electron acceptor once an $n \rightarrow \pi^*$ state has been attained. Oxidation-reduction reactions are very common in biology and $n \rightarrow \pi^*$ states may very well be involved.

4.4 Spin Selection Rule

In the electronic ground state of a molecule, the orbitals of lowest energy are usually occupied by two electrons. The resultant spin of the two electrons in the molecular orbital is given by, $S = 1/2 \pm 1/2$, with + sign for parallel and – sign for antiparallel spins. According to *Pauli Exclusion Principle*, in the ground state, the spins of the two electrons that occupy the same orbital must be antiparallel. Thus the electrons are paired and their spin angular momenta add to give a resultant spin $S = 0$; the multiplicity of this electronic state, $2S + 1 = 1$ and is called a *singlet* (S) state.

When an electron is excited from the ground state to an excited state, the excited electron may or may not have its spin oriented antiparallel to the spin of its counterpart remaining in the ground state (Fig. 4.4). If both spins are antiparallel, the excited state is called a singlet state. If the spins are parallel, the resultant spin $S = 1/2 + 1/2 = 1$ and the spin multiplicity $2S + 1 = 3$. Such a state is called a *triplet* (T) state. Most of the molecules

of biological interest are in the singlet ground state. However, oxygen molecule (O_2) in ground state is in triplet state. The energies of the excited electronic singlet and triplet states are different, because of the difference in interactions between electrons of parallel and antiparallel spins. The triplet state associated with a given singlet state always has a somewhat lower energy.

Transitions between energy states and hence their life times are governed by selection rules. The *spin multiplicity selection rule*, which plays a key role in photophysical processes, states that for a spin allowed transition the spin multiplicity must be conserved. Thus electric dipole transitions between electronic states of different multiplicity are forbidden. Multiplicity describes the perturbation of the state in the presence of a magnetic field. A singlet state is not perturbed by magnetic field; but the triplet state splits into three closely spaced energy levels. An electron has a magnetic moment arising from its orbital motion as well as spin. The interaction of the spin and orbital magnetic moments is called *spin-orbit coupling*. A change in multiplicity, that is, a spin forbidden transition (S↔T) can occur due to a strong internal magnetic field arising from the circulating currents due to orbital motion of electrons. This spin-orbit interaction becomes more effective when heavy atoms with higher nuclear charge are introduced in a molecule.

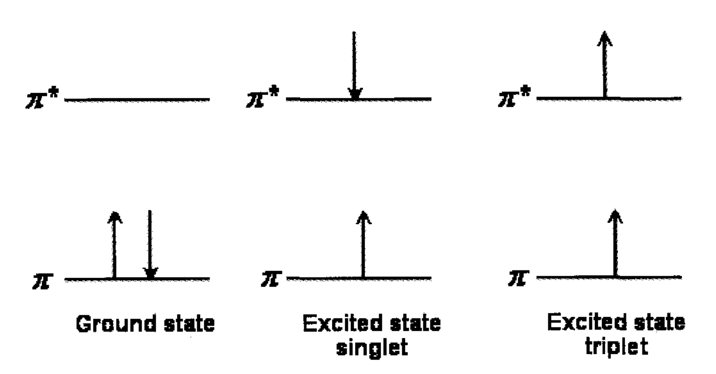


Fig. 4.4. Schematic representation of excited singlet and triplet states for $\pi \rightarrow \pi^*$ transition.

4.5 Franck-Condon Principle

Various quantized electronic, vibrational, and rotational energy states are available to a molecule. To a good approximation, the internal energy of a molecule can be separated into three components.

$$E = E_e + E_v + E_r. \tag{4.1}$$

E_e is the electronic energy, E_v is the vibrational energy of the nuclei in the potential field of the electrons and E_r is the rotational energy of the entire molecule. Energy difference between electronic states is typically in the order of a few eV. Transitions between electronic states require energy found in light quanta of visible and UV regions. Light with proper energy for transitions between vibrational states is found in IR region, as the vibrational states are separated by energies of the order of 0.1 eV. Rotational states are spaced close together, approximately, 0.01 eV apart. Low energy microwaves have the proper energy to excite a molecule from lower to higher rotational state. Pure rotational spectra are rarely observed for substances of biological interest.

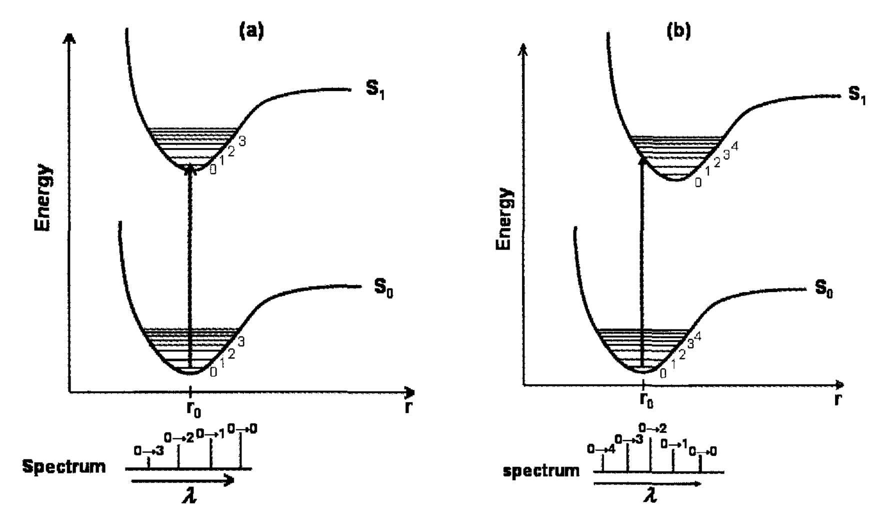


Fig. 4.5. Frank-Condon potential energy diagrams for electronic transitions to different vibrational levels of the excited state. (a) Ground and excited states have the same equilibrium internuclear distance r_0. (b) The equilibrium internuclear distance in the excited state is larger.

For all practical purposes molecules can be considered to be in their ground vibrational and electronic states at room temperature. However, transition to an excited state can be to any of the vibrational levels, but each transition has a different probability, in accordance with the Franck-Condon principle. The Franck-Condon principle is best illustrated using potential energy diagram for a diatomic molecule with abscissa showing the distance r between the nuclei. In Fig. 4.5, lower curves represent the ground electronic state S_0 and upper curves, the excited electronic state, S_1. Each electronic state is composed of several vibrational states indicated by 0, 1, 2, etc. The vibrational states are approximately those of a harmonic oscillator.

The largest probability of finding the nuclei at a certain distance apart is indicated by the potential energy curve for all vibrational states except the ground vibrational state (0 level) in which, the electrons are most likely to be found at the equilibrium distance r_0 between the nuclei corresponding to the mid-point of the zero vibrational level. At room temperature, nearly all molecules in a solution or a solid are in the vibrational ground state. According to Frank-Condon principle, since the absorption of a photon is a practically instantaneous process occurring in femtoseconds (10^{-15}s), and the nuclei are too heavy to move within this time period, the most probable transition is the one which involves no change in the internuclear distance. This transition is represented by a vertical line on the potential energy diagram starting from the mid-point of the zero vibrational level of the ground electronic state. In Fig. 4.5(a), both the upper and lower states have the same internuclear distance. Hence the electronic transition between the ground state vibrational levels ($0 \rightarrow 0$) has the highest probability and represents the maximum intensity in the absorption spectrum. If the equilibrium internuclear distance in the excited state is larger than the ground state as shown in Fig. 4.5(b), the vertical transition $0 \rightarrow 2$ will give intense absorption. It is obvious from Fig. 4.5 that the absorption band is unsymmetrical in case (a) and symmetrical in case (b). Thus the intensity distribution of absorption bands can give important information about an absorbing substance.

4.6 Jablonski Diagram

Excitation of an electron from electronic-vibrational (vibronic) ground state to excited states and subsequent de-excitation processes can be described by the Jablonski energy diagram (Fig. 4.6).

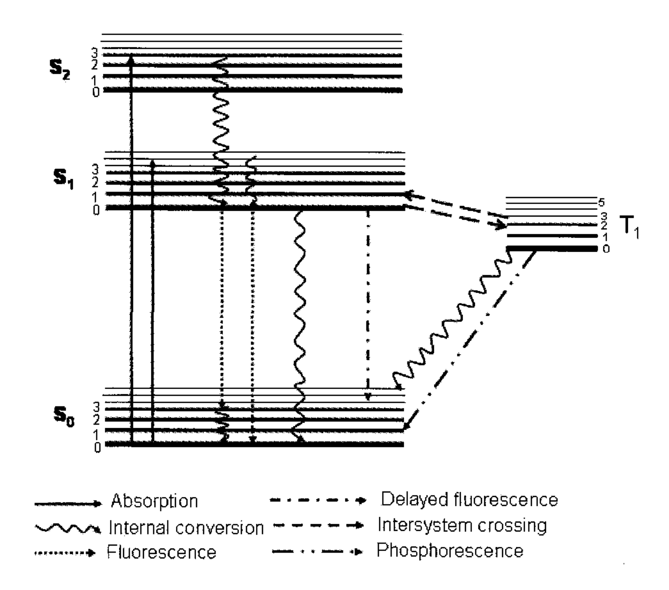


Fig. 4.6. Jablonski energy diagram showing the possible transitions in a molecule and the accompanying photophysical processes.

Absorption process is generally from ground singlet state S_0 to excited singlet states S_n ($n = 1, 2, \ldots$). The spin reversal in the transition from ground singlet state S_0 to excited triplet states T_n is highly improbable since the antiparallel electrons are strongly coupled to the ground state. From the first excited state, a spin reversal can occur more easily since the spin-spin coupling becomes looser. The greater the spin-orbit coupling and the weaker the spin-spin coupling, the more likely can a singlet-triplet transition ($S \rightarrow T$) occur. But such transitions will have very low probability as they violate the spin selection rule. Transition intensities are proportional to the difference in the number of molecules in the initial and final energy states. At room temperature, the population of excited electronic states is negligible. Thus transitions such as $S_1 \rightarrow S_n$ and $T_1 \rightarrow T_n$, for $n > 1$, are possible only after excitation to S_1 state due to

initial absorption from S_0 state, and they need intense flash lamps or laser for excitation. In these processes, energy of the two photons absorbed consecutively (*biophotonic process*) is stored in the molecule. For multiphotonic processes different selection rules apply in order to conserve the total angular momentum of the system comprising the photons and the molecule.

The excited electron can revert to the ground state in several ways which include both radiative and non radiative processes.

Internal conversion: After the photon absorption and excitation to upper electronic states, the molecule finds itself in a non-equilibrium state and begins to vibrate like a spring. The periods of these vibrations are of the order of 10^{-12} s (picosecond). Since the usual lifetimes of excited electronic states are of the order of 10^{-9} s, (nanosecond), there is enough time for the molecule to undergo thousands of vibrations. During this time the vibrational energy is lost by energy exchange with the medium by collision with the solvent molecules in which the excited molecule is dissolved. This process brings the molecule to thermodynamic equilibrium with the environment and is temperature sensitive. With a few rare exceptions, generally all molecules rapidly relax to the lowest vibrational level (level 0) of S_1. The de-excitation from this state can be through three path ways, namely, nonradiative relaxation, fluorescence and intersystem crossing.

Nonradiative relaxation: Several processes like quenching, bleaching and internal conversion can lead to the loss of energy of the excited singlet state and return the molecule to the ground state without emission of a photon, if these processes are faster than the lifetime of the first excited singlet state. If the upper vibrational levels of the ground state overlap the lower vibrational levels of the excited state (degeneracy of vibrational levels), then a nonradiative loss of energy occurs due to the electron cascading through the vibrational states up to the zero vibrational level of S_0.

Fluorescence: From the zero vibrational level of the first singlet S_1, de-excitation can occur by the emission of a photon as the molecule returns to one of the vibrational levels of the ground electronic state S_0. Thus fluorescence is the photon emission which results from the electronic transition between singlet states. Such transitions are quantum

mechanically allowed with high emissive rate (number of emissions per second). These high emission rates result in short fluorescence lifetime of typically a few nanoseconds.

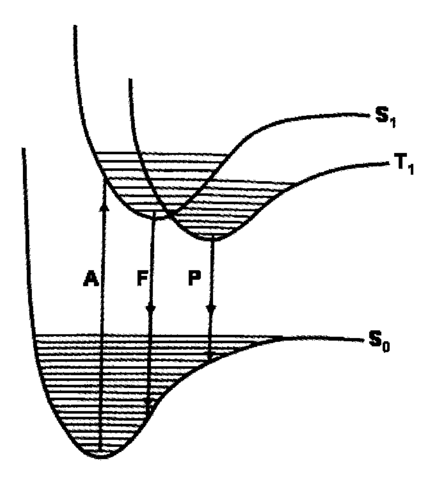


Fig. 4.7. Frank-Condon energy diagram showing the ground (S_0) state and the first excited singlet (S_1) and triplet (T_1) states. The vertical lines marked A, F, and P, respectively, represent absorption, fluorescence and phosphorescence. (Adapted from Ref. 6)

Intersystem crossing: A spin exchange can convert an excited singlet into an excited triplet state. This intersystem crossing occurs when a triplet state lies just below the excited singlet electronic state, that is, there is a near coincidence of two vibrational levels in the excited singlet and triplet states (Fig. 4.7).

Upon excitation to singlet state, if the molecule undergoes intersystem crossing and becomes an excited triplet, it can de-excite to the ground state by nonradiative relaxation, or by emission of a photon. *Phosphorescence*: It is the photon emission which results from a triplet excited state returning to singlet ground state. Because the change in spin violates the quantum mechanical spin conservation rules, decay from the excited triplet to ground singlet state is very slow and occurs only if there are no other allowed energy paths open. Typical phosphorescence lifetimes range from milliseconds to seconds. Collisions with quenchers

and internal conversion can compete effectively with phosphorescence. Hence phosphorescence is rarely observed at room temperature in solutions. Frozen solutions at liquid nitrogen temperature (77 K) or highly viscous solutions at room temperature must be employed to observe phosphorescence, after careful removal of quenchers such as oxygen molecules from the solution.

Delayed fluorescence: It results from two intersystem crossings, first from singlet to triplet ($S_1 \rightarrow T_1$) and then from the triplet back to the singlet ($T_1 \rightarrow S_1$) before de-excitation to the ground singlet state, S_0.

4.7 Stokes Shift

The application of Franck-Condon principle to the absorption and emission processes explains Stokes shift, a long-established experimental fact even before quantum mechanics and Franck-Condon principle provided its interpretation. Stokes shift refers to the displacement of fluorescence and phosphorescence spectra to longer wavelengths (red shift) with respect to the absorption spectrum.

Fig. 4.7 represents the most intense absorption and emission (fluorescence/phosphorescence) lines observed in accordance with the Franck-Condon principle. Absorption corresponds to the vertical upward line (A) from the mid point of zero vibrational level of S_0. This line hits the potential energy curve corresponding to S_1 at an excited vibrational state to which the molecule is raised. After relaxation to zero vibrational level of S_1, fluorescence emission occurs which returns the molecule to an excited vibrational state of S_0 as indicated by the line F. Thus the fluorescence emission photon is of smaller energy than the photon absorbed; that is, $h\nu_e < h\nu_a$. In other words, $\lambda_e > \lambda_a$, where λ_a and λ_e represent the wavelengths of the absorbed and emitted photons of frequencies ν_a and ν_e, respectively. If an intersystem crossing occurs from the excited singlet to the excited triplet, subsequent de-excitation to the ground singlet is by emission of phosphorescence as indicated by the line P. The phosphorescence photon energy being smaller than that of fluorescence, the phosphorescence spectra are red-shifted with respect to fluorescence spectra.

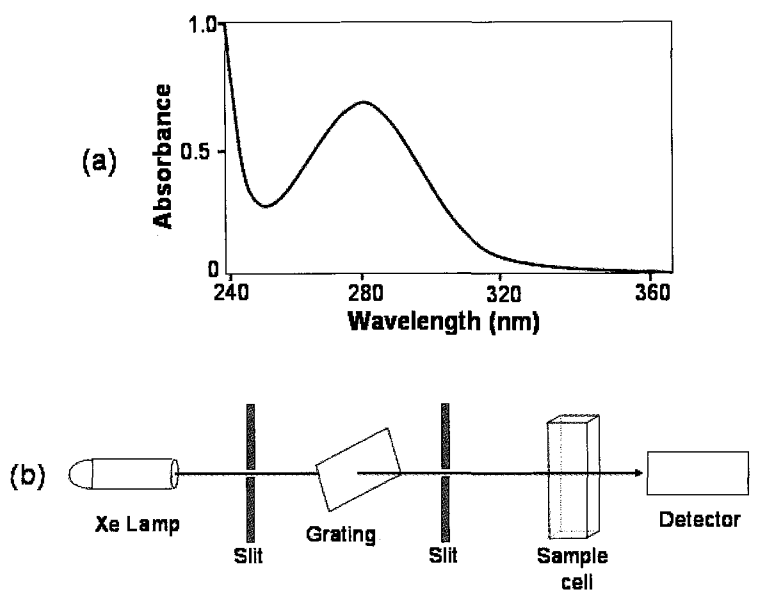


Fig. 4.8. (a) The absorption spectrum of a protein with characteristic absorption peak λ_{max} at 280 nm due to the chromophores tryptophan and tyrosine. (b) Schematic representation of a typical spectrophotometer.

4.8 Spectrophotometry

The chemical groups in a molecule that are involved in electronic transitions are called *chromophores*. Since excitation can be to any of the vibrational levels, each chromophore has a characteristic vibronic absorption band. For molecules in solution, the individual vibronic bands are broadened by collisions with solvent molecules. Thus the absorption spectrum, which is a plot of intensity absorbed versus wavelength of radiation, smears into a broad band. Each chromophore has a characteristic absorption spectrum such as the one shown in Fig. 4.8(a), which can be measured using a spectrophotometer of basic outline as shown in Fig. 4.8(b).

The light source is a lamp such as xenon lamp that emits a wide variety of wavelengths in the UV/visible range from 200 nm to 800 nm. For selection of single wavelengths from the white light emitted by the

lamp, monochromator (prism or grating) is used and the light is focused into the sample cell containing the molecules under investigation. The amount of light that passes through the sample is detected by a photomultiplier or a photodiode. A spectrum is obtained when the wavelength of the light incident on the sample is changed continuously by rotating the monochromator. Sample cells or cuvettes are made up of a material that is transparent in the spectral range of interest. Therefore, quartz or fused silica is used for the UV/visible range. Absorption spectroscopy is usually performed with molecules dissolved in a transparent solvent. The buffers used should not absorb light in the wavelength range of the experiment. In order to obtain a true spectrum for the chromophore of interest, it is essential to determine a blank spectrum of the cuvette plus solvent and to subtract it from the solution spectrum.

The Beer-Lambert law is used in quantitative absorption spectrophotometry. If I_0 is the incident intensity (photons per unit area and time) and I is the transmitted intensity for a particular wavelength λ, the *absorbance A* or *optical density* (O.D.) of the solute is given by the Beer-Lambert law as:

$$A(\lambda) = log_{10}\left(I_0 / I\right) = \varepsilon(\lambda)cl \qquad (4.2)$$

Where ε is the *molar extinction coefficient* of the solute, c is the molar concentration and l is the optical path length through the sample cell. This relationship can also be applied to solution containing mixtures of absorbing species, provided there is no interaction among the various species. The plot of A or ε against λ is the absorption spectrum. Beer-Lambert law is a limiting law since it can only be applied to solutions of relatively low concentrations ($A < 2$). The maximal extinction coefficient ε_{max} of typical single chromophores varies over a wide range of values (1 to 10^5 M^{-1} cm^{-1}).

The peak position (λ_{max}), intensity (ε_{max}), and width of absorption maxima reflect the structure and interaction of the molecules, which in turn depend on solvent conditions (*p*H, ionic strength, polarity), temperature etc. *Hypsochromic* and *bathochromic* shifts are observed when the solvent near the chromophore is changed (*solvent effect*). A band that increases in intensity under certain conditions is said to exhibit

a *hyperchromic* shift. Conversely, a band that decreases in intensity will experience a *hypochromic* shift. Hyperchromism is commonly used to follow the melting behavior of the DNA double helix. Intrinsic chromophores found as part of biomacromolecules, such as aromatic amino acids in proteins and bases in nucleic acids, have generally low extinction coefficients. For example, the aromatic amino acid tryptophan has ε_{max} of 5800 M^{-1}c m^{-1} at 280 nm. Hence use can be made of extrinsic chromophores (*reporter groups*) with strong absorption spectra ($\varepsilon_{max} \sim 10^5$ M^{-1} cm^{-1}). Ideally, reporter groups should have a single site of attachment to the target macromolecule and should not affect its normal structure and function. Absorption spectroscopy is an excellent technique for following ligand-binding reactions, enzyme catalysis and conformational transitions in proteins and nucleic acids.

4.9 Fluorescence Intensity and Lifetime

The number of excited molecules at the exciting wavelength λ_e is proportional to the number of photons absorbed, that is, proportional to $(I_0 - I)$, where I_0 and I are, respectively, the incident and transmitted intensities. From Beer-Lambert law (Eq. 4.2),

$$I = I_0 e^{-2.303A(\lambda_e)} = I_0 e^{-2.303\varepsilon(\lambda_e)cl} \quad (4.3)$$

For low absorbance ($A(\lambda_e) < 0.03$), Eq. 4.3 can be approximated as:

$$I_0 - I = 2.303A(\lambda_e)I_0 = 2.303\varepsilon(\lambda_e)clI_0 \quad (4.4)$$

All excited molecules do not fluoresce as there are other path ways such as internal conversion, intersystem crossing and quenching for de-excitation. The probability that an excited molecule fluoresces is given by the *quantum yield* Φ_F, defined as:

$$\Phi_F = \frac{\textit{Number of photons emitted}}{\textit{Number of photons absorbed}} = \frac{\textit{Rate of fluorescence}}{\textit{Rate of absorption}} \quad (4.5)$$

The fluorescence intensity $F(\lambda)$ measured at a single wavelength is called the *fluorescence yield*. In dilute solutions or suspensions, $F(\lambda)$ depends linearly on the absorbed intensity $(I_0 - I)$, quantum yield Φ_F, and the collection efficiency of the instrument η. Using Eq. 4.4, $F(\lambda)$ can be written as:

$$F(\lambda) = 2.303A(\lambda_e)I_0\Phi_F\eta = 2.303\varepsilon(\lambda_e)clI_0\Phi_F\eta \tag{4.6}$$

When sample absorbance exceeds about 0.05 in a 1 cm path length, the relationship between $F(\lambda)$ and the sample concentration c becomes nonlinear and the measurements will be distorted by self-absorption and inner-filter effect. Self-absorption occurs if there is a large overlap between the absorption and fluorescence emission of the sample. Inner-filter effect is the attenuation of incident light near the front face of the sample cell due to high concentration of the solute.

Integration of Eq. 4.6 over the wavelength λ gives a quantity that is proportional to the number of excited singlet states, and can be obtained from the integrated area under the fluorescence spectrum. If the fluorescence emission spectra of two samples are measured under the same experimental conditions, the ratio of the two observed fluorescence intensities is given by,

$$\frac{F_1}{F_2} = \frac{Area\ 1}{Area\ 2} = \frac{A_1\Phi_{F1}}{A_2\Phi_{F2}} \ . \tag{4.7}$$

If the quantum yield of one substance is known, then that of the other can be calculated. Usually, quinine sulfate in 1 N sulfuric acid ($\Phi_F = 0.7$) or fluorescein in 0.1 N sodium hydroxide ($\Phi_F = 0.93$) is used as a standard to calibrate the instrument and measure the quantum yield of unknown samples.

Quantum yield can also be measured from fluorescence lifetime τ_F which is a measure of the time a *fluorophore* (chromophore that can fluoresce) spends in the excited state before it returns to the ground state. It can be measured by exciting the sample with a short pulse of light and monitoring $I(t)$, the intensity of light emitted as a function of time t as shown in Fig. 4.9. Assuming that the fluorescence arises from a single fluorophore and the decay is a single exponential,

$$I(t) = I_{\max} e^{-t/\tau_F} \tag{4.8}$$

where $I(t)$ and I_{max} are the intensities recorded, respectively, at any time t and at $t = 0$ when the pulse is switched off.

Since internal conversion and intersystem crossing are the other possible pathways for deactivation of the excited singlet state, if the kinetic rate constants for the fluorescence, internal conversion and

intersystem crossing are respectively, k_F, k_{Ic}, and k_{Isc}, then the lifetime of the excited singlet, τ_F is related to these rate constants by,

$$\tau_F = (k_F + k_{Ic} + k_{Isc})^{-1} \tag{4.9}$$

The quantum yield,

$$\Phi_F = \frac{k_F}{k_F + k_{Ic} + k_{Isc}} = \frac{\tau_F}{\tau_{F0}} \tag{4.10}$$

where $\tau_{F0} = k_F^{-1}$ is the lifetime of the fluorophore in the absence of nonradiative processes. The rate of radiative process is not temperature sensitive; but the rate of internal conversion and intersystem crossing increase with temperature because the additional thermal energy can populate the higher vibrational levels. Thus quantum yield of a fluorophore decreases as temperature increases.

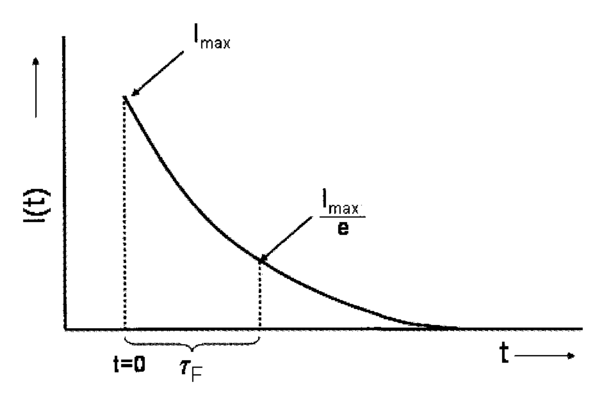


Fig. 4.9. Fluorescence intensity monitored as a function of time of a sample after exciting it with a short pulse of light.

4.10 Spectrofluorimetry

The essential elements of any fluorescence detection system (fluorimetry, microscopy, flow cytometry etc.) are the excitation source, the sample cell containing the fluorophore, wavelength filters/ monochromators to isolate the emission photons from excitation photons, and a detector to record the emission as an electrical output or a photographic image.

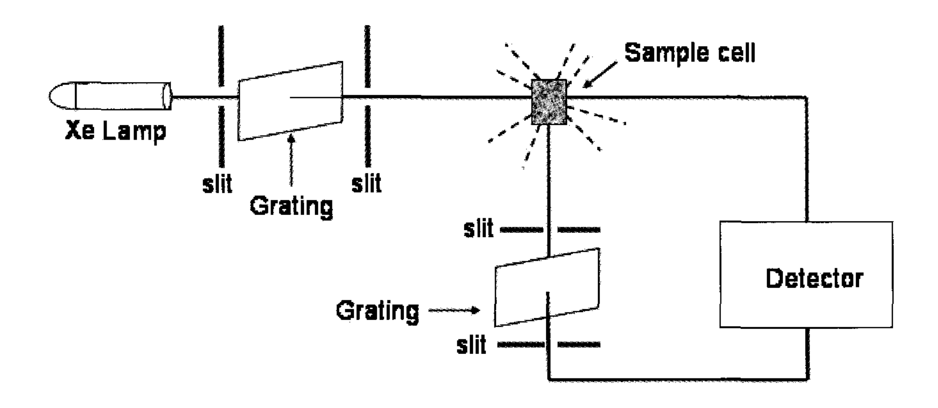


Fig. 4.10. Basic outline of a spectrofluorimeter.

Spectrofluorimeter measures the fluorescence properties of bulk samples (See Fig. 4.10). An incident beam of light of wavelength in the UV/visible range is passed through a sample cell containing the fluorophore. A monochromator (prism/grating) is used to select a proper excitation wavelength. Though fluorescence is emitted in all directions from the fluorophore, usually the emission radiation is detected at right angles to the incident radiation to minimize stray light and exclude the detection of the incident beam. The detector is a photomultiplier tube or a photodiode array.

A spectrofluorimeter can record the fluorescence emission spectrum by keeping the excitation at a constant wavelength or record the excitation spectrum by viewing the emission at a constant wavelength. For a single solute in dilute solution, when the incident intensity is maintained at a constant value, the fluorescence intensity $F(\lambda)$ (Eq. 4.6) is proportional to $\varepsilon(\lambda_e)\Phi_F$. Thus when the emission wavelength is fixed at λ and the excitation wavelength λ_e is varied, the spectrum obtained is a measure of $\varepsilon(\lambda_e)\Phi_F$ versus λ_e. For most molecules the fluorescence quantum yield is approximately independent of the excitation wavelength, and hence the excitation spectrum for dilute solution is a replica of the absorption spectrum. The advantage is that concentrations far too less than what are required for absorption spectrophotometry can be used to record the excitation spectrum.

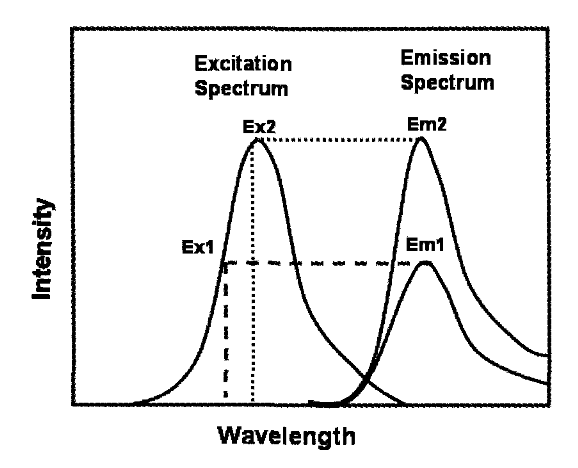


Fig. 4.11. Invariance of the emission wavelength with excitation wavelength and dependence of emission intensity on the excitation intensity.

Under the same conditions, the fluorescence emission spectrum ($F(\lambda)$ versus λ) is independent of the excitation wavelength λ_e due to partial dissipation of excitation energy during the excited state lifetime by vibrational relaxations (see Jablonski diagram, Fig. 4.6). However, as shown in Fig. 4.11, the emission intensity is proportional to the intensity of the excitation spectrum at the excitation wavelength, because $F(\lambda)$ is proportional to the absorbance (Eq. 4.6).

Unless the fluorophore loses it fluorescence property irreversibly (*photobleaching*), the same fluorophore can be repeatedly excited and detected. The fact that a single fluorophore can generate many thousands of detectable photons is fundamental to the sensitivity of fluorescence. The sensitivity of fluorescence is also a consequence of the relatively long time a molecule stays in excited state before de-excitation. During the time the singlet remains excited, all kinds of processes can occur, including protonation and deprotonation reactions, solvent-cage relaxation, local conformational changes, any process coupled to translational or rotational motion etc.

The quantum yield Φ_F and the experimental sensitivity $\varepsilon_{max}\Phi_F$ for most chromophores found in biomacromolecules are quite low and the lifetimes are short. Hence fluorescent probes with large experimental

sensitivity are used, which can bind at some specific site of the molecule and provide a variety of types of structural information. A number of fluorescent molecules have very low fluorescence in aqueous solutions; but their fluorescence gets enhanced by more than a factor of 20 in a nonpolar or a rigid environment.

The position of the fluorescence band is affected by the solvent effects. In solution, dipole moments of the solvent molecules have an ordered distribution around the dipole moment of the fluorophore. Upon excitation, the molecular dipole moment changes and the solvent molecules reorient around the excited fluorophore in a process called *solvent relaxation.* This results in the reduction of the energy separation between the ground and excited states, and a red-shift of the fluorescence emission. Increasing the solvent polarity produces a larger red shift of the fluorescence band. Chemical reactions of the excited state with the solvent such as hydrogen-bonding, formation of charge-transfer complexes etc., also affect the fluorescence spectrum.

4.11 Fluorescence Quenching

Apart from internal conversion and intersystem crossing, two other processes, namely, quenching and fluorescence resonance energy transfer (FRET) can depopulate the excited singlet states. Internal quenching is due to some intrinsic structural feature of the excited molecule. External quenching is a bimolecular process involving the excited molecule and an external quencher and can be of two types – *static quenching* and *collisional* or *dynamic quenching.* In static quenching the excited fluorophore forms a stable complex with the quencher called a 'dark' complex. The energy of the excited state is lost in the complex formation. In collisional quenching, some energy from the excited state is lost as kinetic energy. Oxygen, halogens, amines and many electron-deficient organic molecules behave as collisional quenching agents. If $[q]$ is the quencher concentration and k_q is the rate constant associated with the quenching, then the lifetime of the excited singlet in the presence of external quenching can be written as:

$$\tau_{Fq} = (k_F + k_{Ic} + k_{Isc} + k_q[q])^{-1} \qquad (4.11)$$

The corresponding quantum yield,

$$\Phi_{Fq} = \frac{k_F}{k_F + k_{Ic} + k_{Isc} + k_q[q]} \tag{4.12}$$

Using Eqs. 4.9 to 4.12,

$$\frac{\tau_F}{\tau_{Fq}} = \frac{\Phi_F}{\Phi_{Fq}} = 1 + \tau_F k_q[q] = 1 + K[q] \tag{4.13}$$

Eq. 4.13 is called the Stern-Volmer equation and $K = \tau_F k_q$ is called the Stern-Volmer constant.

4.12 Fluorescence Resonance Energy Transfer (FRET)

If two separate fluorophores (extrinsic or intrinsic) have unique locations in a macromolecular complex, it is possible for the emission light energy from the fluorophore D (*donor*) to be absorbed by the fluorophore A (*acceptor*) with subsequent emission (See Fig. 4.12). This phenomenon is called fluorescence resonance energy transfer (FRET), which results in quenching of donor's fluorescence and enhancement of acceptor's fluorescence (*sensitized fluorescence*). An example of FRET is the quenching of tyrosine fluorescence by nearby tryptophans within the protein molecule by the energy transfer process.

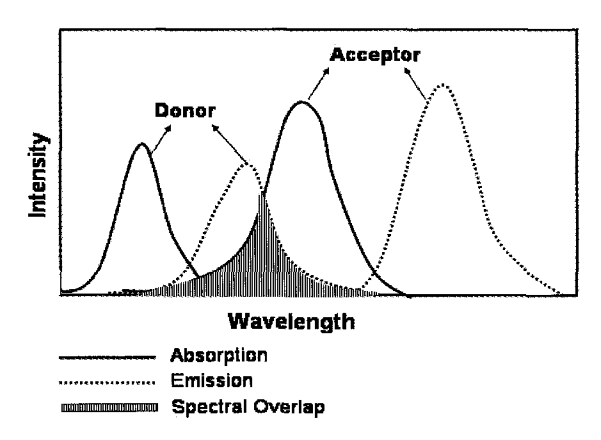


Fig. 4.12. Schematic representation of the absorption and emission spectra of donor and acceptor showing the spectral overlap. (Adapted from Ref. 1)

The probability or rate of energy transfer depends on (i) the spectral energy overlap between the donor and acceptor, (ii) the inverse sixth power of the distance between them, (iii) their relative orientation, and (iv) the intrinsic fluorescence lifetime of the donor. The energy transfer efficiency E called *Förster transfer* depends on the distance R between the donor and acceptor and varies as R^{-6}. In practice, E can be determined from the fluorescence intensity F_{DA} or the excited state lifetime τ_{DA} of the donor determined in the presence of the acceptor and F_D or τ_D determined in the absence of the acceptor.

$$E = \frac{R_0^6}{R_0^6 + R^6} = 1 - \frac{F_{DA}}{F_D} = 1 - \frac{\tau_{DA}}{\tau_D} \quad (4.14)$$

Here, R_0 is a constant related to the donor-acceptor pair. By determining E experimentally, R can be calculated if R_0 is known. This method is well-suited to probe the topology of membrane-bound proteins which are difficult to study by x-ray diffraction and NMR methods. FRET is an important mechanism in photosynthesis for harvesting light energy from the Sun.

4.13 Fourier Transform Infrared (FTIR) Spectroscopy

Atoms combine to form a molecule through chemical bonding. The chemical bonds have characteristic bond length, bond angle and electron density and exist in specific vibrational energy states. If radiation of an appropriate wavelength passes through the sample, the molecules can undergo transitions to a higher vibrational energy state by absorbing the photon energy. Since it is the nuclei that vibrate, the vibrational absorption spectroscopy is concerned with molecules in their ground electronic state. Transition from ground vibrational state to first excited vibrational state due to absorption of radiation is called fundamental absorption and the corresponding frequency is called the *fundamental* frequency. *Overtones* are transitions to higher excited states, but occur much less frequently and have weak absorbance. Absorption bands corresponding to vibrational transitions generally fall in the infrared (IR) region of the electromagnetic spectrum with wavenumber, $\bar{\nu} = 1/\lambda$, in the range 200 cm^{-1} to 5000 cm^{-1}. An IR spectrum consists of a plot of

absorbance versus wavenumber, $\bar{v}$. Absorbance is determined by Beer-Lambert law.

Typically IR absorptions are less intense than electronic (UV/visible) spectra. Hence, much higher sample concentrations are needed. Water has very intense absorption in the IR range. To overcome this problem, IR spectroscopy is carried out on samples dissolved in solvents such as heavy water (D_2O) or chloroform or samples prepared in the form of dry films. Infrared detectors such as thermocouples are much less sensitive than the photodetectors used in UV/visible spectrophotometers. These limitations restrict the application of IR spectroscopy in the study of biological macromolecules in their native state. However, this technique is found quite useful for the study of low molecular mass biomolecules and has the advantage of using sample in different forms – solutions, films, powders, and crystals. Scanning IR spectrometers similar to those used in UV/visible range are not popular as they collect only one frequency at a time in a much slower process and are not suitable for the study of biological macromolecules such as protein and DNA. Most modern instruments use Fourier transform (FT) method and employ a Michelson interferometer instead of the monochromator. The basic outline of the Fourier transform infrared (FTIR) spectrometer is shown in Fig. 4.13.

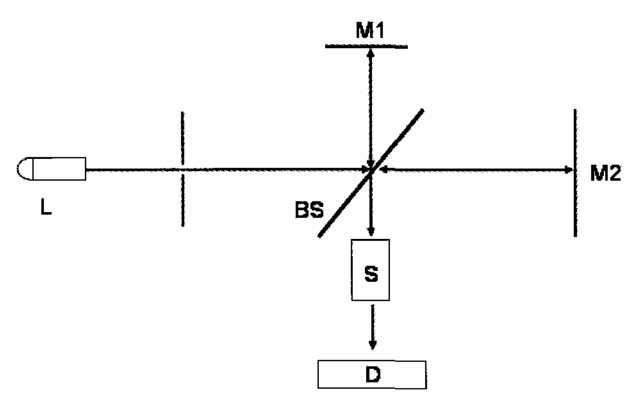


Fig. 4.13. Schematic representation of FTIR spectrometer.

Michelson interferometer consists of a fixed mirror (M1) and a movable mirror (M2) whose positions can be measured very accurately. A beam splitter (BS) inclined at 45° to the incident beam from an IR laser lamp splits the beam into two halves; one-half being reflected towards M1 and the other half being transmitted towards M2. These beams are reflected back by the mirrors M1 and M2 and recombine at the beam splitter to form a resultant beam which passes through the sample. When the beams recombine, they interfere constructively or destructively depending on the position of the moving mirror relative to the fixed mirror. Also different IR wavelengths will interfere constructively at different mirror positions. In the FTIR instrument, intensity of the recombined beam due to all IR frequencies is recorded simultaneously as a function of the mirror position. The resulting signal is called *interferogram* which has all the IR frequencies encoded into it. On passing through the sample, some IR frequencies characteristic of the functional groups in the sample are absorbed. Thus the interferogram recorded by the detector will be characteristic of the sample. The detected interferogram is decoded using Fourier transformation to get the normal IR spectrum which is the plot of absorbance versus wavenumber. In practice, a background spectrum is obtained without the sample and used to normalize the sample spectrum. Transmittance spectrum is obtained from the ratio I/I_0, where I is the intensity measured with the sample in the beam and I_0 is the intensity measured from the background spectrum. Absorbance A is calculated as $A = -\log_{10}T$, where T is the transmittance.

Infrared spectroscopy detects the chemical functional groups in the sample from their characteristic vibrational frequencies. The chemical bonds may stretch, contract or bend as a result of interaction with IR radiation and each of these vibrational modes has a specific wavenumber range regardless of the structure of the rest of the molecule. For example, C=O group has a fundamental stretching mode at about 1700 cm^{-1} in many molecules and N-H group has a fundamental stretching mode around 3400 cm^{-1}. These group wavenumbers are used to identify the chemical groups in a molecule. The intensity of a vibrational band depends on the magnitude of the light-induced dipole. For a vibrational mode to be infrared active, the dipole moment must change during

vibration. Thus for a linear molecule such as CO_2 (O=C=O), the symmetric stretch vibration of the C=O bonds will have no IR absorption, whereas the asymmetric stretch and bending modes will be IR active. Homo-nuclear diatomic molecules such as O=O have no dipole moment and hence no IR absorbance. In contrast, carbon monoxide has a dipole moment and thus an IR spectrum. Hydrogen bonding shifts the characteristic frequencies of the chemical groups. FTIR therefore is particularly useful in the study of the structural and dynamic properties of proteins and peptides, and for following the hydrogen bonding of the DNA bases.

An alternative way of gaining information about the vibrational states of molecules is to use Raman spectroscopy. The energy difference between incident and Raman scattered light corresponds to vibrational transitions. For small molecules Raman and IR spectra are complementary to each other, because certain transitions that are of low intensity in one may have high intensity in the other. However, for large asymmetric molecules, Raman and IR spectra are essentially the same. Water has a fairly weak Raman spectrum. Hence biological samples can be studied conveniently in aqueous solutions using Raman spectroscopy.

4.14 Concluding Remarks

The diverse regions of electromagnetic spectrum used, the distinct aspects of molecular structure probed by various kinds of spectroscopy, and the associated experimental techniques are so vast that all of them cannot be recapitulated in a book chapter of this size. However, all spectroscopic methods share certain fundamental aspects of molecular biophysics which have been addressed with reference to absorption and emission processes.

Acknowledgments

This chapter is based on the course in biophysics taught by the author at the Department of Physics, National University of Singapore.

References

1. C.R. Cantor and P.R. Schimmel, *Biophysical Chemistry*, Part II (W.H. Freeman & Co., San Francisco, 1980).
2. H. Neubacher and W. Lohmann, in *Biophysics*, Eds. W. Hoppe, W. Lohmann, H. Markl and H. Ziegler (Springer-Verlag, Berlin, 1983), p. 100.
3. F. Dörr, in *Biophysics*, Eds. W. Hoppe, W. Lohmann, H. Markl and H. Ziegler (Springer-Verlag, Berlin, 1983), p. 265.
4. J.R. Lakowicz, *Principles of Fluorescence Spectroscopy* (Kluwer Academic/ Plenum, New York, 1999).
5. C. Sybesma, *Biophysics, an Introduction* (Kluwer Academic, Dordrecht, 1989).
6. E. Kohen, R. Santus, and J.G. Hirschberg, *Photobiology* (Academic Press, San Diego, 1995).
7. K.E. van Holde, W.C. Johnson and P.S. Ho, *Principles of Physical Biochemistry* (Prentice Hall, New Jersey, 1998).
8. P.R. Bergethon, *Physical Basis of Biochemistry – The Foundations of Molecular Biophysics* (Springer, New York, 1998).
9. D. Sheehan, *Physical Biochemistry: Principles and Applications* (John Wiley & Sons, New York, 2000).

This page is intentionally left blank

CHAPTER 5

LASERS AND LASER TISSUE INTERACTION

P K Gupta, N Ghosh, and H S Patel

Biomedical Applications Section,
Raja Ramanna Centre for Advanced Technology
E-mail: pkgupta@cat.ernet.in

This chapter provides an overview of lasers and their interaction with biological tissue and how these are exploited for medical applications. The specific points addressed are – how lasers work and their attributes because of which lasers find such a widespread usage. An overview of optical transport parameters of tissue and laser propagation in tissue is presented next. This is followed by a discussion on the applications of scattered or reemitted light from tissue for diagnosis. The photothermal, photochemical and photomechanical effects of absorbed light and their use for surgical and therapeutic applications are also discussed.

5.1 Introduction

Laser is one of the most important inventions of the twentieth century. Due to its remarkable properties it is finding applications in all aspects of human endeavor – industry, medicine, defense, basic research and even home entertainment. The diverse use of lasers can be put in perspective by noting that while lasers are being used to generate the highest temperatures on earth, as high as millions of degree Kelvin, as available in the core of the sun; they are also being used to generate the lowest temperatures on earth, as low as a few nano Kelvin. Similarly while lasers are being used to weld sheets of metal, they are also being used to weld the delicate layers of retina. The list can go on and on! With such a versatile tool in hand it is not surprising that mankind would like to use it

for something it cherishes most – the quality of its health care. Quality health care has two important objectives – ability to detect disease at an early stage before it becomes difficult to manage and to treat the disease with minimal effect on normal tissue. This Chapter will provide an overview of the role lasers are playing in the pursuit of both these objectives. We shall also provide a brief overview of lasers, how they work and their characteristics, which make them such a valuable tool. The discussion is at an introductory level. For details on lasers the reader is referred to references.[1-3] A more comprehensive account of the use of lasers in biomedicine is available in references 4 and 5.

5.2 Laser Basics

The word 'laser' is an acronym for Light Amplification by Stimulated Emission of Radiation. To understand lasers it is necessary to understand the two important phrases "light amplification" and "stimulated emission". For this let us recapitulate how light is emitted. Light emission takes place by two processes. One is spontaneous emission wherein an atom in excited state returns to a lower energy state, on its own, by emission of a photon with energy equal to the difference of the energies of the two atomic energy levels. In this process the atoms radiate randomly and independent of each other leading to incoherent light. The light from all conventional sources of light, which are essentially hot bodies, arises primarily by spontaneous emission of constituent atoms. In these hot bodies, atoms are continuously pumped to excited states and fall back loosing energy by spontaneous emission. It is true that in the low-pressure gas discharge like the one in fluorescent lamps, the glass walls remain cool, but the electrons and gas atoms inside the tube are accelerated to high speeds characteristic of high temperatures. In 1917 Einstein showed that an atom in excited state could also be stimulated to emit a photon in the presence of a photon with energy resonant with the atomic transition. The important characteristics of stimulated emission is that the emitted photon is an exact replica of the stimulating photon i.e. it has the same wavelength, phase, polarization etc. Thus, the process of stimulated emission provides a control on emission by independent atoms and can be used to force the

atoms to emit in phase. This control on emission of individual atoms through the control on stimulating photons is the essence of laser operation. One may ask if stimulated emission was known in 1917, why was the first laser demonstrated only in 1960. The primary reason for this lies in another important result obtained by Einstein. He showed that the a priori probability for an atom in excited state to get de-excited by stimulated emission of a photon is exactly equal to the probability for the atom to reach the excited state by the stimulated absorption of a photon. Thus, in a normal situation of thermal equilibrium where more atoms are in the lower energy state one observes a net stimulated absorption of photons leading to light attenuation. For amplification of light it is necessary that the upper level has more population than the lower level, a condition referred to as "population inversion". It took time to find practical ways to achieve population inversion and thus light amplification.

Laser is basically an oscillator at optical frequencies. The laser oscillator, a schematic diagram of which is shown in Fig 5.1 comprises of three components: a gain medium, an optical resonator with one highly reflecting and one partially transmitting mirror to provide feedback at the frequency of operation and a pump source to achieve "population inversion".

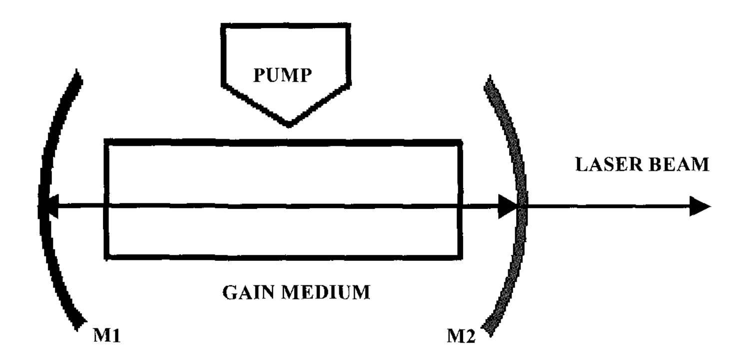


Fig. 5.1. Schematic diagram of a basic laser system. M1 has high reflectance at the laser wavelength and M2 partially transmits this wavelength.

The gain medium can be a gas, a liquid or a solid and accordingly lasers are often classified as gaseous, liquid and solid state lasers. The pump source can be a flash lamp (as in Ruby and Nd: glass lasers) or another laser (N_2 or Cu vapor lasers for pumping dye lasers) or an electric discharge as is the case with He-Ne and CO_2 lasers. It is the combination of stimulated emission process and the control on the stimulating light achieved via the optical resonator that lends lasers its striking properties of high directionality, brightness, intensity, monochromaticity, short pulse duration capability etc.

5.2.1 *Characteristics of Lasers*

Directionality: The directionality of lasers arises because only the radiation propagating exactly normal to mirror surfaces will make repeated passes through the gain medium and get amplified. Typical beam divergence of commercially available lasers is of the order of a few milli-radians. It is important to note that one can obtain a directional beam from even an ordinary source of light, by keeping it at the focal point of a lens or a concave mirror – as in a torch or a lighthouse. However, to enhance the directionality of the beam the source dimension needs to be reduced with consequent reduction in intensity of the beam.

Radiance: Due to their directionality the lasers also have large radiance i.e. power emitted per unit surface area of source per unit solid angle. In fact the radiance of a typical 1 mW He-Ne laser is two orders of magnitude larger than that of sun, a source with black body temperature of ~ 6000°C. Radiance is a fundamental property of the source and its importance lies in the fact that the intensity in the focal plane of any imaging system is proportional to the source radiance and can never exceed it. High radiance also implies that the beam can be propagated to large distances without much loss of intensity (power per unit area).

Focusability: The small laser beam divergence (θ) implies that lasers can be focused to small spot sizes (diameter $\approx f\theta$; f being the focal length of the lens). The focal spot sizes are usually limited to the order of a few wavelengths because of diffraction effects and the aberrations of

the lens. Due to its focusability, laser light can be efficiently coupled to thin optical fibers and can thus be guided endoscopically to internal organs for therapeutic applications without any major incision, considerably reducing the patient trauma and hospitalization time for several surgical procedures.

Short pulse duration capability: Lasers operate in continuous wave (CW) as well as pulsed mode. By exercising control on the stimulating light via techniques like Q-switching and mode locking[1-3], pulses as short as nanoseconds to sub-picoseconds can be generated. One common use of such short pulses is to study ultra-fast processes. Many physical processes, like the first steps in vision or photosynthesis or intermediate chemical reactions and energy exchanges between vibrating molecules in liquids, take place at extremely fast rates. Picosecond and sub-picosecond lasers have helped a great deal in unraveling these processes by taking snapshots of the interacting molecules. Further, even a small energy concentrated in a short pulse will result in very large peak power. For example, the 40 J of energy that a 40 W bulb consumes in 1s, if available in 1 ps, will result in a peak power of 4×10^{13} W.

Intensity (*Irradiance*): By focusing the laser beams to small spot sizes one can obtain very high intensities. A laser beam with power of 1 W focused to a spot diameter of 2 μm will result in an intensity of $\sim 10^7$ W/cm^2. As noted above, for pulsed lasers, peak powers can be very large resulting in enormous intensities. The high intensity of a laser beam can be used to heat, melt or even vaporize small areas of any absorbing material. The use of a pulsed laser offers the added advantage that the irradiated area can be vaporized before heat could flow out to the material in the vicinity of the exposed areas.

Monochromaticity: Laser beam can also be made highly monochromatic i.e. with minimal frequency spread. The frequency spread of typical He-Ne laser used in laboratories is $\sim 10^9$ Hz and only a few Hz for a highly stabilized laser. This may be compared with frequency spread of $\sim 10^{10}$ Hz of yellow sodium light and $\sim 3 \times 10^{14}$ Hz for the visible light from Sun. The high monochromaticity of lasers finds

numerous applications in high-resolution spectroscopy to probe the spectra of atoms, molecules and solid with ever-increasing precision. In medicine the frequency dependence of the absorption by the components of a multi-component system can be exploited for selective processing of a desired component.

Spectral coverage: Lasers are available from vacuum ultra violet to millimeter spectral region. Still shorter frequencies have been generated using non-linear optical techniques. For details on different lasers and their typical operational parameters the reader is referred to references 1 and 2. Table 5.1 enlist some of the lasers which are widely used for medical applications.

5.3 Light Propagation in Tissue

When light falls on a tissue, part of it is reflected, transmitted or scattered from the tissue and a part may be absorbed in the tissue. The absorbed energy may also be reemitted as fluorescence. The light reflected, transmitted, scattered or reemitted as fluorescence depends on the characteristics of the tissue and therefore can be used for tissue diagnostics. For diagnostic applications one would like to minimize absorption in tissue for two reasons; first it would allow probing larger depths of the tissue and secondly deposition of energy in the tissue may result in adverse effects. The biological tissue is not only inhomogeneous but is also turbid due to the presence of microscopic inhomogenities (macromolecules, cell organelles, organized cell structure, interstitial layers etc). An exact modeling of the inhomogeneous and turbid tissue is not presently feasible. The tissue is therefore generally represented as an absorbing bulk material with scatterers randomly distributed over the volume. Further, it is usually assumed to be homogenous, even though this is not a true representation. The parameters used to characterize the optical properties of the tissue are, the absorption coefficient (μ_a), single scattering coefficient (μ_s), the transport coefficient ($\mu_t = \mu_a + \mu_s$) and the phase function $p(s, s')$.[6-8]

The tissue absorption at a given wavelength is a macroscopic average of the absorption by several of its constituents. In Fig. 5.2, we show the wavelength dependence of the absorption co-efficient of some important constituents of the tissue. The major contributors of absorption in tissue in the ultraviolet (UV) spectral range are DNA and proteins. In the visible and near infrared (NIR) wavelength range, the absorption in tissue is dominated by hemoglobin and melanin. Water, the main constituent of all tissues, strongly absorbs beyond about 2 μm. For wavelength greater than ~ 650 nm and smaller than 2 μm the tissue absorption is weak and so the light can penetrate deeper.

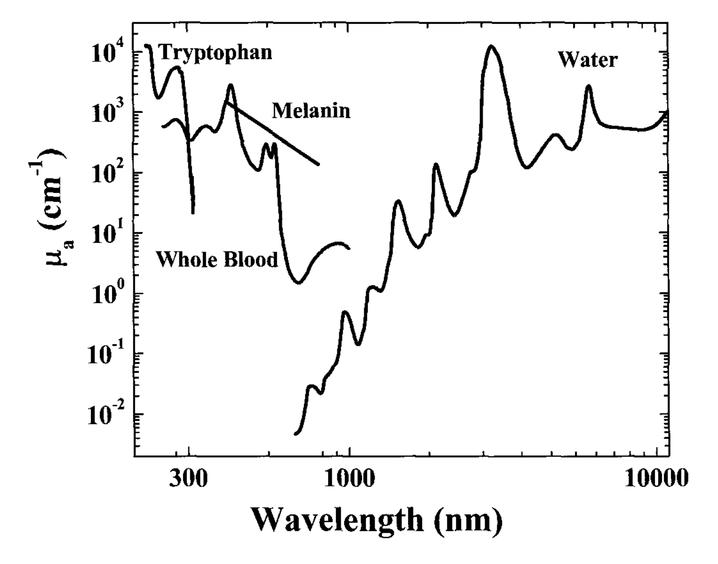
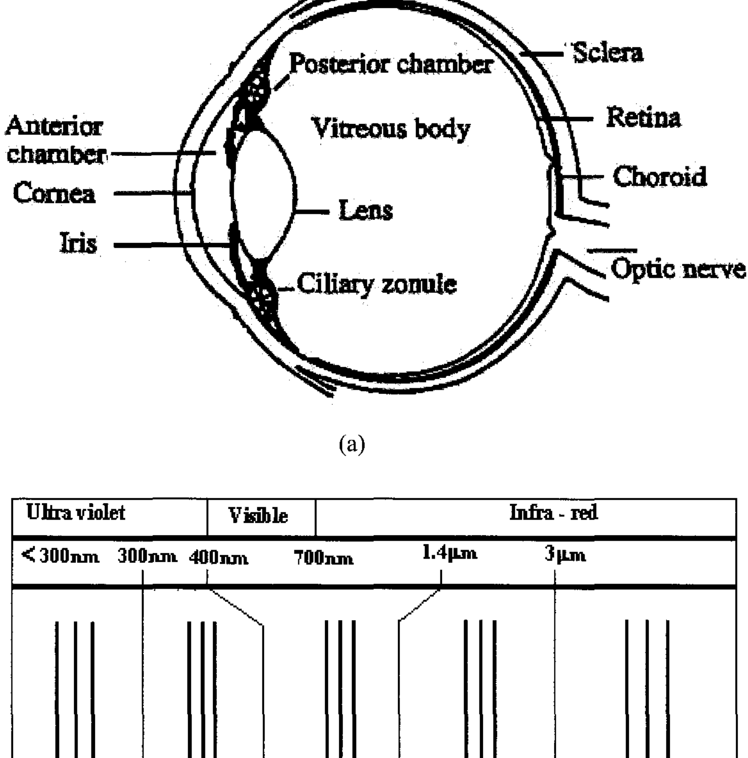


Fig. 5.2. Wavelength dependence of absorption coefficient of some important constituents of tissue.

While a very small penetration depth is advantageous for precision processing a large penetration depth is also required in many situations like for coagulating a large tissue volume. In a multicomponent organ the absorption of laser radiation of a given wavelength will be different in different tissues of the organ and can be exploited for selective interaction with the target tissue. To illustrate the point, we show in Fig. 5.3 (a) schematic diagram of the structure of the eye and the transmission characteristics of its different components (See Fig 5.3 (b)).

Since wavelengths less than 300 nm or greater than 3 μm are absorbed in cornea, lasers operating in these wavelength regions will be appropriate for reprofiling of cornea to correct vision disorders. However, due to the different tissue interaction processes involved in the two spectral regions (which we shall discuss later), the short wavelength lasers are preferred for this purpose. Intraocular applications require that light be transmitted through the ocular tissue, which occurs to different extent between 400 to 1400 nm.



(a)

(b)

Fig. 5.3. The structure (a) and the spectral transmission characteristic (b) of the human eye.

In this range the important light absorbing substances are melanin (in the retinal pigment epithelium (RPE) and iris pigment epithelium), uvea and trabecular meshwork, hermoglobin in blood vessels and xanthophyll in macula. Argon laser emits blue and green light which is highly absorbed in both melanin and hemoglobin and is therefore widely used for intraocular procedures involving RPE, iris, trabecular meshwork etc.[9] For retinal procedures the green light of argon laser is preferred because blue light is strongly absorbed in xanthophyll, which can lead to damage in macular region, the region that has highest visual acuity. There are several other factors that may influence the choice of laser wavelength. For example red light would be preferred for retinal procedures in the presence of vitreous or retinal hemorrhage since it readily passes through hemoglobin. The disadvantage associated with the use of red light is that due to its deeper penetration into the choroidal layer, an increase in pain and possibly choroidal bleeding can result. Thus a clear understanding of the optical characteristic of the tissue is essential for selective deposition of energy at the target site.[10-12] A detailed description of light propagation through tissue and related equations can be found in the chapter 9 of this book.

5.4 Optical Imaging and Diagnosis

5.4.1 *Optical Imaging*

Before we discuss the use of optical techniques for biomedical imaging, it may be pertinent to note that the use of light for biomedical imaging and diagnosis is not new. Much of the conventional diagnosis, be it at out patient department, endoscopy or even histopathology, makes use of the light scattered from the tissue. However, in all the application, one is able to look only at the surface of the tissue and if one wants to peep inside the body one resorts to other techniques like sonography, X-Ray or Magnetic Resonance Imaging (MRI). The inability to image optically the layers beneath the surface is best seen if one shines a torch at one's hand. One can see a pinkish glow but not the outline of the bones in the path of the beam. The pinkish glow arises because the red

component of the light is least attenuated and is therefore dominant in the light that emerges from the hand. The bones are not visible because of the multiple scattering of light in the tissue. It is for the same reason we cannot see a spoon dipped in milk. For optical imaging of objects embedded in a turbid medium, basically two schemes have been used. One scheme is to filter out the multiply scattered light and the other referred to as inverse approach is to map the multiple scattered light at various positions around the object. From the measured transmitted intensities and known optical properties, one can in principle generate a spatial map of the absorption and scattering coefficients leading to imaging of the turbid object.

Several approaches have been used to filter out the multiply scattered light and image objects embedded in a turbid medium.[13-15] These exploit the loss of coherence or depolarization of the scattered light or the fact that the scattered light emerges from the tissue in all directions and also takes longer time to emerge as compared to the unscattered (ballistic) or predominantly forward scattered (snake like) components. The latter essentially travel in forward direction and so arrive earlier. Coherence gating filters out the ballistic photons having the highest image information and hence can provide images with the best resolution (down to few μm). However, the number of ballistic photons decrease exponentially on propagation through a turbid medium and will be of the order of e^{-10} of the incident number of photons on propagation through 1mm thick tissue with a scattering coefficient of ~100 cm^{-1}. Therefore, coherence gating can only be used for imaging of transparent objects (like ocular structure) or thin turbid tissue like mucosal layers of hollow tubes. Optical coherence tomography (OCT), the approach that exploits coherence gating for optical imaging has emerged as a rapid, non-contact and noninvasive high resolution imaging technique and is finding clinical applications in ophthalmology, dermatology etc.[14]

Another approach to filter out the multiply scattered light is to make use of the fact that it travels longer and hence will take longer time to reach the detector. Thus, by use of ultra-short temporal gates (of picosecond / sub-picosecond duration) one can filter out the ballistic and snake like components from the multiply scattered light. Since the biological tissue is highly forward scattering medium the reduced

scattering coefficient is much smaller than μ_s (1/10 of μ_s for $g = 0.9$) and therefore the sum total of snake like and ballistic photons is orders of magnitude larger than the ballistic component facilitating imaging through larger depths. Further, with the use of non-linear optical techniques like stimulated Raman scattering the image-bearing component of light can be selectively amplified to further enhance the depth of imaging. However, due to the use of snake like photons, which have undergone some scattering events, the resolution is poorer (of the order of 100 μm).

For imaging through larger depths as for example for imaging human brain or female breast one has to necessarily work with diffuse photons.[16] Although the spatial resolution possible in imaging using diffuse photons is rather limited (at best few mms) there is considerable interest in this approach because it allows imaging through the largest depths of the turbid medium.

5.4.2 *Optical Spectroscopic Diagnosis*

Single scattering of collimated light is used widely to study cells and subcellular structures in optically thin suspensions. This approach is not directly applicable for tissues due to multiple scattering. Nevertheless, diffusely scattered light from tissue contains information about its underlying structures. Measurements on the angular distribution of scattered light or its wavelength variation can be used to get estimates for scatterer size in tissues.[17] Since multiple scattering in tissue leads to depolarization of light, measurements on the polarized component of back-scattered light can be used to filter out the multiply scattered light and thus look at the light scattered from the superficial tissue layer. This approach has been used to extract the size distribution and the density of the nuclei in superficial epithelial cell layer, which can be used to monitor neoplastic changes in biological tissues.[18]

It is important to note here that the scattered light also has a very weak component which is scattered in-elastically i.e. with a change in frequency via processes like fluorescence, Raman scattering etc. The inelastically scattered light is characteristic of the chemical composition and morphology of the tissue and thus can help in monitoring metabolic

parameters of the tissue and also in discriminating diseased tissue from normal. Since the inelastically scattered light is a very small fraction of incident light, practical applications require use of high brightness sources i.e. lasers and appropriate light delivery and collection systems. Both fluorescence[19,20] and Raman spectroscopic[21, 22] approaches are being actively pursued for their diagnostic potential. While fluorescence technique is more sensitive and presently better developed for clinical applications, the advantage offered by the Raman technique is the ease with which one may get valuable biochemical information of the tissue. The use of Laser-Induced Fluorescence (LIF) offers several important advantages for biomedical diagnosis, like, a very high intrinsic sensitivity, and the use of non-ionizing radiation, which makes it particularly, suited for mass screening and repeated use without any adverse effects. Further the diagnosis can be made near-real time and in-situ whereby no tissue needs to be removed and tissue diagnosis by this technique can be easily automated facilitating use by even less skilled medical personnel. A lot of efforts have been put for evaluation of the use of LIF for diagnosis of cancer. Two approaches have been investigated. One approach involves systemic administration of a drug like haemaotoporphyrin derivative (HpD), which is selectively retained by the tumor. The drug localized in the tumor fluoresces when photoexcited with light of appropriate wavelength. This fluorescence is used for detection and imaging of the tumor. Photoexcitation also leads to populating the triplet state via intersystem crossing. The molecule in the excited triplet state can then directly react with biomolecules or lead to generation of singlet oxygen, which is toxic to the host tissue. The resulting destruction of the host tissue is exploited for photodynamic therapy of tumor.[23] However, from the point of view of use in diagnosis this approach has two drawbacks; a possible dark toxicity of the drug and the possibility of drug induced photosensitization. For example a major drawback with the use of HpD has been drug-induced photosensitization of the skin necessitating the patient to avoid light for a few weeks. Efforts have therefore been made either to reduce the quantity of the administered drug thereby improving fluorescence detection techniques for diagnostics or to develop tumor markers where the triplet state is rapidly quenched and thereby photosensitization is avoided. In other

approach, which has received more attention in recent years, does not use any exogenous tumor markers. Instead it exploits for diagnosis the subtle changes in the fluorescence from native tissues (autofluorescence) as it transforms from normal to the malignant state.

The tissue autofluorescence originates from a number of endogenous fluorophores that are present in tissue. Table 5.1 lists the major endogenous fluorophores, along with their excitation and emission maxima. The fluorescence emission characteristics of these endogenous tissue fluorophores are shown in Fig. 5.4. These fluorophores include aromatic amino acids like tryptophan, structural proteins like collagen and elastin, co-enzymes like NADH and flavins and the porphyrins. Their excitation maxima lie in the range 280–500 nm, whereas their emission maxima lie in the range 300–700 nm. The autofluorescence emission spectrum of tissue is essentially a convolution of the emission spectra of the endogenous fluorophores of tissue and therefore strongly

Table 5.1. Excitation and emission maxima of the major endogenous tissue fluorophores.

Endogenous fluorophores	Excitation maxima (nm)	Emission maxima (nm)
Amino acids		
Tryptophan	280	340
Structural proteins		
Collagen/Elastin	335	400
Coenzymes		
NADH/NADPH	340	460
FAD /flavins	430	550
Porphyrins	400	630,690

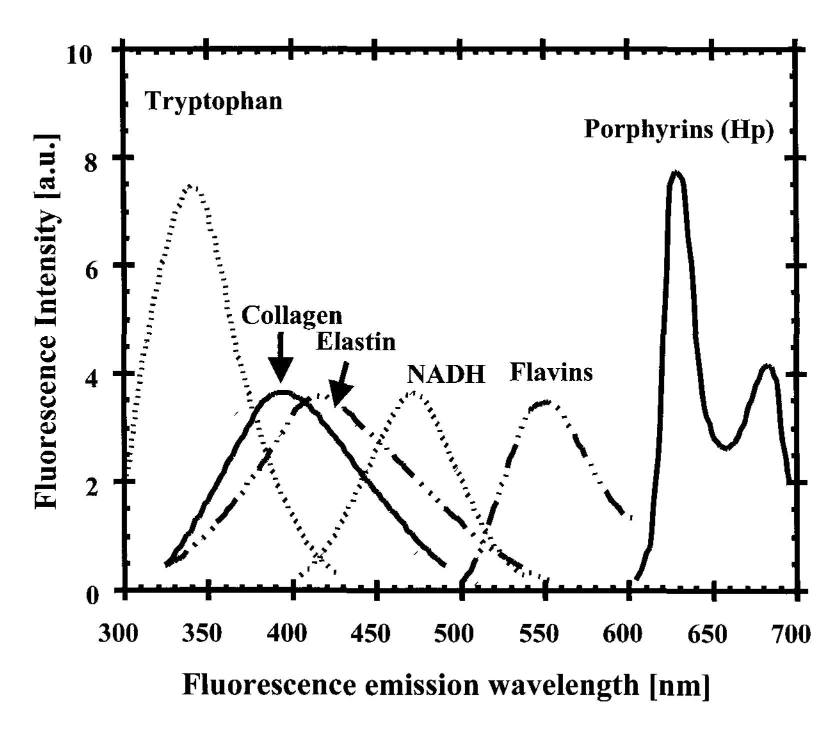


Fig 5.4. Fluorescence emission spectra of the various endogenous tissue fluorophores.

depends on the wavelength of the light of excitation. Only those endogenous fluorophores are excited and emit fluorescence whose absorption bands have an overlap with the wavelength of the excitation light. Since the excitation light and the emitted fluorescence have to propagate through the turbid tissue the measured tissue fluorescence is also influenced by the absorption and scattering at both the excitation and the emission wavelengths.[24] This makes it difficult to extract, from the measured fluorescence, the intrinsic fluorescence of the tissue, which may have valuable biochemical information on the tissue. A typical system for use of LIF for cancer diagnosis is shown in Fig 5.5. It comprises of an excitation laser, a spectrograph coupled to a multi channel detector (CCD) and a fiber optic probe to excite and collect fluorescence from tissue.

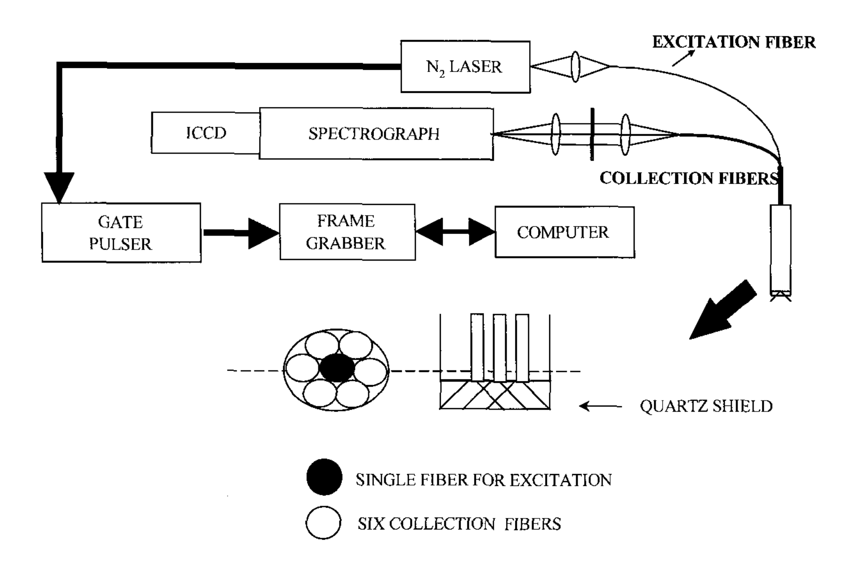


Fig. 5.5. A schematic of the clinical prototype of an N_2 laser based autofluorescence set-up.

Quite often the probe used is an optical fiber bundle with two legs, one having a single optical fiber and the other with six optical fibers. The two legs merge to form a common fiber bundle that consists of a central fiber surrounded by a circular array of six fibers. The central fiber delivers excitation light to the tissue surface and the six surrounding fibers collect tissue fluorescence from the volume illuminated by the excitation light. The light coming from the distal ends of the six collection fibers is imaged via a lens system on the entrance slit of the spectrograph whose output end is coupled to the CCD detector. All the parameters of tissue fluorescence, spectral profile, yield, decay time, and the degree of polarization have been investigated and used to discriminate malignant sites from normal. In Fig 5.6, we show the 337 nm-excited autofluorescence spectra recorded from normal, cancerous (ductal carcinoma) and benign human breast tissues.

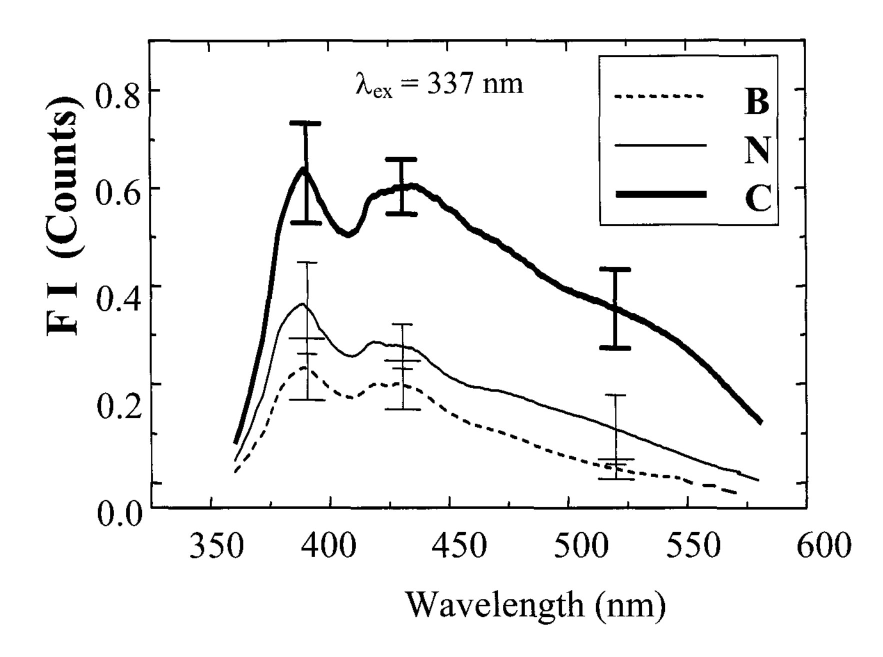


Fig. 5.6. 337 nm excited autofluorescence spectra for the normal breast tissues (N), cancerous breast tissues (C) and benign breast tumors (B). The spectra are the average of the spectra of sixty tissue samples investigated. The error bars represent the standard deviation (from reference 25).

The corresponding spectra from normal and cancerous (Squamous cell carcinoma) tissues of human oral cavity are displayed in Fig. 5.7. For both the tissue types, two emission bands characterize the spectra. The relatively narrow emission band peaking at 390 nm is due to the structural proteins. The other comparatively broader long wavelength band peaking around 460 nm has contributions from the co-enzyme NADPH/NADH, flavins etc. with the contribution from NADH being the dominant.[25,26]

One particularly interesting feature to be noted is that the fluorescence intensity from the malignant breast tissues is higher by about a factor of 3 compared with the normal and benign tumor tissue (see Fig. 5.6).[25] In

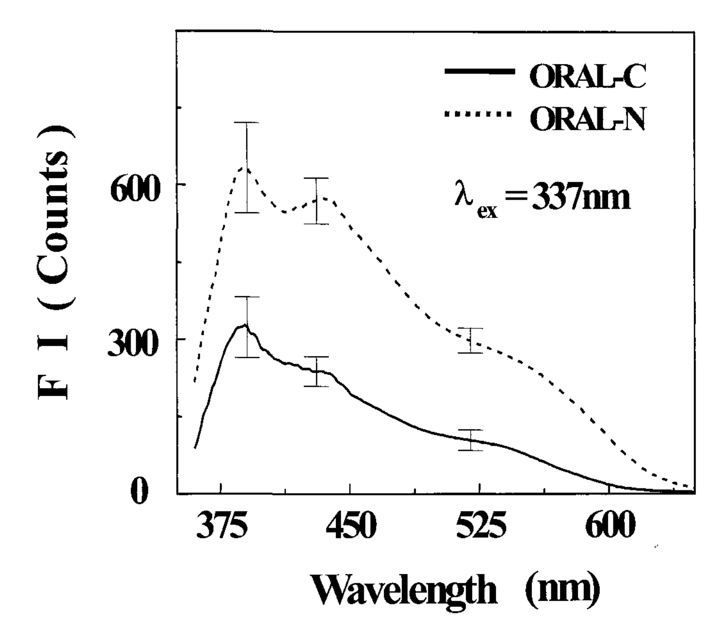


Fig. 5.7. 337 nm excited autofluorescence spectra for the cancerous and normal tissues of human oral cavity. The spectra are the average of the spectra of forty five tissue samples investigated. The error bars represent the standard deviation (from reference 26).

contrast, the fluorescence intensity from malignant sites of the oral cavity is seen to be lower by a factor of ~ 2 compared with intensity from nonmalignant sites (See Fig. 5.7).[26] Excitation/emission spectroscopy[27] and time-resolved measurements[28] of fluorescence from breast and oral cavity tissue suggest that the difference in yield is primarily due to variation in the concentration of the fluorophores in the malignant and non-malignant tissue sites. One of the inferences of these studies was that the concentration of NADH was higher in malignant sites of breast tissue compared to that in the non-malignant sites and the opposite was true for tissues from oral cavity where the concentration of NADH was higher in normal sites. These predictions have also been verified by biochemical measurements.[29] We should also note that the optical properties (absorption and scattering coefficients) of normal and malignant sites

may also show significant differences. Indeed it has been observed that the absorption and scattering coefficients are larger in malignant sites as compared to normal.[17] The larger scattering coefficient of malignant sites has an interesting consequence. Whereas for thin tissue sections (thickness < optical transport length) the depolarization of fluorescence was observed to be smaller in malignant tissues compared to normal the reverse was observed for thicker tissue section because here scattering is the major cause of depolarization.[30,31] As a consequence, the fluorescence from superficial layer of tissue is the least depolarized and that originating from deeper layers becomes increasingly more depolarized. Therefore, measurements on polarized component of fluorescence can be used for depth resolved measurements on fluorescence.[32,33]

Fluorescence spectra measured from a tissue are generally broad and featureless. Moreover, the observed changes in fluorescence spectra from normal and malignant sites are very subtle. Therefore, for use of tissue autofluorescence for cancer diagnosis one requires an appropriate diagnostic algorithm that can best extract the diagnostic features from the tissue spectra and accurately correlate them with the tissue histopathology. Discrimination algorithms with varying degree of sophistication have been developed for this purpose.[34,35] One approach is to empirically select the discrimination parameters from the observed differences in the spectral features. These parameters can be absolute or normalized fluorescence intensities, ratio of intensities at selected pairs of emission wavelengths or ratio of integrated intensities over appropriately chosen wavelength bands. These have been used either directly for discrimination or as inputs to statistical analytical techniques like multivariate linear regression (MVLR) analysis to form a discrimination function. Recent efforts are directed towards using statistical pattern recognition techniques to exploit the information content of the complete spectra for extracting the best diagnostic features and use these to accurately classify the tissue sites into the corresponding histopathologic categories. Although linear techniques like Fisher's linear discriminant (FLD), principal component analysis (PCA) etc. have been used successfully for algorithm development, the use of artificial

neural network (ANN)[36], wavelet transforms[37], maximum representation and discrimination feature (MRDF)[38] and more recently support vector machine (SVM)[39,40] have been found to provide superior performance. Amongst all these, SVM in particular, is the best suited for this kind of supervised classification problems. The use of the theory of relevance vector machine (RVM),[35] for development of a probability based algorithm for optical diagnosis of cancer has also been reported. The information on the posterior probabilities of class membership is particularly important in clinical settings where the misclassification cost associated with some classes (false negative for cancer) may be significantly higher than that of others (false positive for cancer).

Optical spectroscopic techniques are also being investigated for a variety of other diagnostic applications for example, diagnosis of caries in dental tissues,[41-43] non-invasive monitoring of blood glucose level,[44] functional imaging of brain by monitoring spectral changes in absorption of blood depending on its oxygenation state.[45] Fiber optic sensors used for monitoring of blood parameters like pH, partial pressure of oxygen etc. also make use of the changes in the optical properties of the optrode caused by the change in blood parameter being monitored.[46]

5.5 Optical Processing of Tissue

The diagnostic applications of lasers are based on scattered or reemitted light. Surgical and therapeutic applications depend on absorption of light. The absorbed laser energy can broadly lead to three effects. Most common effect is a rise in tissue temperature (photothermal effect). At high intensities associated with lasers operating in short pulse duration (nanosecond, picosecond) absorption of laser-radiation may lead to generation of pressure waves or shock waves (photomechanical effects). Short wavelength lasers can cause electronic excitation of chromophores in the tissue and thus initiate a photochemical reaction (photochemical effect). The relative role played by the three depends primarily on the laser wavelength, irradiance and pulse duration.

5.5.1 *Photothermal Effects*

Most of the surgical applications of lasers exploit laser induced photothermal effect that is a rise in tissue temperature subsequent to absorption of laser radiation. The biological effect depends on the level of rise in tissue temperature which is determined by two factors - the tissue volume in which a given laser energy is deposited and the time in which the energy is deposited vis a vis the thermal relaxation time (the inverse of which determines the rate of flow of heat from heated tissue to the surrounding cold tissue). Small rise in temperature (5–10 °C) can influence the activity of enzymes and lead to changes in blood flow and vessel permeability. Tissues heated to a temperature of 45–80 °C may get denatured due to breakage of Van der Wall bonds, which stabilize the conformation of proteins and other macromolecules. Thermal denaturation is exploited in several ways for therapy like in tissue welding or hemostasis (arrest bleeding). Denaturation of collagen with consequent uncoiling of its triple helical structure and interaction between collagen strands is believed to play an important role in tissue welding. Hemostasis occurs because of increased blood viscosity caused by denaturation of plasma proteins, hemoglobin and perivascular tissue. When the temperature exceeds 100 °C boiling of water in the tissue takes place. Due to the large latent heat of water, the main constituent of tissue, energy added to tissue at 100 °C first results in generation of steam without further increase in temperature. A volume expansion by ~ 1670 fold occurs when water is vaporized isobarically. When this large and rapid expansion occurs within tissue, physical separation or "cutting" occurs. This is the mechanism by which a laser knife is used in surgery. Tissue surrounding the region being vaporized will also be heated, with the temperature getting decreased as one shifts away from the target site. Hemostasis occurs because the heat coagulates the tissue at the wound edges. Generally it is desirable to have no bleeding but it is also desirable to have the coagulated region as thin as possible. Lasers with short penetration depth (that is with a wavelength for which absorption in tissue is very large) will have a smaller thermally affected region. For some applications like treatment of bleeding ulcers of the stomach and intestine, it is required to coagulate a large volume of tissue mass. For

this purpose a laser with larger depth of penetration such as Nd: YAG laser operating at 1.06 μm will be more appropriate.

If the rate of deposition of energy is faster than that required for boiling of water, the tissue is superheated and can be thermally ablated. Thermal ablation or explosive boiling is similar to what happens when cold water is sprinkled on a very hot iron. Both ablation and vaporization result in tissue removal and these are extensively used for surgical applications. In vaporization, tissue temperature is about 100 °C and water present in the tissue is vaporized. In contrast, for ablation, the tissue temperature is much higher (500 °C or more) and the kinetics involved is considerably faster. In ablation practically all the energy deposited in the tissue is converted into the kinetic energy of the ablation products, with the result of minimal thermal damage to the adjoining tissues.

It is pertinent to emphasis that although tissue heating can be achieved by several other means, none can provide the selectivity made possible by the exquisite control on laser parameters. By use of laser pulses of duration shorter than the thermal relaxation time, heat can be confined within the target tissue so that it can be vaporized without significant effect on surrounding tissue. Further, selectivity is possible by selecting laser wavelength such that it is preferentially absorbed in some target having greater absorption than the surrounding tissue. Hemoglobin and melanin with strong absorption in visible region have proven particularly useful for such selective photothermolysis. For example, before lasers no satisfactory treatment existed for portwine stains (purple birthmark), a cutaneous vascular disorder. In laser treatment of portwine stains, where the micro-vessels have a thermal relaxation time of 0.05-1.2 ms, it is possible to damage selectively only the vasculature by using a short pulse laser, tuned to hemoglobin absorption peaks. This effectively removes these birthmarks without any damage to overlying or nearby structures. The same concept of selective photothermolysis has also been employed to treat structures in the skin that are smaller than micro-vessels like sub-cellular melanosomes by using even shorter pulses.[47]

5.5.2 *Photomechanical Effects*

Photomechanical effects are usually important only at high intensities typical of short duration (10^{-9}–10^{-12} s) laser pulses. Even a small energy of 1 μJ in 1ps corresponds to a peak power of 10^6 W and when focused to a 10 μm spot would lead to an intensity of about 10^{12} W /cm^2. The localized absorption of intense laser radiation can also lead to very large temperature gradients, resulting in enormous pressure waves and localized photomechanical disruption. Such disruption is useful, for example, in laser removal of tattoo marks. Tattoo ink has molecular particles too large for the body's immune system to eliminate. Photo-disruption of these into smaller particles enables body's lymphatic system to dispose them, resulting in removal of tattoo mark.

At high intensities, the electric field strength of radiation is also very large. For example, at an intensity of 10^{12} W/cm^2 the electric field strength of radiation is about 3x10^7 V/cm, which is sufficient to cause dielectric breakdown in the tissue. The resulting plasma absorbs energy and expands creating shock waves, which can shear off the tissue. These plasma-mediated shock waves are used for breaking stones in the kidney or urethra (lithotripsy) and in posterior capsulotomy for removal of opacified posterior capsule of the eye lens.

5.5.3 *Photochemical Effects*

For laser irradiation at power levels where there is no significant rise in temperature of the tissue, the photothermal and photomechanical effects are not possible. In such a situation, only photochemical effects can take place provided the energy of laser photon is adequate to cause electronic excitation of biomolecules, which can be either endogenous or externally injected. The photo-excitation of molecules and the resulting biochemical reactions can lead to either bio-activation exploited in various phototherapies[48-50] or generation of some free radicals or toxins, which are harmful for the host tissue. The latter process is used for photodynamic therapy of cancer.[23] Short wavelength radiation of sufficient energy can also break molecular bonds and impart kinetic energy to the fragments by which they get ejected from the tissue. This

photochemical removal (photo-ablation) can occur only from the area of tissue exposed to the light and will have no effect on the surrounding unexposed tissue. In photo-ablation there is no rise in the tissue temperature and the tissue removal can be achieved in an extremely precise manner, owing to the small penetration depth of light at these short wavelengths. It is for this reason that UV excimer lasers are being widely used for reprofiling the cornea to correct vision disorders. Though conventional light sources are also useful for phototherapy, a better control on laser light characteristics can often make phototherapy more convenient with the use of laser.

5.5.4 *Applications of Laser Processing of Tissue*

The use of the different laser tissue interaction mechanisms for cutting, coagulating or removal of tissue is being used for surgical procedures in most of the clinical specialties - ophthalmology, gynecology, urology, dentistry, and surgery of ear, nose and throat, to name a few. This is motivated by the fact that the exquisite control on laser parameters allows ultra-precise surgical procedures without any adverse effect on surrounding normal tissue. Further, due to the fact that tissue cutting and removal occurs at high temperatures in laser surgery, small blood vessels and nerve-endings cut during surgery get coagulated resulting in reduced blood loss and the sensation of pain. Another important advantage with lasers operating in 0.2 to 3 μm spectral range is that their radiation can be transported via thin, flexible optical fibers to internal organs endoscopically, through natural body orifices or minor incisions. Thus, major incisions required in conventional surgery, can be avoided using laser endoscopic surgery and some of the potentially major operations are even reduced to an outpatient treatment. This considerably reduces patient trauma and hospitalization time. In Table 5.2, we list some lasers used for medical applications and their important characteristics.

Table 5.2. Some important laser systems.

Laser system	λ (nm)	Transport Parameters (μ_a and μ_s in cm^{-1})	Penetration depth (δ)	Remarks
Excimer lasers ArF KrF XeCl XeF	 193 249 308 351	μ_a ~ 50 – 2000 ($\mu_s' << \mu_a$)	5 – 200 μm (~ $1/\mu_a$)	Operates in pulsed mode (typical pulse duration 1 ns – 300 ns). Low penetration depth. Therefore useful for precise tissue removal. High photon energy of shorter wavelength excimer lasers can cause photo-ablation. Used for re-profiling of cornea or Laser Assisted In-Situ Keratomileusis (LASIK).
Argon ion laser	488 514.5	μ_a ~ 2 – 3 μ_s' ~ 10	< 1 mm (~ $1/\mu_{eff}$)	Has been a workhorse for high average power blue / green output. Strongly absorbed by blood. Therefore, widely used for coagulation of blood vessels and haemostasis. Owing to very poor efficiency (0.05 – 0.001%), limited operational lifetime and relatively large size these systems are slowly being replaced by all solid state laser systems.
Ruby laser	694	μ_a ~ 0.2 – 0.5 μ_s' ~ 10	~ 2– 4 mm (~ $1/\mu_{eff}$)	First man made laser system. Generally pulsed operation. Earlier was used for a large number of applications, particularly for retinal photocoagulation. However, cw Ar-ion lasers proved to be better for the latter purpose.

Table 5.2. (*Continued*)

Laser system	**λ (nm)**	**Transport Parameters (μ_a and μ_s in cm^{-1})**	**Penetration depth (δ)**	**Remarks**
Dye lasers	~ 300 – 1000	$\mu_a \sim 0.1 - 5$ $\mu_s' \sim 5 - 15$	0.5 – 4 mm ($\sim 1/\mu_{eff}$)	Offers wide tunability. Using different dyes, output can be tuned from near UV to near IR. Has the disadvantage associated with handling of liquid dyes some of which are toxic. Getting replaced by all solid-state laser system.
Diode lasers	400 – 40000			Compact, efficient (>20%) reliable and high operational lifetime. Operates well in both CW and pulsed mode. Operating wavelength depends on the choice of semiconducting material. Emerging as the lasers of choice for most applications.
Ti: Sapphire	700 – 1000	μ_a $\sim 0.1 - 0.5$ $\mu_s' \sim 5$	2 – 6 mm	Offers widely tunable output without requiring change of gain medium. By second harmonic generation tunability can be extended to cover the spectral range 350 nm – 1000 nm. Can be pumped by diode pumped solid state laser to provide an all solid state laser system.

Table 5.2. (*Continued*)

Laser system	λ (nm)	Transport Parameters (μ_a and μ_s in cm^{-1})	Penetration depth (δ)	Remarks
Nd: YAG	1064	μ_a ~ 0.1 – 0.2 μ_s' ~ 5	~ 4 – 8 mm (~ 1 /μ_{eff})	Operates well in both CW and pulsed mode. Larger depth of penetration. Therefore, useful for coagulation of large tissue volume and hyperthermia. Can be coupled to optical fibers for endoscopic applications.
Er: YAG	2940	μ_a ~ 10000 (μ_s' << μ_a)	~ 1 μm (~ 1/μ_a)	Wavelength corresponds to the absorption peak of water. The strong absorption by hydroxyapatite and water makes it attractive ablating enamel and dentin.
CO_2 laser	10600	μ_a ~ 1000 (μ_s' << μ_a)	~ 10 μm (~ 1/μ_a)	Strongly absorbed in H_2O, the major constituent of tissue. Therefore, can be used as general purpose surgical tool.

5.6 Concluding Remarks

The interaction of light with biological matter plays an important role in our life; photosynthesis and vision are good examples. Therefore, understanding of this interaction and its exploitation for practical use has always remained an important scientific pursuit. The growing maturity of laser systems, availability of sensitive detection systems, large information processing capability of present day computers etc. is facilitating the use of light tissue interaction for noninvasive and sensitive biomedical imaging and diagnosis, ultra-precise and minimally invasive surgery as well as therapy with high selectivity. The use of lasers is also facilitating studies on biological systems with spatial and temporal resolutions that would be difficult to achieve with any other

technique. Such studies are contributing enormously to a better understanding of biological systems, which in turn should also help in a better understanding of diseases and their treatment modalities. Therefore, with the continued developments in the field of lasers and the associated technologies the use of lasers in medicine and surgery is expected to grow even more rapidly in the coming decades.

Acknowledgments

Authors would like to thank Dr. S. M. Oak and Dr. A. Srivastava for a critical reading of the manuscript.

References

1. A. Yariv, Quantum Electronics (Wiley, New York, 1989).
2. O. Svelto, Principles of Lasers (Plenum, New York, 1989).
3. K. Thyagarajan and A.K. Ghatak, Lasers, Theory and Applications (Plenum Publishing Corporation, New York, 1981).
4. M.L. Wolbarsht, Ed., Laser applications in medicine and biology, Vol. 1-5, (Plenum, New York, 1971, 1974, 1977, 1989 and 1991).
5. P.N. Prasad, Introduction to Biophotonics (Wiley-Interscience, New Jersey, 2003).
6. A. Ishimaru, Wave propagation and scattering in random media, Vol.1 (Academic press, New York, 1978).
7. A.J. Welch and M.J.C. van Gemert, Optical-thermal response of laser-irradiated tissue (Plenum Press, New York, 1995).
8. P.K. Gupta, Current Science, **76**, 1341 (1999).
9. J.M. Krauss and C.A. Puliafito, Lasers in Surgery and Medicine, **17**, 102 (1995).
10. S. Chandrasekhar, Radiative Transfer (Oxford University Press, Oxford, 1960).
11. B.C. Wilson and S.L. Jacqes, IEEE Journal of Quantum Electronics, **26**, 2186 (1990).
12. L. Wang. S.L Jacques, and L. Zheng, Computer Methods and Programs in Biomedicine, **47**, 131 (1995).
13. J.C. Hebden, S.R. Arridge, D.T. Delpy, Physics in Medicine and Biology, **42**, 825 (1997).
14. Joseph M. Schmitt, IEEE Journal of Selected Topics in Quantum Electronics, **5**, 1205 (1999).
15. C. Dunsby and P.M.W. French, Journal of Physics D: Applied Physics, **36**, R207 (2003).

16. D.A. Baos, D.H. Brooks, E.L. Miller, C.A. DiMarzio, M. Kilmer, R.J. Gandette, Q. Zhang, IEEE Signal Processing Magazine, 57 – 75 (November 2001).
17. N. Ghosh, S.K. Mohanty, S.K. Majumder and P.K. Gupta, Applied Optics, **40**, 176 (2001).
18. V. Backman, R. Gurjar, K. Badizadegan, I. Itzkan, R.R. Dasari, L.T.Perelamn and M.S. Feld, IEEE Journal of Selected Topics in Quantum Electronics, **5**, 1019 (1999).
19. G.A. Wagnieres, W.M. Star, and B.C. Wilson, Photochemistry and Photobiology, **68**, 603 (1998).
20. N. Ramanujam, Neoplasia, **2,** 1 (2000).
21. A. Mahadevan – Jansen and R.R. Kortum, Journal of Biomedical Optics, **1**, 31 (1996).
22. G. Ullas, S.S. Nayak, K. Gopalakrishna, J. Jacob, J. Kurien, K.M. Pai, M. Vengal, M. Valiathan|, R. Jyothi Lakshmi, K. Venkata Krishna, K. Raghavendra and V.B. Kartha, Current Science, 77, 908 (1999).
23. B.W. Henderson and T.J. Doughetry Eds., Photodynamic Therapy: Basic principles and applications (Marcel Dekker, New York, 1992).
24. M.G. Muller, I. Gergakoudi, Q. Zhang, J. Wu, M.S. Feld, Applied Optics, **40**, 4633 (2001).
25. P.K. Gupta, S. K. Majumder, and A. Uppal, Lasers in Surgery and Medicine, **21**, 417 (1997).
26. S.K. Majumder, P.K. Gupta and A.Uppal, Lasers in Life Sciences, **8**, 211 (1999).
27. S.K. Majumder, P.K. Gupta, B. Jain, A. Uppal, Lasers in the Life Sciences, **8**, 249 (1999).
28. B. Jain, S.K. Majumder and P.K. Gupta, Lasers in the Life Sciences, **8**, 163 (1998).
29. A. Uppal and P.K. Gupta, Biotechnology and Applied Biochemistry, **40**, 1 (2004).
30. S.K. Mohanty, N. Ghosh, S.K. Majumder, and P.K. Gupta, Applied Optics, **40**, 1147 (2001).
31. N. Ghosh, S.K. Majumder and P.K. Gupta, Physical. Review E, **65**, 26608 (2002).
32. N. Ghosh, S.K. Majumder, and P.K. Gupta, Optics Letters, **27**, 2007 (2002).
33. N. Ghosh, S. K. Majumder, H. S. Patel and P. K. Gupta, Optics Letters, **30**, 162 (2005).
34. N. Ramanujam, Encyclopedia of Analytical Chemistry, R.A. Meyers Ed., John Wiley & Sons Ltd., 20 – 56 (2000).
35. S.K. Majumder, N. Ghosh and P.K. Gupta, Lasers in Surgery and Medicine, **36,** 323 (2005).
36. K. Tumer, N. Ramanujam, J. Ghosh, R. Richards-Kortum, IEEE Trans BME; **45**, 953 (2001).
37. N. Agrawal, S. Gupta, Bhawna, A. Pradhan, K. Viswanath and P. K. Panigrahi, IEEE Journal of Selected Topics in Quantum Electronics, **9**, 154 (2003).
38. S.K. Majumder, N. Ghosh, S. Kataria and P.K. Gupta, Lasers in Surgery and Medicine, **33**, 48 (2003).

39. W.M. Lin, X. Yuan, P. Yuen, W.I. Wei, J. Sham, P.C. Shi, and J. Qu, Journal of Biomedical Optics, **9**, 180 (2004).
40. S.K. Majumder, N. Ghosh and P.K. Gupta, Journal of Biomedical Optics, **10**, 024034 (2005).
41. J. Vaarkamp, J.J. ten Bosch, E.H. Verdonschot and S. Tranaeus, Journal of Dental Research, **76**, 875 (1997).
42. E de Josselin de Jong, F. Sundstrom, H. Westerling, S. Tranaeus, J.J. ten Bosch, B. Angmar Mansson, Caries Research, **29**, 2 (1995).
43. R. Hibst, R Gall, Caries Research, **32**, 294 (1998).
44. R.J. McNichols, G.L. Cote, Journal of Biomedical Optics, **5**, 5 (2000).
45. A. Viillringer, B. Chance, Trends in Neuroscience, **20**, 435 (1997).
46. A.G. Mignani, F. Baldini, Reports on Progress in Physics, **59**, 1 (1996).
47. R.G. Wheeland, Clinical use of lasers in dermatology, Lasers in Surgery and Medicine, **16**, 2 (1995).
48. T. Ohshirao, Low reactive level laser therapy: practical applications (John Wiley and Sons, Chichester, 1991).
49. G.D. Baxter, Therapeutic lasers, Theory and Practice (Churchill Livingstone, Edinburgh, 1994).
50. T.I. Karu, Journal of Photochemistry and Photobiology B: Biology, **49**, 1 (1999).

This page is intentionally left blank

CHAPTER 6

MECHANISMS AND APPLICATIONS OF PHOTODYNAMIC THERAPY

Zheng Huang

Radiation Oncology Department, University of Colorado at Denver Health Sciences Center, Aurora, Colorado 80045, USA
E-mail: zheng_huang@msn.com

Hong Liu

Center for Bioengineering and School of Electrical and Computer Engineering, University of Oklahoma, Norman, Oklahoma 73019, USA

Wei R. Chen

Department of Physics and Engineering, University of Central Oklahoma, Edmond, Oklahoma 73034, USA

Photodynamic therapy (PDT) is a relatively new treatment modality. It involves the administration of a photosensitizer followed by local illumination with visible light of specific wavelength(s). In the presence of oxygen, the light illumination of photosensitizer can lead to a series of photochemical reactions and consequently the generation of cytotoxic species. The nature, quantity, and location of PDT-induced cytotoxic species determine the nature and consequences of PDT treatment. PDT has received increased attention since the regulatory approvals of several photosensitizers and light applicators in many countries and regions around the world. Much progress has been seen in both basic research and clinical application in recent years. This chapter will introduce the new developments in PDT basic sciences, clinical investigations and clinical applications, and the usefulness of various forms of PDT techniques for curative or palliative treatment of malignant and non-malignant diseases. PDT in dentistry will also be discussed.

6.1 Historical Background

Light has been used in the treatment of diseases for a long time. The ability of visible light to destroy living organisms in the presence of a photosensitizer was initially observed by Oscar Raab more than 100 years ago.[1] As a medical student he worked on the effect of acridine on the behavior of paramecia in the pharmacological laboratory of Professor Hermann von Tappeiner in Munich Dermatology Clinic (Germany) and found that the acridine dye only killed the paramecia in the presence of light. Hermann von Tappeiner et al. later recognized that oxygen was essential for the cytotoxic effect and he introduced the term *Photodynamic Therapy* (*Photodynamische Wirkung*) to describe this phenomenon.[2,3]

However, modern photodynamic therapy (PDT) only began to form in the 1960s after Richard Lipson and Edward Baldes at Mayo Clinic (USA) reported that neoplastic tissues containing porphyrin mixtures could fluoresce under ultraviolet light irradiation.[4] The porphyrin mixture, prepared by Samuel Schwartz (also Mayo Clinic), and formally named as hematoporphyrin derivative (HpD), was found to have a better affinity for tumor tissue and stronger phototoxicity than crude hematophorphyrin.[5] Early studies were quickly expanded to investigate the photodynamic effects of HpD in both preclinical and clinical studies in the 1970s. An effort led by Thomas Dougherty at Roswell Park Cancer Institute (USA) to prepare a drug grade HpD produced the first approved photosensitizer agent, Photofrin, for tumor ablation in Canada in the early 1990s. This was an important milestone in modern PDT. Several non-laser and laser light applicators were also developed to facilitate various clinical protocols.[6] Regulatory approvals for the clinical use of several photosensitizers and PDT light applicators for treatment of non-malignant and malignant diseases now exist in many countries around the world.[7] The number of scientific articles on PDT, clinical application as well as basic sciences, steadily increases in both English language and non-English language literatures while new PDT technology and promising clinical applications continue to be discovered.

6.2 Photosensitizers

Photosensitizer is considered to be a critical element in PDT. In general, photosensitizers can be divided into three broad families based on their origin and structure:

(1) *porphyrin-based photosensitizer* (e.g. Photofrin, ALA/PpIX, BPD-MA),

(2) *chlorophyll-based photosensitizer* (e.g. chlorins, bacteriochlorins, purpurins), and

(3) *dye* (e.g. phthalocyanine series, phenothiazinium series).

Traditionally, the porphyrins and those photosensitizers developed in the 1970s and early 1980s (e.g. Photofrin and other hematoporphyrin derivatives) are called first generation photosensitizers. Porphyrin derivatives or synthetics (e.g. ALA) made since the late 1980s are called second generation photosensitizers. Third generation photosensitizers generally refer to the modifications such as biologic conjugates (e.g. antibody conjugate, liposome conjugate) and built-in photo quenching or bleaching capability.[8] These terms are still being used, although not accepted unanimously since dividing photosensitizers into such generations may be confusing. In many cases, the claim that newer generation drugs are better than older ones is unjustified.[9] The premature conclusions on some novel investigational photosensitizers may send a misleading message by suggesting that the older drugs should be replaced by the newer ones or wrongly imply that newer photosensitizing drugs are superior to older ones.

An ideal photosensitizer should meet most of the following criteria that are clinically relevant:

- a commercially available pure chemical
- low dark toxicity but strong photocytotoxicity
- good selectivity towards targeted cells
- strong absorption of long-wavelength light
- rapid removal from the body and therefore less skin photosensitization, and
- ease of administration through various routes.

Although some photosensitizers satisfy some or all of these criteria, there are currently only a few PDT photosensitizers that have received

national or regional regulatory approval or are under clinical trials (see Table 6.1). In addition, many other photosensitizers are undergoing pre-clinical studies. The chemical structures of these photosensitizers are given in Fig. 6.1.

6.3 Light Applicators

The first light sources used in PDT were non-coherent light sources (e.g. conventional arc lamps). Non-coherent light sources are safer, easy to use, and less expensive. They can produce a wide spectrum of wavelengths to accommodate different photosensitizers. They can be used in conjunction with optical filers to output selective wavelength(s). The disadvantages of conventional lamps include significant thermal effect, low light intensity and difficulty in controlling light dose. Light emitting diode (LED) is another emerging PDT light applicator. LED can generate high energy light of desired wavelengths and can be assembled in different geometries and sizes. For intra-operative PDT of brain tumor, LED-probe may be arranged in a cylinder tip to fit into a balloon catheter,[10] whereas for minimally invasive interstitial PDT, the small and flexible light delivery LED catheter can be implanted into the solid tumor percutaneously.[11,12] Large LED array may be more suitable for flat surface illumination of a wide-area superficial lesion.

However, the most commonly used PDT light sources are lasers.[13] They produce high energy monochromatic light of a specific wavelength with a narrow bandwidth. The laser light can be focused, passed down an optical fiber and directly delivered to the target site through a specially designed illuminator tip. Four light delivery modes are commonly used in clinical settings: (1) *Front superficial irradiation* – a uniform irradiance incident beam delivered to a surface by a microlens fiber externally; (2) *Cavity superficial irradiation* – an isotropic source centered in a spherical cavity and delivering light to the cavity surface; (3) *Cylindrical superficial irradiation* – a cylindrical diffuser source centered in a cylindrical lumen; and (4) *Cylindrical interstitial irradiation* – a cylindrical diffuser source embedded in the target tissue.

Table 6.1. Regulatory Status of some common PDT Photosensitizers.

Photosensitizer	Abbreviation	Generic name	Manufacturer
Approved			
Polyhematoporphyrin ether/ester	Porfimer sodium	Photofrin	Axcan Pharma, Inc.
Hematoporphyrin derivative	HpD	Photogem	Moscow Institute of High Chemical Technologies
Benzoporphyrin derivative monoacid ring A	BPD-MA, verteporfin	Visudyne	Novartis Pharmaceuticals
5-aminolevulinic acid	ALA	Levulan	DUSA Pharmaceuticals, Inc.
Methyl aminolevulinate	MLA	Metvix	PhotoCure ASA
Meta-tetrahydroxyphenylchlorin	mTHPC, temoporfin	Foscan	Biolitec AG
Mono-L-aspartyl chlorin e6 or talaporfin sodium*	NPe6, ME2906	Laserphyrin	Meiji Seika Kaisha, Ltd.
Sulfonated aluminum phthalocyanine	$AlPcS_{2-4}$	Photosens	General Physics Institute
Tolonium chloride or Toluidine Blue O	TBO	SaveDent PAD System	Denfotex Ltd.

Table 6.1. (*Continued*)

Photosensitizer	Abbreviation	Generic name	Manufacturer
Under clinical trial			
Lutetium(III) texaphyrin or motexafin lutetium	Lutex	Antrin	Pharmacyclics Inc.
Tin ethyl etiopurpurin	SnET2, purlytin	Photrex	Miravant Medical Technologies
Hematoporphyrin monomethyl ether	HMME	Hemoporfin	Fudanzhangjiang BioPharmaceutical Co., Ltd.
2-[1-Hexyloxyethyl]-2-devinyl pyropheophorbide-a	HPPH	Photochlor	Roswell Park Cancer Institute
Pd-bacteriopheophorbide	WST09	Tookad	Negma-Lerads and Steba Laboratories Ltd.

*Also under clinical trials under different names: LS11 or Litx, Light Science Corporation

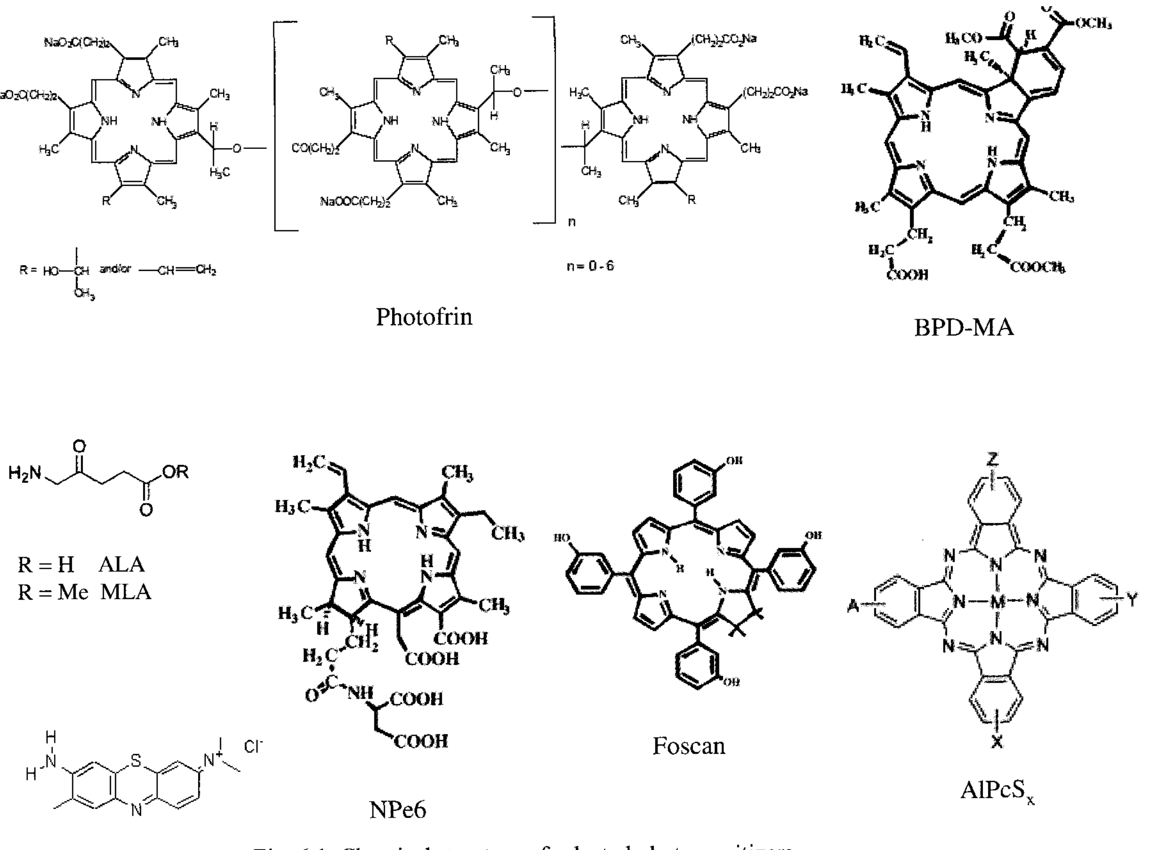


Fig. 6.1. Chemical structure of selected photosensitizers.

SnET$_2$

Tookad

Lutex

HPPH

HMME

Fig. 6.1. (*Continued*)

In cavitary and intraluminal PDT, balloon catheters and light diffusing media can be used to provide uniform dosimetry and better positioning. Argon dye, potassium-titanyl-phosphate (KTP) dye, metal vapor lasers and, most recently, diode lasers, have been used in clinical PDT. The KTP-dye modular combination system was the most widely used PDT laser prior to the approval of portable, lightweight and less expensive diode lasers.

6.4 PDT Mechanisms

6.4.1 *Photophysics and Photochemistry*

Upon capturing light energy the photosensitizer can be excited to a triplet state *via* the intersystem crossing process. While returning to the ground state the excited photosensitizer can undergo Type I and Type II reactions (see Fig. 6.2).[14] In a Type I reaction, the excited photosensitizer can interact directly with certain substrates, such as the cellular component or a molecule, and transfer a proton or an electron to form a radical anion or radical cation, respectively. These radicals may further interact with oxygen to produce oxygenated products. In a Type II reaction, the excited photosensitizer can transfer its energy directly to molecular oxygen to generate singlet oxygen ($^1O_2$). Singlet oxygen is highly destructive because it reacts with most organic molecules at almost diffusion controlled rates, that is its rate of reaction is limited only by the speed at which it diffuses. It is involved in addition reactions to enes and dienes, forming hydroperoxides and endoperoxides which can further propagate free radical chain reactions.[15] The co-existence of both reactions and their photogenerated products have been demonstrated experimentally.[16] Both reactions are oxygen dependent and can occur simultaneously, and the ratio and yield of radicals and $^1O_2$ are affected by photosensitizer properties and tissue partial oxygen pressure (pO_2). The generation of reactive oxygen species (ROS) can subsequently induce therapeutic effects, such as cell death (necrosis and apoptosis) and tissue destruction, through several well known mechanisms. Also, photobleaching is light mediated destruction of photosensitizer, and it is not clear whether photobleaching affects PDT activity.

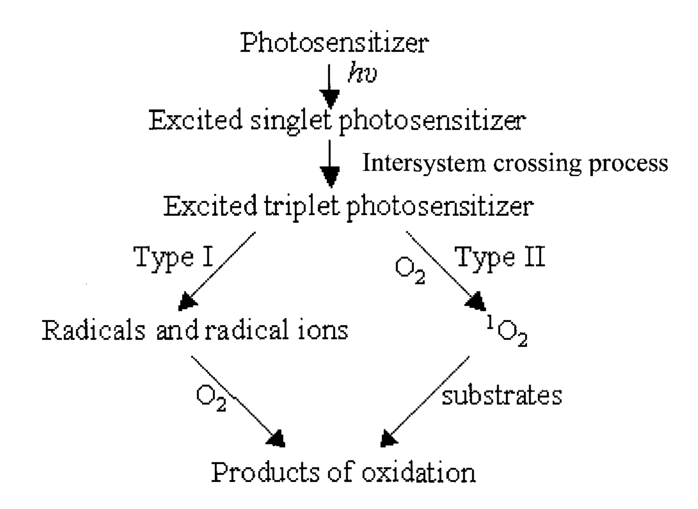


Fig. 6.2. Type I and Type II pathways.

6.4.2 *Biological Effect*

6.4.2.1 *Direct Cytotoxicity*

PDT-induced cytotoxic species have a short lifetime and only act within a limited distance. Therefore, the uptake and subcellular localization of photosensitizer by tumor or other cells is critical in PDT-mediated direct cytotoxicities.[17,18] The subcellular localization is determined by the chemical properties, formulation, concentration and delivery route of the photosensitizing drug, the microenvironment of the lesion, and to a certain degree the phenotype of the target cell. The plasma membrane, intracellular membranes and organelles such as the endoplasmic reticulum, Golgi apparatus, lysosomes, mitochondria and nucleus, have been identified as subcellular PDT targets for many photosensitizers. Some photosensitizers distribute very broadly in these membranes and organelles. Some distribute specifically in lysosomes or mitochondria. Some might redistribute during light irradiation. The subcellular localizations of various photosensitizers have been summarized in a recent review article.[19]

The cell genotype, photosensitizer subcellular location and the PDT dose might determine whether cell death occurs by apoptosis or necrosis. In general, the mode of cell death switches from apoptosis to necrosis with the increase of the intensity of the insult. High-dose PDT induced apoptosis might be a stochastic rather than a threshold effect. Interestingly, some researchers show that subthreshold low-dose ALA-PDT can induce selective apoptosis of tumor cells, without detectable (apoptotic or necrotic) damage to normal cells. This might offer the possibility of treating patients with low-dose ALA-PDT to minimize PDT damages to the normal tissue.[20]

In recent years there has been a steady increase in knowledge about the roles of the intracellular signaling machinery in cell response to PDT and, particularly, apoptotic pathways in PDT. Advances in understanding the intracellular signaling and the molecular targets of PDT have been summarized in recent review articles.[21-23] Understanding PDT-induced unique changes and molecular events in signal transduction pathways, transcription factors and regulating mechanisms may provide a means to modulate or enhance the cellular PDT effects at the molecular level. Two major apoptotic pathways have been characterized: the death receptor-mediated, or extrinsic pathway, and the mitochondria-mediated apoptosis, or intrinsic pathway. The links between PDT effects and several apoptotic pathways have been clearly identified in numerous photosensitizers and cell lines in both *in vitro* and *in vivo* animal studies. In general, experimental evidence shows a large heterogeneity in the mechanisms leading to cell death in cellular-targeted PDT. However, in addition to the activation of the molecular machinery leading to direct cell death, PDT may also initiate some metabolic reactions that could protect cells from oxidative damage. Therefore, it has been suggested that the control of these protective mechanisms is likely to enhance the direct cytotoxicity of cellular PDT effects on target cells.[24]

There is no doubt that advances in cell and molecular biology allow a better understanding of subcellular pathways and consequences of PDT induced direct cytotoxicity. Although such advances help the rational design and choice of photosensitizers, the golden standard of evaluation of the efficacy of clinical PDT still relies on the gross response of the lesion or disease to PDT. For instance, in tumor ablation,

the typical clinically relevant response or biological endpoint would be acute tumor necrosis, the duration and rate of this response, and the length of the tumor-free period. These might be affected not only by the direct cytotoxicity but also other PDT effects as well as the tumor sensitivity to various PDT effects.

6.4.2.2 *Vascular Effect*

It has long been recognized since the early 1980s that an additional indirect mechanism, coexisting with the primary direct cytotoxicity of PDT, is the vascular effect in which vascular damage causes ischemic death and therefore provides another approach to treat solid tumors.[25] Later, several preclinical experiments demonstrate that the mechanisms underlying the PDT-mediated vascular effects differ greatly with different photosensitizers, PDT approaches, and target tissues. The biological effects of vascular PDT have been summarized in recent reviews.[26,27]

Irradiation of photosensitizers, either confined in the blood circulation or accumulated in endothelial cells or bound to the vessel walls, results in collateral damage to endothelial cells. The PDT-induced direct damage to endothelial cells can be characterized by the loss of tight junctions between cells and exposure of vascular basement membranes. This primary damage within the vessel lumen leads to the formation of thrombogenic sites and initiation of a physiological cascade of reactions such as platelet aggregation, the release of vasoactive molecules, leukocyte adhesion, increase in vascular permeability and vessel constriction. Microvascular collapse, blood flow stasis and tissue hemorrhages can lead to severe persistent post-PDT tumor hypoxia and long-term tumor control.[28-30]

Photosensitizers bound to carrier molecules, such as albumin, HDL or LDL, appear to have an active affinity to endothelial cells and tumor microvascular endothelium because of the existence of specific receptors in high numbers in these structure.[31,32] This might be an additive factor in photosensitizer uptake and retention in the tumor tissue. Although one can expect that the localization of photosensitizer in

both vascular and target cell compartment might produce a stronger combination effect,[33] several investigations have also shown that tumor response to vascular-targeted PDT does not correlate with cellular concentration of photosensitizer in the treated tumor. In vascular-targeted PDT mode, therefore, the light irradiation should be applied during photosensitizer infusion and continued after the completion of infusion so as to center the light delivery period around the peak of the plasma concentration of photosensitizer and hence, putatively, should be maximizing the effect.[34] Vascular-targeted PDT has certainly extended the application of PDT from the destruction of solid tumor to the treatment of clinical conditions such as vascular lesion and neoangiogenesis.

6.4.2.3 *Immune Responses*

Photodynamic therapy induced immune responses and particularly antitumor-specific immunity has been studied in various animal models. PDT causes noticeable but short-term and reversible immune suppression under certain experimental conditions. However, unlike chemotherapy and irradiation therapy, PDT does not cause severe negative effects on the host immune system. Substantial evidence has demonstrated that antitumor immune process and enhancement of host immune system might play important roles in secondary cytotoxicity, long-term tumor control and/or complete tumor response to PDT, although these effects are not necessarily lethal to all tumor cells or relevant to the initial tumor ablation.[35-38]

In vivo animal studies show that pro-inflammatory damages formed in cellular membranes and the blood vessel walls of treated sites start to recruit neutrophils, mast cells and monocytes/macrophages after PDT. These cells can also release more inflammatory mediators to enable massive recruitment of immune cells to tumor site. These immune cells and nonspecific immune effector cells have a profound impact on PDT-mediated destruction of tumor.[39-41] PDT can also activate the expression and production of several cytokines, such as IL-1β, IL-2, IL-6, IL-10, TNF-α, and G-CSF. These cytokines play important roles in regulating

host immune response involving both lymphoid and non-lymphoid cells.[42] Recent human trial suggests that PDT could enhance the uptake and presentation of tumor antigens by tumor-associated antigen presenting cells (APC) and could ensure lymphocyte involvement.[43] Complement-activating agents may further enhance the antitumor effect of PDT.[44] Recent studies also demonstrate that PDT-treated tumor cell lysates can be effective tumor vaccines, although the mechanism for enhancement of host anti-tumor immune responses to PDT vaccines is still unclear.[45] These advances in understanding PDT-induced immune responses might lead to an attempt to optimize PDT-mediated antitumor modality through the modulation of important inflammatory/immune mediators.

While immune responses may be considered as a secondary effect of PDT, a combination modality designed to activate host immunological stimulation has been pursued. An effective approach is to use immunoadjuvants. This can in general enhance the host immune system and improve long-term tumor control in animal models.[35] A novel immunoadjuvant, glycated chitosan (GC), has been used in combination with Photofrin-PDT and Foscan-PDT in treatment of metastatic mammary tumors, and the preliminary results are encouraging. The combination of GC and PDT can significantly improve the cure rate in poorly immunogenic tumor models.[46]

6.5 PDT Dosimetry

Analytical optical modeling is a commonly used optical dosimetry approach based on the assumption that PDT is a threshold process, in which a minimum light energy density must be absorbed by the localized photosensitizer in order to initiate desired biological effects, for instance, tissue necrosis. The necrosis depth can be predicted based on optical parameters such as energy fluence parameter and light penetration depth. These key parameters can be measured directly or calculated from the tissue optical constants for different light delivery modes.[47] However, successful PDT requires sufficient light dose, photosensitizer dose and oxygen to generate sufficient cytotoxic species throughout the target

tissue.[48] Therefore, the concept of PDT dosimetry has extended from optical dosimetry to quantify the distribution of the light fluence rate and the tissue optical properties as well as the photosensitizer concentration and the tissue oxygenation during PDT for optimizing or maximizing photodynamic effect while minimizing the dose to proximal normal structures.

New development in dosimetry instrumentation allows several important PDT dosimetry parameters such as light fluence rate, photosensitizer fluorescence intensity, and changes in local oxygen profile to be measured *in situ* in real-time. It is not surprising that it has drawn criticism that clinical PDT is still largely based upon empirical dose escalation trials without much consideration of the individual variations amongst patients. The protocols employed for clinical trials do not always consider important factors relevant to the PDT response, especially the dimensions and optical properties of the target tissue. Implementation of real-time PDT dosimetry will provide individualized treatment plan and thereby improve clinical PDT outcomes and reduce medical complication.

Singlet oxygen ($^1O_2$) has recently been proposed as PDT dose metric since it has long been considered as one of the primary cytotoxic species in PDT process. Its direct detection and quantification in biological systems by its luminescence at 1270 nm might be useful as an *in vivo* PDT dosimetry after demonstrating for the first time *in vivo* an unequivocal mechanistic link between $^1O_2$ generation and photodynamic effect.[49]

6.6 Progress in Clinical Application

Since the first health agency approval was granted for Photofrin-PDT for treating bladder cancer in Canada in 1993, the use of PDT in the treatment of non-malignant and malignant lesions has increased dramatically. Indeed, Photofrin along with several photosensitizers and light sources are now licensed for various indications in many countries around the world. In the following section, progress in clinical PDT will be summarized and references can be found in recent reviews.[6,7,50-53]

6.6.1 *Non-Malignant Diseases*

6.6.1.1 *Dermatological Disease*

The importance of antibiotic resistance in dermatological practice is increasing. An alternative approach may be to use PDT. One of the advantages of the broad spectra of antimicrobial PDT is the development of resistance to photodynamically induced direct killing would be unlikely.[54] A number of other clinical conditions, such as acne vulgaris, psoriasis, viral warts and hair removal, are currently under clinical investigation. Another potential application is the treatment of port-wine stain (PWS), a capillary vascular malformation, with vascular targeted PDT to induce selective injury of only the abnormal blood vessels in the dermis while sparing the normal overlying epidermis although the clinical outcomes are still controversial.[55-58]

6.6.1.2 *Ophthalmic Disease*

Liposome-encapsulated BPD-MA (benzoporphyrin derivative monoacid ring A) under the generic name of Verteporfin or Visudyne® was synthesized in the mid-1980s with an intention for cancer treatment. However, it has been used primarily for ocular PDT. Several well designed clinical studies in North America and Europe show that age-related macular degeneration (AMD) treated with Verteporfin are more likely to experience stabilized vision than the control group. Therefore, Verteporfin-PDT, approved for AMD worldwide since 2000, should be considered as a first-line therapy in these difficult-to-manage conditions such as subfoveal choroidal neovascularisation secondary to AMD, pathological myopia or presumed ocular histoplasmosis syndrome. Several clinical trials are currently under way to evaluate the efficacy of ocular PDT of other promising photosensitizers including tin ethyl etiopurpurin, motexafin lutetium and mono-L-aspartyl chlorine e6.

6.6.1.3 *Cardiovascular Disease*

Preclinical studies show motexafin lutetium could be taken up by atherosclerotic plaque and concentrated within macrophages and vascular smooth muscle cells. This leads to several Phase I trials in US and Japan to develop endovascular photoangioplastic modality for cardiovascular diseases such as intimal hyperplasia, and atherosclerosis or vulnerable plaque, and prevention of restenosis after coronary-stent placement. Preliminary results suggest that PDT might be useful for the treatment of flow-limiting coronary atherosclerosis or vulnerable plaque while sparing normal surrounding vascular tissues. A recent animal study also suggests that PDT may be beneficial in reducing intimal hyperplasia.

6.6.1.4 *Urological Disease*

Benign prostatic hyperplasia (BPH) is a common condition of the aging male. There has been a renewed interest in transurethral PDT in recent years and there is an ongoing Phase I/II dose escalation study to assess the feasibility of transurethral PDT for the management of BPH with lemuteporfin (also known as QLT0074).

6.6.2 *Malignant Diseases*

6.6.2.1 *Skin Premalignant and Malignant Diseases*

The feasibility and efficacy of PDT for skin diseases are among the first to be studied due to the easy accessibility of the skin to the topical application of photosensitizer and light. In the 1970s, HpD and xenon arc lamp have been used to treat skin cancers. Early studies demonstrated that the primary skin cancers that showed a 20–80% complete response (CR) included squamous cell carcinomas (SCCs), basal cell carcinomas (BCCs) and malignant melanomas, and the secondary cancers originated from primary breast cancer, colon cancer and endometrium cancer.

Since the discovery of endogenous protoporphyrin IX (PpIX) photosensitization induced by exogenous administration of prodrug ALA, skin premalignant and malignant lesions also became a target of ALA-PDT. Early multi-center clinical studies of actinic keratosis (AK) showed that ALA-PDT (Levulan and Blu-U blue light system) resulted in high CR and disease-free rate. AK became the first approved dermatologic indication of ALA-PDT in US in 2000. Recently, methyl aminolevulinate has also been approved for AK in Australia and Europe.

Clinical investigations of skin PDT have also been extended to BCCs, basaloid follicular hamartomas, SCC *in situ* (Bowen's disease), cutaneous T-cell lymphoma, and sebaceous gland hyperplasia in recent years. PDT may be useful for both Mediterranean and HIV-related Kaposi's sarcomas since it can be repeated and will not cause immunosuppression. Recent clinical data also suggests that PDT might be useful for the treatment of the pigmented malignant melanomas, although in general PDT is considered unsuitable for the pigmented lesion due to a limited light penetration.

6.6.2.2 *Ophthalmic Tumor*

Several case studies have demonstrated that Verteporfin-PDT could resolve the exudative retinal detachment associated with a diffuse choroidal haemangioma. A pilot study of circumscribed choroidal haemangioma showed evidence of flattening tumor, reducing subretinal fluid and choroidal vasculature.

6.6.2.3 *Head and Neck Cancer*

Photodynamic therapy is particularly suitable for head and neck cancer because it has little effect on underlying functional structures and has an excellent cosmetic outcome. The Chinese pioneered PDT protocol for nasopharyngeal carcinoma in the 1980's. Three-year and five-year survival was reported as 44.6% and 25.4%, respectively.[58] Foscan-PDT was approved in Europe in 2001 for the palliative treatment of patients with advanced head and neck cancer who have exhausted other treatment options. Foscan-PDT can have significant clinical benefits and improve

the quality of life.[59] Several clinical trials are currently under way to evaluate the efficacy of other promising photosensitizers including Photofrin, ALA and Photosens. For patients with advanced disease, the combination of PDT and radiotherapy or surgery could also improve cure rates. An early Photofrin-PDT study of 107 patients shows that cures for T1 and *in situ* cancer of the vocal cords could be achieved with a single treatment. There was only one recurrence in 25 patients in 79 months follow-up. All patients responded initially and the cure rate for early oral cavity tumors was 80% after 70 months.[60]

6.6.2.4 *Brain Tumor*

Cavitary PDT procedure was introduced in the 1990s, which utilizes an optical fiber in a light-diffusing medium, to irradiate the cavity following surgical resection. Several multi-center studies are currently under way to evaluate the efficacy of Photofrin, ALA, BPD-MA and Foscan PDT. Preliminary results have shown prolongation of survival in patients with malignant gliomas. Optimizing photosensitizer uptake, elevating light dose and fluorescence-guided resection might further improve the efficacy of intra-operative PDT. Photofrin-PDT for pituitary adenomas is currently under clinical investigation.

6.6.2.5 *Pulmonary and Pleural Mesothelial Cancer*

Photofrin-PDT has been used to treat bronchogenic carcinoma in Japan in the 1980s. The worldwide data now show that bronchoscopic PDT appears to be as effective as a curative therapy for superficial and early stage non-small cell lung cancer (NSCLC) and as palliative therapy in obstructive cancers of the tracheobronchial tree. Bronchoscopic PDT has now achieved the status of a standard protocol for centrally located early-stage lung cancer in Japan. PDT of endobronchial metastatic tumors effectively decreased the amount of endobronchial obstruction, and improved quality of life. Recently, a new protocol using percutaneous insertion and intra-tumoral illumination has been developed for the curative treatment of localized peripheral lung cancer (< 1 cm) unsuitable for surgery or radiotherapy. Preliminary results have

shown a partial response in the majority of patients.[61] The same Japanese group also studied the efficacy and mechanisms of Npe6-PDT for SCCs.

Malignant pleural mesothelioma, often related to asbestos exposure, responds poorly to conventional therapies. Photofrin-PDT has been tested as an adjuvant intra-operative modality in several countries. The data demonstrate the safety and feasibility of intrapleural PDT which offers good survival results for stage I or II patients. However, for patients of stage III or IV, PDT could not significantly prolong survival or increase local control. In recent years the improvement in photosensitizers and PDT technique has led to a renewed interest in intrapleural PDT.[62] Hyperoxygenation is an effective means to enhance PDT cytotoxicity.[63] Therefore, it is expected that to carry out the intrapleural PDT under hyperoxygenation might further enhance the PDT efficacy.[64]

6.6.2.6 *Breast Cancer*

Locally recurrent breast carcinoma on the chest wall occurs in 5–20% of breast cancer patients. Several reports suggest that Photofrin-PDT and Foscan-PDT can offer 14–73% complete response and 14–45% partial response, but the duration of response was variable (6 weeks – 8 months). It is expected that the photosensitizer acting at longer wavelengths could achieve deeper tissue penetration thereby greatly expanding the patient population for which this modality become more acceptable and useful. PDT may also play a role in treating the primary breast cancer and allowing for breast conservation based in part on the emerging success of partial breast radiation.[65]

6.6.2.7 *Gastroenterological Cancer*

Endoscopically accessible premalignant or malignant lesions located within the esophagus, the stomach, the bile duct or the colorectum with a high surgical risk are favorable targets of endoscopic PDT. Photofrin-PDT has been approved for obstructing esophageal cancer, early-stage esophageal cancer and Barrett's esophagus (endobrachyesophagus) in

several countries. A longer diffuser tip and light centering balloon are able to treat a large area of esophageal mucosa during a single treatment. It is suggested that optimizing light dose and re-treating small areas of residual or untreated Barrett's mucosa may reduce the post-PDT stricture formation and improve the overall efficacy.

Recent pilot studies have demonstrated that Photofrin-PDT is also effective in the palliative treatment of hilar cholangiocarcinoma. Preliminary results confirm that endoscopic illumination of the biliary tract is safe and effective for inoperable cholangiocarcinoma and can improve cholestasis and quality of life for an extended period. Preliminary studies suggest that operative PDT might also improve survival for those patients undergoing surgical resection.[66]

Due to advances in light applicators, the interstitial PDT is now becoming a practical option for solid lesions, including those in parenchymal organs such as the liver and pancreas. The first pilot study of Foscan-PDT on inoperable pancreatic cancer was carried out in the UK. The percutaneous interstitial protocol, of multiple diffuser fiber illumination, could produce significant necrosis and prolong survival time. In most cases, the necrotic area of the treated tumor healed safely. There was no sign of a pseudocyst, abscess, or pancreatic duct leak. These promising results encourage larger scale trials to further assess the feasibility of pancreas PDT.[67]

An earlier pilot study of interstitial PDT for the treatment of advanced liver cancer has been reported by Chinese clinicians.[68] The preliminary results indicated that PDT was effective and safe for the treatment of large primary and recurrent liver cancers. More than one fourth of the patients (8/30) survived over one year.[58]

6.6.2.8 *Urological Cancer*

Photofrin obtained its first Canadian regulatory approval for recurrent papillary tumors in 1993. Intravenous Photofrin administration followed by intravesical illumination became an option for patients with refractory tumors. The initial responses to a single treatment of the whole bladder tended to be good, but side effects such as bladder contraction and bladder irritation are noticeable and the incidence of relapse within a

year is high. Since the side effects are dose dependent, fractionating drug and light doses in a sequential PDT mode might subside cancerous cells and meanwhile reduce local toxicity. Bladder cancer tends to be a superficial condition, a superficial treatment mediated with ALA or its ester derivatives may be better. Nonetheless, intravesical instillation of ALA can eliminate cutaneous phototoxicity. Several clinical investigations show that ALA-PDT is an effective treatment option for patients with superficial bladder cancer who have failed transurethral resection and/or intravesical BCG immunotherapy. It has been shown that by repeating treatments, it is possible to further inhibit the progression of bladder cancer.

Prostate cancer is still a significant health problem in the Western world. Recent clinical trials of Foscan-PDT and ALA-PDA on patients who had failed radiotherapy showed a post-PDT decrease in prostate specific antigen (PSA) levels. The preliminary results from two ongoing clinical trials of motexafin lutetium-PDT and Tookad-PDT designed to totally ablate the entire prostate gland are also encouraging. The total ablation approach involves the implantation of multiple diffuser fibers into the prostate gland through a transperineal brachytherapy template. It should be fully recognized that characterization of light penetration and distribution in prostate PDT is important due to the significant inter- and intra-prostatic differences in the tissue optical properties. Several recent studies suggest that a real-time drug/light dosimetry measurement and feedback systems for monitoring drug concentrations and light fluences during interstitial PDT should be considered.[69,70]

6.6.2.9 *Gynecological Cancer*

Prior to and after its regulatory approval in Japan in 1994, Photofrin has been used successfully to treat carcinoma *in situ* and dysplasia of the uterine cervix. Several Japanese studies have shown that colposcopic-assisted cervical canal illumination after intravenous Photofrin administration can achieve a high CR (< 94%) and preserve fertility.

A modified protocol that combined topical administration of Photofrin and superficial illumination demonstrated that CR was light

dose dependent for cervical intraepithelial neoplasia (CIN). Several *in vivo* studies have demonstrated selective absorption of ALA by dysplastic cervical cells. This led to the presumption that ALA represents a promising photosensitizing prodrug for the treatment of CIN with ALA-PDT.[71] However, several randomized, double-blind, placebo-controlled clinical trials showed that ALA-PDT was well tolerated by patients but the general consensus is that ALA-PDT has minimal effect in the treatment of CIN 2 and CIN 3.[72]

A recent pilot study of topical application of ALA and superficial illumination for the treatment of vulvar and vaginal intraepithelial neoplasia (VIN, VAIN) shows that ALA-PDT is as effective as conventional treatments though not equally efficacious for all subgroups, but with shorter healing time and excellent cosmetic results.[73]

Photodynamic therapy has also been employed to treat ovarian cancer and both benign and malignant lesions of the endometrium. But no conclusive clinical results have yet been shown in limited clinical trials.[71]

6.7 PDT in Dentistry

6.7.1 *Technical Challenges*

The human mouth is a very unique and complex structure. It contains exquisitely sensitive tissues that are constantly used for complicated multitasks such as tasting, chewing, digesting, swallowing, speech, and facial expression. The mouth has one of the highest concentrations of sensory and motor nerves in the body, four different types of calcified tissue, and contains numerous species of microbes that maintain a delicate balance between health and disease. Not surprisingly, there are a multitude of diseases and conditions that affect the oral cavity and related dental and craniofacial structures, including the teeth, soft tissues, salivary glands, the temporomandibular joint, jaws, facial bones, muscles, nerves, and skin.

Technical challenges of conventional therapeutic procedures extend from the continued struggle against two of the most common infectious diseases – dental caries and periodontal diseases – to eliminating life-threatening oral and pharyngeal malignancies and other conditions that

can compromise oral health and the quality of life. Adoption and implementation of PDT techniques for the treatment of oral infection and malignancy face similar or even greater challenges due to the need of delivering sufficient photosensitizer and light to a complex structure.

6.7.2 Current Status

It has been shown that PDT mediated with phenothiazinium dyes is effective for killing bacteria in complex biofilms, such as subgingival plaque, which are typically resistant to the action of antimicrobial agents.[74] Systems using tolonium chloride (toluidine Blue O, TBO) and low power 635 nm laser for the treatment of endodontics and caries are now available commercially under the trademark of PAD (Photo-Activated Disinfection). Since 635 nm laser light transmits well across dentine, locally applied TBO can be used effectively in carious lesions. In dental caries the use of PAD can eliminate residual bacteria in softened dentine and provide an environment which encourages rapid healing. This means that less tissue is removed and thus cavities are more conservative. In addition, endodontic PAD might lead to accelerated post-operative bone regrowth. Other possible clinical applications of PAD or other photosensitizers include disinfection of root canals, periodontal pockets, deep carious lesions and sites of peri-implantitis, and prevention of alveolar ostitis and post-extraction pain. In such locations, PDT does not give rise to thermal effects; therefore, adjacent tissues are not subjected to thermal injury.

PDT has been employed in the treatment of malignancies of the oral mucosa, particularly multi-focal SCC. Clinical investigations have shown positive results in PDT treatment of hyperplasia, carcinoma-*in-situ* and SCC in the oral cavity, with high response rates. The treated sites characteristically show erythema and edema, followed by necrosis and frank ulceration. The ulcerated lesions typically take up to eight weeks to heal fully, and supportive analgesia is required in the first few weeks. Other than short-term photosensitivity, the treatment is safe and tolerable.[59,75]

6.8 Concluding Remarks

There is a strong and increasing interest and research effort internationally focused on developing new photosensitizers, exploring PDT mechanisms at molecular level, enhancing PDT efficacy with combined modality and evaluating potential clinical indications. The birth of a new international journal titled *Photodiagnosis and PhotodynamicTherapy*[a], now entering its 3rd year, highlights the new era of PDT. The number of scientific articles on PDT clinical application as well as basic science steadily increases in both English language and non-English language literatures. Review articles on past work, new aspects and future applications have been published on a regular basis while new technology and promising applications continue to be discovered. Each year several national, regional and international meetings are held regularly which bring together these interests and research. Examples include the World Congress of International Photodynamic Association (IPA)[b], the annual symposium of Biomedical Optics of Photonics West organized by the International Society for Optical Engineering (SPIE), the annual meeting of European Society for Photodynamic Therapy in Dermatology (Euro-PDT), and the International Symposium on Photodynamic Diagnosis and Therapy in Clinical Practice. PDT sessions could also be found in laser medicine, biophotonics and photobiology meetings.

Although regulatory approvals for the clinical use of PDT photosensitizers and light applicators now exist in many countries around the world, the total number of approved clinical indications is still limited. It is expected that the involvement of pharmaceutical industry and research institute will continue to launch new clinical trials to evaluate applications of PDT in conjunction with or as a replacement for

---

[a] *Photodiagnosis and Photodynamic Therapy* website http://www.sciencedirect.com/science/journal/15721000

[b] International Photodynamic Association website http://www.ipa-net.org/

traditional methods. There is little argument that over the past decade PDT has moved beyond lab bench into the general practice. Some of clinical applications such as the treatment of AMD, AK and malignant diseases have entered the mainstream of medical specialties. Looking into the future, it is expected that combined modality and individualized treatment plan will become an essential component of contemporary PDT practice over the next decade.

References

1. O. Raab, *Z. Biol.*, 524 (1900). (in German).
2. L. Ledoux, *Ann. Inst. Pasteur*, 587 (1902). (in French)
3. H. von Tappeiner and A.U. Jodlbauer, *Deutsches Arch. Klin. Med.*, 427 (1904). (in German).
4. R.L. Lipson and E.J. Baldes, *Arch. Dermatol.*, 508 (1960).
5. T.J. Dougherty, BW. Henderson, S. Schwartz, J.W. Winkelman and R.L. Lipson, in *photodynamic Therapy*, Eds., B.W. Henderson and T.J. Dougherty (Maurice Dekker, New York, 1992), p. 1.
6. T.J. Dougherty, C.J. Gomer, B.W. Henderson, G. Jori, D. Kessel, M. Korbelik, J. Moan and Q. Peng, *J. Natl. Cancer Inst.*, 899 (1998).
7. Z. Huang, *Technol Cancer Res. Treat.*, 283 (2005).
8. J.G. Moser, in *Photodynamic Tumor Therapy – 2nd & 3rd Generation Photosensitizers,* Ed., J.G. Moser (Harwood Academic Publishers, London, 1997), p. 3.
9. R.R. Allison, G.H. Downie, R. Cuenca, X.H. Hu, C.J.H. Childs and C.H. Sibata, *Photodiag. Photodyn. Therapy*, 27 (2004).
10. M.H. Schmidt, D.M. Bajic, K.W. Reichert II, T.S. Martin, G.A. Meyer and H.T. Whelan, *Neurosurgery*, 552 (1996).
11. R.A. Lustig, T.J. Vogl, D. Fromm, R. Cuenca, A.R. His, A.K. D'Cruz, Z. Krajina, M. Turic, A. Singhal and J.C. Chen, *Cancer*, 1767 (2003).
12. J. Chen, L. Keltner, J. Christophersen, F. Zheng, M. Krouse, A. Singhal and S.S. Wang, *Cancer J.,* 154 (2002).
13. T.S. Mang, *Photodiag. Photodyn. Therapy*, 43 (2004).
14. D. Phillips, *Sci. Progress*, 295 (1994).
15. C.S. Foote, F.C. Shook and R.B. Abakerli, *Methods Enzymol.*, 36 (1984).
16. Y.Z. Song, J. An and L. Jiang, *Biochim. Biophys. Acta.*, 307 (1999).
17. D. Kessel, Y. Luo, Y. Deng and C.K. Chang, *Photochem. Photobiol.*, 422 (1997).
18. B.C. Wilson, M. Olivo and G. Singh, *Photochem. Photobiol.*, 166 (1997).

19. P. Castano, T.N. Nemidova and M.R. Hamblin, *Photodiag. Photodyn. Therapy*, 279 (2004).
20. S.K. Bisland, L. Lilge, A. Lin, R. Rusnov and B.C. Wilson, *Photochem. Photobiol.*, 22 (2004).
21. R.D. Almeida, B.J. Manadas, A.P. Carvalho and C.B. Duarte, *Biochim. Biophys. Acta*, 59 (2004).
22. P. Castano, T.N. Nemidova and M.R. Hamblin, *Photodiag. Photodyn. Therapy*, 1 (2005).
23. D. Nowis, M. Makowski, T. Stokłosa, M. Legat, T. Issat and J. Gołąb, *Acta Biochimica Polonica*, 339 (2005).
24. C.J. Gomer, M. Luna, A. Ferrario, S. Wong, A.M. Fisher and N. Rucker, *J. Clin. Laser Med. Surg.*, 315 (1996).
25. W.M. Star, J.P. Marijnissen, A.E. van den Berg-Blok and H.S. Reinhold, *Prog. Clin. Biol. Res.*, 637 (1984).
26. B. Krammer, *Anticancer Res.*, 4271 (2001).
27. P. Castano, T.N. Nemidova and M.R. Hamblin, *Photodiag. Photodyn. Therapy*, 91 (2005).
28. W. Henderson and V.H. Fingar, *Cancer Res.*, 3110 (1987).
29. V.H. Fingar, *J. Clin. Laser Med. Surg.*, 323 (1996).
30. C. Abels, *Photochem. Photobiol. Sci.*, 765 (2004).
31. W.G. Roberts and T. Hasan, *Cancer Res.*, 924 (1992).
32. W.G. Roberts and T. Hasan, *Cancer Res.*, 153 (1993).
33. D.E. Dolmans, A. Kadambi, J.S. Hill, K.R. Flores, J.N. Gerber, J.P. Walker, I.H. Rinkes, R.K. Jain and D. Fukumura. *Cancer Res.*, 4289 (2002).
34. Z. Huang, Q. Chen, D. Luck, J. Beckers, B.C. Wilson, N. Trncic, S.M. LaRue, D. Blanc and F. W. Hetzel, *Lasers Surg. Med.*, 390 (2005).
35. M. Korbelik, *J. Clin. Laser Med. Surg.*, 329 (1996).
36. G. Canti, A. De Simone and M. Korbelik, *Photochem. Photobiol. Sci.*, 79 (2002).
37. F.H. van Duijnhoven, R.I.J.M. Aalbers, J.P. Rovers, O.T. Terpstra and P.J.K. Kuppen, *Immunobiol.*, 105 (2003).
38. D. Nowis, T. Stokłosa, M. Legat, T. Issat, M. Jakóbisiak and J. Gołąb *Photodiag. Photodyn. Therapy.* 283 (2005).
39. N. Yamamoto, S. Homma, T.W. Sery, L.A. Donoso and J.K. Hoober, *Eur. J. Cancer,* 467 (1991).
40. G. Krosl, M. Korbelik and G.J. Dougherty, *Br. J. Cancer*, 549 (1995).
41. M. Korbelik, G. Krosl, J. Krosl and G.J. Dougherty, *Cancer Res.*, 5647 (1996).
42. S.O. Gollnick, S.S. Evans, H. Baumann, B. Owczarczak, P. Maier, L. Vaughan, W.C. Wang, E. Unger and B.W. Henderson, *Br. J. Cancer*, 1772 (2003).
43. E.S. Abdel-Hady, P. Martin-Hirsch, M. Duggan-Keen, P.L. Stern, J.V. Moore, G. Corbitt, H.C. Kitchener and I.N. Hampson, *Cancer Res.*, 192 (2001).

44. M. Korbelik, J. Sun, I. Cecic and K. Serrano, *Photochem Photobiol Sci.*, 812 (2004).
45. S.O. Gollnick, L. Vaughan and B.W. Henderson, *Cancer Res.*, 1604 (2002).
46. W.R. Chen, M. Korbelik, K.E. Bartels, H. Liu, J. Sun and R.E. Nordquist, *Photochem. Photobiol.*, 190 (2005).
47. L.I. Grossweiner, *J. Photochem. Photobiol. B: Biol.*, 258 (1997).
48. J. MacDonald and T.J. Dougherty, *J. Porphyrins Phthalocyanies*, 105 (2001).
49. M.J. Niedre, C.S. Yu, M.S. Patterson and B.C. Wilson, *Br. J. Cancer*, 298 (2005).
50. R. Ackroyd, C. Kelty, N. Brown and M. Reed, *Photochem. Photobiol.*, 656 (2001).
51. S.L. Marcus and W.R. McIntyre, *Expert. Opin. Emerg. Drugs*, 321 (2002).
52. S.B. Brown, E.A. Brown and I. Walker, *Lancet Oncol.*, 497 (2004).
53. R.R. Allison, H.C. Mota and C.H. Sibata, *Photodiag. Photodyn. Therapy*, 263 (2004).
54. M. Wainwright, *J. Antimicrob. Chemother.*, 13 (1998).
55. X.X. Lin, W. Wang, S.F. Wu, C. Yang and T.S. Chang, *Plast Reconstr Surg.*, 1826 (1997).
56. L. Jiang, Y. Gu, X. Li, X. Zhao, J. Li, K. Wang, J. Liang, Y. Pan and Y. Zhang, *Chin. Med. J.*, 136 (1998).
57. V. Evans, A. Robson, R.J. Barlow and H.A. Kurwa, *Lasers Surg. Med.*, 266 (2005).
58. Z. Huang, Photodynamic therapy in China: 25 years of unique history. Part II – clinical experiences, *Photodiag. Photodyn. Therapy*, (2006). (in press).
59. C. Hopper, A. Kubler, H. Lewis, I.B. Tan and G. Putnam, *Int. J. Cancer*, 138 (2004).
60. M.A. Biel, Laryngoscope, 1259 (1998).
61. H. Kato, M. Harada, S. Ichinose, J. Usuda, T. Tsuchida and T. Okunaka, *Photodiag. Photodyn. Therapy*, 49 (2004).
62. S.M. Hahn, R.P. Smith and J. Friedberg, *Curr. Treat. Options Oncol.*, 375 (2001).
63. Z. Huang, Q. Chen, A. Shakil, H. Chen, J. Beckers, H. Shapiro and F.W. Hetzel, *Photochem. Photobiol.*, 496 (2003).
64. V. Matzi, A. Maier, O. Sankin, J. Lindenmann, M. Woltche, J. Smolle and F.M. Smolle-Juttner, *Photodiag. Photodyn. Therapy*, 57 (2004).
65. R.R. Allison, C. Sibata, G.H. Downie and R.E. Cuenca, Photodynamic therapy of the intact breast, *Photodiagnosis and Photodynamic Therapy*, (2006). (in press).
66. M.A. Ortner, *Photodiag. Photodyn. Therapy*, 85 (2004).
67. S.G. Bown, A.Z. Rogowska, D.E. Whitelaw, W.R. Lees, L.B. Lovat, P. Ripley, L. Jones, P. Wyld, A. Gillams and A.W.R. Hatfield, *Gut*, 549 (2002).
68. C. Zeng, D. Yang, P. Huang, H. Zhang, M. Huang, J. Chen and G. Lu, *Proc. SPIE*, 2887:68 (1996).
69. N.E. Martin and S.M. Hahn, *Photodiag. Photodyn. Therapy*, 123 (2004).
70. H. Pinthus, A. Bogaards, R. Weersink, B.C. Wilson, J. Trachtenberg, *J. Urol.*, 1201 (2006).
71. R.R. Allison, R. Cuenca, G.H. Downie, M.E. Randall, V.S. Bagnato and C.H. Sibata, *Photodiag. Photodyn. Therapy*, 51 (2005).

72. A. Barnett, J.C. Haller, F. Cairnduff, G. Lane, S.B. Brown and D.J. Roberts, *Int. J. Cancer*, 829 (2003).
73. M.K. Fehr, R. Hornung, A. Degen, V.A. Schwarz, D. Fink, U. Haller and P. Wyss, *Lasers Surg. Med.*, 273 (2002).
74. M. Wilson, *Photochem. Photobiol. Sci.*, 412 (2004).
75. J. Walsh, *Aust Dent. J.*, 146 (2003).

CHAPTER 7

DENTAL PHOTO-BIOMECHANICS

Anil Kishen

Biophotonics Laboratory, Faculty of Dentistry Research Laboratory
National University of Singapore, Republic of Singapore
E-mail: rsdak@nus.edu.sg

This chapter discusses common photomechanical experiments used in dental biomechanics. Methods such as photoelasticity, moiré interferometry and electronic speckle pattern interferometry are described with relevance to applications in dentistry.

7.1 Introduction

Biomechanical studies will indicate the stress-bearing regions, the areas of weakness, and locations of potential failure in natural structures and prosthesis. An understanding of biomechanical principles is mandatory to approximate the properties of artificial materials with natural teeth. Application of photomechanical experiments in biomechanics is termed photobiomechanics. Traditionally, photobiomechanical experiments are considered laborious and time consuming. Other factors that make these methods strenuous are the wide variation in material properties and complex shapes of biological structures, nature of external forces and intricate boundary conditions in clinical situations. An ideal biomechanical experiment should be able to test specimens under clinically realistic conditions. These techniques are non-destructive, whole-field methods, which provide specific deformation (in-plane or out-of-plane) information. Common photobiomechanical techniques applied in dentistry are (1) Photoelasticity (2) Moiré interferometry and (3) Speckle pattern

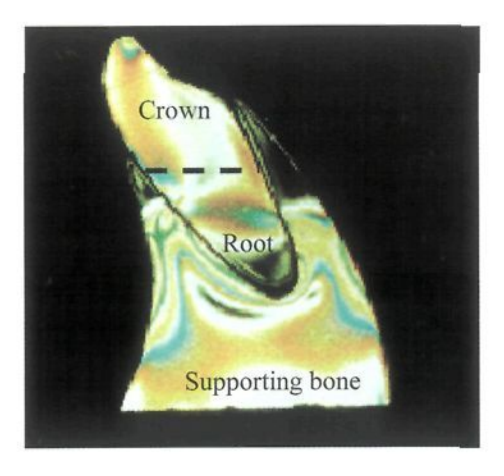


Fig. 7.1. Photoelastic color fringe pattern of a tooth-bone model.

correlation interferometry. More details about these techniques are presented in the Chapter 2 of this book.

7.2 Photoelasticity

7.2.1 *Introduction*

Photoelasticity is used to study stress distribution in biological structures subjected to external forces. This method is based on the principle of load induced double-refraction or birefringence exhibited by some transparent materials. When these materials are loaded and viewed under polarized light, bands of light called fringes will appear. These fringe patterns represent the distribution of internal stresses within the structure. Photoelastic fringe pattern in a tooth-bone model is shown in Fig. 7.1. Photoelastic fringes are classified as isoclinic and isochromatic fringes. Figure 7.2 shows the isoclinic and isochromatic fringes in a tooth model. The isoclinic fringes indicate the direction of principal stresses, while the isochromatic fringes indicate the magnitude of principal stresses. Photoelastic experiments consist of three stages, namely (1) model preparation (2) testing and acquisition of fringe patterns, and (3) analysis of fringe patterns.

7.2.2 Photoelastic Models

Photoelastic models are prepared using specialized plastic material (e.g.: epoxy), which has the property of birefringence. There are two main factors to be considered when modeling dental structures or prosthesis. First consideration is to reproduce the geometry of the structure. The model should reflect either the full or partial geometry of the structure. These models may be of life-size, smaller than life-size or larger than life-size. Generally larger than life-size models are used to examine miniature structures, while smaller than life-size models are used to examine large structures. The foremost intention is to obtain sufficient fringes for fringe analysis. Enlarging and reducing the size of the models will aid in acquiring adequate number of fringes for further analysis. The second consideration is to relate mechanical properties such as elastic modulus of the biological structure with that of the model.[1] Since it is not possible to simulate all the mechanical properties when more than one structure is involved, model simulation can be ideally based on the relative elastic modulus difference between anatomical structures. For example, when preparing a tooth-supporting bone model, the relative elastic modulus difference between enamel-dentine, dentine-periodontal ligament, and dentine-supporting bone can be considered for modeling.[2]

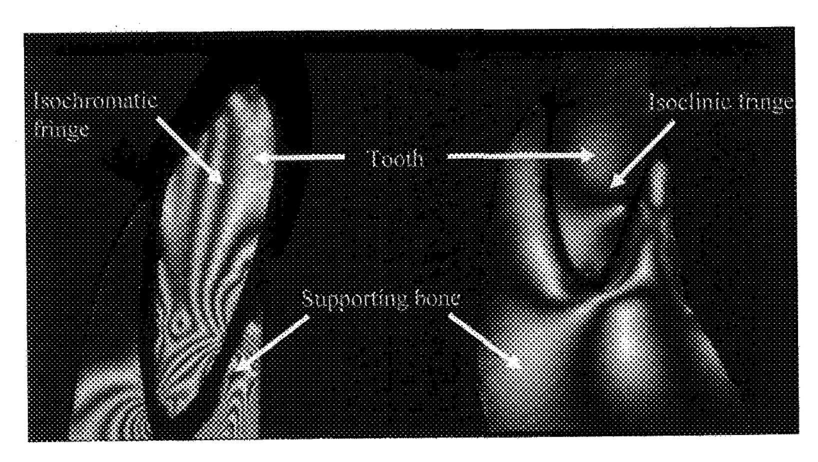


Fig. 7.2. Shows a typical (A) isochromatic (B) isoclinic fringe pattern in a tooth-bone model.

Two-dimensional and three-dimensional models are used in photoelasticity. Some two and three dimensional models are shown in Fig. 7.3. Two-dimensional models simulated the geometry of a structure in one plane. The primary requirement for a two-dimensional analysis is that there is no variation of stress through the thickness of the model, and the force applied must be distributed in the plane of the model. Two-dimensional models are relatively easy to fabricate, and are used to test different conditions in the same model. Computer numerical control (CNC) machining can be used to fabricate sectional photoelastic models. Coordinates measured from the digitized image of the specimen is used for CNC machining.[2]

Three-dimensional models are prepared using a special plastic material that permits freezing of stress patterns at high temperature. Stress-freezing procedure is an important step in three-dimensional photoelasticity.[1] During stress-freezing, the models are subjected to load at a specific elevated temperature. The load induced stress patterns are then frozen within the model during the cooling phase. The stress frozen models are later sliced along different planes of interest and each section is analyzed as a two-dimensional section. Analysis of all the sections allows construction of the three-dimensional stress picture. However since the model has to be sliced, different experimental conditions require fabrication of new models. Three-dimensional photoelasticity is considered a laborious technique to practice. A three-dimensional photoelastic model of a human mandible is shown in Fig. 7.3(A). Fig. 7.3(B) shows a three dimensional model of a human mandibular central incisor before and after sectioning. Silicone rubber dental impression materials can be used to prepare the negative replica (mould) of the structure for three-dimensional models.[3] Often the most efficient means to obtain solutions for difficult problems in biomechanics is to combine two and three-dimensional analyses.

7.2.3 *Polariscope*

The polariscope is an optical arrangement used to visualize the phase differences produced when polarized light passes through a loaded

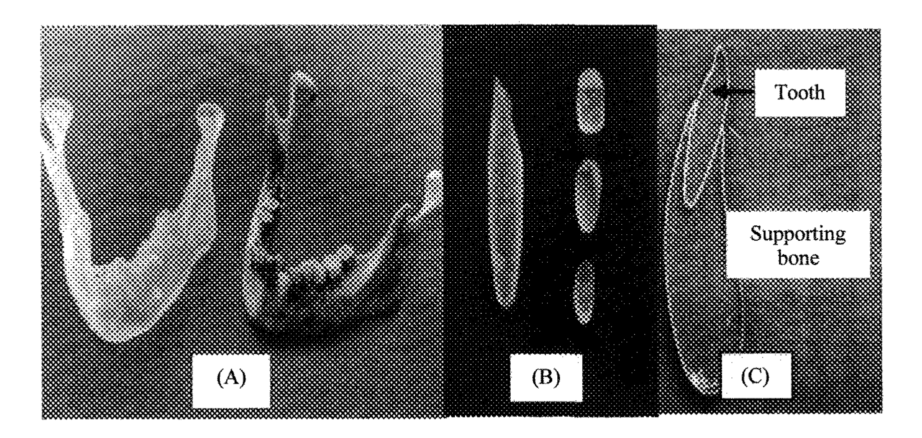


Fig. 7.3. (A) Three-dimensional model of human mandible (on left) and natural mandible (B) three-dimensional model of lower incisor tooth before sectioning (on left) and after sectioning, and (C) two-dimensional model of tooth and supporting bone.

birefringent model. The basic components of a polariscope are the polarizing filters and the light source. There are mainly three kinds of polariscope, namely plane polariscope, circular polariscope and reflection polariscope. A plane polariscope consists of a polarizer and an analyzer. A schematic diagram of a plane polariscope is shown in Fig. 7.4. A plane polariscope will display both isoclinic and isochromatic fringes together. A circular polariscope consists of four optical elements (two quarter-wave-plates (QWP), a polarizer and an analyzer) and a light source. A schematic diagram of a circular polariscope is shown in Fig. 7.5. The polarizer converts the incident polarized light from the source into plane polarized light. The QWP I converts plane polarized light to circularly polarized light, and QWP II converts circular polarized light back to plane polarized light. A circular polariscope is used to visualize the isochromatic fringe patterns.[4]

Standard polariscopes can be coupled with an image processing system, which include a Charge Coupled Device (CCD) and a personal computer. These systems are called digital polariscope. They aid in the real-time acquisition and analysis of fringe patterns. Schematic diagram

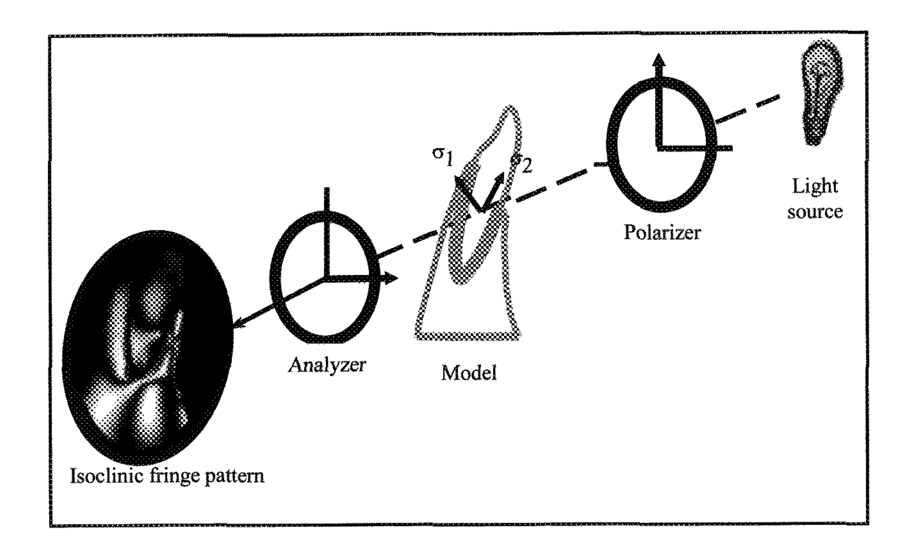


Fig. 7.4. Schematic diagram of the plane polariscope.

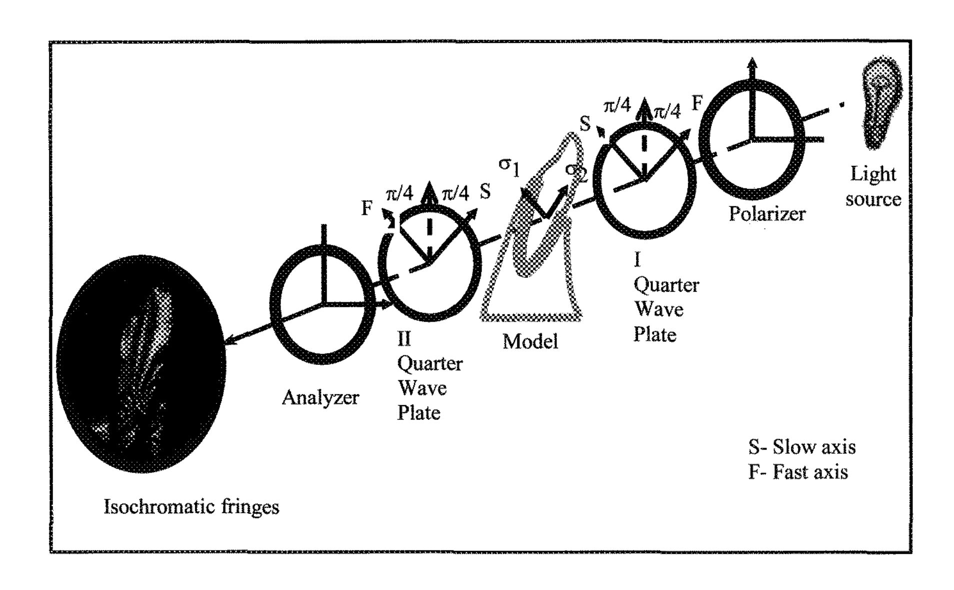


Fig. 7.5. Schematic diagrams of the circular polariscope.

of a digital polariscope is shown in Figure 7.6. The digital polariscope facilitates testing of miniature biological specimens at physiologically realistic loads.[2] A reflection polariscope consists of two sets of polarizer and QWPs attached to a common frame. These assemblies are connected mechanically so that they rotate in unison. A schematic diagram of a reflection polariscope is shown in the Fig. 7.7. In reflection photoelasticity a thin layer of birefringent material is coated on the specimen. While testing, the deformation of the specimen is expected to transfer to the coating, and the resultant photoelastic patterns are analyzed. In reflection photoelasticity, the strains in the test structure and the coating are assumed to be the same.[4, 5]

7.2.4 *Photoelastic Fringe Analysis*

In the past, photoelastic fringes are photographed, traced and analyzed manually. Traced isoclinic and isochromatic fringe patterns obtained from a tooth-bone model is shown in Fig. 7.8. The intermediate points in between two fringe orders are determined by linear interpolation. The fundamental relationship applied in photoelastic fringe analysis is that the stress is a product of fringe order (N) and photoelastic material constant (K). Therefore the most important parameter that has to be recorded during an analysis is the fringe order at every point on the fringe pattern. The manual analysis of fringe patterns is considered time consuming and tedious. In a digital fringe analysis, the fringe patterns are acquired in a digital format. This facilitates application of software based programs for further processing. The digital fringe analysis can be applied to analyze fringe patterns obtained from any photomechanical experiments. The most common methods of digital fringe analysis are phase shifting technique, fractional fringe method and Fast Fourier Transform method (FFT). The advantage of the phase shift technique over fractional fringe method and FFT method is its ability to identify the signs of the fringe order. Figure 7.6 shows the phase map of the stress distribution pattern observed in a tooth model.[6]

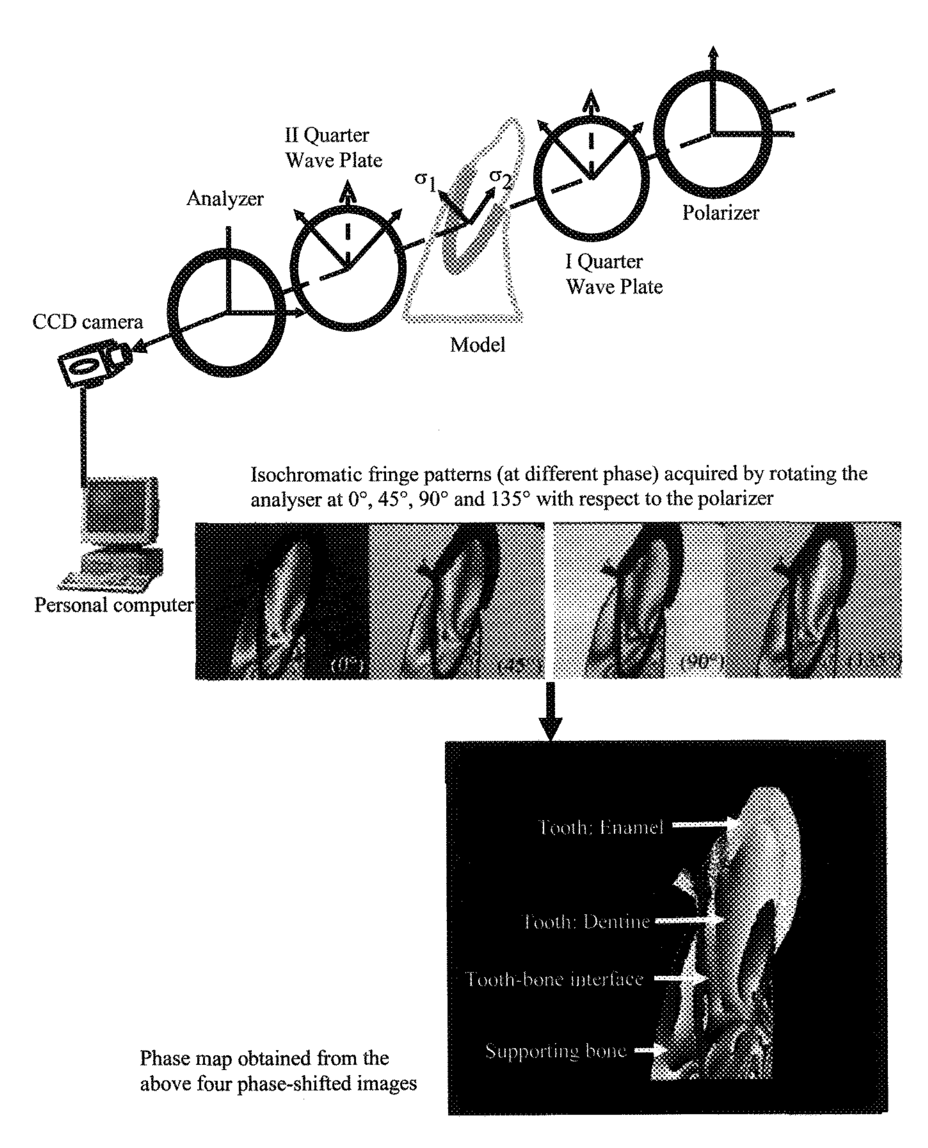


Fig. 7.6. Schematic diagram of the digital photoelastic experiment.[6]

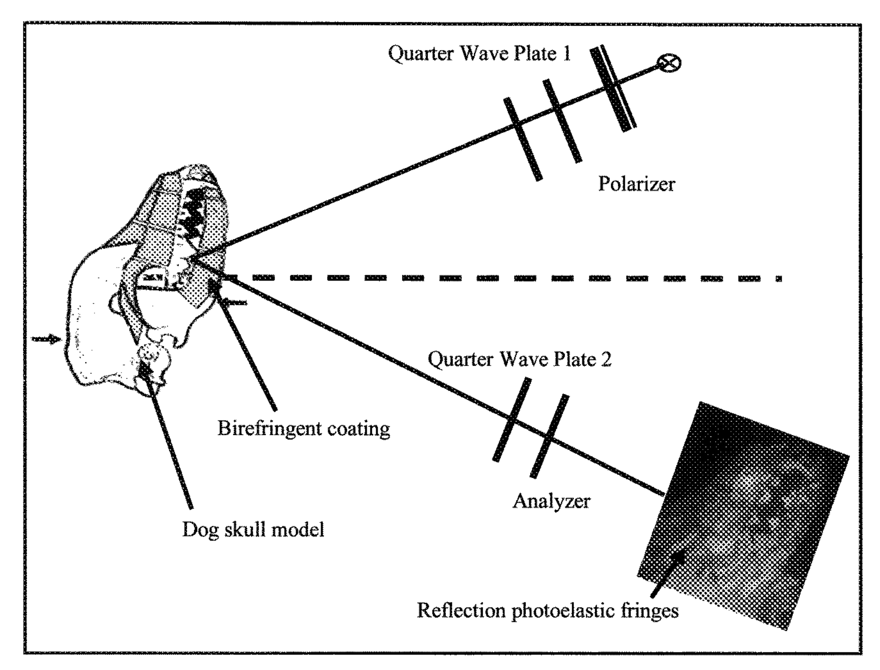


Fig. 7.7. Schematic diagram of the reflection photoelastic system (*with permission*).[5]

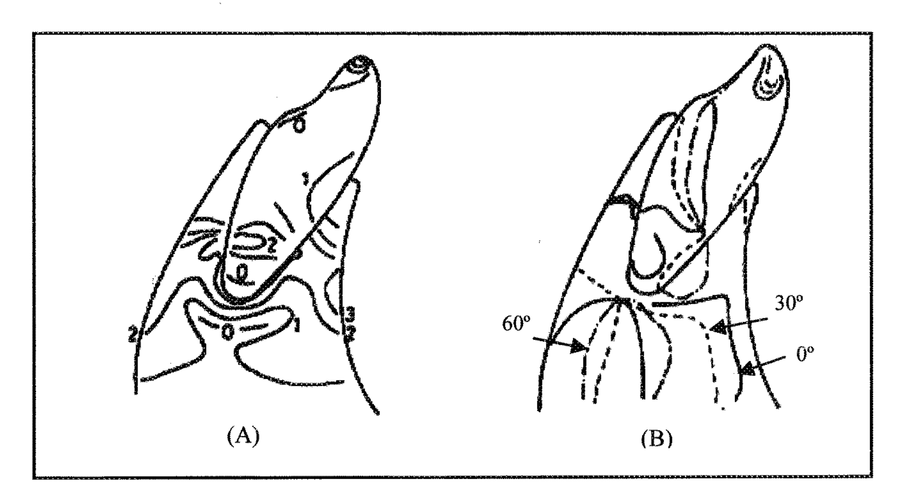


Fig. 7.8. (A) The tracings of the isochromatic fringe patterns (0, 1, 2, 3 are fringe orders representing higher magnitude of stress) and (B) the isoclinic fringes (0°, 30°, 60° represent directions of stresses for loads directed along the long axis of the tooth, 30° and 60° lingual to the long axis of the tooth).[7]

7.2.5 *Applications of Photoelasticity in Dentistry*

Photoelasticity has been an accepted technique to study stress distribution in dentistry since 1955.[8] This technique has been employed to study stress distribution in natural and restored tooth structure, cranial and jaw bones and implants. Initially, three-dimensional photoelasticity was applied to study stress distribution associated with different cavity preparations prior to restorations. These experiments highlighted that sharp and acute line angles produced stress concentrations. Rounding the internal line angles and decreasing the undercut of the axial wall reduces stress concentrations significantly. Minimizing stress concentration allowed clinicians prevent premature fracture of dental restorations.[9] Although doubts have been raised occasionally on the relationship between the results obtained from homogeneous, isotropic photoelastic models and the biologic systems, many investigations that compared in vitro and invivo findings have reported that the photoelastic technique predicted biologic responses.

One of the earliest example is the demonstration of a correlation between a three-dimensional, stress-frozen photoelastic model and histologic specimens in a case of canine root tipping in a cat.[10] The region where tension was observed in the photoelastic model corresponded with the periodontal ligament fibers stretching in the histological material. The region where the model showed compression corresponded with compression of the periodontal ligament fibers in the histological sections. Further, the region where high fringe orders were present in the model corresponded with the region of hyalinization in the histological specimen. The homogeneous, isotropic photoelastic model in this study was observed to be a good predictor of the cellular response in the clinical situation of root tipping. In another study that investigate the effects of orthodontic intermaxillary Class lll mechanics on craniofacial structures.[11,12] A stress freezing, quasi-three-dimensional analysis revealed that Class lll elastics affected various sutures of the craniofacial complex of the photoelastic skull. It was shown that a positive relationship existed between computerized cephalometrics and photoelastic models in the analysis of ten treated cases. This study highlighted that specific changes that took place during treatment were

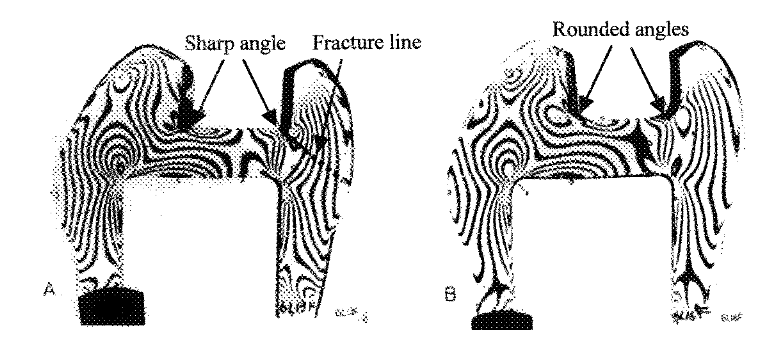
consistent with the stresses observed in the photoelastic models. These experiments revealed the effectiveness and importance of photoelasticity to predict the effects of stress in biologic systems. However, importance of sound modeling procedures was emphasized for clinically useful data from these analyses.

Photoelasticity has been applied to study how internal stresses due to biting forces are distributed within tooth and supporting bone (dento-alveolar system). This experiment showed distinct bending stress distribution in these structures during biting. However, compressive stresses produced are substantially higher than the tensile stresses. This increased distribution of compressive stresses was due to the shape of the tooth, direction of biting force, angulations of the tooth, and reactant compressive forces produced by the supporting bone. The elastic modulus gradients within the dental structures allow uniform distribution of stresses within the dento-osseous structures.[2,6]

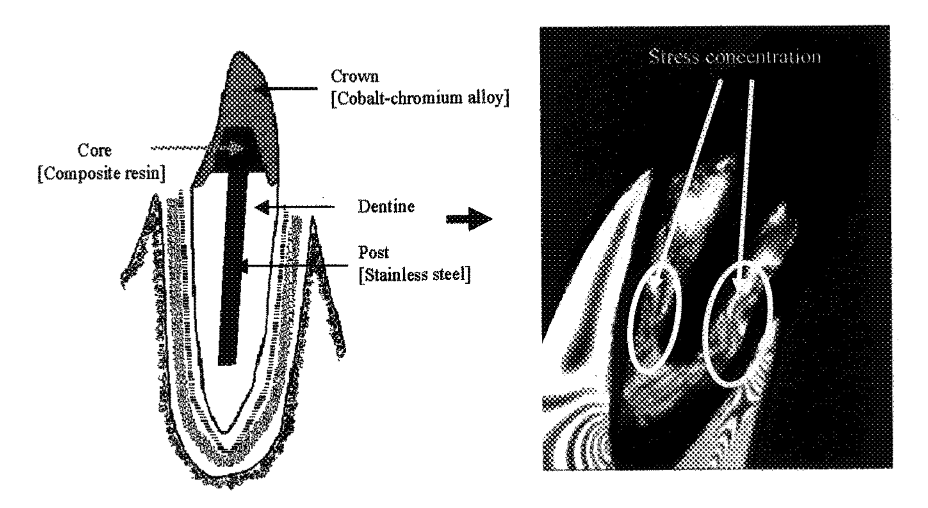
Photoelastic experiments have also been used to understand the stress distribution associated with different retainers for overdentures, archwire slot profile on orthodontic brackets, distal extension removable partial denture, full-crowns, endodontic implants and dental endosseous implants.[13-18] When the marginal design of full crown restoration was studied using photoelasticity, it was found that the change in marginal designs affected the stress distribution at the level of the gingiva or subgingiva. In addition, due to the cusp-to-fossa type of occlusion, more shearing stresses concentrated on the buccal side than the lingual side of the models. Symmetry in the shear stress distribution was observed in the mesial and distal sides. The chamfer geometry displayed minimum shear stress at the margins, followed by the chisel edge and the shoulder. When normal occlusion was attained (in the absence of premature contact), there did not seem to be a major change in the distribution of the shear stress in the tooth model, regardless of the type of marginal configuration.

Photoelastic investigations on the post-core restored teeth demonstrated regions of high tensile stresses and locations of stress concentrations that increase the risk of fracture in post-core restored teeth.[18] Some examples of the applications of photoelasticity in dentistry are shown in Fig. 7.9. Most of tthese experiments highlighted the

significance of sharp margins, stiff restorations and angulation of restorations on stress distribution. These investigations are mainly used to assess the reliability of different designs in dental restorations and devices.

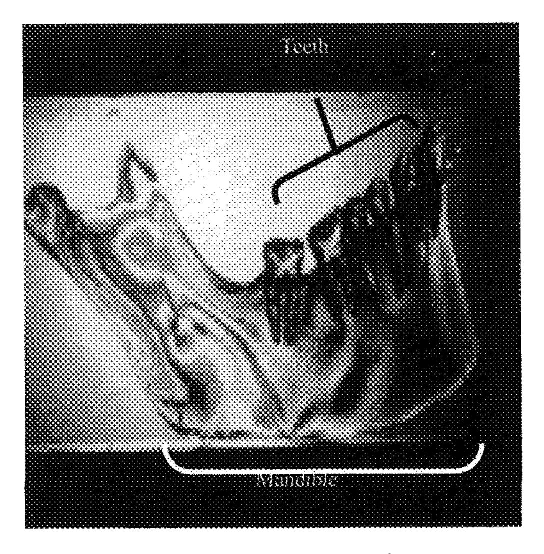


(A) Cavity with sharp angles at the base.[9] (B) Cavity with rounded angles at the base (*with permission*).[9]



(C) Schematic of a post-core restored tooth. (D) Stress distribution in post-core restored tooth.[18]

Fig. 7.9. Shows (A-F) Different applications of photoelasticity in dentistry (*with permission*).[1]



(E) Stress distribution in a mandible[1]



(F) Stress distribution by a bridge[1]

Fig. 7.9. (*Continued*)

7.3 Moiré Interferometry

7.3.1 *Introduction*

Moiré method is based on the optical phenomenon observed when two closely spaced arrays of lines (or the gratings) are superimposed. If the two arrays consist of opaque parallel lines, which are not identical in either spacing or orientation, then interference between the two arrays occurs and moiré fringes are produced. In practice, one array is placed on the surface of the test specimen (specimen grating) and a reference array (reference grating), usually of the same pitch is placed adjacent to the specimen and aligned parallel to the specimen array. As the specimen is loaded the specimen grating will deform and follow the surface displacement induced in the specimen. The reference grating does not change as the model is loaded, and as a consequence moiré interference pattern, called moiré fringes are formed when light is transmitted through the two grating (see Fig. 7.10). Moiré fringes represent points having the

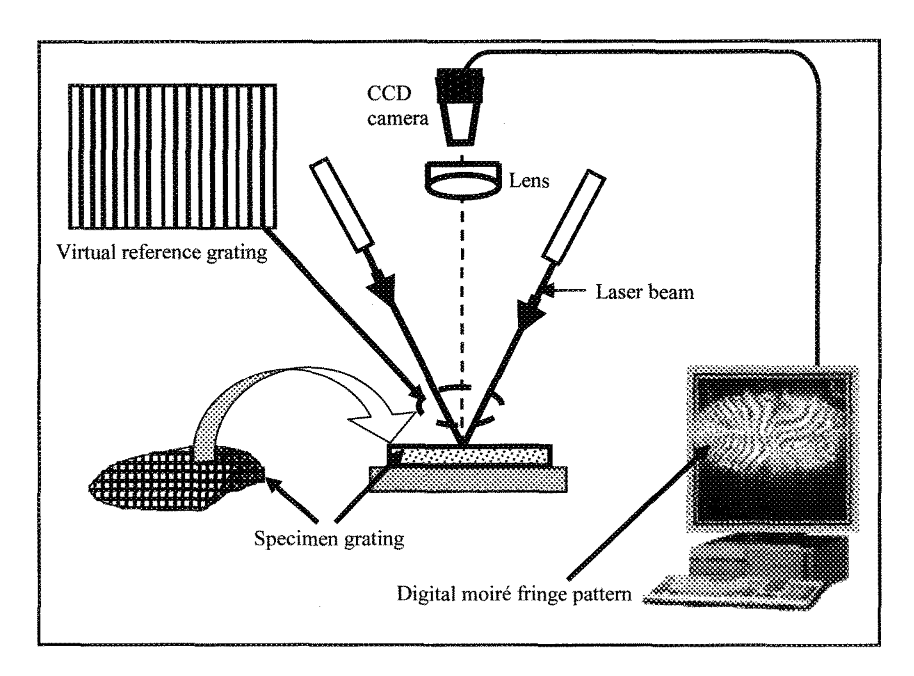


Fig. 7.10. Schematic diagram of the digital moiré interferometry arrangement.

same component of displacement in the direction perpendicular to the grid lines of the undistorted reference grating. Moiré fringes used to – determine the in-plane displacement along the x-axis is called the U-field, and the displacement along the y-axis is called the V-field. They have high spatial resolution as measurements can be made in minute zones. They are compatible to a large range of displacements, strains and strain gradients.[19] Although moiré interferometry is a sensitive technique for strain measurements in miniature specimens, to date there are only limited studies on their applications in dentistry. Detailed description on the fundamentals of this technique is presented in the Chapter 2 of this book.

7.3.2 *Specimen Grating and Moiré Interferometer*

Grating is the deformation sensing element used in moiré interferometry. The grating is routinely replicated on the surface of the specimen using certain special adhesives. Although it is easy to replicate

grating on to the surface of dry specimen, it is laborious to replicate grating on to the surface of wet specimen. Gently wiping the surface with ethanol swab can facilitate grating replication on wet specimens. A moiré interferometer usually consists of three parts. (1) the illumination system, consisting of a coherent light source, beam expander and collimator (2) the moiré interferometer, which divides the input beam into two or four separate beams and directs them onto the specimen grating, and (3) the camera system. Moiré interferometers have been designed to provide two-beam or four-beam inputs to produce virtual reference grating. Four-beam system provides the complete state of in-plane displacements and surface strains. Two-beam systems may pose difficulties in the determination of shear strains, because rotation of interferometer or specimen is required to obtain both U and V-fields precisely. Further, the displacement sensitivity in moiré interferometry is equal to the frequency f of the reference grating. The sensitivity will increase with frequency of the reference grating.[19, 20]

7. 3.3 *Applications of Moiré Technique in Dentistry*

Earlier studies in dentistry utilized moiré projections for topographic measurements. Fig. 7.11 shows moiré fringes projected on maxillary molar. Such topographic measurements were used to study the pattern of tooth wear in three-dimension. It was observed that the moiré techniques can be used to evaluate small amounts of wear that was difficult to quantify. However, this technique is not recommended when the wear pattern included greater convexity of the tooth crown or the central fossa.[21] Moiré topography provided 3D information based on the contour fringes and fringe intervals. When this technique is employed, difficulties are encountered if a surface has sharp features, while better results can be obtained on smoothly contoured faces.[22]

Biomechanical studies have used moiré interferometry to understand the mechanical and temperature change induced stresses and strains in tooth structure.[20, 23,24] In one study the cuspal deformation of tooth with a MOD (Mesio-Occluso-Distal) cavity preparation and restored with composite resins. Wang and Weiner (1998) used moiré fringes to study strain-structure relationship in enamel and dentine. They concluded that

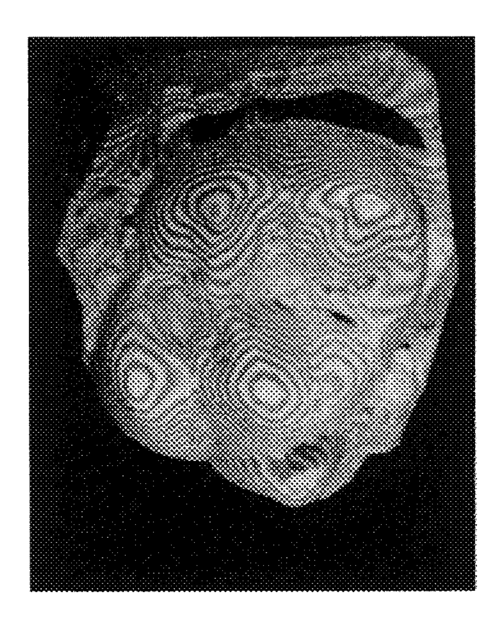


Fig. 7.11. Moiré fringes projected on a maxillary first molar. This technique is used for topographical measurements (*with permission*).[21]

the strain exhibited in the enamel is significantly lower than that in the dentine. A 200 μ thick zone in the dentine beneath the dentino-enamel junction, which experienced larger strain than the remaining bulk of the coronal dentine, was identified in this study.[25]

Moiré interferometry was used to study the effect of changes in humidity on the deformation of dentine sections, constrained and unconstrained by enamel. This study recommended moiré interferometry as a powerful tool to study the deformation of materials that are not isotropic and are not linearly elastic. Deformation patterns observed in this study indicated that the Dentino-Enamel Junction (DEJ) zone is a unique material interface that needs to be better understood in terms of normal tooth function.[26] In another moiré investigation, the role of water of hydration on the mechanical behavior of bulk dentine was evaluated. This study showed that the water of hydration influenced the stress-strain response in both axial (perpendicular to the dentinal tubules) and lateral directions (parallel to the dentinal tubules) in the dentine. The presence

of water of hydration resulted in increased deformation of dentine to applied loads, which contributed to toughness. Loss of water of hydration resulted in brittle response and strain hardening in dentine. This moiré interferometric analysis also demonstrated that free water was significant for the uniform distribution of strains within dentine structure.[23]

Moiré interferometry was also applied to study the biomechanical principles underlying the cause of Non Carious Cervical Lesions (NCCL) in teeth. Fig. 7.12 shows the U-field and V-field moiré fringe patterns formed on the tooth sections loaded at 30N. This experiment showed that the enamel and dentine displayed a unique in-plane deformation in the direction perpendicular (axial direction) and parallel to the long axis (lateral direction) of the teeth. The strains in the lateral direction within the enamel and the strains in the axial direction within the dentine concentrated with higher loads towards the cervical region adjacent to the cemento-enamel junction (CEJ) on the facial side. This study supported the hypothesis that biting forces will contribute to the loss of dental hard tissue in the cervical region.[27]

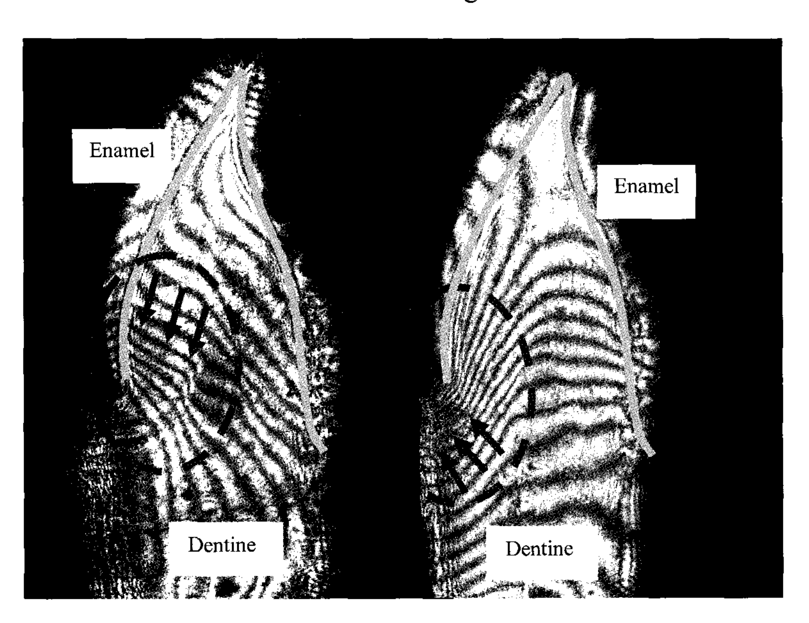


Fig. 7.12. Shows the (A) V-field and (B) U-field moiré fringe patterns conducted to study the cause of biting forces on Non-Carious Cervical Lesions (NCCL) (*with permission*).[27]

7.4 Electronic Speckle Pattern Correlation Interferometry

7.4.1 *Introduction*

Speckles are the grainy structure observed on the surface of objects illuminated by laser light. They are formed due to the random interference of coherent waves scattered from the rough object surface.[28] Speckle pattern correlation interferometry is a technique, which compares the speckle patterns at two different states of the object (deformed and undeformed) to obtain the desired displacement information. In speckle interferometry, when the surface of the specimen is displaced by means of mechanical or thermal loads, the resultant speckle pattern on the specimen surface undergoes a change. If the surface is displaced by an integral multiple of half wavelengths, the resultant speckle pattern will undergo a phase change by an integral multiple of 2π and subsequently returns to the original texture. The speckle patterns in the original and the displaced states of the specimen surface are then said to be correlated. Light will be transmitted in those parts of the image where the speckle patterns are not correlated, while no light will be transmitted in the correlated areas. This gives rise to the speckle correlation fringes. The correlation property between the original and the displaced states of the specimen will fail to exist for very large displacements. This is because of change in the entire speckle structure. A CCD camera linked to a computer is used to record the real time images. Speckle methods are used to measure surface roughness, deformations, displacement components and their derivatives.

The speckle correlation fringes compared to the true interference fringes are grainy and display poor contrast. Therefore fringe processing methods are applied to improve the quality of speckle fringes. In the Electronic Speckle correlation Pattern Interferometry (ESPI) a digital image processing system is used in conjunction with the conventional speckle interferometry arrangement. This facilitates the electronic recording of fringe patterns, which in turn enables application of opto-digital fringe processing methods to extract better information from the raw pattern. The spatial resolution of speckle method is considered

relatively low since the speckle size is typically in the range of 5 μm–100 μm. However, the speckle size can be controlled by varying the f-number of the imaging lens.[28] The advantages of ESPI techniques are: (1) they provide whole-field information of the specimen. (2) It is a non-contact technique. (3) The experimental arrangement can be configured to a particular configuration that is sensitive only to a particular displacement (in-plane or out-of-plane). (5) This technique is more versatile and robust when used in combination with digital fringe processing techniques.

7.4.2 *ESPI Experimental Arrangement*

A low power laser can be used as the coherent light source. Two output beams from a single laser source is used as the illumination ports for an in-plane sensitive system (see Fig. 7.13). While, only one output port is used as illumination port for an out-of-plane sensitive configuration (see Fig. 7.14). A CCD camera with an optimum spatial resolution is used for fringe acquisition. In an out-of-plane configuration the test specimen is mounted in a loading fixture and another similar specimen (reference specimen) is used as reference. The test and reference specimens are placed at the same distance from the beam splitter, at the same height. This aided in superimposing both the images on the CCD plane. In an in-plane setup, the two illumination ports are made to incident obliquely on the surface of the specimen. The intensities of the two beams as well as the angles subtended by the illumination and observation directions are kept equal. The illuminated specimen is imaged on the CCD plane and the real-time fringes are displayed on the monitor.

7.4.3 *Applications of ESPI Technique in Dentistry*

In one of the earlier applications, ESPI was used to study the mechanical behavior of the human mandible during mastication. In this study, a dry mandible was subjected to compressions and tensions, and the in-plane and the out-of-plane deformations were determined. This

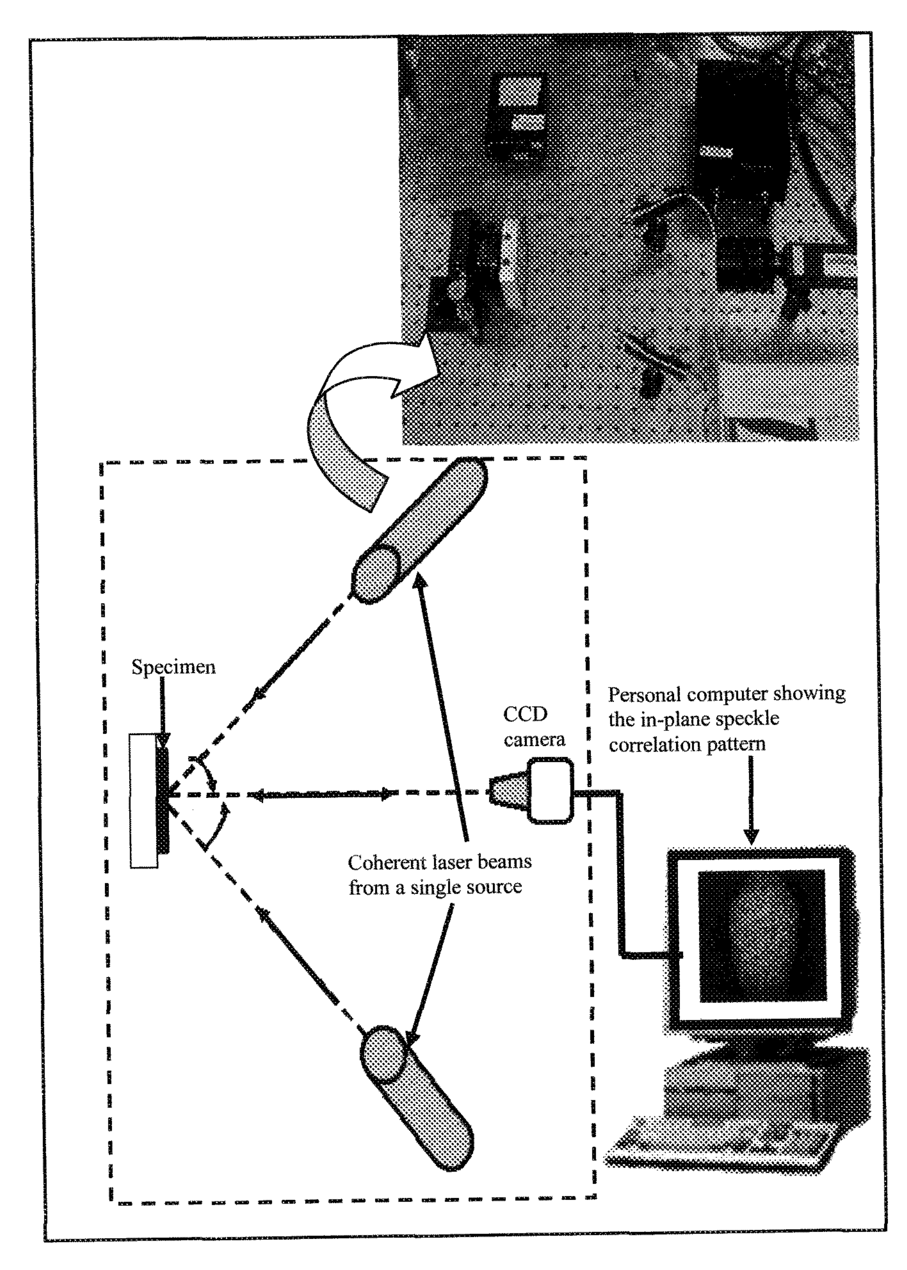


Fig. 7.13. Schematic diagram showing the in-plane ESPI arrangement.[29,30]

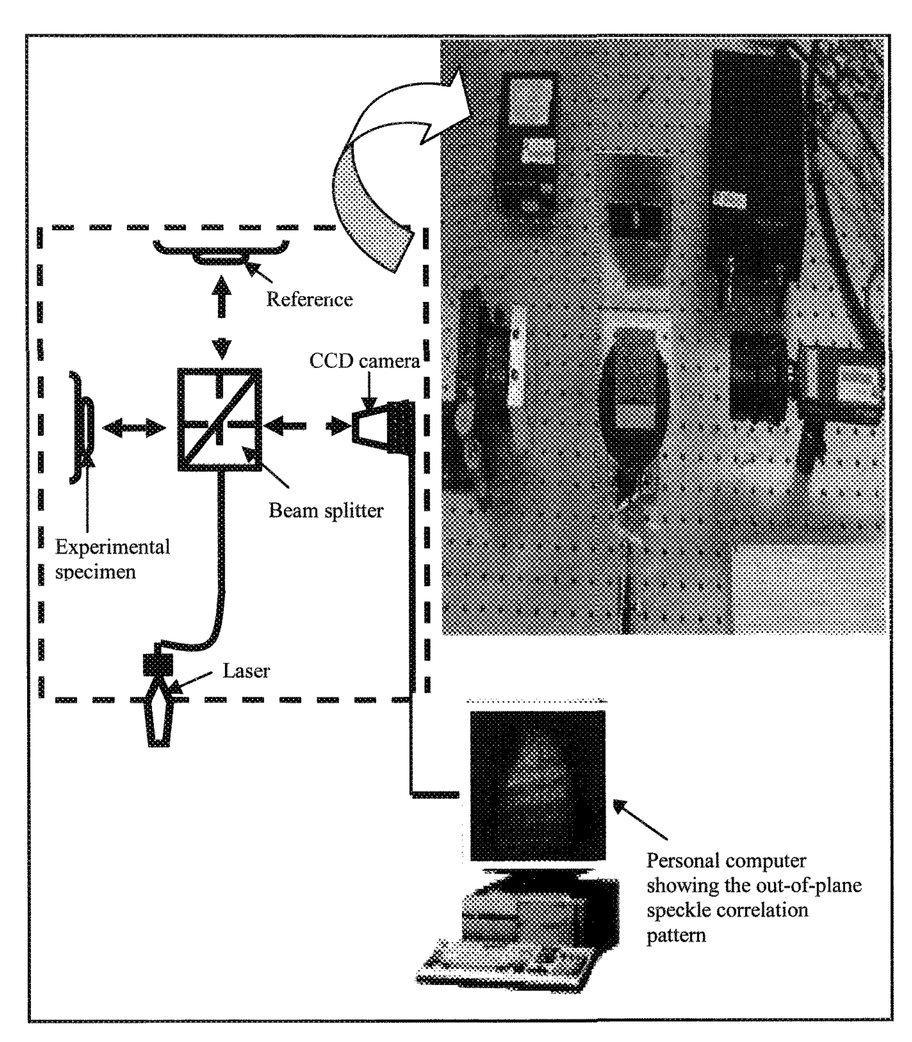


Fig. 7.14. Schematic diagram showing the out-of-plane ESPI arrangement.[29,30]

study highlighted that the capability of the mandible to bend is superior to its capability to stretch. ESPI was applied to characterize the elastic modulus of light cured dental composite resin materials. This study highlighted that ESPI may be a viable method for characterizing the elastic modulus and time-dependent effects of resin-based filling materials. ESPI was also utilized to understand the thermal response of dentine. It was shown that the dentine at the cervical region of the tooth exhibited conspicuous and distinct deformation to thermal stimulation. The out-of-plane deformations in the dentine, as shown in Fig. 7.15, progressed from the cervical region to the apical region of the dentine, while the in-plane deformations progressed from the outer surface to the inner region of the dentine.[29]

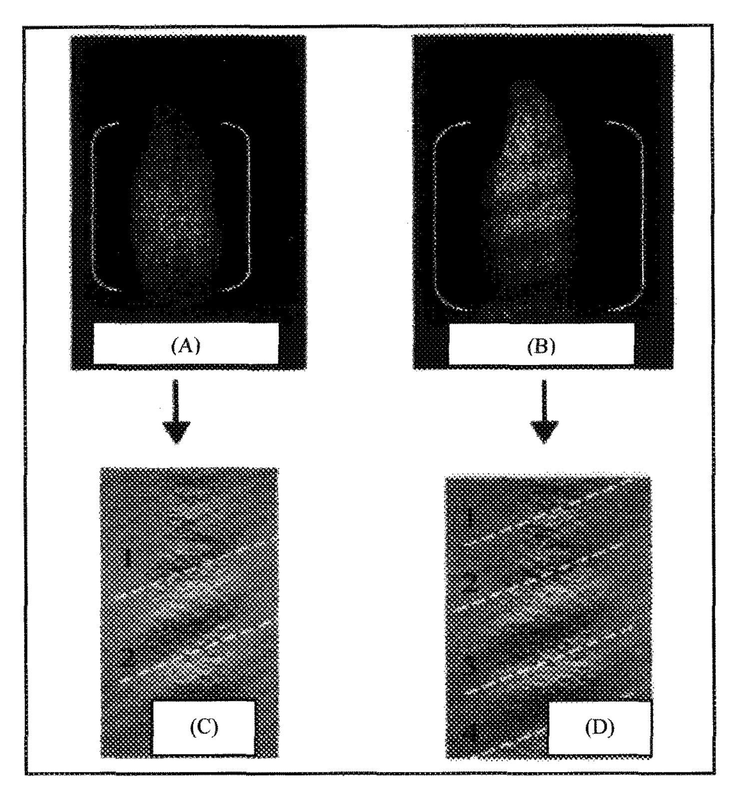


Fig. 7.15. Typical preprocessed out-of-plane ESPI fringe pattern obtained from dentine surface at (A) 40°C (B) 45°C and (C, D) the corresponding Radon transformed digital speckle patterns (*with permission*).[29]

In another study a combination of ESPI with mechanical compression testing was used to measure the strain and Young's modulus of root dentin specimens (1 x 1 x 2 mm) compressed under water. Calibration experiments in this study were conducted using aluminum, and the measurements were found to be accurate within 3% of the compression modulus reported for standard aluminum. This study displayed regional variation in the compression moduli of root dentin, and highlighted the potential of ESPI method to map deformations on irregular surfaces, and wet samples of varying sizes. This method can be valuable to study deformations on other biological and synthetic biomaterials.[31]

3D-ESPI was applied in dentistry to assess the influence of different restorative materials on the deformation of teeth in 3-dimensions. In this study MOD cavity preparations were prepared in extracted premolars and were restored with gold inlays, ceramic inlays, composite resin inlays, amalgam, or composite resin. The restorations and cusps were loaded and the deformation was assessed by a 3D-ESPI. The 3D-ESPI system illuminated tooth surface with a 512 nm argon laser to create speckle patterns on the tooth surface. A double exposure technique was used to record images of this speckle pattern before (first exposure) and during (second exposure) the application of force with a CCD video camera. The "before" and "after" video signal intensity for each speckle point was plotted to form the interferograms. In order to assess the 3D deformations and to produce 3D interferograms, all specimens were illuminated simultaneously from three directions. Switching the direction of the laser beam with a mirror system aided in producing three resultant images of the specimen with the information about the deformation. The deformation information is then separated into three orthogonal components (3D-information) by vector calculations. Figure 16 shows the 3D in-plane and out-of-plane deformation patterns obtained on a tooth specimens with a MOD composite resin inlay, loaded with 30N force. The results from this experiments showed that the deformation pattern of restored teeth was material-specific but the extent of deformation is primarily limited by the remaining tooth structure.[32]

ESPI has been applied to determine the tooth deformation in response to polymerization of five resin composites with different levels of

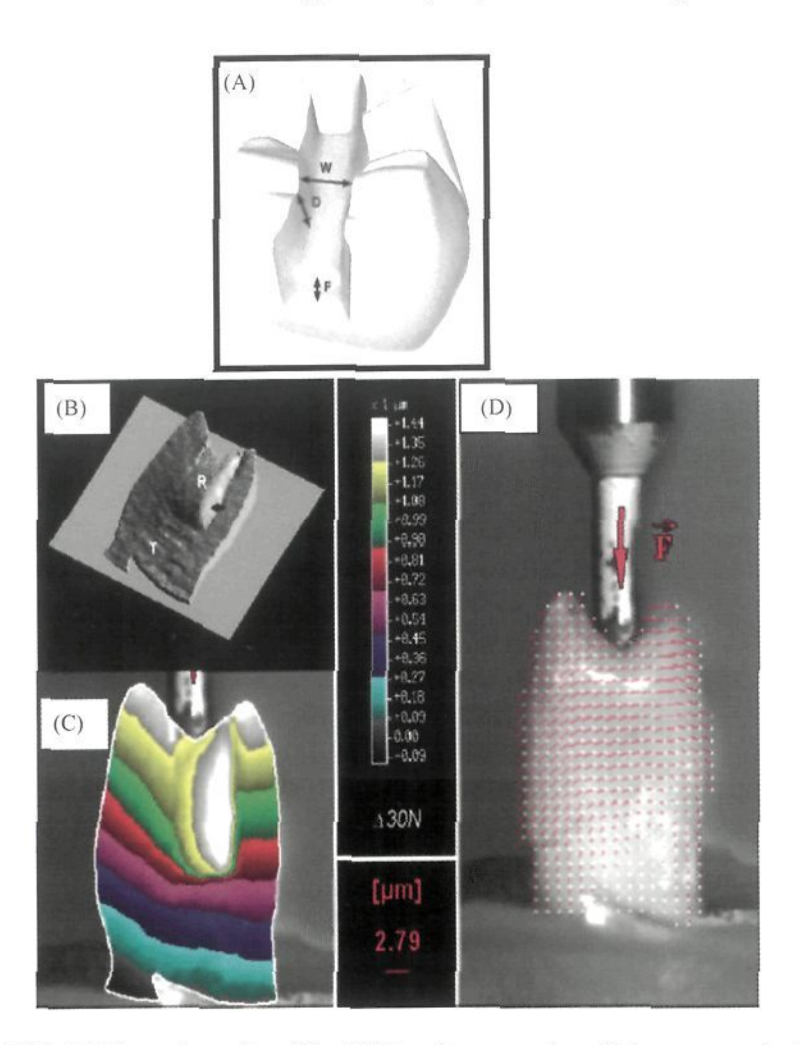


Fig. 7.16. (A) Shows the outline of the MOD cavity preparation which was restored using composite resin inlay and loaded with 30N force. The deformation pattern comprises both deformation and translation: the elastic material (composite resin) is deformed (proximal curvature—black arrow), while the complete inlay is moved within the cavity. The higher elasticity of cementing composite resin (relative to the inlay composite resin) caused the composite resin inlay to act like at rigid restoration. (B) Shows a descriptive, non-quantitative 3D out-of plane overview. (C) Shows the quantitative data of the out-of-plane deformation and (D) shows the in-plane deformation [Scale (out-of-plane) and bar (in-plane) indicate the degree of deformation (R-restoration; T-tooth)] (*with permission*).[32]

polymerization shrinkage. This work recommended ESPI as a viable method for assessing cuspal strain induced by shrinkage of bonded composite restorations. It was apparent from this study that the rate of polymerization shrinkage mediated the development of cuspal strain.[33] Zaslansky et al. reported the use of ESPI combined with a mechanical compression apparatus to measure the strain and Young's modulus of root dentin compressed under water. Their results revealed that the compression moduli of root dentin from the buccal and lingual sides of the root are quite different from the moduli of the interproximal sides. Root dentin from interproximal locations was found to have an average modulus of 21.3 GPa, which was about 40% stiffer than root dentin from the buccal and lingual locations, found to have a modulus of 15.0 GPa.[34] In a recent study the same group has applied ESPI to study the deformation of the DEJ.[35]

7.5 Concluding Remarks

This chapter has focused on photomechanical techniques such as photoelasticity, moiré interferometry and ESPI that is commonly applied in dental biomechanics. Specific advantages of applying different photomechanical techniques in dentistry, particularly in understanding biological structures have been highlighted.

References

1. A.A. Caputo, JP Standlee, Biomechanics in Clinical Dentistry. Quintessence Publishing (IL) (1987).
2. A. Asundi , A. Kishen, *J Biomed Opt.* 6, 224 (2001).
3. A. Kishen, A. Asundi, *J Biomed Opt.* 10, 034010 (2005).
4. J.W. Dally, W.F. Riley, *Experimental Stress Analysis*, 3[RD] Edition, McGraw Hill (1991).
5. R.B. Judge, J.E. Palamara, R.G. Taylor, H.M. Davies, J.G. Clement, *J Prosthet Dent.* 90, 92 (2003).
6. A. Kishen, U. Ramamurty, A. Asundi, *J Biomed Mater Res.* 51, 650 (2000).
7. A. Asundi, A. Kishen, *Arch Oral Biol.* 45, 543 (2000).
8. D.B. Mahler, F.A. Peyton, *J Dent Res.* 34, 831 (1955).
9. E.W. Johnson, C.R. Castaldi, D.J. Gau, G.P. Wysocki, *J Dent Res.* 47, 548 (1968).

10. J.F. Brodsky, A.A. Caputo, L.L. Furstman, *Am. J Orthod.* 67, 1 (1975).
11. J.A. de Alba, A.A. Caputo, S.J. Chaconas, *Angle Orthod.* 49, 21 (1979).
12. J.A. de Alba, A.A. Caputo, S.J. Chaconas, *Angle Orthod.* 49, 29 (1979).
13. C.P. Fernandes, P.O. Glantz, *Eur J Prosthodont Restor Dent.* 6, 63 (1998).
14. Y.J. Yoon, W.J. Jeong, S.H. Jang, G.W. Hwang, K.W. Kim, *Angle Orthod.* 72, 593 (2002).
15. T. Brosh, R. Pilo, D. Sudai, *J Prosthet Dent.* 79, 328 (1998).
16. G.D. Mattison, *J Prosthet Dent.* 48, 407 (1982).
17. A. Asundi, A. Kishen. *Endod Dent Traumatol.* 15, 83 (1999).
18. A. Kishen, A. Asundi. *J Biomed Opt.* 7, 262 (2002).
19. D. Post, B. Han, P. Ifju. High sensitivity moiré: Experimental analysis for mechanics and materials. New York: Springer-Verlag (1994).
20. A. Kishen, A. Asundi, *J Biomed Mater Res.* 55, 121 (2001).
21. E. Kanazawa, M. Sekikawa, T. Ozaki, *J Dent Res.* 63, 1298 (1984).
22. M.Y. Hajeer, D.T. Millett, A.F. Ayoub, J.P.Siebert, *J Orthod.* 31, 62 (2004).
23. A. Kishen, A. Asundi, *J Biomed Mater Res.* 73A, 192 (2005).
24. A. Kishen, A. Asundi, *J Biomed Opt.* 10, 034010 (2005).
25. R.Z. Wang, S. Weiner, *J Biomech.* 31, 135 (1998).
26. J.D. Wood, R. Wang, S. Weiner, D. H. Pashley, *Dent Mater.* 19, 159 (2003).
27. A. Kishen, K. B. Tan, A. Asundi, *J. Dent.* 34, 12 (2006).
28. J.C. Dainty, Laser Speckle and Related phenomena. London: Springer Verlag Series (1975).
29. A. Kishen, V.M. Murukeshan, A. Asundi, *J Dent.* 29, 531 (2001).
30. A. Kishen, V.M. Murukeshan, V. Krishnakumar, C.S. Lim, A. Asundi, *Opt Laser Eng.* 39, 489 (2003).
31. A.U. Yap, A.C. Tan, C. Quan, *Dent Mater.* 20, 377 (2004).
32. H. Lang, M. Rampado, R. Mullejans, W. H. Raab, *Lasers Surg Med.* 34, 300 (2004).
33. S. Bouillaguet, J. Gamba, J. Forchelet, I. Krejci, J.C. Wataha. *Dent Mater.* [Epub] (2005).
34. P. Zaslansky, J.D. Currey, A.A. Friesem, S. Weiner, *J Biomed Opt.* 10, 024020 (2005).
35. P. Zaslansky, A.A. Friesem, S. Weiner, *J Struct Biol.* 153, 188 (2006).

CHAPTER 8

MICRO-RAMAN SPECTROSCOPY: PRINCIPLES AND APPLICATIONS IN DENTAL RESEARCH

Paulette Spencer and Yong Wang

Department of Oral Biology, University of Missouri-Kansas City School of Dentistry, 650 E 25th St, Kansas City, MO 64108, USA
E mails: spencerp@umkc.edu; wangyo@umkc.edu

The development of tissue-engineered materials that could serve as natural tissue replacements is one of the most exciting areas of investigation in both medicine and dentistry. In the exploration of these new materials, one area that has been largely overlooked is chemical and mechanical characterization of the material/tissue interface. This is a particularly challenging area of investigation since many of the current analytical techniques do not offer the required spatial resolution to study reactions occurring at the interface or the conditions, i.e. temperature, vacuum, and so forth, under which the sample must be analyzed destroy or significantly damage/alter the biologic tissue. To address these problems, we have developed a novel technique using confocal Raman microspectroscopy to characterize and quantify reactions at tissue/tissue and material/tissue interfaces. The analysis is completed under normal atmospheric conditions and the tissue is maintained in a "wet" environment throughout the process. The purpose of this chapter is to provide an overview of the application of this technology to dental substrates and material/tissue interfaces relevant to the development of new materials for dentistry.

8.1 Introduction

Oral diseases and disorders are progressive, cumulative and become more complex over time. If current trends persist, millions of Americans

will needlessly lose teeth, endure pain and develop oral infections that can contribute to worsened chronic diseases thus, compromising their overall health and well being. Adults lose more than 164 million work hours each year due to dental disease or dental visits.[1] It is estimated that children lose more than 51 million school hours annually due to dental related illness and the pain associated with dental disease.[1]

The Health Care Financing Administration estimated that expenditures for dental treatment approached $70.3 billion in 2002.[2] Most of this money was spent repairing teeth and periodontal (gum) tissues. In general dentistry practices, nearly 75% of the dentist's time and effort is devoted to replacing fillings that fail prematurely.[3] The increased need for replacement of these failed fillings requires additional visit(s) to the dentist taking time away from other activities, leads to the loss of additional healthy tooth structure, and involves additional cost to the individual.

The development of durable biomaterials that can be used to replace oral or skeletal tissues lost because of age, cancer or trauma is a major area of emphasis for future biomedical research. Major aspects of research for orthopedic and dental diseases are devoted to new approaches for tissue regeneration and the identification of suitable biomaterials for hard tissue replacement. The demand in the United States for suitable materials that can be used as biological substitutes to restore and improve tissue function is staggering. For example, it is estimated that these materials will be used in millions of dental-oral-craniofacial procedures, ranging from tooth restorations to major reconstruction of facial hard and soft tissues. Although these procedures have improved the quality of life for many patients, the clinical lifetime of these synthetic replacement materials is often less than one-tenth that of the original tissue.

8.2 Breakdown of Composite Repair/Replacement Materials

The emphasis on replacement therapy in general dentistry practices is only expected to grow as the public's concern about mercury release from dental amalgam and environmental issues associated with discharge

of mercury into the waste water, forces dentists to select alternative restorative materials, such as composite resin. The failure rate for large to moderate posterior composite restorations can be 2–3 times that of high copper amalgam.[4] After 10 years, 86% of Class I and II composite resin restorations placed in young adult patients had failed [5]. Based on the poor performance of these materials, previous authors have concluded that extended moderate to large class II composite restorations must be regarded as a clinical compromise.[6]

The reduced clinical lifetime of moderate to large composite restorations can be particularly detrimental for our patients because removal of these restorations can lead to extensive loss of sound tooth structure. As an example, in comparison to the removal of amalgam, the removal of tooth-colored restorations produced significantly greater increases in cavity volume.[7] The increase in cavity volume and increased frequency of replacement means that significantly greater amounts of tooth structure will be lost. Over the lifetime of the patient, the additional loss of tooth structure with treatment and re-treatment of these intracoronal composite fillings will translate to the need for enlarged and more complex restorations. The reduced longevity, increased frequency of replacement and the need for a more complex restoration means increased cost to the patient in terms of both time and money.[8]

8.3 Material/Tissue Interface

The premature failure of materials such as composite restorations that are used to repair and replace damaged tissues in the mouth can be traced to breakdown of the bond or seal formed at the interface between the synthetic material and tooth surface.[4,9,10] and increased levels of the cariogenic bacteria, Streptococcus mutans, at the perimeter of these materials.[11,12] Acid-etching provides effective mechanical bonding between the composite restoration and treated enamel, but a breakdown at the dentin surface continues to threaten the long-term viability of large posterior composite restorations.[10,11,13] For example, at 9.6 years 30% of the Class II composites in one clinical study had failed and half of these failures were due to recurrent caries at the gingival margin [10]. Generally

there is very little enamel available for bonding at this site and thus, the integrity of the gingival margin depends on the bond formed with dentin.[14] Previous investigators have reported that under clinical conditions one can frequently detect a separation between the composite material and the tooth surface at the gingival margin.[13] These gaps have been related to dentin bonding that is both technique-sensitive and unreliable.[13,14]

The material/tooth interface is the most active part and in many cases, the most complex aspect of the treatment area. The molecular structure and micro-mechanical properties of this area have been largely overlooked during the development of new restorative dental materials. One reason that this area has been neglected is because chemical and mechanical characterization of the interface components in situ is a particularly challenging problem. For example, many of the current analytical techniques do not offer the required spatial resolution to study reactions occurring at the interface or the conditions (i.e., temperature, vacuum, etc.) under which the sample must be analyzed, destroy or significantly damage/alter the biologic tissue. To address these problems, we have developed a novel technique using confocal Raman microspectroscopy to characterize and quantify reactions at the material/tissue interface. The analysis is completed under normal atmospheric conditions and the tissue is maintained in a "wet" environment throughout the process.

This chapter will discuss the application of Raman microspectroscopy in the characterization of dental substrates and material/tissue interfaces. The chapter begins with a brief introduction to the theory of Raman spectroscopy. The remainder of the chapter is devoted to an overview of the use of this technology in the study of reactions at tissue/tissue and material/tissue interfaces relevant to the development of new materials for dentistry.

8.4 Brief Introduction to Raman Spectroscopy

Infrared and Raman spectroscopy are not identical but rather complementary techniques for obtaining information about the structure

and properties of molecules from their vibrational transitions. The data from these techniques arise from two different physical effects on the molecule. Infrared absorption represents a one-photon event and infrared spectra portray vibrational motions that produce a change in the permanent dipole moment of the molecule. In contrast, Raman scattering is a two-photon event and Raman spectra reflect vibrational motions that cause a change in a source-induced molecular dipole moment. Infrared spectroscopy is a measurement of a simple absorption process while Raman spectroscopy is the measurement of the re-emission of the incident source energy.[15-19]

In the broadest sense, the Raman effect involves the scattering of light as a result of its interaction with matter. Monochromatic light from a laser strikes a sample and almost all of the light is scattered elastically, i.e., there is no change in energy or frequency of the incident light. This is known as Rayleigh scattering and is the strongest component of the scattered radiation. By comparison, the Raman effect can be regarded as an inelastic collision between the incident photon and the molecule. As a result of the inelastic collision the vibrational or rotational energy of the molecule is changed by an amount ΔE_m. In order for energy to be conserved, the energy of the scattered photon, $h\nu_s$ must be different from the energy of the incident photon $h\nu_i$ by an amount equal to ΔE_m. If the molecule gains vibrational energy, then ΔE_m is positive and ν_s is smaller than ν_i. The scattering is called Stokes Raman. If the molecule loses energy, then ΔE_m is negative, ν_s is larger than ν_i. and this process gives rise to anti-Stokes lines in the Raman spectrum. The Stokes lines are of higher intensity than the anti-Stokes lines due to the Boltzmann distribution, i.e., due to the higher population of molecules in the ground vibrational state as compared to those in the excited state at room temperature. Detailed explanations of Raman spectroscopy and its application in a variety of areas are provided in references 15–19.

To summarize, the scattered photon in Raman scattering has a frequency either higher or lower than the incident photon. The photon frequency difference is the same as the molecular vibrational frequency. The Raman spectrum represents the intensity of the scattered photons as a function of the difference in frequency. The particular molecule and its

environment will determine what Raman signals will be observed. Thus, information about the composition, secondary structure and interaction of molecules, including the chemical micro-environment of molecular subgroups, can be determined through careful analysis of the positions of the Raman spectral features.

The Raman spectrum is similar to an infrared spectrum in that it provides a "fingerprint" of the molecules present within the sample and can be used for qualitative identification and quantitative determination.[18,19] However, unlike infrared spectroscopy water does not present a strong Raman signal within the biological "fingerprint" region. Thus, specific functional groups of molecules can be identified in wet biological specimens with minor spectral interference from water. Additional differences between the two techniques are related to sample preparation. For example, a limitation of infrared spectroscopy in transmission mode is the requirement for a finite thickness of the sample to control the absorption intensity of the molecular vibrations. Hygroscopic infrared transmitting materials must be used for many of the sample handling applications because a majority of the infrared wavelengths are obscured by glass or quartz windows. In contrast, Raman has no restriction with respect to sample size, shape or thickness and glass or quartz is a suitable sample containment material for Raman samples.

By combining spectroscopy with microscopy, Raman microspectroscopy can be used to detect and quantify the molecular chemistry of microscopic samples; molecular information can be obtained at a spatial resolution comparable to optical microscopy. In this technique, the spatial resolution is defined by the laser profile used to excite a particular part of the specimen. Functional groups are identified by their specific wavenumber position in the Raman spectrum, and the relative amounts of these groups are determined by the magnitude of intensity at each wavenumber. Samples can be analyzed directly, in air or water, at room temperature and pressure, wet or dry, without destroying the sample. The capability of performing spatially resolved chemical analyses of microscopic regions of samples in situ has been applied to both material science and the biological sciences. Raman

microspectroscopy is an exceptional tool for investigating the chemistry of material/tissue interfaces, because it does not rely on homogenization, extraction or dilution, but rather each structure is analyzed *in situ*.

8.5 Applications of Micro-Raman Spectroscopy in Dental Research

We use the Raman microspectroscopic results in conjunction with micro-mechanical and morphologic analyses to explain the fundamental phenomena controlling reactions at the interface between biologic tissues and synthetic materials. The knowledge gained from these analyses is applied to the development of new materials and techniques for craniofacial and dental applications. For example, we have used Raman microscopy to determine for the first time the molecular structure of acid-etched smear layers[20] and smear debris[21], to quantify the diffusion of single-bottle adhesives into the "wet" demineralized dentin matrix,[22-25] to quantitate demineralization in hydrated dentin specimens [20,21] and to determine the molecular structure at the material/tissue interface in Class II composite restorations.[25,26]

8.5.1 *Characterization of the Smear Layer*

The bond at the tooth surface/composite material interface actually involves two distinctly different substrates, i.e., dentin and enamel. The composition of the enamel is approximately 98% mineral and 2% protein while the dentin is 50% mineral, 30% protein and 20% water by volume.[27] Acid-etching provides effective mechanical bonding between the composite restoration and treated enamel, but there is substantial evidence that the bond at the dentin surface experiences premature degradation.[10,11,28] Breakdown of the bond at the tooth surface/composite material interface has thus, been linked directly to the failure of our current materials to consistently seal and adhere to the dentin.[29]

In our efforts to identify those factors that promote the formation of an ideal bond at the adhesive/dentin interface, one element that has been largely overlooked is the smear layer. Based on morphologic studies, it is commonly reported that acid pre-treatment regimens remove the smear

layer but to date, there has been no chemical evidence to support these findings. The purpose of this in vitro study was to determine at the molecular level the composition of acid-etched smear layers formed using carbide and diamond burs.

8.5.1.1 *Materials and Methods*

Specimen Preparation: Extracted unerupted human third molars stored at 4°C in 0.9% w/v NaCl containing 0.002% sodium azide were used to prepare the demineralized dentin collagen. The teeth were collected after the patient's informed consent was obtained under a protocol approved by the UMKC adult health sciences institutional review board. Multiple cubes of dentin, approximately 2 x 2 x 2 mm, were demineralized for 7 days at 25°C in 0.5M EDTA (pH 7.3). Complete demineralization was determined by the absence of Raman spectral features associated with the mineral component.

Smear Layers: The occlusal one-third of the crown was removed from twelve extracted unerupted human third molars. Smear layers were created by abrading the dentin with either a 557 carbide or medium-grit diamond bur in a high-speed handpiece under copious air-water spray. The smear layers were created by a single experienced dentist.

Using a water-cooled low-speed diamond saw, specimens were sectioned perpendicular and parallel to the smeared surface. The resultant 10 x 2 x 2 mm beams were submersed in liquid nitrogen and immediately fractured perpendicular to the smeared surface using a sharp chisel and mallet. The smeared surfaces were treated for 15 seconds with 35% phosphoric acid gel (3M Dental Products Corp., St. Paul, MN, USA) or 4 h with 0.5M EDTA. The treated samples were rinsed thoroughly with water, immediately attached to the floor of a petri dish and covered with water for spectroscopic analysis. The fracture technique separated the specimen such that the smeared surface/demineralized dentin/undisturbed dentin interfaces could be directly imaged with the 60x water immersion lens that is an integral part of the confocal micro-Raman spectrometer used in this study.

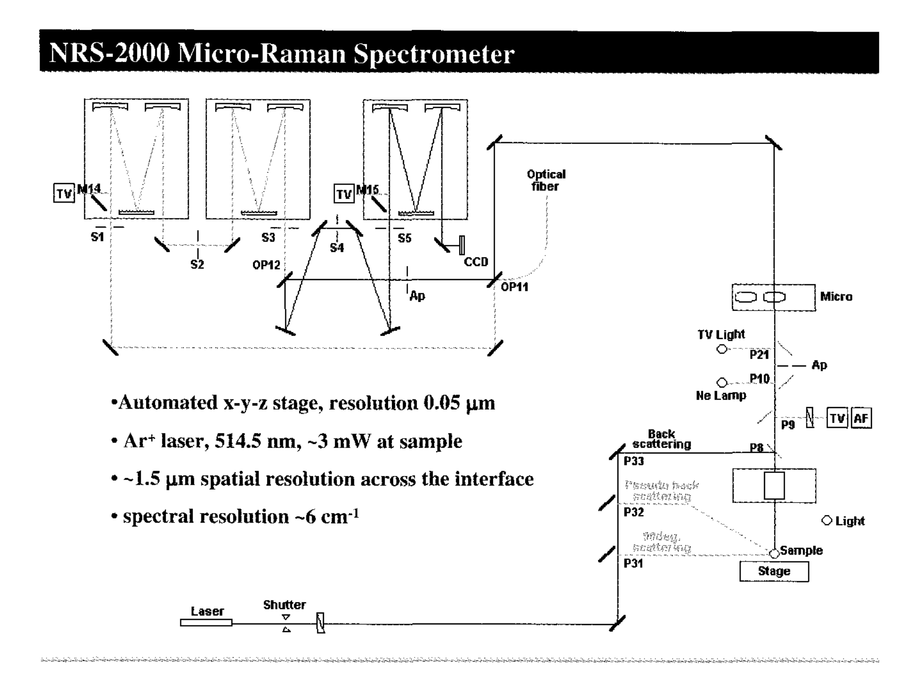


Fig. 8.1. Schematic representation of the micro-Raman spectrometer setup.

The micro-Raman spectra were recorded with a Jasco NRS 2000 Raman spectrometer equipped with Olympus lenses and a liquid nitrogen-cooled CCD detector (See Fig. 8.1). The excitation source was an Argon laser, operating at 514.5 nm. After passing through the bandpass filter and condensing optics, ~3 mW of laser energy was incident upon the sample. The laser beam was focused through a X60 Olympus Plan Neofluar water-immersion objective (NA 1.2); the focus of the laser beam in combination with a 25 μm confocal aperture provided a spatial resolution of ~1.5 μm. For the fracture specimens, Raman spectra were acquired at positions corresponding to 1.0 μm intervals across the smeared surface/demineralized dentin/undisturbed dentin interfaces using the computer controlled x-y-z stage with a minimum step width of 50 nm. Raman spectra of the completely demineralized dentin samples as well as the EDTA-treated samples were collected with the laser focused perpendicular to the surface of the

specimen. Spectra were obtained at a resolution of ~8 cm^{-1} over the spectral region of 875–1785 cm^{-1} and with an integration time of 120 seconds. The spectral feature at 1453 cm^{-1} (CH_2 deformation) associated with the collagen was used as an internal standard in the quantitative evaluation of the demineralized dentin spectra.

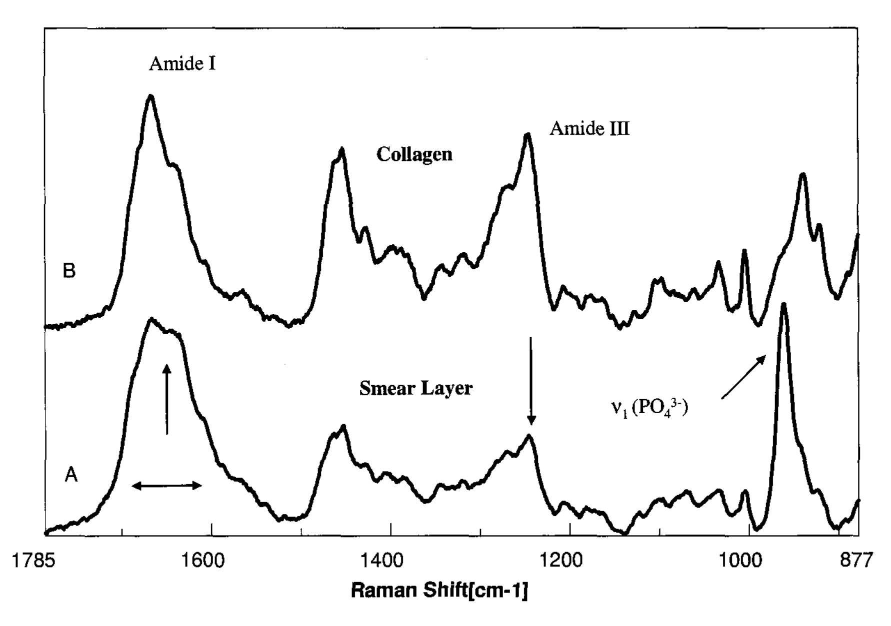


Fig. 8.2. Raman spectra of the acid-etched carbide-bur-created smear layer (A); and demineralized dentin with features associated with the collagen (B).

8.5.1.2 *Results and Discussion*

In the Raman spectrum of the acid-etched carbide bur smear layer (See Fig. 8.2 (A)), the most intense peak at 960 cm^{-1} (P-O symmetric stretch) is associated with the mineral component. Complete demineralization is indicated by the absence of this feature in the spectrum of the demineralized dentin collagen (See Fig. 8.2 (B)). In comparing the spectra of the carbide bur smear layer and the completely demineralized dentin, the spectral features associated with amide I and III are broadened and exhibit a loss of fine structure in the smear layer (See Fig. 8.2 (A)). The relative intensity of the Amide III is reduced and

contribution from the C-C stretch (935 cm^{-1}) is diminished, i.e., this feature appears as a small shoulder on the peak at 960 cm^{-1} in the spectrum of the acid-etched carbide bur smear layer.

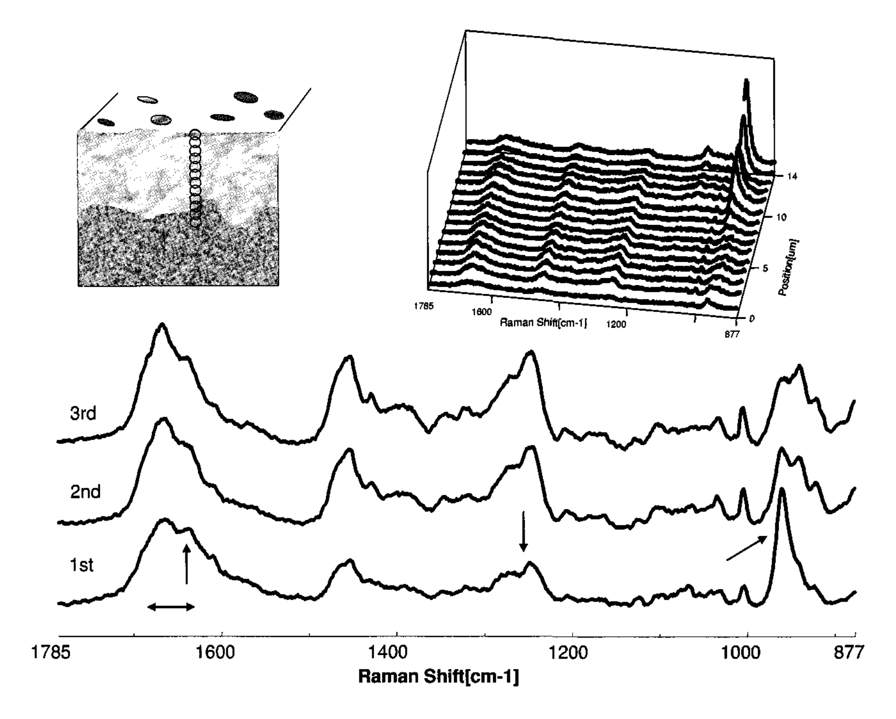


Fig. 8.3. Raman map of dentin specimen fractured to provide cross-sectional view of the acid-etched carbide-bur-created smear layer/demineralized dentin/undisturbed dentin. Spectra acquired at 1-μm intervals beginning at the acid-etched carbide-bur-created smear layer, extending into the demineralized dentin and finally, into the undisturbed dentin.

Using acid-etched smear layer-covered dentin specimens that had been fractured to provide a cross-sectional view of the smear layer/demineralized/undisturbed dentin interface, multiple micro-Raman spectra were obtained in 1 μm steps beginning at the smear layer and extending about 15 μm distant to the smear layer (See Fig. 8.3). In the micro-Raman map of the acid-etched carbide bur smear layer (See Fig. 8.3), the second and third spectra show a relative increase in the

intensity of the features associated with the organic component and a concomitant decrease in the mineral. The regions associated with the amide I and III in the second and third spectra (See Fig. 8.3) have regained much of the detail that was apparent in the spectrum of the demineralized dentin collagen (See Fig. 8.2 (B)). In comparison, in the first through third spectra of the acid-etched diamond bur smear layer (See Fig. 8.4) there is distinct contribution from the spectral feature associated with the mineral component (960 cm^{-1}). The relative intensity of the amide III is significantly reduced in the first spectrum of the acid-etched diamond bur-created smear layer (See Fig. 8.4). The C-C stretch (935 cm^{-1}) associated with the organic component is not observed in the first through third spectra of this figure, but this may be attributed in part to overlap from the intense mineral peak (960 cm^{-1}).

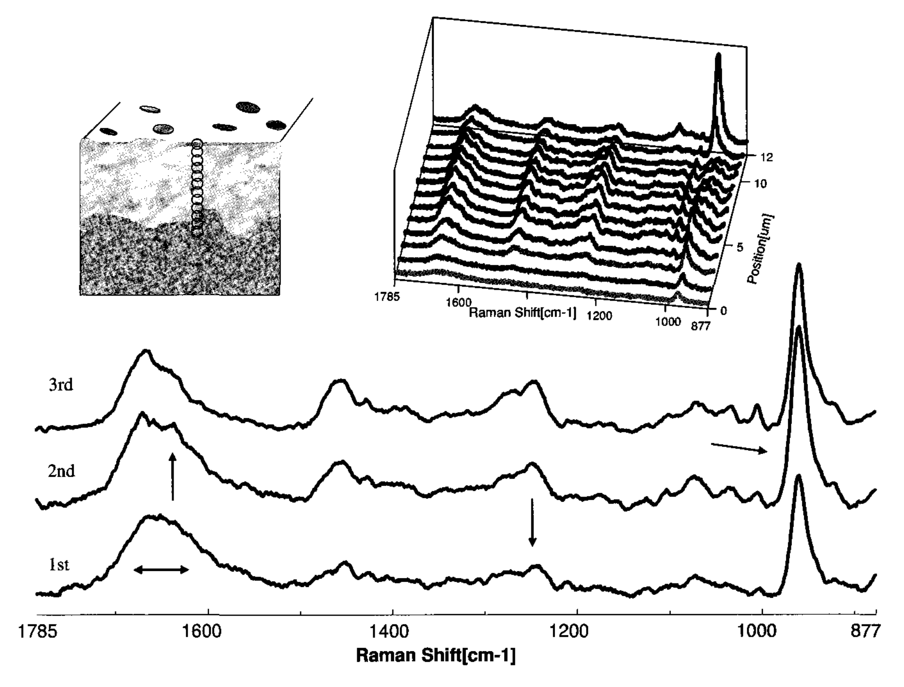


Fig. 8.4. Raman map of the molecular structure of the acid-etched diamond-bur-created smear layer and subjacent demineralized/undisturbed dentin. Spectra acquired at 1-μm intervals beginning at the acid-etched diamond-bur-created smear layer and continuing into the undisturbed dentin.

The degree of demineralization, as a function of spatial position (See Fig. 8.5), was determined from the ratios of the relative intensities of spectral features associated with the mineral (P-O symmetric stretch) and collagen (CH_2 deformation). There is mineral in the superficial layer of both the acid-etched carbide and diamond bur-created smear layers. The mineral contribution persists through several microns of the acid-etched diamond smear layer (See Fig. 8.5). For three types of smear layers, the mineral content decreases as a function of spatial position from the smear to the completely demineralized dentin. Analysis of the interface from complete to partially demineralized dentin shows a gradual change in the relative intensity of the P-O group in the acid-etched carbide bur-created smear layers. In comparison, there is an abrupt change in the relative intensity of this feature in the acid-etched smear layers formed with the diamond bur (See Fig. 8.5).

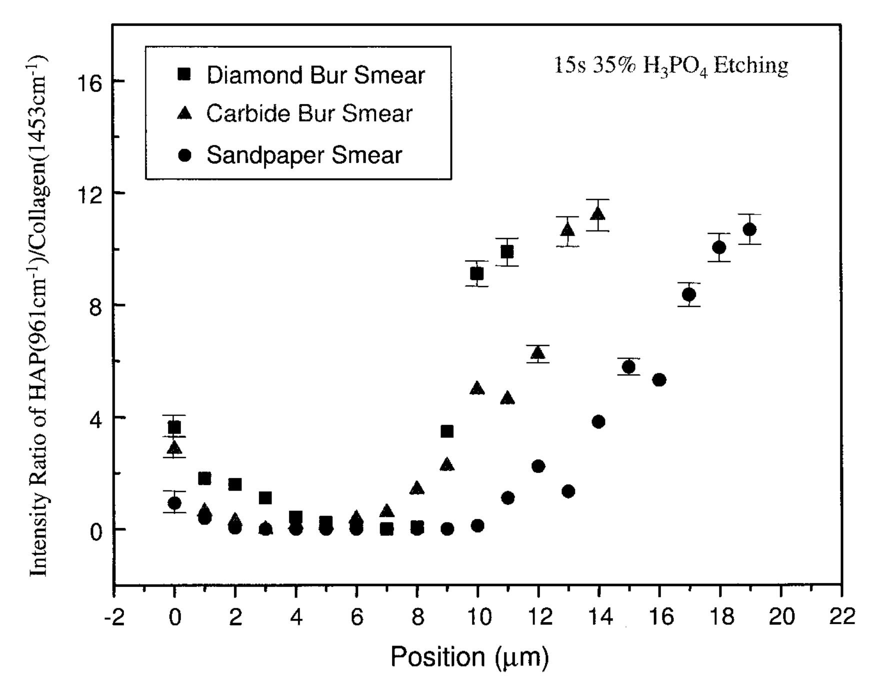


Fig. 8.5. Effect of smear layer type on degree of demineralization produced by H3PO4 gel etching for 15s. The profile of demineralization of dentin is dramatically different.

There are no spectral features associated with the mineral component in the Raman spectra of carbide and diamond bur smear layers treated with O.5M EDTA for 4 h (See Fig. 8.6A and B, respectively). Amide I and III appear broadened (See Fig. 8.6A and B), but the ratio of the relative intensities of these groups is similar to the ratio recorded with the demineralized dentin collagen (See Fig. 8.2).

Numerous studies have suggested that acids, such as phosphoric, remove the smear layer and increase the porosity of the underlying dentin substrate. With few exceptions, these studies largely disregarded the collagen remnants of the smear or overlooked the inability of acid to act as a solvent for collagen.[30,31] This oversight may be attributed in part to the microscopic nature of the smear layer and lack of resolution of many of the techniques used to study dentin demineralization.[30] The conclusions that acid removes the smear layer are based primarily on morphologic evidence of open dentin tubules, but these observations largely reflect the effect of the acid-etchant on smear plugs overlying the tubules.

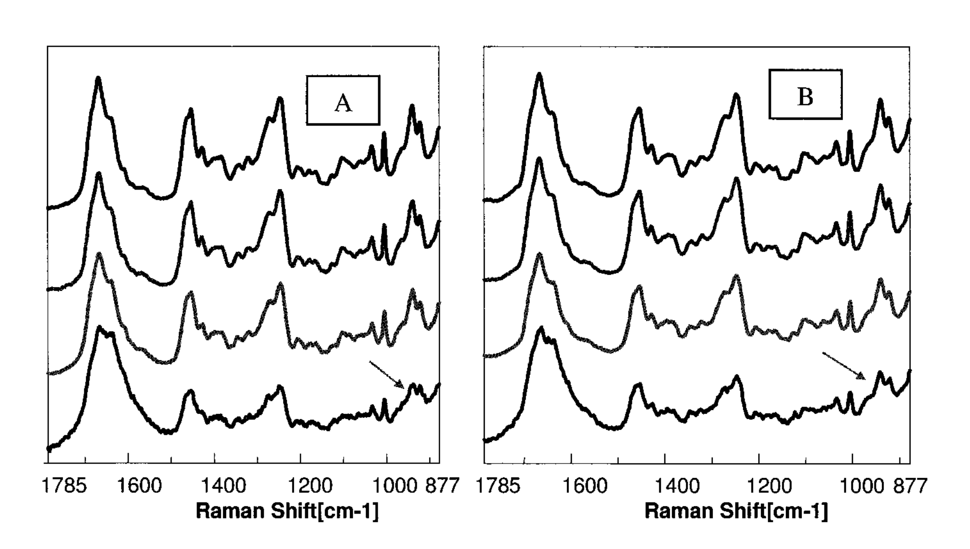


Fig. 8.6. Carbide (A) and diamond (B) bur smear layers treated by 0.5 M EDTA for 4 hrs.

Confocal Raman microspectroscopy was used to characterize the chemical nature and structural changes of the constituents of the smear layer before and after acid-etching. Raman spectroscopy permits structural analysis of samples by identifying specific light-induced molecular vibrations. Characteristic functional groups give rise to vibrational bands near the same frequency irrespective of the molecule in which they are found. Information about the composition, secondary structure and interaction of molecules, including the chemical micro-environment of molecular subgroups, can be determined through careful analysis of the positions, intensities and widths of the bands in the Raman spectra of biological tissues such as collagen.

A distinct advantage of the micro-Raman spectroscopic technique described in this study is the ability to record spectral data from samples that are wet throughout the analysis. Collecting spectral data from the demineralized dentin under wet conditions reduces the potential for collagen collapse as a result of desiccation. Environmental SEM has been used to image wet demineralized dentin specimens, but image resolution was unsatisfactory.[32] Although the surface of interest is imaged in the micro-Raman spectroscopic technique, image resolution does not interfere with the collection of data exhibiting an adequate signal/noise ratio. Finally, unlike infrared spectroscopy, water does not present a strong Raman signal within the biological fingerprint region thus, compound specific molecules can be identified in hydrated dentin samples without processing the data to remove spectral interferences from water.[33]

Raman spectroscopy is sensitive to the backbone conformation or secondary structure of proteins. Thus, it can provide critical data on triple helix to random coil transitions that may occur in dentin collagen as a result of heat, acid or other degrading reagents. In the Raman spectra of collagen, bands associated with amide I and III are particularly sensitive to conformational changes in the triple helix.[34] The micro-Raman spectral data indicate that 15 seconds acid-etching with 35% phosphoric acid gel demineralized dentin to a depth of ~10 μm (See Fig. 8.5). This work represents the first study to quantitate dentin demineralization

under conditions that permit hydration of the specimen throughout the analysis. Hydration is critical to these efforts since it is widely accepted that the collagen within the demineralized dentin will collapse if it is allowed to dry,[35] such collapse would lead to inaccurate characterization of the extent or degree of dentin demineralization.

The spectral results indicate that collagen within the smear layer is disorganized but not denatured. This disorganized collagen is denatured by the 15 seconds acid-treatment used in this study. The results provide clear evidence that the collagen of the smear layer is not removed by acid-etching and residual mineral is trapped in the denatured, gelatinized collagen.[20] Ultimately, this gelatinous layer could inhibit the formation of an impervious seal at the adhesive/dentin interface, i.e., it could act as a weak link in the coupling of adhesive to dentin.

8.5.2 *Characterization of Smear Debris*

After acid etching and rinsing, smear plugs have been removed from dentinal tubules and the surface of the intertubular dentin appears free of solid deposits and relatively smooth with a gelatinous quality. These features are commonly observed in SEM images of acid-etched dentin and based on this appearance, it has been concluded that smear layers can be easily removed by acids or chelating agents.[36-39] Some authors even concluded that the ratio of open tubules/total dentinal surface area could provide a quantitative evaluation of smear layer removal.[40] One factor that was potentially overlooked in these morphological investigations is that much of the detail associated with the intertubular area of the acid-etched dentin surface is actually hidden by the smooth surface. Critical detailed information about the structure of this area is obscured; the effect of acid on the organic and inorganic components of the smear layer covering the intertubular dentin cannot be disclosed using this technique.

We determined at the molecular level, the composition of the smear layer and smear debris formed with 600 grit silicon carbide sandpaper

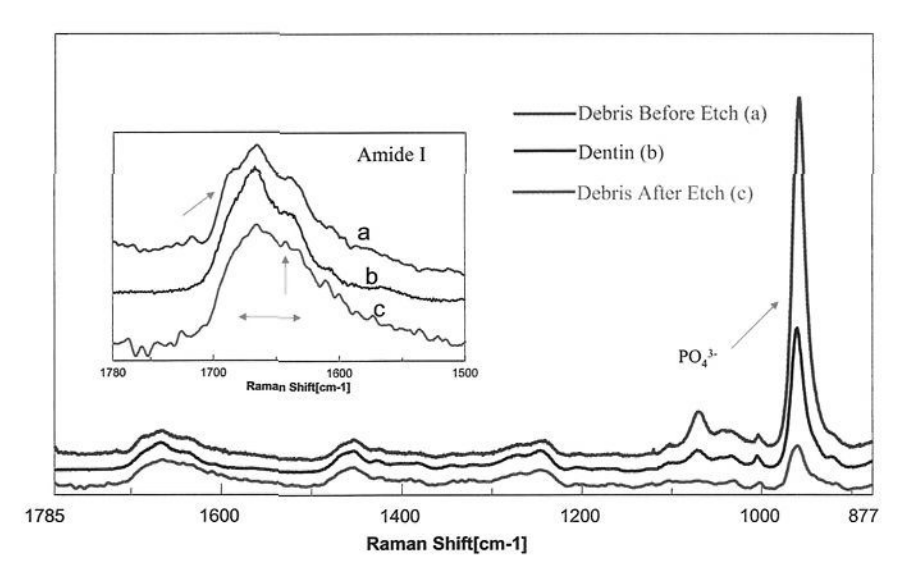


Fig. 8.7. Comparison of Raman spectra obtained from (a) smear debris on sandpaper before 60 s of 35% H3PO4 etching, (b) bulk dentin, and (c) and smear debris on sandpaper after 60 s of 35% H3PO4 etching.

and abrasive quality is commonly used to create smear layers on dentin that is prepared for conventional bond strength testing.) The use of smear debris collected on sandpaper and the confocal Raman microspectroscopic technique allowed us to study the effect of acid on the dentin smear layer in great detail.[21] By using smear debris, we performed a detailed Raman analysis of the chemical nature of the debris before and after acid treatment (See Fig. 8.7). The mineral content in the smear debris decreased dramatically after acid-treatment, but the mineral content did not disappear even after 60s exposure to 35% H_3PO_4 (See Fig. 8.7). These results suggest that the mineral is not accessible to the acid. The mineral is apparently trapped within the matrix created by the organic components of the smear debris.

The collagen in the smear debris has been disturbed/disorganized; following acid-treatment this disorganized collagen spectroscopically

resembles gelatin. Based on these results, it is concluded that the disorganized collagen in the smear debris is denatured by the acid treatment, while the mineral is trapped within this gelatinous matrix and is shielded from the acid. Ultimately, this gelatinous layer could inhibit the formation of an impervious seal at the adhesive/dentin interface; it could act as a weak link in the coupling of adhesive to dentin.

Acids with a high reactivity rate with the mineral component of dentin have been considered a good reagent for removing the smear layer. These evaluations were based largely on SEM micrographs of acid-etched dentin which portrayed a smooth dentin surface, free of solid deposits and open tubules. The Raman results from our study showed that the collagen component was not dissolved and only a portion of the mineral in the smear debris was dissolved in the acids.[21] Presumably, after acid etching, the dissociated organic debris in the smear layer and the smear plugs on the top of dentin could be rinsed off, however, the mineral trapped within the gelatinized collagen and/or the disorganized/denatured collagen in contact with the substrate could not be so easily removed. The results from the in situ micro-Raman mapping of the smear layer/demineralized/mineralized dentin interfaces support these suggestions, i.e., spectral features associated with both the mineral component and denatured collagen were observed in the acid-etched smear layer; these results are consistent with our observations on the acid-treated smear debris. Similar phenomena were also recorded in acid-etched dentin covered with smear layers created with dental burs.[20]

8.5.3 *Quantifying Reactions at the Adhesive/Dentin Interface*

A key factor in the long-term clinical success of composite repairs completed on posterior and anterior teeth is successful attachment or bonding of the material to the tooth surface. Breakdown of the composite/tooth bond leads to the formation of gaps at the material/tooth interface; the gaps act as a conduit for penetration of bacterial enzymes, bacteria, fluids, and ions. This exchange of fluids and bacteria at the interface is commonly referred to as microleakage and is recognized as a major factor contributing to hypersensitivity[28] as well as secondary caries.[11] Results from clinical studies have suggested that the durability

of composite restorations depends on the quality of the bond formed at the adhesive/dentin interface.

Current theories on dentin bonding suggest that two fundamental processes are involved in bonding an adhesive to dentin. First, the mineral phase must be extracted from the dentin substrate without damaging the collagen matrix and second, the voids left by the mineral must be filled with adhesive resin that undergoes complete in situ polymerization, i.e., the formation of a resin-reinforced or hybrid layer.[41] Ideally, the hybrid layer would be represented as a structurally integrated resin-collagen network that is impervious to oral or dentinal fluids. Recent in vitro[22,42-46] and in vivo studies[47,48] have shown that this objective is not achieved. Hybrid layers are instead characteristically porous; they are readily penetrated and degraded by aqueous solutions and/or oral fluids.[26,47-49] Because of this rapid deterioration in aqueous environments, the hybrid layer has been described as the weakest link in the attachment of adhesive to dentin.[48]

The hybrid layer could be portrayed as the 'Achilles heel' of the adhesive/dentin bond. This characterization is based on the results of several in vitro investigations as well as a recent in vivo study which suggests that the hybrid layer is not stable in aqueous environments.[47-49] Although the results from these morphologic investigations in conjunction with bond strength measurements have allowed comparison among commercial products; they provide only an indirect assessment of the quality and little information on the composition and chemistry of the hybrid layer. Based on the results of these studies, it still is not clear how well the resin monomers are wetting the collagen fibrils and how far they penetrate into the zone of demineralized dentin.

The purpose of this study was to develop a method for quantitative determination of the degree of adhesive penetration at the adhesive/dentin interface. In general, the Raman microscopy technique has not been regarded as the foremost technique for quantifying adhesive penetration, but has been favored more as a "qualitative only" technique. In this study, by generating calibration curves from model mixtures of known composition, a new method for estimating adhesive penetration within the hybrid layer and at the adhesive/dentin interface using laser micro-Raman spectroscopic data has been developed.

8.5.3.1 *Materials and Methods*

The model mixtures were made from 1% w/v solutions of rat-tail type I collagen and adhesive. In this study, three commercially available adhesive systems were used.[23] Acid-soluble rat-tail type I collagen (c8897, Sigma Type VII, Sigma, St. Louis, MO) was used. The concentrations of the dentin adhesives were calculated by the weight loss method. One percent weight/volume solutions of adhesive in ethanol and collagen in 0.5M acetic acid were prepared. The model mixtures of collagen and adhesive were obtained by blending the solutions in appropriate ratios. The composition of these collagen/adhesive mixtures was 100/0, 80/20, 70/30, 60/40, 50/50, 40/60, 30/70, 20/80 and 0/100. The mixtures were transferred to small petri dishes, the solvent was evaporated, and the mixtures were polymerized for 30 seconds using a visible light source. Polymerized specimens, measuring 3 x 2 mm, were washed with distilled water and dried. The experimental apparatus is described above. Raman spectra of model mixtures were acquired at a resolution of ~6 cm^{-1} from a minimum of six-to eight different sites on each sample.

Adhesive/dentin specimen preparation: Extracted noncarious, unerupted human third molars stored at 4C in 0.9% w/v NaCl, containing 0.002% sodium azide, were used in this study. Teeth were collected after a patient's informed consent was obtained under a protocol approved by the UMKC adult health sciences institutional review board. Dentin disks were prepared by first cutting the roots at the cementum-enamel junction with a water-cooled low speed diamond saw (Buehler, Lake Bluff, IL), then the occlusal one-third of the crowns was removed by means of a second, parallel section. Dentin disks without any enamel remnants or exposure of the pulp chamber were prepared. Uniform standardized smear layers were created by wet-sanding for 1 min the exposed dentin surface with 600-grit silicon carbide sandpaper. The prepared dentin specimens were randomly selected for treatment with one of the three commercial adhesives; manufacturer's instructions were followed for the application of these adhesives. The "wet" bonding technique was used throughout the bonding procedure. The dentin

adhesives were polymerized for 30 seconds by exposure to a visible light source. Cross-sectional samples of the adhesive/dentin interface, approximately 1.5 mm thick, were cut from the teeth.

The adhesive/dentin specimen was placed at the focus of a 100x objective with a 0.95 numeric aperture and 0.3 mm working distance. Spectra were acquired at positions corresponding to 1 μm intervals across the adhesive/dentin interface using the computer-controlled x-y-z stage with a minimum step width of 50 nm. For each specimen, Raman maps were collected from six different sites across the adhesive/dentin interface. Confocal Raman microscopy offers the investigator the unique opportunity to both image the interface and obtain chemical information. The focus of the laser beam in conjunction with a 25 μm confocal aperture provided a spatial resolution of ~1 μm. Spectra were obtained at a resolution of ~6 cm^{-1} over the spectral region of 875–1785 cm^{-1} and they had an integration time of 60 seconds. A digital image of the adhesive/dentin interface with demarcations identifying the position of each spectrum was recorded simultaneously. Multiple sites across the interface of each specimen were examined spectroscopically. No postprocessing of the data was performed. Quantitative Raman analysis of adhesive diffusion was carried out by comparing spectral features from the chemical maps of the adhesive/dentin interface to calibration curves generated from the model mixtures of adhesive and type I collagen. Details for this technique are provided in the following reference.[23]

8.5.3.2 *Results and Discussion*

In this study, we described the use of Raman microspectroscopy in the qualitative and quantitative analysis of adhesive penetration at the interface with dentin. In order to obtain quantitative information about the composition of the adhesive/dentin interface, it is desirable to generate a calibration curve using the components of the interface because this curve can provide an effective means of accounting for the effects of the overlapping spectral features of the adhesive and demineralized dentin in the interface. It is difficult, however, to homogeneously disperse a quantitative amount of adhesive onto a

demineralized layer (dentin collagen network); and, also, dentin collagen is insoluble. Therefore, we used a model mixture in which acid soluble rat-tail type I collagen was mixed with adhesives in solution.

The development of a model mixture system for a Raman study of the composition at the adhesive/dentin interface must have the following criteria: 1) the model mixture should show Raman spectral characteristics similar to those of the adhesive/dentin interface; and 2) known quantities of the components must be mixed uniformly in the model mixture. If these requirements are fulfilled, then an accurate calibration curve can be prepared.

This Raman study was the first to clearly demonstrate the ability of this technique to quantify adhesive penetration at the adhesive/dentin interface.[23] This technique offers distinct advantages in comparison to other analytical methods. Unlike Raman microspectroscopy, imaging by light and electron microscopy does not provide chemical information. These morphologic techniques also require preparatory procedures that can introduce artifacts. Other methods of contrast that use X-rays and Auger electrons do not reveal as much about the underlying chemistry as Raman does. Using these techniques it is difficult to evaluate the distribution of adhesive resins because resin monomers are electron lucent and usually are made up of carbon, hydrogen and oxygen atoms that also occur in the substrate. In addition, these techniques require high vacuum conditions that can damage or alter the native biologic tissue. The only competing technology that truly gives the same type of microbeam molecular information is FTIR microspectroscopy. But a disadvantage of FTIR is that not all materials will fit into this device. Samples must be made very thin (~8 μm). Due to its limited spatial resolution and the unknown sample thickness, the infrared results cannot be used quantitatively in determining penetration of adhesive at the interface.[50] In summary, the Raman microspectroscopic technique described in these studies holds considerable promise for future in vitro and in vivo investigations of the adhesive/dentin interface.[22,23] The technique offers distinct advantages, including minimal sample preparation and both qualitative and quantitative analysis at ~1 μm spatial resolution. The nondestructive nature of this analysis also allows investigation of the same sample using complementary techniques.

8.5.4 *Investigation of Adhesive Phase Separation*

Under in vivo conditions, there is little control over the amount of water left on the tooth. There is the danger of leaving the dentin surface so wet that the adhesive actually undergoes physical separation into hydrophobic and hydrophilic-rich phases. Previous reports of the sensitivity of our current commercial dentin adhesives to excess moisture[51,52] have included morphologic evidence of water-blisters in adhesives applied to over-wet surfaces.[53-55] Although water blisters may be one manifestation of phase separation, the adhesive components involved in this phenomenon cannot be directly determined using morphologic techniques. The twofold purpose of this study was: 1) to investigate phase separation of BisGMA/HEMA model mixtures and commercial BisGMA-based adhesive in the presence of water using molecular microanalysis and 2) to examine the effect of adhesive phase separation on the quality of the hybrid layer.[56]

8.5.4.1 *Materials and Methods*

BisGMA/HEMA/water mixtures: Phase separation was investigated at different concentrations of water and varying concentrations of BisGMA (Polysciences Inc., Warrington, PA) and HEMA (Polysciences Inc., Warrington, PA). The BisGMA/HEMA weight ratios were 70/30, 60/40, 50/50, 40/60 and 30/70. These mixtures were made with and without 45 vol% ethanol (the approximate concentration of ethanol in the commercial BisGMA-based adhesive). Water was added to the BisGMA/HEMA mixtures at concentrations ranging from 0 to 50 vol%. All mixtures were made in triplicate at 25°C. The BisGMA/HEMA/water mixtures were sonicated for 30 seconds and then inspected for homogeneity. A loss in clarity, as noted by visual examination, was interpreted as evidence of phase separation, i.e., prior to phase separation the mixture is a clear liquid, the mixture is opaque when phase separation occurs. This rough, optical method can be used prior to any Raman spectroscopic investigations.

Single Bond adhesive/water mixtures: Single Bond (SB) adhesive (3M Corp., St. Paul, MN, USA) was mixed with 5, 10, 15, 25, 30, and 40 vol% distilled water in 1.5 mL micro-centrifuge tubes. The mixtures were made in triplicate. The composition of SB adhesive is 60–70 wt% 2,2-bis[4(2-hydroxy-3-methacryloyloxy-propyloxy)-phenyl] propane (BisGMA), 40–30 wt% 2-hydroxyethyl methacrylate (HEMA), and 45 vol% ethanol; camphoroquinone and dihydroxylethyl-para-toluidine are included as photoinitiators. The SB/water mixtures were cast as films on glass slides, covered with mylar, and polymerized with visible light for 20 seconds. Following polymerization, the mylar was removed and the specimens were imaged using an Nikon (Eclipse ME 600) reflected light microscope.

Micro-Raman Spectroscopic Investigation of SB Adhesive/water: Micro-Raman spectra were collected on SB adhesive mixed with water. Spectra were collected using a Jasco NRS 2000 Raman spectrometer equipped with Olympus lenses and a liquid-nitrogen-cooled CCD detector. The optical microscope allowed for visual identification of the position at which the Raman spectrum was obtained. The excitation source was an Argon laser, operating at 514.5 nm. The estimated power at the laser was 100 mW, after passing through the bandpass filter and condensing optics, approximately 3 mW power was incident upon the sample. The sample was placed at the focus of a 50x objective and spectra were recorded from the distinct features that were clearly visible in the films cast from the mixtures of SB adhesive with water.

Adhesive/Dentin Interface Specimen Preparation: Preparation of these specimens followed the protocol described under Section 8.5.3.1. In brief, the occlusal one-third of the crown was sectioned perpendicular to the long axis of the tooth by means of a water-cooled low-speed diamond saw (Buehler, Lake Bluff, IL). A smear layer was created by abrading the exposed dentin surface with 600 grit silicon carbide under water. The prepared dentin specimens were treated with Single Bond adhesive according to manufacturer's instructions. The dentin is etched with 35% phosphoric acid gel (15 seconds) and rinsed with water; excess water is removed but the dentin surface remains visibly moist. The

adhesive is applied and polymerized for 30 seconds by exposure to visible light (Spectrum light, Dentsply, Milford, DE, USA). Five prepared teeth were treated with the adhesive; these specimens were stored for a minimum of 24 hrs in water at 25°C before sectioning. The treated dentin surfaces were sectioned perpendicular and parallel to the bonded surface using a water-cooled low-speed diamond saw. The Raman microscopic investigation of the adhesive/dentin interface specimens similarly followed the protocol described under 8.5.3.1.

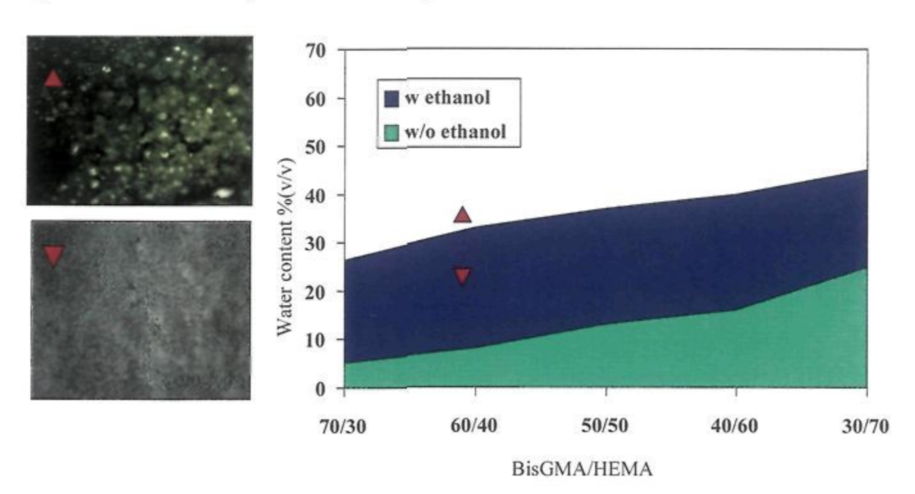


Fig. 8.8. Phase diagram of the BisGMA/HEMA/water mixtures. (Reference: Spencer P and Wang Y, J Biomed Mater Res 62:447–456, 2002).

8.5.4.2 *Results and Discussion*

Partitioning of BisGMA/HEMA Mixtures in Water: The diagram shown in Fig. 8.8 is based on the visual observation of a loss of clarity in the BisGMA/HEMA/water mixtures. The 70/30 BisGMA/HEMA formulation with 45 vol% ethanol (solvent) exhibits macrophase separation at ~28 vol% water. Without solvent macrophase separation in this formulation (70/30 BisGMA/HEMA) occurs at ~5 vol% water. If the concentration of HEMA is increased such that the formulation is 30/70 BisGMA/HEMA with solvent, phase separation occurs at ~45 vol% water. Without solvent phase separation in the 30/70 BisGMA/HEMA occurs at ~25 vol% water.

Partitioning of BisGMA-based Adhesive in Water: Morphology and Composition: Representative light micrographs of the films cast from SB adhesive mixed with 15, 25 and 30 vol% water are shown in Fig. 8.9 (A, B, C), respectively. The distinct particles in Figs. 8.9 (B, C) clearly demonstrate phase separation that occurs when SB adhesive is mixed with 25 and 30 vol% water. It appears that the adhesive when mixed with water at these concentrations forms an oil-in-water microemulsion. Distinct particles are not apparent in the mixture of SB adhesive and 15 vol% water.

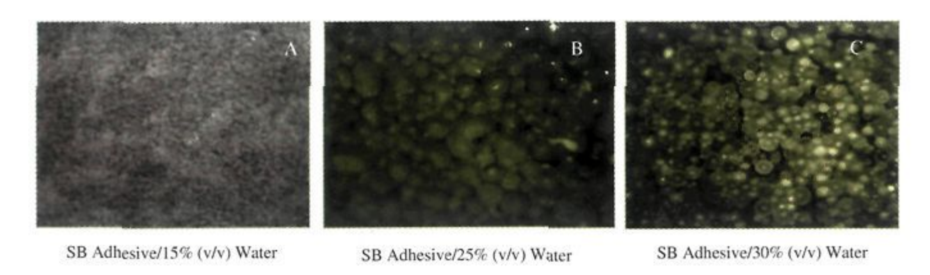


Fig. 8.9. Light micrographs of Single Bond adhesive (62 wt% BisGMA/38 wt% HEMA) mixed with water, light cure for 20 seconds. (Reference: Spencer P and Wang Y, J Biomed Mater Res 62:447-456, 2002).

The Raman spectra of the distinct features apparent in the mixture of SB adhesive with 25 vol% water are shown in Fig. 8.10. Spectrum A was acquired from the matrix or material surrounding the particles while spectrum B was acquired from the particles. A comparison of the spectral features suggests that spectrum B is composed primarily of BisGMA. The difference spectrum suggests that HEMA is the primary constituent contributing to the spectrum recorded from the matrix. The composition was determined from the relative integrated intensities associated with 1610 (C=C in phenyl of BisGMA) and 1454 (CH def) using standard BisGMA/HEMA mixtures ranging from 0–100 wt%.[23] Based on these calculations, the composition of spectrum A is approximately 21 wt% BisGMA while the composition of spectrum B is 67 wt% BisGMA.

The image presented in Fig. 8.10 represents phase separation in a BisGMA-based adhesive as a result of water exposure. A unique

characteristic of micro-Raman spectroscopy is the ability to focus the incident beam such that the spectrum is acquired at a spatial resolution comparable to the light microscope. Utilizing this capability the spectra shown in Fig. 8.10 were acquired from the distinct spatially resolved features, i.e. particles and matrix formed in the adhesive upon exposure to 25 vol% water. Since the particles are opaque in nature, *in situ* chemical analysis by conventional spectroscopic techniques is difficult. Raman spectroscopy differs from other spectroscopic techniques in that it involves the measurement of scattered light from molecules and thus, is appropriate for the analysis of complex, nontransparent materials. The Raman effect can also be used to study aqueous solution. This is, of course, in distinct contrast to IR spectroscopy where spectral interference

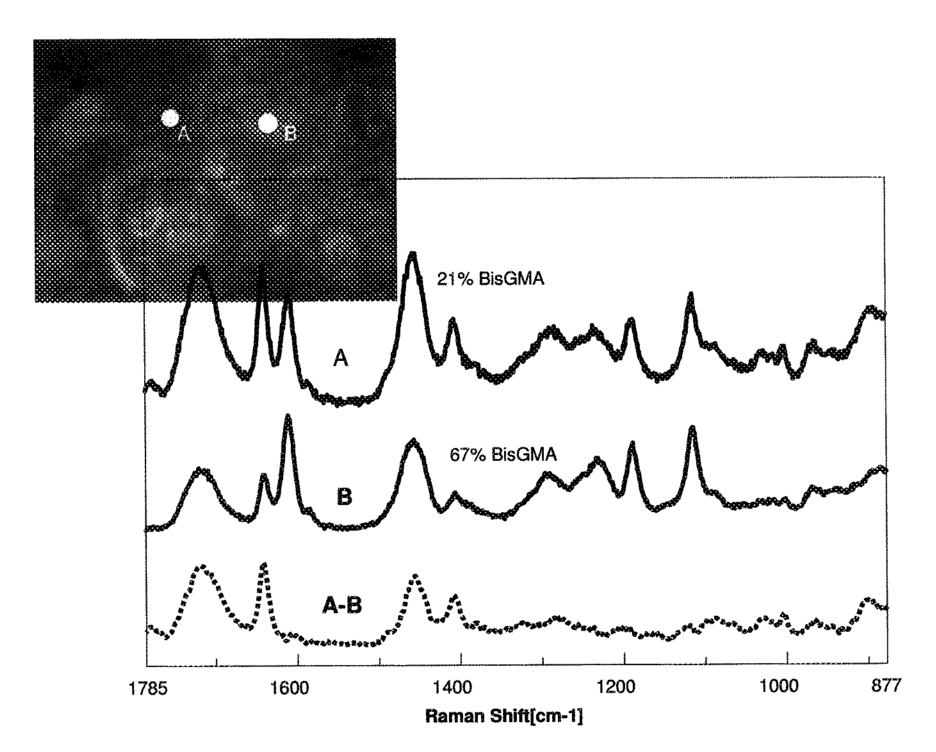


Fig. 8.10. Micro-Raman spectra recorded from SB adhesive following macrophase separation upon exposure to 25% (vol/vol) water. (A) Spectrum recorded from phase between the particles; (B) spectrum recorded from the particle; (A-B) difference spectrum. (Reference: Spencer P and Wang Y, J Biomed Mater Res 62:447–456, 2002).

from water inhibits one's ability to investigate "wet" samples. Changes in Raman spectra during the reaction of a commercial BisGMA-based adhesive (60–70 wt% BisGMA/40–30 wt% HEMA) with water at varying concentrations have been determined. At water concentrations $\geq$ 25 vol% the adhesive/water solutions mimicked oil and water mixtures in that they separated into distinct phases immediately following sonication. A comparison of the spectral features of the adhesive mixed with 30 vol% water suggests that at this concentration of water the adhesive separates into distinct particles that are made up primarily of BisGMA. The difference spectrum suggests that HEMA is the primary constituent contributing to the spectrum recorded from the matrix or material surrounding the particles.

Phase separation of the adhesive that infiltrates the demineralized dentin matrix would compromise the structural integrity of the resultant hybrid layer. In contrast to an impervious 3-dimensional collagen/polymer network, adhesive phase separation would lead to a very porous hybrid layer characterized by hydrophobic BisGMA-rich particles distributed in a hydrophilic HEMA-rich matrix. The large interfacial void noted in scanning electron micrographs of the adhesive/dentin interface suggests that protein (demineralized dentin collagen) that was not encased in adhesive was effectively removed by treatment with NaOCl.[56] These results underscore the porosity of the hybrid layer. In addition, the adhesive tags are easily broken when the NaOCl-treated adhesive/dentin interface is sonicated, suggesting that the adhesive does not have the structural integrity to resist even gentle vibratory forces.[56]

In corroboration with our micro-Raman spectroscopic data, one reason for this lack of structural integrity is physical separation of the adhesive as it mixes with water in the demineralized dentin matrix, leading to partitioning of the adhesive into hydrophobic BisGMA- and hydrophilic HEMA-rich phases. Based on previous studies, the hydrophobic BisGMA-rich phase is relatively stiff in comparison to the HEMA-rich phase.[57] It is likely that stress concentration at the boundary of the BisGMA-rich and HEMA-rich phases was one factor contributing to the fracture of the adhesive tags in the sonicated specimen.

Phase separation in conjunction with partitioning of the adhesive components inhibits not only the formation of an integrated collagen/polymer network, but suppresses adhesive infiltration throughout the width of the demineralized dentin matrix and the subjacent, intact dentin. Adhesive infiltration of the subjacent, intact dentin is paramount to the development of durable adhesive/dentin bonds.[58] Thus, phase separation in BisGMA/HEMA bonding resins can lead to adhesive/dentin bond failure through at least two fundamental mechanisms. As the adhesive diffuses into the wet demineralized dentin matrix, the components separate into hydrophobic BisGMA-rich and hydrophilic HEMA-rich phases. Because of its low cross-link density HEMA is unstable in aqueous environments and thus, this phase will degrade when exposed to oral fluids. Isolated particles of BisGMA infiltrate the wet, demineralized dentin matrix. The collagen fibrils of the demineralized dentin matrix are not protected by an impervious 3-dimensional polymer, but isolated BisGMA particles in a hydrolytically unstable HEMA-rich matrix. The BisGMA particles, which tend to form at the top of the demineralized dentin where there is the least amount of water, inhibit resin infiltration into the subjacent demineralized matrix and intact dentin.

The first direct spectroscopic evidence of possible phase separation in a commercial BisGMA/HEMA adhesive at the interface with wet demineralized dentin was presented in a previous study from our laboratory.[22] Using the intrinsic vibrational signatures of the constituents at the adhesive/dentin interface, chemical maps of the hybrid layer were generated at 1 μm spatial resolution. Adhesive diffusion was quantified by comparing spectral features from the chemical maps of the hybrid layer to calibration curves generated from model compounds of adhesive and type I collagen. With the commercial BisGMA/HEMA based bonding resin (Single Bond) used in this study, there was spectral evidence of possible phase separation at ~2 μm into the wet, demineralized dentin matrix. The majority of the intertubular adhesive/dentin interface was characterized by collagen fibrils from the demineralized dentin matrix with limited spectral contribution from the critical dimethacrylate component (BisGMA). Further, because of the non-destructive, non-invasive nature of the micro-Raman spectroscopic

technique used in the above study, the specimens were available for micro-mechanical analysis using scanning acoustic microscopy.[57] The elastic moduli (GPa) of the components of the adhesive/dentin interface were determined by comparing the recorded acoustic impedance values to a calibration curve generated on standard materials. The elastic modulus for fully mineralized dentin was 28 GPa. The elastic modulus of the commercial BisGMA/HEMA-based adhesive was 5 and the elastic modulus of the region of the interface that was spectroscopically characterized as predominantly demineralized dentin was < 2 GPa.[57]

In the mouth, clinicians have reported that there is frequently a gap between the composite and the tooth at the gingival margin of class II composite restorations.[13] When such a gap is present, it is likely that the adhesive/dentin interface will be exposed to oral fluids. If water absorption occurs at the adhesive/dentin interface there may be fluid movement at the junction of the adhesive resin and hybrid layer during flexing of the restoration and tooth.[48] This exchange of fluid could promote degradation of the HEMA-rich phase in a BisGMA/HEMA adhesive that undergoes phase separation.[59-62] In the mouth, the network of collagen fibrils that had been infiltrated by the HEMA-rich phase would now be exposed to oral fluids. The exposed collagen could be attacked and degraded by bacterial enzymes.[63,64] The cumulative effect would be breakdown of the adhesive/dentin bond and ultimately, undermining of the marginal integrity of the composite restoration.

One approach to the problem of phase separation involves optimizing the ratio of the hydrophobic and hydrophilic components that make up the adhesive, i.e. the BisGMA/HEMA ratio. The concentration of water required for phase separation of model adhesives, ranging in composition from 70/30 to 30/70 BisGMA/HEMA, was investigated with and without the addition of 45 vol% ethanol (approximate concentration in the commercial adhesive, SB). In the absence of ethanol, the volume of water increased from 5 to 25% as the weight ratio in the BisGMA/HEMA mixtures varied from 30 to 70% HEMA. The inclusion of ethanol allowed for even higher water levels before phase separation was detected, i.e. 28 to ~45 vol% water at 70/30 and 30/70 BisGMA/HEMA ratios, respectively. These results suggest that one way to address the problem of phase separation is optimization of the

BisGMA/HEMA ratio, but the content of BisGMA cannot be decreased unlimitedly. Previous studies have suggested that because of its low cross-link density, HEMA is unstable in aqueous solutions.[59] Additionally, in our hands, the handling characteristics of high content HEMA formulations appear less than optimum, i.e., the mixture is very fluid and difficult to control.

This study represents the first spectroscopic investigation of spatially resolved features that develop in a BisGMA-based adhesive as a result of phase separation during water exposure. Detection at this resolution points to the utility of micro-Raman spectroscopy for analysis of multiphased biomaterials. A unique characteristic of micro-Raman spectroscopy is the ability to focus the incident beam such that the spectrum is acquired at a spatial resolution comparable to the light microscope. Utilizing this capability the spectra shown in Fig. 8.10 were acquired from the distinct spatially resolved features, i.e. particles and matrix. Since the particles are opaque in nature, in situ chemical analysis by conventional spectroscopic techniques is difficult. Raman spectroscopy differs from other spectroscopic techniques in that it involves the measurement of scattered light from molecules and thus, is appropriate for the analysis of complex, nontransparent materials. The Raman effect can also be used to study aqueous solution. This is, of course, in distinct contrast to IR spectroscopy where spectral interference from water inhibits one's ability to investigate "wet" samples.

8.6 Concluding Remarks

In summary, the results presented in this chapter demonstrate the advantages of using molecular microanalysis to identify those factors that inhibit the development of an ideal bond at the adhesive interface with "wet" dentin. They demonstrate the utility of Raman microspectroscopy in characterizing the fundamental phenomena underlying reactions at material/tissue interfaces. Details regarding the specimen preparation protocols and/or instrumentation are provided in the following references: [21-26,56,65]. A distinct advantage of this technique is the non-destructive nature which permits analysis of the same sample using complementary methods such as those described in the following

references.[57,66-68] These structure/property measurements have been utilized by our group in mathematical models to simulate the behavior of the adhesive/dentin interface under occlusal function and loading conditions. Details regarding these models are provided in the following references.[69,70]

By combining spectroscopy with microscopy, Raman microspectroscopy can be used to detect and quantify the molecular chemistry of microscopic samples; molecular information can be obtained at a spatial resolution comparable to optical microscopy. In this technique, the spatial resolution is defined by the laser profile used to excite a particular part of the specimen. Functional groups are identified by their specific positions of wavenumbers in the Raman spectrum, and the relative numbers of these groups are determined by the magnitude of intensity at each wavenumber. Samples can be analyzed directly, in air or water, at room temperature and pressure without destroying the sample. The capability of performing spatially resolved chemical analyses of microscopic regions of samples in situ has been applied to both material science and the biological sciences.

Raman microspectroscopy is an exceptional tool for investigating the chemistry of material/tissue interfaces because it does not rely on homogenization, extraction or dilution, but rather each structure is analyzed in situ. Investigation at this level of resolution is critical to our ability to isolate the factors that promote adhesive phase separation, to identify those components that prevent such separation, and to understand how these components work synergistically to inhibit adhesive phase separation at the interface of this material with "wet" demineralized dentin matrices. Such investigations are fundamental to the development of adhesives as well as other materials that will provide durable, long-term clinical function for our patients.

Acknowledgments

A contribution of the University of Missouri-Kansas City Center for Research on Interfacial Structure and Properties (UMKC-CRISP), work presented in this chapter was supported in part by USPHS Research Grants DE12487, 14392 and 15281 from the National Institute of Dental

and Craniofacial Research, National Institutes of Health, Bethesda, MD 20892. The authors are grateful to Jim Swafford for his assistance with the projects involving the smear layer. The authors gratefully acknowledge 3M Espe, Pulpdent Co and Dentsply Caulk for donating the dentin adhesive products used in these investigations. The authors gratefully acknowledge the oral surgeons and their staff for collecting the teeth used in these investigations, none of this work would be possible without their help.

References

1. R. Carmona, U.S surgeon general annual report (2003).
2. ADA, **35**, 1 (2004).
3. E.A.M. Kidd and D. Beighton, *J. Dent. Res.*, **75**, 1942 (1996).
4. C.J. Collins, R.W. Bryantand, K.L.V. Hodge, *J. Dent.*, **26**, 311 (1998).
5. A. Raskin, B. Michottetheall, J. Vrevenand, N.H.F. Wilson, *J. Dent*, **27**, 13 (1999).
6. A. Schriever, J. Becker, D. Heidemann, *Clinical Oral Invest*, **3**, 30 (1999).
7. A.R. Hunter, E.T. Treasueand, A.J. Hunter, *Oper. Dent.*, 2 (1995).
8. H. Tobi, C.M. Kreulen, H. Vondeling, W.E. van Amerongen, *Community Dent. Oral Epidemiol.*, **27**, 137 (1999).
9. L.H. Mair, *Quintessence Int*, **29**, 483 (1998).
10. H. Nordbo, J. Leirskar, F.R. von der Fehr, *Quintessence Int.*, **29**, 5 (1998).
11. S.M. Dunne, I.D. Gainsford, N.H.F. Wilson, *International Dent. J.*, **47**, 123 (1997).
12. M. Svanberg, I.A. Mjor, D. Orstavik, *J. Dent. Res.*, **69**, 861 (1990).
13. J.F. Roulet, *J. Dent.*, **25**, 459 (1997).
14. J.F. Roulet and M. Degrange, Eds. *Adhesion: The Silent Revolution in Dentistry*, Quintessence Publishing Co., Inc., 2000.
15. M.J. Pellitier. Blackwell Science Ltd., Annarbor, MI, 1999, p 1-52.
16. L.A. Nafie. in *Handbook of Raman Spectroscopy.*; I.R. Lewisand H.G.M. Edwards, Eds.; Marcel Dekker, Inc., New York, 2001, p 1-10.
17. R.A. Larsen. in *Applied Polymer Science 21st Century*; C.D. Craverand C.E. Carraher, Eds.; Elsevier, New York, 2000, p 759-785.
18. B. Chase, *Appl. Spectrosc.*, **48**, 14A (1994).
19. G. Turrell and J. Corset, *Raman Microscopy-Developments and Applications*, Academic Press, New York, 1996.
20. P. Spencer, Y. Wang, M.P. Walker, J.R. Swafford, *J. Dent. Res.*, **80**, 1802 (2001).
21. Y. Wang and P. Spencer, *J. Biomed. Mater. Res.*, **60**, 300 (2002).
22. P. Spencer, Y. Wang, M.P. Walker, D.M. Wieliczka, J.R. Swafford, *J. Dent. Res.*, **79**, 1458 (2000).
23. Y. Wang and P. Spencer, *J. Biomed. Mater. Res.*, **59**, 46 (2002).

24. Y. Wang and P. Spencer, *J. Dent. Res.*, **82**, 141 (2003).
25. Y. Wang and P. Spencer, *J. Biomed. Mater. Res.*, **75A**, 580 (2005).
26. P. Spencer, Y. Wang, B. Bohaty, *J. Biomed. Mater. Res. B: Appl. Biomater.*, **in press** (2005).
27. G.W. Marshall, S.J. Marshall, J.H. Kinney, M. Balooch, *J. Dent.*, **25**, 441 (1997).
28. M.F. Chan and J.C. Glynn Jones, *J. Dent. Res.*, **20**, 287 (1992).
29. J.C. Meiers and J. Kresin, *Oper. Dent.*, **21**, 153 (1996).
30. D.H. Pashley, *Proc. Finn. Dent. Soc.*, **88 Suppl. 1**, 215 (1992).
31. D.H. Pashley, B. Ciucchi, H. Sano, J.A. Horner, *Quintessence Int.*, **24**, 618 (1993).
32. A.J. Gwinnett, *Dent. Mater.*, **10**, 150 (1994).
33. G. Eliades, G. Vougiouklakis, *Dent. Mater.*, **15**, 310 (1999).
34. B.G. Frushour and J.L. Koenig, *Biopolymers*, **14**, 379 (1975).
35. G.W. Marshall, N. Inai, I.C.W. Magidi, M. Balooch, J.H. Kinney, J. Tagami, S.J. Marshall, *Dent. Mater.*, **13**, 338 (1997).
36. E.A. Berry III, W.N. Von der Lehr, H.K. Herrin, *JADA*, **115**, 65 (1987).
37. R.L. Bowen, *Int. Dent. J.*, **28**, 97 (1978).
38. M. Brannstrom, K.J. Nordenvall, P.O. Glantz, *J. Dent. Res.*, **59**, 1127 (1980).
39. C.L. Mader, J.C. Baumgartner, D.D. Perters, *J. Endodon*, **10**, 477 (1984).
40. R. Di Lenarda, M. Cadenaro, O. Sbaizero, *Inter. Endodon. J.*, **33**, 46 (2000).
41. N. Nakabayashi, K. Kojima, E. Masuhara, *J. Biomed. Mater. Res.*, **16**, 265 (1982).
42. H. Sano, T. Takatsu, B. Ciucchi, H.J.A., W.G. Matthews, D.H. Pashley, *Oper. Dent.*, **20**, 18 (1995).
43. P. Spencer and J.R. Swafford, *Quintessence Int.*, **30**, 501 (1999).
44. P. Spencer, Y. Wang, J.L. Katz, A. Misra, *J. Biomed. Opt.*, **10**, 031104 (2005).
45. P. Spencer and D.M. Wieliczka, *Recent Res. Devel. Applied Spectroscopy*, **2**, 183 (1999).
46. Y. Wang and P. Spencer, *Am. J. Dent.*, **18**, 66 (2005).
47. M. Hashimoto, H. Ohno, M. Kaga, K. Endo, H. Sano, H. Oguchi, *J. Dent. Res.*, **79**, 1385 (2000).
48. H. Sano, T. Yoshikawa, P.N.R. Pereira, N. Kanemura, M. Morigami, J. Tagami, D.H. Pashley, *J. Dent. Res.*, **78**, 906 (1999).
49. M.F. Burrow, M. Satoh, J. Tagami, *Dent. Mater.*, **12**, 302 (1996).
50. R.M. Lemor, M.B. Kruger, D.M. Wieliczka, J.R. Swafford, P. Spencer, *J. Biomed. Opt.*, **4**, 22 (1999).
51. T. Jacobsen and K.-J. Soderholm, *Dent. Mater.*, **11**, 132 (1995).
52. J. Kanca, *Am. J. Dent.*, **5**, 213 (1992).
53. F.R. Tay, A.J. Gwinnett, K.M. Pang, S.H.Y. Wei, *Am. J. Dent.*, **9**, 43 (1996).
54. F.R. Tay, A.J. Gwinnett, S.H.Y. Wei, *Am. J. Dent.*, **9**, 161 (1996).
55. F.R. Tay, A.J. Gwinnett, S.H.Y. Wei, *Dent. Mater.*, **12**, 236 (1996).
56. P. Spencer and Y. Wang, *J. Biomed. Mater. Res.*, **62**, 447 (2002).
57. J.L. Katz, S. Bumrerraj, J. Dreyfuss, Y. Wang, P. Spencer, *J. Biomed. Mater. Res. (Appl Biomater)*, **58**, 366 (2001).

58. J.D. Eick, A.J. Gwinnet, D.H. Pashley, S.J. Robinson, *Critical Reviews in Oral Biology & Medicine*, **8**, 306 (1997).
59. S.J. Paul, M. Leach, F.A. Rueggeberg, D.H. Pashley, *J. Dent.*, **27**, 209 (1999).
60. P. Spencer, Y. Wang, J.L. Katz, *J. Adhesive Dent.*, **6**, 91 (2004).
61. Y. Wang and P. Spencer, *Oper. Dent.*, **29**, 650 (2004).
62. Y. Wang and P. Spencer, *J. Biomed. Mater. Res.*, **68A**, 735 (2004).
63. M. Hashimoto, H. Ohno, M. Kaga, K. Endo, H. Sano, H. Oguchi, *J. Dent. Res.*, **79**, 1385 (2000).
64. T. Sorsa, T. Ingman, K. Suomalainen, M. Haapasalo, Y. Konttinen, O. Lindy, H. Saari, V. Uitto, *Infection and Immunity*, **November**, 4491 (1992).
65. Y. Wang and P. Spencer, *J. Dent. Res.*, **84**, 350 (2005).
66. J.L. Katz, A. Misra, P. Spencer, Y. Wang, S. Bumrerraj, T. Nomura, S.J. Eppell, M. Tabib-Azar, *Materials Science and Engineering C: Nanostructured Materials for Biomedical Applications* (2005).
67. J.L. Katz, P. Spencer, T. Nomura, A. Wagh, Y. Wang, *J. Biomed. Mater. Res.*, **66A**, 120-128 (2003).
68. J.L. Katz, P. Spencer, Y. Wang, A. Wagh, T. Nomura, S. Bumrerraj. in *Tissue Engineering and Biodegradable Equivalents: Scientific and Clinical Applications*; K. Lewandrowski, D. Wise, D. Trantolo, J. Gresser, M. Yaszemski and D. Altobelli, Eds.; Marcel Decker, 2002, p 775-793.
69. A. Misra, P. Spencer, O. Marangos, Y. Wang, J.L. Katz, *J. Biomed. Mater. Res.*, **70B**, 56 (2004).
70. A. Misra, P. Spencer, O. Marangos, Y. Wang, J.L. Katz, *J R Soc Interface*, **2**, 145 (2005).

CHAPTER 9

DENTAL AND ORAL TISSUE OPTICS

Valery V. Tuchin

Institute of Optics and Biophotonics, Saratov State University,
83 Astrakhanskaya str., Saratov, 410012, Russia
E-mail: tuchin@sgu.ru

Gregory B. Altshuler

Palomar Medical Technologies, Inc., 82 Cambridge str.,
Burlington, MA 01803, USA
E-mail: galtshuler@palomarmedical.com

This chapter summarizes recent studies on tissue optics and overviews different light scattering approaches that already applied or could be potential for designing of noninvasive technologies for tooth and oral soft tissue examination. Diffusion time- and spatially-resolved, polarization sensitive, optothermal, speckle, and OCT approaches are considered.

9.1 Introduction

Light propagation within hard or soft tissues depends on the scattering and absorption properties of their components: cells, cell organelles, various fiber and matrix structures and/or quasi-ordered crystal arrays.[1-22] The size, shape, and density of these structures; their refractive index, relative to the tissue ground substance; and the polarization state of the incident light, all play important roles in the propagation of light in tissues.

Two approaches are currently used for tissue modeling. In the framework of the first one, tissue modeled as a medium with a continuous random spatial distribution of optical parameters,[3,6,20,21] and the second one, considers tissue as a discrete ensemble of scatterers.[1-6,18,19,22] The choice of the approach is dictated by both the structural specificity of the tissue under study and the kind of light scattering characteristics that are to be obtained. Most tissues are composed of structures with a wide range of sizes, and most can be described as a random continuum of the inhomogeneities of the refractive index with a varying spatial scale. The second approach to tissue modeling is its representation as a system of discrete scattering particles. In particular, this model has been advantageously used to describe the angular dependence of the polarization characteristics of scattered radiation.[24-26]

Biological media are often modeled as ensembles of homogeneous spherical particles, since many cells are close in shape to spheres or ellipsoids. A system of noninteracting spherical particles is the simplest tissue model. Mie theory rigorously describes the diffraction of light in a spherical particle.[23] The development of this model involves taking into account the structures of the spherical particles, namely, the multilayered spheres and the spheres with radial nonhomogeneity, anisotropy, and optical activity.[24,25]

Because connective tissue consists of fiber structures, a system of long cylinders is the most appropriate model for it. Skin dermis, epithelial tissue stroma, and muscular tissue, belong to this type of tissue formed essentially by collagen fibrils. More than 25% of dentin volume is occupied by collagen fibrils and dentin tubules can be presented as a grid of two-layered cylinders of ~1.6 μm in diameter and axis-to-axis-spacing of ~ 6 μm.[10,15] The solution of the problem of light diffraction in a single homogeneous or multilayered cylinder is also well understood.[23]

A collimated (laser) beam is attenuated in a thin tissue layer of thickness d in accordance with the exponential law, Bouguer–Beer–Lambert law[5],

$$I(d) = (1 - R_F)\, I_0 \exp(-\mu_t d), \qquad (9.1)$$

where $I(d)$ is the intensity of transmitted light measured using a distant photodetector with a small aperture (on-line or collimated transmittance), W/cm^2; R_F is the coefficient of Fresnel reflection; at the normal beam incidence, $R_F = [(n-1)/(n+1)]^2$; n is the relative mean refractive index of tissue and surrounding media; I_0 is the incident light intensity, W/cm^2;

$$\mu_t = \mu_a + \mu_s \tag{9.2}$$

is the extinction coefficient (interaction or total attenuation coefficient), 1/cm, where μ_a is the absorption coefficient, 1/cm, and μ_s is the scattering coefficient, 1/cm. Strictly speaking, Eq. (9.1) is valid only for a highly absorbing media, when $\mu_a >> \mu_s$.

The extinction coefficient is connected with the extinction cross section σ_{ext} as

$$\mu_t = \rho_s \sigma_{ext}, \tag{9.3}$$

where ρ_s is the density of particles (tissue and cell compounds). For a system of particles with absorption,

$$\sigma_{ext} = \sigma_{sca} + \sigma_{abs}, \tag{9.4}$$

$$\mu_s = \rho_s \sigma_{sca}, \qquad \mu_a = \rho_s \sigma_{abs}. \tag{9.5}$$

The average scattering cross section per particle can be presented in the form suitable for experimental evaluations:[23]

$$\sigma_{sca} = (\lambda^2 / 2\pi)(1/I_0)\int_0^{\pi} I(\theta)\sin\theta d\theta, \tag{9.6}$$

where I_0 is the intensity of the incident light, $I(\theta)$ is the angular distribution of the scattered light by a particle, θ is the scattering angle. For macroscopically isotropic and symmetric media, the average scattering cross section is independent of the direction and polarization of the incident light. The average extinction, σ_{ext}, and absorption, σ_{abs}, coefficients are also independent of the direction and polarization state of the incident light. The mean free path length (MFP) between two interactions is denoted by

$$l_{ph} = \mu_t^{-1}. \tag{9.7}$$

9.2 Continuous Wave Light Interaction with Tissues

To analyze light propagation under multiple scattering conditions, it is assumed that absorbing and scattering centers are uniformly distributed across the tissue. When the scattering medium is illuminated by unpolarized light and/or only the intensity of multiply scattered light needs to be computed a sufficiently strict mathematical description of continuous wave (CW) light propagation in a medium is possible in the framework of the scalar stationary radiation transfer theory (RTT).[1-6,18,24,25,27-32] This theory is valid for an ensemble of scatterers located far from one another and has been successfully used to work out some practical aspects of tissue optics. The main stationary equation of RTT for monochromatic light has the form:[1]

$$\frac{\partial I(\bar{r},\bar{s})}{\partial s} = -\mu_t I(\bar{r},\bar{s}) + \frac{\mu_s}{4\pi}\int_{4\pi} I(\bar{r},\bar{s}')p(\bar{s},\bar{s}')\mathrm{d}\Omega', \tag{9.8}$$

where $I(\bar{r},\bar{s})$ is the radiance (or specific intensity) – average power flux density at a point $\bar{r}$ in the given direction $\bar{s}$ (W/cm^{2}sr); $p(\bar{s},\bar{s}')$ is the scattering phase function, 1/sr; and $d\Omega'$ is the unit solid angle about the direction $\bar{s}'$, sr. It is assumed that there are no radiation sources inside the medium. The scalar approximation of the radiative transfer equation (RTE) gives poor accuracy when the size of the scattering particles is much smaller than the wavelength, but provides acceptable results for particles comparable to and larger than the wavelength.[25] There is an ample literature on the analytical and numerical solutions of the scalar RTE.[1-6,18,30] For hard tooth tissues RTT is applicable for tissue samples thicker than 300 μm when no light transportation anisotropy with respect to the orientation of enamel prisms and/or dentin tubules is observed.

The phase function $p(\bar{s},\bar{s}')$ describes the scattering properties of the medium and is in fact the probability density function for scattering in the direction $\bar{s}'$ of a photon traveling in the direction $\bar{s}$; in other words, it characterizes an elementary scattering act. If scattering is symmetric relative to the direction of the incident wave, then the phase function depends only on the scattering angle θ (angle between directions $\bar{s}$ and $\bar{s}'$), i.e.,

$$p(\bar{s},\bar{s}') = p(\theta). \tag{9.9}$$

The assumption of random distribution of scatterers in a medium (i.e. the absence of spatial correlation in the tissue structure) leads to normalization

$$\int_0^{\pi} p(\theta) 2\pi \sin\theta d\theta = 1. \tag{9.10}$$

In practice, the phase function is usually well approximated with the aid of the postulated Henyey–Greenstein function:[1-6]

$$p(\theta) = \frac{1}{4\pi} \cdot \frac{1-g^2}{(1+g^2-2g\cos\theta)^{3/2}}, \tag{9.11}$$

where g is the scattering anisotropy parameter (mean cosine of the scattering angle θ)

$$g \equiv \langle \cos\theta \rangle = \int_0^{\pi} p(\theta)\cos\theta \cdot 2\pi \sin\theta d\theta . \tag{9.12}$$

The value of g varies in the range from –1 to 1:[24,25] $g = 0$ corresponds to isotropic (Rayleigh) scattering, $g = 1$ to total forward scattering (Mie scattering at large particles), and –1 to total backward scattering.

The integro-differential Eq. (9.8) is frequently simplified by representing the solution in the form of spherical harmonics that gives a system of $(N + 1)^2$ connected differential partial derivative equations known as the P_N approximation. This system is reducible to a single differential equation of order $(N + 1)$. At simplest case a diffusion-type equation that has the following form for an isotropic medium is valid.[1-6,33–36]:

$$(\nabla^2 - \mu_{eff}^2)U(\bar{r}) = -(cD)^{-1} q(\bar{r}), \tag{9.13}$$

where

$$\mu_{eff} = [3\mu_a(\mu_s' + \mu_a)]^{1/2} \tag{9.14}$$

is the effective attenuation coefficient or inverse diffusion length, $\mu_{eff} = 1/l_d$, 1/cm; $q(\bar{r})$ is the source function (i.e., the number of photons injected into the unit volume),

$$D = \frac{1}{3(\mu_s' + \mu_a)} \tag{9.15}$$

is the photon diffusion coefficient, cm^2/c;

$$\mu_s' = (1 - g)\mu_s \tag{9.16}$$

is the reduced (transport) scattering coefficient, 1/cm, and c is the velocity of light in the medium. The transport mean free path of a photon (cm) is defined as

$$l_t = (1/\mu_t') = (\mu_a + \mu_s')^{-1}, \tag{9.17}$$

where $\mu_t' = \mu_a + \mu_s'$ is the transport coefficient.

The transport mean free path (TMFP) in a medium with anisotropic single scattering significantly exceeds the MFP in a medium with isotropic single scattering $l_t >> l_{ph}$ [see Eq. (9.7)]. The TMFP l_t is the distance over which the photon loses its initial direction.

Diffusion theory provides a good approximation in the case of scattering anisotropy factor $g < 0.9$, when the optical thickness τ of an object is of the order 10–20. However, the diffusion approximation is inapplicable for beam input near the object's surface where single or low-step scattering prevails. For accurate use of diffusion theory, one must accurately convert the narrow light beam into isotropic photon sources that must be sufficient deep in the medium comparable with photon TMFP, l_t; and the absorption coefficient μ_a should be much less than the reduced scattering coefficient μ_s'.[37]

For the source term modeled as a point scattering source at a depth of one TMFP, l_t, and extrapolated boundary approach satisfying the boundary condition, the spatially-resolved steady-state reflectance per incident photon, $R(r_{sd})$, is expressed as[38]

$$R(r_{sd}) = \frac{F_U}{4\pi}\left\{ l_t\left(\mu_{eff} + \frac{1}{r_1}\right)\frac{\exp(-\mu_{eff}r_1)}{r_1^2} + (l_t + 2z_b)\left(\mu_{eff} + \frac{1}{r_2}\right)\frac{\exp(-\mu_{eff}r_2)}{r_2^2}\right\} + \frac{F_F}{4\pi D}\left\{\frac{\exp(-\mu_{eff}r_1)}{r_1} - \frac{\exp(-\mu_{eff}r_2)}{r_2}\right\}, \tag{9.18}$$

where r_{sd} is the distance between light source and detector at the tissue surface (source-detector separation), cm; $r_1 = \sqrt{l_t^2 + r_{sd}^2}$; $r_2 = \sqrt{(l_t + 2z_b)^2 + r_{sd}^2}$; $z_b = 2AD$ is the distance to the extrapolated boundary, $A = (1 + R_{eff})/(1 - R_{eff})$, R_{eff} is the effective reflection coefficient, which can be found by integrating the Fresnel reflection coefficient over all incident angles, and D is the diffusion coefficient [see Eq. (9.15)]. The parameters F_U and F_F represent the fractions of the fluence rate and the flux which exit the tissue across the interface. These values are obtained by integration of the radiance over the backward hemisphere and depend on refractive index mismatch on the boundary.

The development of methods for the solving forward and inverse scattering problems in media with arbitrary configuration and boundary conditions is crucial for the reliable layer-by-layer measurements of laser radiation inside tissues and is necessary for practical purposes such as diffuse optical tomography and the spectroscopy of biological objects, specifically teeth. The Monte Carlo (MC) method appears to be especially promising in this context, being widely used for the numerical solution of the RTT equation in different fields including tissue optics.[1–6,15,37,39-42] The method is based on the numerical simulation of photon transport in scattering media. Random migrations of photons inside a sample can be traced from their input until absorption or output. Known algorithms allow a few tissue layers with different optical properties to be characterized along with the final incident beam size and the reflection of light at interfaces. Typical example of multilayer scattering tissues is tooth.

The MC technique is used to simulate the diffuse reflectance or transmittance for one wavelength or for a whole spectrum,[1-6,39-42] other optical characteristics at various experimental geometries also can be modeled, such as angular distributions of light scattering.[15] Because the implicit photon capturing technique is used during the MC simulation, a photon packet with an initial weight of unity is launched perpendicularly to the tissue surface along the light beam direction for the problem of a pencil beam propagation and isotropically for the problem of light distribution of isotropic light source inserted into a tissue. Other geometries are also possible. Then, a step size is chosen statistically using the expression[37]:

$$l = \frac{-\ln(\xi)}{\mu_a + \mu_s} \tag{9.19}$$

where ξ is a random number equidistributed between 0 and 1 ($0 < \xi \leq 1$). Due to absorption in the system, the photon packet partially loses its weight at the end of each step. The amount of weight loss is the photon weight at the beginning of the step multiplied by $(1-\Lambda)$, where $\Lambda = \mu_s / \mu_t$ is the albedo. The photon with the remaining weight is scattered. A new photon direction is statistically determined by a phase function [see Eq. (9.9)], which according to the scattering anisotropy factor g can be taken in the form of Henyey–Greenstein postulated function [see Eq. (9.11)]. A new step size is then generated by Eq. (9.19), and process is repeated. When the photon does try to leave the medium, the probability of an internal reflection is calculated using Fresnel's equation.[40] When the photon weight is less than a preset threshold (usually 10^{-4}), "Russian roulette" is used to determine whether the photon should be terminated or propagated further with an increased weight. If the photon packet crossed the surface boundary into the ambient medium, the photon weight contributes to the diffuse reflectance or transmittance. If a reflection occurs, then the photon packet is reflected back into the medium the appropriate distance and migration continues. Otherwise, the migration of that particular photon packet halts and a new photon is launched into the medium at the predefined source location. Multiple photon packets are used to obtain statistically meaningful results; at present 1–10 million photon packets are usually used.

In particular, basing on results of MC simulation attenuation of a wide laser beam of intensity I_0 at depths $z > l_d = 1/\mu_{eff}$ [see Eq. (9.14)] in a thick tissue may be described as[5]

$$I(z) \approx I_0\, b_s \exp(-\mu_{eff} z), \tag{9.20}$$

where b_s accounts for additional irradiation of upper layers of a tissue due to backscattering (photon recycling effect). Respectively, the depth of light penetration into a tissue

$$l_e = l_d[\ln b_s + 1]. \tag{9.21}$$

Typically, for tissues b_s = 1–5 for beam diameter of 1–20 mm.

A noninvasive optical technique based on diffuse reflectance spectroscopy was recently suggested to measure oral epithelial thickness as an index of tissue inflammation that may contribute to the process of carcinogenesis.[43] Although any optical measuring system has the potential for probing near-surface structures, traditional methods of accounting for scattering of photons are generally invalid for typical epithelial thicknesses.[43] Thus, a single-scattering theory that accurately predicts epithelial tissue thickness from the intensity measurements for two different angles relative to the tissue surface was developed.[43] Prior pilot clinical studies this differential method was tested using MC simulations and measurements for 2-layered tissue phantoms. Clinical studies using a simple two-source, four-detector probe also gave promising results on quantifying epithelial thickness *in vivo*.

9.3 Time-Resolved Diffusion Measurements

To provide a rationale for non-invasive optical diagnostic methods a time-resolved measurement of reflectance or transmittance in tissues can be used. The time-dependent RTT is the basis for analysis of the time response of scattering tissue.[1-6] When probing the plane-parallel layer of a scattering medium with an ultrashort laser pulse, the transmitted pulse consists of a ballistic (coherent) component, a group of photons having zigzag trajectories, and a highly intensive diffuse component.[1-6] Both unscattered photons and photons undergoing forward-directed single step scattering contribute to the intensity of the ballistic component (composed of photons traveling straight along the laser beam). This component is subject to exponential attenuation with increasing sample thickness [see Eq. (9.1)].

The group of snake photons with zigzag trajectories includes photons that have experienced only a few collisions each. They propagate along trajectories that deviate only slightly from the direction of the incident beam and form the first-arriving part of the diffuse component. These photons carry information about the optical properties of the random

medium and parameters of any lesion (caries for instance) which they may happen to come across during their progress.

The diffuse component is very broad and intense since it contains the bulk of incident photons after they have participated in many scattering acts and therefore migrate in different directions and have different path lengths. Moreover, the diffuse component carries information about the optical properties of the scattering medium, and its deformation may reflect the presence of local inhomogeneities in the medium. The resolution obtained by this method at a high light-gathering power is much lower than in the method measuring straight-passing photons. Two probing schemes are conceivable, one recording transmitted photons (transillumination) and the other taking advantage of their backscattering.

At investigation in the backscattering mode of inhomogeneous and semi-infinite tissue satisfying to diffusion approximation ($\mu_a << \mu_s'$), when the size of both the source and the detector is small compared with the distance r_{sd} between them at the sample surface and the pulse may be regarded as single, the light distribution is described by the time-dependent diffusion equation which is in fact the generalization of the CW Eq. (9.13).[1-6,44,45] The solution of the time-dependent diffusion equation yields the following relation for the number of backscattered photons at the surface for unit time and from unit area $R(r_{sd}, t)$[44,45]:

$$R(r_{sd}, t) = \frac{z_0}{(4\pi D)^{3/2}} t^{-5/2} \exp\left(- \frac{r_{sd}^2 + z_0^2}{2Dt} \right) \exp(-\mu_a ct), \qquad (9.22)$$

and correspondingly for transmittance

$$\begin{aligned} T(r_{sd}, d, t) = (4\pi D)^{-3/2} t^{-5/2} \exp(-r_{sd}^2/4Dt)\{(d - z_0)\exp[-(d - z_0)^2/4Dt] \\ -(d + z_0)\exp[-(d + z_0)^2/4Dt] + (3d - z_0)\exp[-(3d - z_0)^2/4Dt] \qquad (9.23) \\ -(3d + z_0)\exp[-(3d + z_0)^2/4Dt]\}\exp(-\mu_a ct), \end{aligned}$$

where t is the time, $z_0 = (\mu_s')^{-1}$, d is the tissue thickness, and D is the photon diffusion coefficient defined by Eq. (9.15)

In practice, μ_a and μ_s' are estimated by fitting Eq. (9.22) or Eq. (9.23) with the shape of a pulse measured by the time-resolved photon counting technique. Experimentally measured optical parameters of many tissues and model media obtained by the pulse method can be found in Refs. 1–6, 44–46. An important advantage of the pulse method is its applicability to *in vivo* studies owing to the possibility of the separate evaluation of μ_a and μ_s' using a single measurement in the backscattering or transillumination mode.

Another time-resolved method, the so called frequency-domain (FD), measures the modulation depth of the scattered light intensity $m_U \equiv AC_{detector}/DC_{detector}$ and the corresponding phase shift relative to the incident light modulation phase $\Delta\Phi$ (phase lag).[1-6,47] The method allows one to evaluate the dynamic response of scattered light intensity to modulation of the incident laser beam intensity in a wide frequency range, typically 50 to 1000 MHz. This method is more reliable in terms of data interpretation and immunity from noise, because of light intensity modulation at low peak powers, slow rise time, and hence smaller bandwidths compare to short pulse measurements.

The development of the theory underlying this method resulted in the discovery of a new type of wave: photon-density waves or waves of progressively decaying intensity. Microscopically, individual photons make random migrations in a scattering medium, but collectively they form a photon-density wave at a modulation frequency ω that moves away from a radiation source. Photon-density waves possess typical wave-properties, e.g., they undergo refraction, diffraction, interference, dispersion, and attenuation.[1-6,47-51]

Medical FD equipment is more economic and portable. The measuring schemes are based on heterodyning of optical and transformed signals; typically phase shift $\Delta\Phi$ (phase lag) is measured, thus it also called phase method or phase-array method, if photon density waves interference is explored.[47] In strongly scattering media with weak absorption far from the walls and a source or a receiver of radiation, the light distribution may be regarded as a decaying diffusion process described by the time-dependent diffusion equation for photon density phase shift is defined as[49]

$$\Delta\Phi(\bar{r},\omega) = \bar{r}(\omega / 2D)^{0.5} \tag{9.24}$$

The predicted resolving power of diffuse tomography using photon-density waves is close to 1 mm, i.e., it is comparable to that of positron-emission and magneto-resonance tomography.[47]

9.4 Optical Properties of Dental Enamel and Dentin

9.4.1 *Structure of Enamel and Dentin*

Human teeth consist of three primary tissue components: enamel, dentin, and pulp (see Fig. 9.1). The bulk of the tooth consists of the bonelike semitransparent material – dentin, which is thickest in the crown and gradually tapers as it reaches the apex of the root. In the tooth crown the dentin is covered by a thin and transparent layer of enamel that consists of almost entirely of calcium salts in the form of large apatite crystals. Dental enamel is an ordered array of such crystals surrounded by a protein/lipid/water matrix.[7-9,14,15,52,53] Fairly well-oriented hexagonal crystals of hydroxyapatite of approximately 30–40 nm in diameter and up to 10 μm in length, are packed into an organic matrix to form enamel prisms (or rods) with an overall cross section of 4–6 μm. Enamel prisms are roughly perpendicular to the tooth surface.[8] In the interprismatic space of enamel is protein, which occupies as much as 2% of the volume.

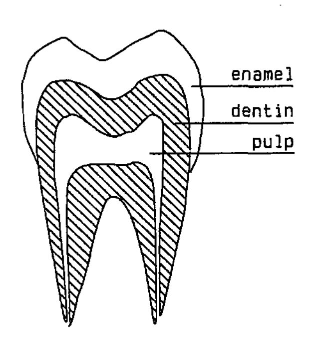


Fig. 9.1. Schematic cross section of a tooth.[10]

Similar to bone, whole dentin consists of organic (28–30 vol.%), mostly collagen, fibrils and mineral (48–50 vol.%) components incorporated into hydroxyapatite crystals and of water (20–24 vol.%). Tooth dentin is a complex structure, honeycombed with dentinal tubules, which are shelled organic cylinders with a highly mineralized shell (Fig. 9.2).[7-10,14-17,52]

Bulk dentin forms the major bulk of dentin material, and consists of peritubular dentin (circumferential to the dentinal tubules) and intertubular dentin (Fig. 9.3). Intertubular dentin consists of collagen fibrils and interfibrillar compartments. The dentine material consists of mineral crystals of hydroxyapatite. These crystals are needle shaped with a thickness of ~5 nm, and length ~20 nm length.[10] The index of refraction of hydroxyapatite in the visible range is ≈ 1.62 (see Table 9.1). Tubules are micrometer-sized dentinal structures, which radiate with an S-shaped curve from the pulp cavity toward the dental-enamel junction, and in a small sample they lie more or less parallel (Fig. 9.2, Fig. 9.3). Tubules average diameter is 1.58 (±0.28 s.d.) μm, and their number density is in the range $(1.5–6.5)\times 10^{6}$ cm^{-2}, the average being $\sim 3.5\times 10^{6}$ cm^{-2}. The tubules are surrounded by peritubular dentin with a diameter of 3.0 (±1.8 s.d.) μm and a mineral content of 90 (±6 s.d.) vol.%. Between the tubules with their peritubular dentin lies

Table 9.1. Experimental mean values of phase n or group n_g refractive indices of tooth tissues measured *in vitro*; r.m.s. values are given in parentheses.

Tissue	λ, nm	n, n_g	Reference
Enamel	220	1.73	107
Enamel	400 — 700	1.62	
Apatite	400 — 700	> 1.623	
Dentin matrix	Visible	1.553(0.001)	11
Enamel	856	n_g = 1.62(0.02)	52
Dentin	856	n_g = 1.50(0.02)	
Enamel	850	n_g = 1.65	108
Dentin	850	n_g = 1.54	

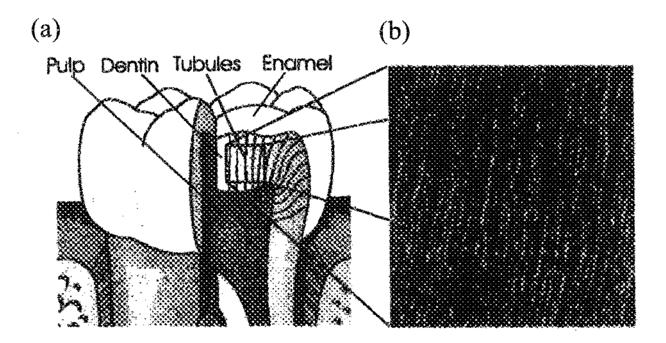


Fig. 9.2. (a) Scheme of the tooth including dental tubules. (b) Laser scanning microscope reflection pattern of the tubules (extensions of the pattern: ≈ 90 × 90 μm).[17]

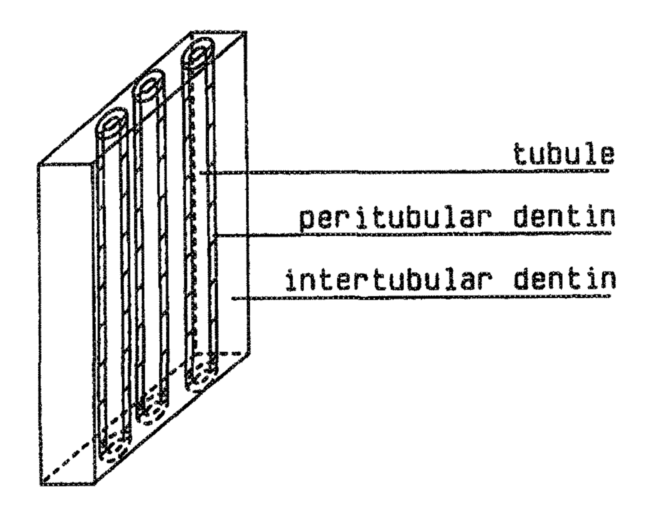


Fig. 9.3. Schematic diagram of a thin slice of dentin, cut parallel to the dentinal tubules (not to scale).[10]

intertubular dentin with a mineral content of 40 (±6 s.d.) vol.%. Intertubular dentin consists of 90-vol.% fibrils of collagen and incorporated mineral crystals and 10-vol.% interfibrillar dentin. The tropocollagen molecules in the fibrils are characterized as long thin rods of 280 × 1.5 nm with a molecular weight of ~360,000. The fibrils, with diameters of 50–150 nm, are more or less randomly oriented in this material.

9.4.2 *Spectral Properties of Enamel and Dentin*

Since both scattering and absorption of light are much stronger in dentin than in enamel, dentin plays the predominant role in tooth color.[10,14] In both enamel and dentin the light scattering coefficient is much larger than the absorption coefficient; thus scattering properties are quite important. Figure 9.4 presents spectra of transmittance (T), reflectance (R), and absorptance (A) (T + R + A = 100%) measured for sound enamel and dentin using an integrating sphere spectrophotometer in the wavelength range from 250 to 2500 nm. It should be noted that in spite of small value of absorption coefficient of enamel and dentin in the visible and NIR range (1–4 cm^{-1}) (see Table 9.2) compare to the value of the scattering coefficient (15–280 cm^{-1}), absorbed light energy is rather high, of 10–20%. This is caused by a high efficiency of traveling photons to be absorbed in a scattering medium due to much longer photon path ways within the scattering medium compare to a nonscattering one. The major peaks at 283 nm, 1234 nm, and 1944 nm of the absorption spectrum of sound enamel and the major peaks at 283 nm, 1471 nm and 1942 nm and a few other minor peaks at 1184 nm, 1737 nm, 2164 nm, and 2264 nm of dentin, as well as some other spectral peculiarities, correspond to water (300, 980, 1180, 1450, 1900, and 2940 nm) and hydroxyapatite bands (~250, 1434, 2145, and 2410 nm).[14] In the ultraviolet organic tooth tissue components (proteins) are also responsible for the absorption.

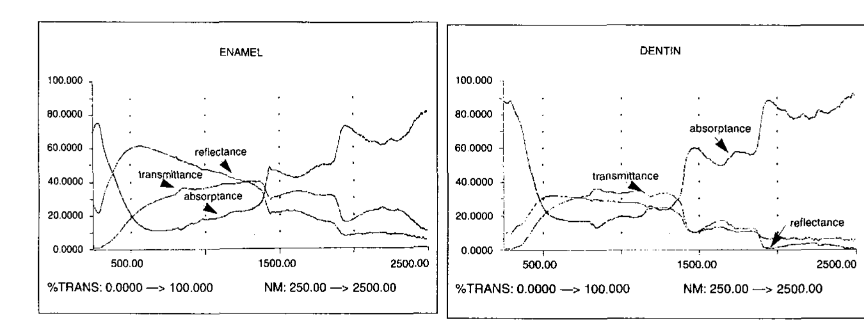


Fig. 9.4. The spectra of transmittance (T), reflectance (R), and absorptance (A) for sound enamel and dentin measured using an integrating sphere spectrophotometer in the wavelength range from 250 to 2500 nm, T + R + A = 100%.[14]

Table 9.2. Optical properties of tooth hard tissues (r.m.s. values are given in parentheses).

Tissue	λ, nm	μ_a, cm^{-1}	μ_s, cm^{-1}	g	Remarks
	543	4	180	–	Integrating sphere (IS)
Dentin	633	4	130	–	and gonio-photometric
	633	6.0*	1200*	0.44*	measurements (GPM),* Refs.
	543	<1	45	–	9,15,16
Enamel	633	<1	25	–	
	543	3-4	280(84)	0.93(0.02)	GPM, double HGPF,
Dentin	633	3-4	280(84)	0.93(0.02)	fractions of isotropic
	1053	3-4	260(78)	0.93(0.02)	scatterers are 0–2% for dentin
	543	<1	105(30)	0.96(0.02)	and 60–35% for enamel;
	633	<1	60(18)	0.96(0.02)	polished plane-parallel
Enamel	1053	<1	15(5)	0.96(0.02)	sections of 30–2000-μm[15]
	200	≈10	≈450	–	Compiled data of a few
Enamel	300	≈5	≈270	–	papers, from graphs of Ref. 7
	400	≈1	≈150	–	
	500	<1	≈73	–	
	600	<1	≈64	–	
	700	<1	≈50	–	
	800	<1	≈33	–	
	1000	<1	≈16	–	
Dentin	2940	2200	–	–	Time-resolved radiometry,
	2790	1500	–	–	data from graphs of Ref. 7
	9600	6500	–	–	
	10600	800	–	–	
Enamel	2940	800	–	–	
	2790	400	–	–	
	9600	8000	–	–	
	10600	800	–	–	
Dentin	2790	988(111)	–	–	Transmission measurements[7]
	10300	1198(104)	–	–	
	10600	813(63)	–	–	
Enamel	2940	768(27)	–	–	
	2790	451(29)	–	–	
	10300	1168(49)	–	–	
	10600	819(62)	–	–	

9.4.3 *Scattering Properties of Enamel*

In experimental studies, described in Ref. 15, scattering properties of enamel plano-parallel polished sections of 30–2000-μm thickness from extracted, un-erupted, human third molars were studied. An automated goniometer with 0.1° angular resolution at excitation on three laser wavelengths 543, 633 and 1053 nm was used. The cylindrical shape of the bath filled up by an index-matching liquid and inserted sample maintained normal incidence for all scattered light and the incident laser beam, thus requiring no subsequent refraction corrections. This is very important when scattering anisotropy is under study.

Fig. 9.5 shows the angular scattering distributions for two, thin and thick, sections of enamel measured at λ = 1053 nm. The scattering distributions for these samples are highly forward directed. All the thin enamel sections exhibited a diffraction pattern in the plane perpendicular to the enamel rods. The rod orientation can be determined by rotating the sample in the laser beam. Since the contribution of the diffraction pattern to the overall scattering distribution is quite small, it can be ignored, especially for thick samples.

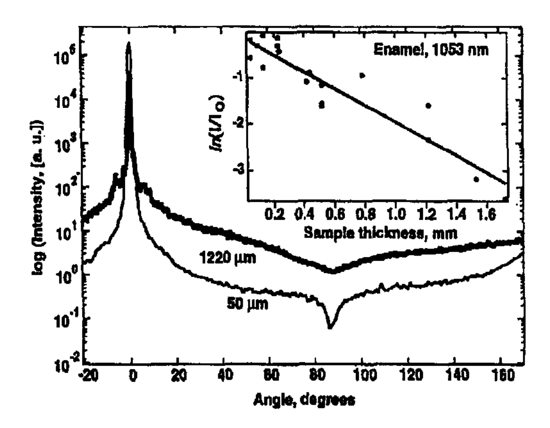


Fig. 9.5. Angular scattering distributions for 50- and 1220-μm-thick sections of enamel at 1053 nm.[15] Insert: transmission of unscattered (ballistic) light, slope $\mu_t = \mu_a + \mu_s \approx$ 18 cm^{-1}. The intensity does not drop to zero (background signal) at 90° (Lambert's cosine law) because of scattered light from the sides of the sample, particularly for thicker samples.

The dependence of collimated transmission on sample thickness, presented in the insert to Fig. 9.5, was measured for the random enamel-rod orientation of the samples. The collimated transmission values were calculated by integrating the scattering distributions from −2° to 2° and dividing by integrated intensity of the laser beam. Basing on these measurements the total attenuation coefficient was estimated $\mu_t = \mu_a + \mu_s$ as ≈ 18 cm^{-1}. A similar analysis for shorter wavelengths, 633 and 543 nm yields significantly higher attenuation coefficients of 60 and 105 cm^{-1}, respectively. These estimates were used as the starting values for subsequent Monte Carlo (MC) simulations. Furthermore, assuming that absorption is negligible, the scattering coefficient wavelength dependence was estimated as $\mu_s \sim \lambda^{-3}$. This scaling law is considerably weaker than Rayleigh scattering ($\sim \lambda^{-4}$) and is indicative of a more complex scattering process.

To simulate light scattering distributions in dental hard tissues authors of Ref. 15 used MC code described in Refs. 39 and 40. The code utilized the index of refraction, the absorption and scattering coefficients, and the g value of each layer to generate a point-spread function of the intensity versus scattering angle. The probability of absorption and scattering was described by exponential law [see Eq. (9.1)], and a Henyey-Greenstein (HG) phase function [see Eq. (9.11)] was used to calculate the polar angle for the new photon propagation direction after each scattering event. Because of complex nature of light scattering, anisotropic (induced by big particles) and isotropic (induced by small particles) scattering components contributions were different for small and big scattering angles, thus in order to fit to entire range of scattering angular dependences a double HG phase function accounting for isotropic and anisotropic portions of scattering was used:

$$p(\theta)=\frac{1}{4\pi}\left[f_d+(1-f_d)\cdot\frac{1-g^2}{(1+g^2-2g\cos\theta)^{3/2}}\right], \tag{9.25}$$

where f_d is the volume fraction of isotropic scatterers ($f_d \leq 1$).

Accurate values of the scattering coefficient (μ_s), the scattering anisotropy factor (g), and the magnitude of the Rayleigh (isotropic) scattering component (f_d) were obtained from the MC simulations based

on the measurements of collimated transmittance and angular scattering distributions of optically thin enamel sections.[15] The magnitude of the ballistic component is given mainly by μ_s; g mostly effects the small-angle scattering, $\theta < 30°$; and f_d primarily determines the scattering profile at $\theta > 30°$. Then the same set of parameters was used to model the scattering distributions measured for thick samples and excellent fit between experimental and calculated angular distributions was found. However, it should be noted that low bulk absorption makes thin sections insensitive to the exact values of the absorption coefficient μ_a, whereas reasonable estimate of μ_a value was obtained from thick samples studies.[15] Determined values of these parameters for $\lambda = 1053$ nm and for two other wavelengths 543 and 633 nm are listed in Table 9.2.

For *in vivo* studies of tooth scattering properties, light reflection and scattering at the enamel surface is important.[13] At a collimated laser beam irradiation the angular distribution of the backscattered light is defined by the enamel surface curvature, surface macroroughness (large surface irregularity compare to the wavelength mostly of genetic nature), and surface microroughness (comparable with the wavelength irregularities). Owing to the first two reasons the specular component of reflected light may change its direction and angular distribution within only a several degrees in dependence of incident light beam location. The third component is diffusive in nature and mostly connected with processes of tooth demineralization. However, some specific precautions should be provided to separate this diffusion component from the bulk diffusion component described above. If successful separation is done (using, for example, a specific wavelength, scattering angle or state of polarization), surface diffuse component may serve as an indicator of tooth surface demineralization process or precaries (white spots detection).

9.4.4 *Scattering Properties of Dentin*

The scattering process in dentin is characterized by a more expressed orientation anisotropy than in enamel.[8,10,12,13,15-17] The scattering can be divided into two major processes[10]: 1) the processes centered symmetrically around the incident beam, caused by randomly oriented

mineral crystals ($\mu_s \sim 10^{-3}$–10^{-4} cm^{-1}) and collagen fibrils ($\mu_s \sim 190$ cm^{-1}), and 2) asymmetrical processes, caused by the oriented tubules ($\mu_s \sim 1400$ cm^{-1}). In these estimates the mineral crystals of dentin was considered as Rayleigh scatterers because their sizes are considerably smaller than the wavelength of light; scattering cross section per collagen fibril was calculated using the formulas for the scattering cross section of an infinitely long cylinder as given by van de Hulst,[27] and for asymmetrical scattering processes Fraunhofer diffraction, the interference of light scattered by a grid of single cylinders, and the interference of light scattered by a grid of concentric double cylinders were accounted for.[10] As it seen in Fig. 9.3 the intertubular butt straps of dentin between approximately equidistant tubules with an axis-to-axis spacing of 6 (±0.5) μm can act as Fraunhofer diffracting slits with an average width of 4.4 (±1) μm. A grid of 140 tubules which corresponds to illumination of the sample by a light beam of 0.83 mm in diameter was considered. It was found that for asymmetric scattering processes the model of the interference of light scattered by a grid of single cylinders is the most appropriate to describe experimental data, thus the tubules can be considered as the predominant scatterers in these processes. The scattering measured in the plane parallel to the tubules is much smaller than in the plane perpendicular to the tubules, but not zero. The reason for none zero scattering in this plane is probably that in real dentin the tubules are not straight circular parallel cylinders.

For dentin samples thicker than 300 μm no scattering anisotropy with respect to the orientation of dental tubules was observed.[15] This observation is partly attributed to continuous change in the orientation of tubules with depth. Such sufficiently thin samples were used for accurate evaluation of values of μ_s, μ_a, g, and f_d from the MC simulations based on the measurements of angular scattering distributions. Determined values of these parameters for $\lambda = 1053$, 543 and 633 nm are shown in Table 9.2.

9.4.5 *Waveguide Effects*

Enamel and dentin waveguide properties also may have effects on anisotropy of light transportation within a tooth.[8,12,13] The role of

waveguides in enamel and dentin is played by enamel prisms and intertubular butt straps, respectively (Fig. 9.6). These waveguides are distinguished from conventional optical fibers by being nonuniform and containing scattering particles, such as hydroxyapatite microcrystals. However, they have waveguide properties and radiation scattered in enamel and dentin can be entrapped by these natural waveguides and transported to the pulp chamber.

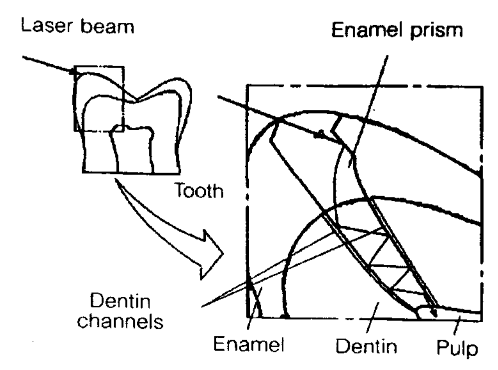


Fig. 9.6. Schematic representation of waveguides in a human tooth.[13]

The waveguide light propagation in a tooth causes the following optical effects[8,12,13]: 1) *Image transmission effect* – each point of the enamel surface is optically connected with a certain point of the pulp chamber surface, thus light distribution on the enamel surface would be transmitted to the pulp chamber surface. Obviously, this image could be rather distorted, because of scattering and waveguide nonuniformity. For instance, 1-mm layer of dentin would limit resolution to 10 lines/mm. 2) *Anisotropy of optical transparency* – light transmission along and transverse to waveguides is not equal. For a section of dentin cut longitudinally and transversally relative to the dental tubules, this difference could be as large as several dozen times. Besides discussed above Fraunhofer diffraction, waveguide effect also could have a considerable influence on orientation anisotropy of transmittance. 3) *Light field compression effect* – this effect is caused by the difference of surface areas of the waveguides at the enamel/dentin junction and at the pulp chamber surface as well as number of waveguides is equal (Fig. 9.6). The light field compression effect can create an increase in

light flux density whenever light is propagating from the enamel/dentin junction to the pulp. Flux density rise is proportional to the ratio of the area of enamel/dentin junction and the part of pulp chamber area that is optically connected with enamel/dentin junction.

9.5 Propagation of Polarized Light in Tissues

9.5.1 *Basic Principles*

Many biological tissues, including tooth tissues, are optically anisotropic.[5-13,15-17,19,31,32,52,53] Tissue birefringence results primarily from the linear anisotropy of fibrous structures. The refractive index of a medium is higher along the length of a fiber than along the cross section. A specific tissue structure is a system composed of parallel cylinders that create a uniaxial birefringent medium with the optic axis parallel to the cylinder axes. This is called birefringence of form. A large variety of tissues, such as tendon, cartilage, eye cornea, sclera and retina, muscle, bone, tooth enamel exhibit form birefringence. All of these tissues contain uniaxial and/or biaxial birefringent structures. For instance, in bone and tooth, these are mineralized structures originating from hydroxyapatite crystals, which play an important role in hard tissue birefringence.[7-9,15-17,52,53]

Form birefringence arises when the relative optical phase between the orthogonal polarization components is nonzero for forwardly scattered light. After multiple forward scattering events, a relative phase difference accumulates and a delay (δ_{oe}) similar to that observed in birefringent crystalline materials is introduced between orthogonal polarization components. For organized linear structures, an increase in phase delay may be characterized by a difference (Δn_{oe}) in the effective refractive index for light polarized along, and perpendicular to, the long axis of the linear structures. The effect of tissue birefringence on the propagation of linearly polarized light is dependent on the angle between the incident polarization orientation and the tissue axis. Phase retardation, δ_{oe}, between orthogonal polarization components, is proportional to the distance (d) traveled through the birefringent medium[54]

$$\delta_{oe} = \frac{2\pi d \Delta n_{oe}}{\lambda_0}. \tag{9.26}$$

A medium of parallel cylinders is a positive uniaxial birefringent medium [$\Delta n_{oe} = (n_e - n_o) > 0$] with its optic axis parallel to the cylinder axes. Therefore, a case defined by an incident electrical field directed parallel to the cylinder axes will be called "extraordinary," and a case with the incident electrical field perpendicular to the cylinder axes will be called "ordinary." The difference ($n_e - n_o$) between the extraordinary index and the ordinary index is a measure of the birefringence of a medium comprised of cylinders. For the Rayleigh limit ($\lambda \gg$ cylinder diameter), the form birefringence becomes.[55]

$$\Delta n_{oe} = (n_e - n_o) = \frac{f_1 f_2 (n_1 - n_2)^2}{f_1 n_1 + f_2 n_2}, \tag{9.27}$$

where f_1 is the volume fraction of the cylinders; f_2 is the volume fraction of the ground substance; and n_1, n_2 are the corresponding indices. For a given index difference, maximal birefringence is expected for approximately equal volume fractions of thin cylinders and ground material. For systems with large diameter cylinders ($\lambda \ll$ cylinder diameter), the birefringence goes to zero.[56]

Linear dichroism (diattenuation), i.e., different wave attenuation for two orthogonal polarizations, in systems formed by long cylinders is defined by the difference between the imaginary parts of the effective indices of refraction. Depending on the relationship between the sizes and the optical constants of the cylinders, this difference can take both positive and negative values.[57] Reported birefringence values for tendon, muscle, coronary artery, myocardium, sclera, cartilage, and skin, contain a considerable amount of collagen fibrils, and tooth enamel, contains fairly well-oriented hexagonal crystals of hydroxyapatite, are on the order of 10^{-3} (see, for instance, Refs. 52–54, 58–64). Such birefringence provides 90% phase retardation at a depth on the order of several hundred micrometers. The magnitude of birefringence and diattenuation are related to the density and other properties of the hydroxyapatite crystals that enamel consist of. In tooth carious early diagnostics, the

polarization state measurements could provide valuable information, since the de- and reminiralization processes of dentin leading to carious lesions change the tooth tissue birefringence.[65]

Although dentin contains a considerable amount of collagen fibrils, no features characteristic of birefringence were observed in its images received by a polarization sensitive optical coherence tomography (PS OCT).[52] That happened because the collagen fibrils in dentin form a structurally irregular network extending over a wide spatial area: they are positioned circumferentially around the surface of the dentinal tubules and between the dental tubules, in general, the course of collagen fibrils is perpendicular to the tubules. Because the fibrils are randomly curved and cross linked within the plane, the birefringence was not observed in PS OCT images of dentin.

9.5.2 *Transillumination Polarization Technique*

Comparison of polarization and conventional transillumination imaging was carried out in Refs. 66 and 67. The absorbing inhomogeneity, such as the absorbing plate placed in a scattering slab (carious lesion model), was probed by a linearly polarized laser beam (Fig. 9.7). The shadow images were reconstructed from the profiles of the intensity and the degree of polarization P of the transmitted light (Fig. 9.8). Note that the dependencies of the degree of linear polarization on the edge position exhibit an increase in P in the vicinity of the edge. The explanation of this peculiarity is similar to that proposed by Jacques *et al.*[68] for the polarization-sensitive detection of backscattered light and is connected with that near the absorber edge, the degree of polarization may be approximately doubled in value (for a highly scattering media) because no $I_{\perp}$ photons are scattered into the shadow-edge pixels by the shadow region, while $I_{//}$ photons are directly scattered into these pixels. The better quality of the shadow images of the object is obtained with the use of the polarization imaging technique in comparison with the conventional transillumination.

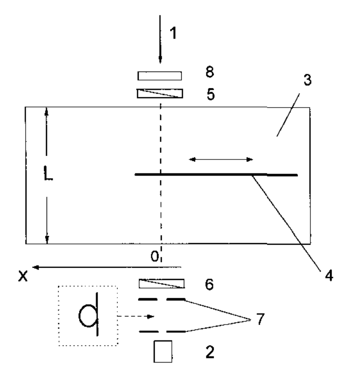


Fig. 9.7. Scheme of the experimental setup for transillumination polarization imaging.[66] 1, Linearly polarized beam of He:Ne laser (633 nm); 2, detector; 3, glass tank filled by scattering medium (diluted milk); 4, absorbing half-plane; 5, polarizer; 6, analyzer; 7, collimating diaphragms or light-collecting optical fiber; 8, chopper.

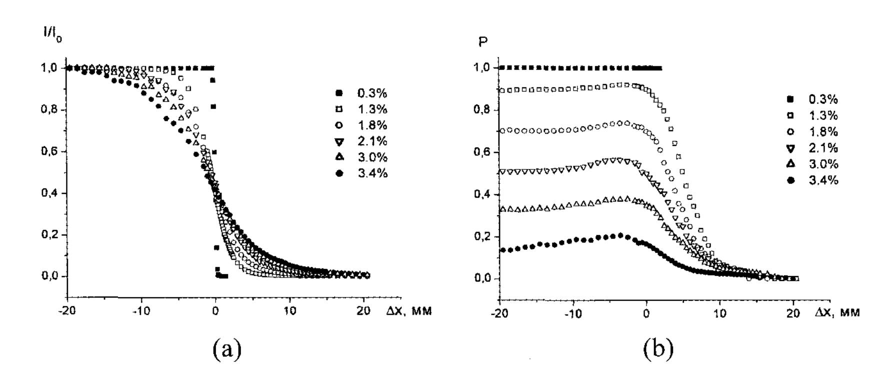


Figure 9.8. Experimental dependencies of (a) the normalized intensity and (b) degree of linear polarization of transmitted light on the absorbing half-plane edge position at different concentrations of the background scattering medium (diluted milk).[66]

9.5.3 *Backscattering Polarization Imaging*

The principle of polarization discrimination of multiply scattered light has been fruitfully explored by many research groups in morphological analysis and visualization of subsurface layers in strongly scattering tissues.[6,19,31,32,66-68] One of the most popular approaches to polarization imaging in heterogeneous tissues is based on using linearly polarized

light to irradiate the object (the chosen area of the tissue surface) and to reject the backscattered light with the same polarization state (co-polarized radiation) by the imaging system. Typically, such polarization discrimination is achieved simply by placing a polarizer between the imaging lens and the object. The optical axis of the polarizer is oriented perpendicularly to the polarization plane of the incident light. Thus, only the cross-polarized component of the scattered light contributes to the formation of the object image. Despite its simplicity, this technique has been demonstrated to be an adequately effective tool for functional diagnostics and for the imaging of underlying tissue layers. Moreover, the separate imaging of an object with co-polarized and cross-polarized light permits separation of the structural features of the shallow tissue layers (such as grooves or fissures in the occlusal surfaces of molars and premolars), and the deep layers (such as dentino-enamel junction, or subsurface lesions). The elegant simplicity of this approach should stimulate its widespread application in both laboratory and clinical dental diagnostics.

A typical system for polarization imaging uses an expanded laser probe beam and a CCD camera with a lens to detect backreflected light and to capture the image. A first polarizer, placed after the beam expander, is used to ensure illumination with linearly polarized light. A second polarizer positioned in front of the CCD camera with its polarization orientation perpendicular or parallel to that of the illumination. The surface image of an object is presented by the co-polarized image and subsurface image – by the cross-polarized. A similar camera system, but one that uses an incoherent white light source such as xenon lamp, is described in Ref. 68. The image processing algorithm used is based on evaluation of the degree of polarization which is then considered as the imaging parameter. Two images are acquires: one "parallel", I_{par}, and one "perpendicular," I_{per}. These images are algebraically combined to yield polarization image:

$$PI = \frac{I_{par} - I_{per}}{I_{par} + I_{per}} \tag{9.28}$$

Important to note that in the polarization image the numerator rejects randomly polarized diffuse reflectance, therefore *PI* may be used to monitor tissue birefringence. Normalization by the denominator cancels in *PI* common to separate polarization components attenuation due to tissue absorption, i.e., superficial dark carious lesions or enamel coloration by tea, coffee, red wine or smoke.

The evaluation of the quality of the polarization images is based on the presentation of multiply scattered light as a superposition of partial contributions characterized by different values of the optical paths s in the scattering medium.[31] The statistical properties of the ensemble of partial contributions are described by the probability density function of the optical paths $\rho(s)$, whereas the statistical moments of the scattered light are represented by the integral transforms of $\rho(s)$ with the properly chosen kernels. The degree of polarization of multiply scattered radiation with initial linear polarization can be approximately represented in the form of the Laplace transform of $\rho(s)$:

$$P_L = \frac{I_{II} - I_{\perp}}{I_{II} + I_{\perp}} \approx \frac{3}{2}\int_0^{\infty} \exp\left(-\frac{s}{\xi_L}\right)\rho(s)ds, \tag{9.29}$$

where I_{II} and $I_{\perp}$ are, respectively, the intensities of the co- and cross-polarized components of the scattered light. The parameter ξ_L is the depolarization length for linearly polarized light.

By considering the polarization visualization of the absorbing macroheterogeneity, with the degree of polarization of backscattered light as the visualization parameter, the contrast of the polarization image can be defined as[31]:

$$V_P = \frac{P_L^{in} - P_L^{back}}{P_L^{in} + P_L^{back}}, \tag{9.30}$$

where P_L^{in} is the degree of residual linear polarization of the backscattered light detected in the region of the localization of the heterogeneity and P_L^{back} is the analogous quantity determined far from the region of localization. The contrast V_P of the reconstructed polarization image can be represented as a function of the scattering

layer thickness l, the depth of inhomogeneity position h, the transport mean free path l_t of the scattering medium, the scattering anisotropy factor g, and the depolarization length ξ_L.[31] The probability density function of the optical paths $\rho(s)$ can be obtained by a Monte Carlo simulation. Comparison of the experimental data and the MC simulations[31,66] allows one to conclude that maximal contrast in the polarization image is obtained at the depth of an inhomogeneity position on the order of $(0.25–0.6)\xi_L$, typically for soft tissues of 100–150 μm.[68]

9.5.4 *In-Depth Polarization Spectroscopy*

Imaging and monitoring of the morphological and functional state of biological tissues may be provided on the basis of spectral analysis of polarization properties of the backscattering light.[69] Tissue probing by a linear polarized white light and measuring of the spectral response of co- and cross polarized components of the backscattered light allow one not only to quantify chromophore tissue content, but also to estimate in-depth chromophore distribution.

In the visible wavelength range dentin may have reduced scattering coefficient $\mu_s' \sim 20\ \text{cm}^{-1}$ and absorption coefficient $\mu_a \sim 3\ \text{cm}^{-1}$ (see Table 9.2), therefore expected transport mean free path of a photon $l_t = (\mu_a + \mu_s')^{-1}$ [see Eq. (17)] is ~ 430 μm. Because of dominating of scatterers with sizes, characterized by a diffraction parameter $ka > 1$, the depolarization length ξ_L in dentin is comparable with the transport scattering length l_t. On the other hand, endogenous and exogenous absorbers in dentin (defining tooth color) must increase the degree of the residual polarization of the backscattered light in the spectral ranges corresponding to absorbing bands of dominating chromophores. Moreover, these chromophores may be concentrated on different depths, thus their localization may be estimated owing to characteristic absorbing bands on the differential polarization spectra.[31,69] Such an instrument is able to measure reflectance spectra at in parallel and perpendicular orientations of filters, $R_{II}(\lambda)$ and $R_{\perp}(\lambda)$, respectively. From these spectra differential residual polarization spectra $\Delta R^r(\lambda)$ or residual polarization degree spectra $P_L(\lambda)$ are calculated:

$$\Delta R^r(\lambda) = R_{II}(\lambda) - R_\perp(\lambda), \tag{9.31}$$

$$P_L^r(\lambda) = \frac{R_{II}(\lambda) - R_\perp(\lambda)}{R_{II}(\lambda) + R_\perp(\lambda)}. \tag{9.32}$$

9.5.5 *Superficial Epithelial Layer Polarization Spectroscopy*

One of the promising approaches to early oral cancer diagnosis may be based on the analysis of a single scattered component of light perturbed by tissue structure.[26,70,71] The wavelength dependence of the intensity of the light elastically scattered by the tissue structure appears sensitive to changes in tissue morphology that are typical of pre-cancerous lesions. In particular, it has been established that specific features of malignant cells, such as increased nuclear size, increased nuclear/cytoplasmic ratio, pleomorphism, etc., are markedly manifested in the elastic light scattering spectra of probed tissue. A specific fine periodic structure in the wavelength of backscattered light has been observed for mucosal tissue.[70] This oscillatory component of light scattering spectra is attributable to a single scattering from surface epithelial cell nuclei and can be interpreted within the framework of Mie theory. Analysis of the amplitude and frequency of the intensity spectrum fine structure allows one to estimate the density and size distributions of these nuclei. However, the extraction of a single scattered component from the masking multiple scattering background is a problem. Also absorption of stroma related to the hemoglobin distorts the single scattering spectrum of the epithelial cells. Both these factors should be taken into account when interpreting the measured spectral dependencies of the backscattered light.

The negative effects of a diffuse background and hemoglobin absorption can be significantly reduced by the application of a polarization discrimination technique in the form of illumination of the probed tissue with linearly polarized light followed by separate detection of the elastic scattered light at parallel and perpendicular polarization states.[26,71] This approach, called polarized elastic light scattering spectroscopy, or polarized reflectance spectroscopy (PRS), will

potentially provide a quantitative estimate not only of the size distributions of cell nuclei but also of the relative refractive index of the nucleus. These potentialities, which have been demonstrated in a series of experimental works with tissue phantoms and *in vivo* epithelial tissues,[26,70-72] allow one to classify the PRS technique as a new step in the development of noninvasive optical devices for real-time diagnostics of tissue morphology and, consequently, for improved early detection of pre-cancers *in vivo*. An important step in the further development of the PRS method will be the design of portable and flexible instrumentation applicable to *in situ* tissue diagnostics on the basis of fiber technology.[73]

9.5.6 *Polarization Microscopy*

Polarized light microscopy has been used in biomedicine for more than a century to study optically anisotropic biological structures that may be difficult or even impossible to observe using a conventional light microscope. A number of commercial microscopes are available on the market, and numerous investigations of biological objects have been made using polarization microscopy. However, modern approaches in polarization microscopy have the potential to enable ones to acquire new and more detailed information about biological cells and tissue structures. At present it is possible to detect optical path differences of even less than 0.1 nm.[31,74] Such sensitivity as well as the capability to examine scattering samples are due to recent achievements in video, interferential, and multispectral polarization microscopy. Full Mueller matrix measurements and other combined techniques, such as polarization/confocal and polarization/OCT microscopy, promise new capabilities for polarization microscopy including *in vivo* measurements.

9.5.7 *Digital Photoelasticity Measurements*

Photoelasticity is another application of polarized light. This technique has wide application in dental biomechanics and has been dealt in detail in the Chapter 2 and Chapter 7 of this book.[75,76]

9.6. Optothermal Radiometry

Pulse laser heating of a tissue causes temperature perturbations and the corresponding modulation of its thermal (infrared) radiation. This is the basis for pulse optothermal radiometry (OTR).[5,7,77-80] The maximum intensity of the thermal radiation of living objects falls at the wavelength range close to 10 μm. A detailed analysis of OTR signal formation requires knowledge of the internal temperature distribution within the tissue sample, the tissue thermal diffusivity, and its absorption coefficients at the excitation μ_a and emission μ_a' (10 μm) wavelengths. At the same time, knowledge of some of the parameters mentioned allows one to use the measured OTR signal to reconstruct, for example, the depth distribution of μ_a.

The characteristic thermal time response of a bioobject is defined by its dimension R_o (the radius for a cylinder form) and the thermal diffusivity of its material a_T (see Ref. 5):

$$\tau_T \sim (R_o)^2 / a_T. \tag{9.33}$$

For many soft human tissues experimental values for the thermal diffusivity a_T lie within the rather narrow range defined by the thermal diffusivity of tissue components: Type I hydrated collagen (50% water), $1.03 \cdot 10^{-3}$ cm^2/s; and pure water, $1.46 \cdot 10^{-3}$ cm^2/s.[5,77] Therefore, the characteristic thermal time response for various organs is mainly defined by their dimensions and can be estimated as 10^{-3} s for a cell, $3 \cdot 10^{-2}$ s for a small blood vessel, and more than 10^3 s for a tongue. For tooth $a_T = 4.09 \cdot 10^{-3}$ cm^2/s, thus expected characteristic thermal time response is of about 10 sec.

The pulse OTR method has good potentialities in the study of the optical and thermal properties of tissues *in vitro* and *in vivo*.[5,7,77-80] Sequences (pairs) of infrared emission images recorded following pulsed laser irradiation were used to determine the thermal diffusivity of the biomaterial with a high precision.[77] The mean thermal diffusivity of an *in vitro* Type I hydrated (50% water) collagen film structure at room temperature (22°C) deduced from 60 recorded infrared emission image pairs is equal to $a_T = (1.03 \pm 0.07) \cdot 10^{-3}$ cm^2/s. The time-resolved OTR was used to determine the absorption coefficients of dental enamel and

dentin at 2.79, 2.94, 9.6, and 10.6 μm.[7] These data are presented in Table 2 and are potentially important in the application of erbium [Er:YSGG (2.79 μm) and Er:YAG (2.94 μm)], or CO_2 (9.6 and 10.6 μm) lasers for the ablation of hard dental tissue. On the other hand, the OTR technique may serve for the online monitoring of tooth ablation or hard tissue depth profilometry for the inspection of dental defects.

The frequency-domain OTR technique uses an intensity-modulated laser radiation for inducing modulation frequency-dependent infrared optothermal radiometric (FD-OTR) signals from tissue lesions or defects.[79,80] The significance to dentistry of this technique is caused by its potentiality to monitor dental lesions at the early stages of carious decay where lateral and subsurface spatial resolution on the order of the crack sizes and subsurface depths investigated in Refs. 79 and 80 (100–300 μm) may be required. FD-OTR exhibits much higher signal-to noise ratio than its pulsed counterpart and a fixed probe depth with the use of a single modulation frequency. For an image to be formed, either the source or the detector must be localized. Photothermal imaging generally falls into category of scanned microscopy with a localized source. The temperature modulation allows for thermal energy to reach the surface diffusively from a depth approximately equal to the length of thermal diffusivity (thermal length), which for the pulse excitation is estimated as[5]

$$l_T \approx \{4a_T \tau_L\}^{1/2}, \tag{9.34}$$

where τ_L is the duration of a laser pulse. Scatterers located within a fraction of a thermal length from the source dominate the contrast of radiometric images. In this way, when the thermal length is varied, e.g., by changing the laser-beam modulation frequency, the region of the specimen that contributes to the image is also varied.

In dental practice, it is often desirable to obtain detailed local information on potential lesions, and inside pits and fissures with high spatial resolution, such as that achieved with a focused laser source. To meet these objectives, recently, a combination of FD-OTR and FD-LUM (luminescence) was used as a fast dental diagnostic tool to quantify sound enamel or dentin as well as subsurface cracks in human teeth.[79,80] Under laser excitation and modulation frequencies in the range from

10 Hz to 10 kHz, it was found that OTR images are complementary to LUM images as a direct result of the complementary nature of nonradiative (thermal) and radiative (fluorescence) deexcitation processes, which are responsible for the OTR and LUM signal generation, respectively. Measurements were performed at the wavelengths 488, 659, and 830 nm.

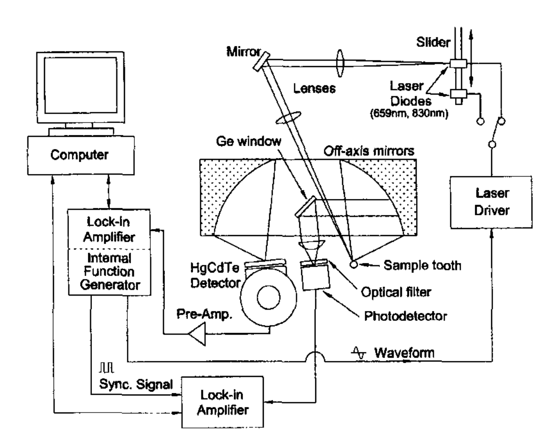


Fig. 9.9. Schematic diagram of experimental setup for combined OTR and LUM monitoring of a tooth.[80]

Figure 9.9 shows the experimental setup combined OTR and LUM probing at two excitation wavelengths provided by 659-nm and 830-nm laser diodes.[80] This method was used to detect artificial and natural subsurface defects in human teeth. It was shown experimentally that OTR is sensitive to very deep (>5 mm) defects at low modulation frequencies (5 Hz). Both OTR and LUM amplitudes exhibit a peal at tooth thickness of 1.4 to 2.7 mm. OTR is sensitive to various defects such as a deep carious lesion, a demineralized area, an edge, a crack, and a surface stain, while LUM exhibits low sensitivity and spatial resolution. OTR frequency scans over the surface of a fissure into demineralized enamel and dentin show higher amplitude than those for healthy teeth, as well as a pronounced curvature in both the amplitude and phase signal channels. These can be excellent markers for the diagnosis of subsurface carious lesions. OTR amplitude-frequency scans over the surface of enamels of variable thickness exhibit strong thickness

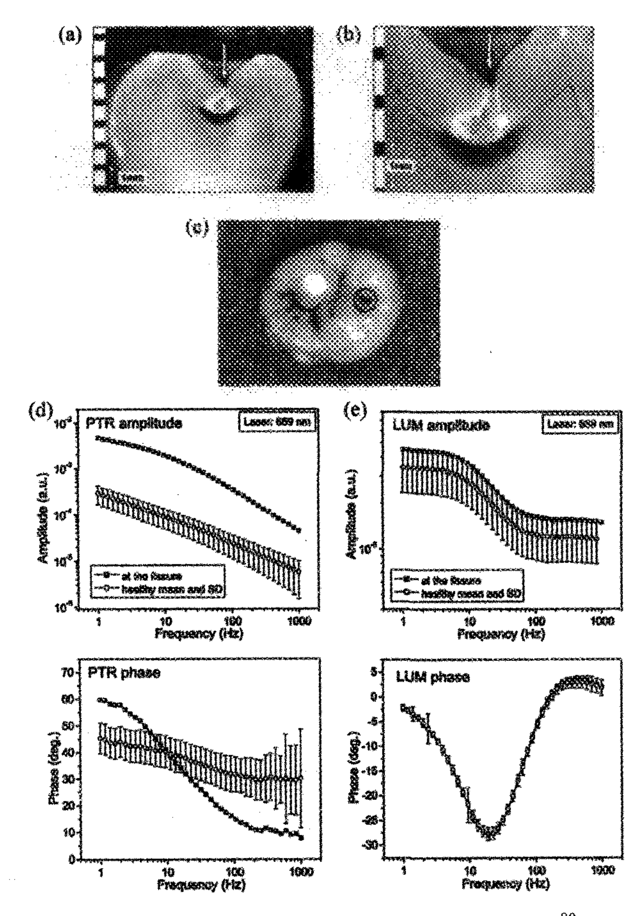


Fig. 9.10. Photographs and experimental results of a sample tooth.[80] (a) Vertical cross-section through the occlusal fissure with the measurement point indicated by a white arrow. (b) A magnified view of (a) showing the extent of subsurface deminiralization (the dense white region around the fissure). The dashed lines indicate the dentin/enamel junction. (c) Biting occlusal surface of the tooth with the measurement area spot circled. (d) Photothermal radiation (PTR) or OTR and (e) LUM amplitude and phase frequency scans at the fissure compared with the healthy mean value and population-weighted standard deviation.

dependence, thus establishing depth profilometric sensitivity to subsurface interfaces such as the dentin/enamel junction.

Figures 9.10a and 9.10b show the cross-section of one of the occlusal fissures. It is clear that the demineralization in quite advanced, spreading

out away from the fissure wall into enamel, the dental/enamel junction, and the dentin. In contrast, visual inspection of the outer edges of the fissure before sectioning, shown in Fig. 9.10c, could not reveal the extent of the demineralization and carious lesions. Fig. 9.10d shows OTR amplitude and phase frequency scans obtained with the laser incident directly on the fissure surface. It is clear that the OTR signal indicates a strong deviation from the healthy signal norm. The amplitude is more than one order of magnitude higher than the healthy mean and exhibits a pronounced curvature around 10 to 20 Hz, instead of the nearly straight-line behavior of the healthy mean-value curve. The OTR phase in Fig. 9.10d also shows features that are remarkably dissimilar to the healthy mean value, both in total phase shift over the frequency range of the scan as well as in the much steeper slope in the range coinciding with the pronounced amplitude curvature. These dissimilarities are expected from the depth profilometric character of OTR since the geometry and thermal properties of the region that produces the signal determine its frequency dependence.

9.7 Thermal Imaging

Thermal imaging is based on sensing the IR radiation that is emitted by all objects at any temperature above absolute zero temperature.[81] Such emission is due to molecular transitions from a high-energy to a low-energy state and for condense media its energy distribution between different wavelengths is described by the Plank curve. At the normal temperature of the human body, the peak of the Plank curve occurs in the mid-IR between 9- and 10-μm wavelengths. The Plank function is exponentially nonlinear in temperature; it follows from this function that the lower-temperature objects emit orders of magnitude less energy than do higher-temperature objects. Human body belongs to the low-temperature objects therefore accurate detection of IR radiation from the body is not simple. Moreover, usually a human body and its surroundings emit comparable amounts of IR energy, which leads to additional difficulties in measurements. Often the SNR is low and to detect signal specialized background correction instrumentation, lock-in signal processing techniques, and careful analysis of the resulting data

are required.[81] The technologies of IR array detectors, associated electronics, image processing, and noise reduction have been significantly improved over the last 10 years. Infrared cameras suitable for medical thermal imaging are reviewed in Ref. 81. At present the accuracy with which temperature and temperature changes can be measured has reached 10^{-3} K.

Many applications of IR thermal imaging have been reported, some of them are overviewed in Ref. 81. The basic measurements involve tissue temperature distributions resulting from a variety of internal and external conditions affecting blood microcirculation and metabolic processes. The thermal imaging was used for detection of tumors, monitoring of inflammatory state of human gingiva, for identifying the health status of the thyroid gland, to measure the depth of burns, in the management of pain, in monitoring surgical tendon repair, and etc. The main disadvantages of thermal imaging for monitoring of any disease state, is its nonspecific nature connected with tissue blood perfusion response and tissue metabolic activity, and providing only surface temperature measurements. Therefore, this technique must be used as an adjunct to other diagnostic techniques and in conjunction with newly designed instrumentation, analytical and numerical computational tools.[81]

9.8 Coherent Effects in the Interaction of Laser Radiation with Tissues and Cell Flows

Speckle structures are produced as a result of interference of a large number of elementary waves with random phases that arise when coherent light is reflected from a rough surface or when coherent light passes through a scattering medium.[5,21,82-85] The speckle phenomenon is a three dimensional interference effect that exists in all points of space where the reflected or transmitted waves from an optically rough surface or volume intersect. Speckles are formed in a free space and are usually observed on a screen placed at a certain distance from an object. Since a tooth is optically nonuniform, its irradiation by a coherent light always gives rise to speckle structures that either distort the results of measurements and, consequently, should be eliminated in some way, or

provide new information concerning the structure and the motion of its components.

Displacement of the observation point over a screen (x) or the scanning of a laser beam over a tooth with a certain velocity v when the observation point remains stationary gives rise to spatial or temporal fluctuations of the intensity of the scattered field. These fluctuations are characterized by the mean value of the intensity $\langle I \rangle$ and the standard deviation σ_I. The object itself is characterized by the standard deviation σ_h of the altitudes (depths) of inhomogeneities and the correlation length L_c of these inhomogeneities (random relief).

Statistical properties of speckles can be divided into statistics of the first and second orders. Statistics of the first order describe the properties of speckle fields at each point. Such a description usually employs the intensity probability density distribution function $p(I)$ and the contrast

$$V_I = \sigma_I / \langle I \rangle, \sigma_I^2 = \langle I^2 \rangle - \langle I \rangle^2, \tag{9.35}$$

where $\langle I \rangle$ and σ_I^2 are the mean intensity and the variance of the intensity fluctuations, respectively. For ideal conditions, when the complex amplitude of scattered light has Gaussian statistics, the contrast is $V_I = 1$ (developed speckles), and the intensity probability distribution function (PDF) is represented by a negative exponential function:

$$p(I) = (1/\langle I \rangle) \exp\{-I/\langle I \rangle\} \tag{9.36}$$

Thus, the most probable intensity value in the corresponding speckle pattern is equal to zero; i.e., destructive interference occurs with the highest probability.

Laser speckle patterns originating from most biological tissues are not "fully developed" in the sense that their intensity distribution does not follow negative exponential relationship [Eq. (9.36)]. Such "partially developed" speckle patterns may have a distinctly different intensity PDF and characterized by a contrast V_I differs from 1. Statistics of the second order show how fast the intensity changes from point to point in the speckle pattern, i.e., they characterize the size and the distribution of speckle sizes in the pattern. The statistics of the second order are usually

described in terms of the autocorrelation g_2 or structural function D_I of intensity fluctuations

$$g_2(\Delta\xi) = \langle I(\xi+\Delta\xi)I(\xi)\rangle,\; D_I(\Delta\xi) = \langle [I(\xi+\Delta\xi) - I(\xi)]^2 \rangle, \quad (9.37)$$

where $\xi \equiv x$ or t is the spatial or temporal variable; $\Delta\xi$ is the change in variable; the angular brackets $\langle\rangle$ stand for the averaging over an ensemble or the time. The structure function is more sensitive to small-scale intensity oscillations. Fig. 9.11 displays typical structure functions measured for normal and pathological tissue—human tooth enamel.[83]

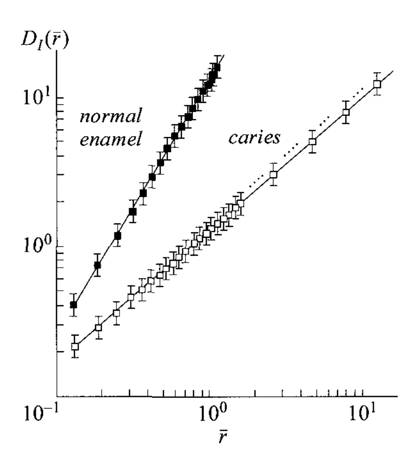


Fig. 9.11. The difference between the structure functions of speckle fluctuations for the scattering of a focused laser beam from normal and pathological (caries) human tooth enamel.[83]

Generally, owing to the considerable contribution of bulk scattering, the reflection of laser radiation from a tooth gives rise to the formation of partially developed speckle structures with comparatively small sizes of speckles, a contrast different from unity, and random polarization of light in individual speckles. In the elementary case when reflected light in speckle structures retains linear polarization, the intensity distribution at the output of a dual-beam interferometer can be written as[5,83]

$$I(r,t)=I_r(r)+I_s(r)+2[I_r(r)I_s(r)]^{1/2}|\gamma_{11}(\Delta t)|\cos\{\Delta\Phi_I(r)+\Delta\Psi_I(r)+\Delta\Phi_I(t)\}, \quad (9.38)$$

where I_r (r) and I_s (r) are intensity distributions of the reference and signal fields, respectively; r is the transverse spatial coordinate; $\gamma_{11}(\Delta t)$ is the degree of temporal coherence of light; $\Delta\Psi_I(r)$ is the deterministic phase difference of the interfering waves; $\Delta\Phi_I(r) = \Phi_{Ir}(r) - \Phi_{sr}(r)$ is the random phase difference; and $\Delta\Phi_I(t)$ is the time-(or temperature) dependent phase difference related to the motion of an object surface. In the absence of speckle modulation, the deterministic phase difference $\Delta\Psi_I(r)$ governs the formation of regular interference fringes.

The speckle correlation fringes compared to the true (deterministic) interference fringes are grainy and display poor contrast. Therefore different fringe processing methods are applied to improve the quality of speckle fringes. For so called electronic speckle pattern interferometry (ESPI), a digital image processing system is used in conjunction with the conventional speckle interferometry arrangement.[86,87] Details description of the principles of ESPI is provided in the Chapter 2 and its applications in dental biomechanics is mentioned in the Chapter 7 of this book.

9.9 Dynamic Light Scattering

9.9.1 *Quasi-Elastic Light Scattering*

Quasi-elastic light scattering (QELS) (photon-correlation spectroscopy, spectroscopy of intensity fluctuations, and Doppler spectroscopy) is related to the dynamic scattering of light.[5,83] The implementation of the single-scattering regime and the use of coherent light sources are of fundamental importance in this case. The spatial scale of testing of a colloid structure (an ensemble of biological particles) is determined by the inverse of the wave vector module:

$$|\bar{q}|^{-1} = (4\pi n/\lambda_0)\sin(\theta/2), \tag{9.39}$$

where n is the refractive index of the ground substance of the medium and θ is the angle of scattering.

With allowance for self-beating due to the photomixing of the electric components of the scattered field, the intensity autocorrelation function

of detected intensity fluctuations for Gaussian statistics is related to the first-order autocorrelation function $g_1(\tau)$ by the Siegert formula:

$$g_2(\tau)=A\left[1+\beta_{sb}\left|g_1(\tau)\right|^2\right], \tag{9.40}$$

where τ is the delay time; $A = \langle i \rangle^2$ is the square of the mean value of the photocurrent, or the baseline; β_{sb} is the parameter of self-beating efficiency; for a monodispersive system of Brownian particles $g_1(\tau) = \exp(-\Gamma_T\tau)$, $\Gamma_T = q^2D_T$ is the relaxation parameter and $D_T = k_BT/6\pi\eta r_h$ is the coefficient of translation diffusion, k_B is the Boltzmann constant, T is the absolute temperature, η is the absolute viscosity of the medium, and r_h is the hydrodynamic radius of a particle.

9.9.2 *Dynamic Speckles*

The specific features of the diffraction of laser beams from moving rough surfaces underlie speckle methods of structure diagnostics and monitoring of blood flows and motion parameters of biological objects, which are easy to implement technically.[5,6,21,31,32,82-85] The fluctuations of individual speckles can be analyzed to provide information about the movement of the scatterers producing the fluctuations. In the case of diffraction of a sharply focused Gaussian beam from a moving rough surface with the Gaussian statistics of phase inhomogeneities and a Gaussian correlation function, the power spectrum of intensity fluctuations in the far-field zone can be represented in the form of a homodyne (I) and heterodyne (II) parts.[88] In the case of thin vessels, a high-frequency peak in the spectrum of intensity fluctuations (the heterodyne part of the spectrum) is appeared owing to the interference interaction of the specular and scattered components. The specular component (in transmission or reflection) serves as a reference wave. The position of the peak on the frequency scale depends on the observation angle. Since the standard deviation of profile fluctuations is small ($\sigma_h << \lambda$), the spectrum $S(\omega)$ of intensity fluctuations features only high-frequency components. By contrast, for a highly scattering media,

because of suppression of the specular component, such interference interaction vanishes, and the spectrum features only the homodyne part. For sufficiently large number of scatterers irradiated by a laser beam ($N > 5$), similar to the QELS spectroscopy, the frequency shift is a linear function of both the velocity of a scatterer and the observation angle of speckles.[89]

9.9.3 *Full-Field Speckle Technique-LASCA*

The contrast of a speckle pattern used as a measure of time-integration of a fluctuating speckle pattern can be employed as a detecting parameter to provide a full-field technique. If the integration time is comparable with the period of the intensity fluctuations caused by dynamic light scattering, it is clear that the effect will be a blurring of the recorded speckle pattern – a reduction in the speckle contrast. The method has been developed into a fully digital, real-time technique for the mapping of blood flow in tissues and called "laser speckle contrast analysis" (LASCA).[82,84]

LASCA uses only a laser with diverging optics, a CCD camera, a frame-grabber and a personal computer. Specially developed software computes the local contrast and converts it to a false-color map of contrast (and hence of velocity). A time-integrated image of a moving object exhibits blurring. In the case of a laser speckle pattern, this appears as a reduction in the speckle contrast, defined as $\sigma_I / \langle I \rangle$ [see Eq. (9.35)]. The higher the velocity, the faster are the fluctuations and the more blurring occurs in a given integration time. As all the *temporal* frequency measurement techniques, LASCA suffers on the problem of relating the correlation time τ_c to the velocity distribution of the scatterers. It is not straightforward and depends on the effects of multiple scattering, the size and the shape of the scattering particles, non-Newtonian flow, non-Gaussian statistics resulting from a low number of scatterers in the measuring volume, spin of the scatterers, etc. Because of the uncertainties caused by these factors, it is common in all these techniques to rely mainly on calibration rather than on absolute measurements.

9.9.4 *Diffusion Wave Spectroscopy*

Diffusion wave spectroscopy (DWS) is a class of studies in the field of dynamic light scattering related to the investigation of the dynamics of particles within very short time intervals.[5,83,90] A fundamental difference of this method compared with the spectroscopy of QELS is that this approach is applicable in the case of dense media with multiple scattering, which is very important for tissues. DWS uniquely suited for the measurements of the average size of particles and their motion within the turbid macroscopically homogeneous highly scattering media. Despite the define similarity between the experiments on DWS and conventional experimental schemes of correlation spectroscopy of optical mixing [see Eq. (9.40)], the DWS theory is based on a qualitatively different interpretation of radiation propagation in strongly scattering media. It is assumed thereby that due to multiple scattering the each photon that has reached given observation point of the detector experiences a great number of scattering events.

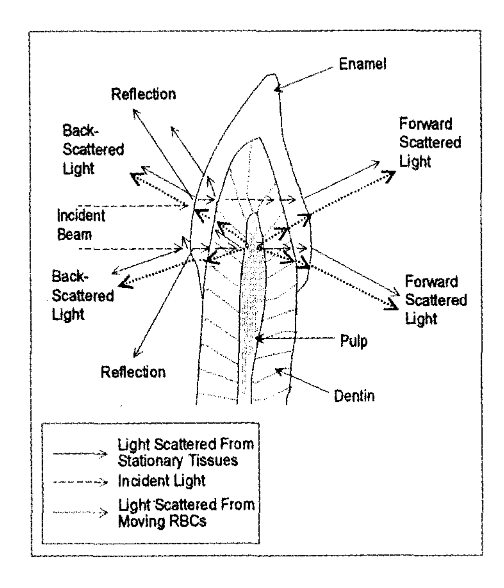


Fig. 9.12. Optical pathways of back-scattered and forward scattered light in a tooth.[92]

9.9.5 *Experimental Studies*

Experimental studies of blood flow in tooth pulp and gingival mucous, corresponding experimental arrangements, and discussion of difficulties in a proper interpretation of measured data can be found in references 91–94. Early papers on pulp blood flow monitoring are overview in reference 93. As it follows from Fig. 9.12, the incident light beam is scattered by moving red blood cells (RBCs), and the probability of photon-RBC interaction is small and should be detected on the background of a significantly scattered light by enamel and dentin. The backscattering geometry, typically used in tooth laser Doppler flowmetry, is less sensitive than a forward scattering technique.[92] In the forward scattering technique the receiving fiber located on the opposite side of the tooth collects only the transmitted light escaping from the tooth surface. The transmitted light contains signal and reference light beams. The reference beam scattered by stationary tissues and the signal beam scattered by RBCs and their product determine the Doppler signal. Both signal and reference beams travel through the whole length of the tooth. Therefore, the ratio of the signal and reference beams is mostly determined by the probability of photon-RBC interaction and independent of optical coupling conditions. Such reference-signal correlation provides a calibration basis for blood flux measurements.

However, as it was shown in reference 93, there is difficult to separate two major inclusions in the Doppler signal from tooth pulp and surrounding gingiva, because due to high scattering in enamel and dentin scattered light penetrates to surrounding soft tissues with intensive blood circulation and being scattered could be easily detected. Various attempts were undertaken to avoid such cross-talk in measurements of tooth pulp blood flow, including placing opaque plastic film in the gingival sulcus, which caused attenuation of light passing through molar and bicuspid teeth, and application of vasoconstricting drugs near the gingival margin.

9.10 Coherent Backscattering

The use of ultrafast laser pulses gives rise to a local peak of intensity backscattered within a narrow solid angle owing to scattered light

interference.[95] In the exact backward direction, the intensity of the scattered light is normally twice the diffuse intensity. Such coherence interference arises from the time reversal symmetry among various scattered light paths in the backscattering direction. The profile of the angular distribution of the coherent peak depends on the transport mean path l_t and the absorption coefficient μ_a. The angular width of the peak is directly related to l_t, $\Delta\theta \approx \lambda/(2\pi l_t)$. In many hard and soft tissues, such as human fat, myocardial, mammary, and dental tissues, the backscattered coherent peak occurs when the probing laser pulse is shorter than 20 ps.[95]

9.11 Optical Coherence Tomography (OCT)

9.11.1 *Introduction*

OCT is analogous to ultrasonic imaging that measures the intensity of reflected infrared light rather than reflected sound waves from the sample. Time gating is employed so that the time for the light to be reflected back, or echo delay time, is used to assess the intensity of backreflection as a function of depth. Unlike ultrasound, the echo time delay of an order of femtosecond cannot be measured electronically due to the high speed associated with the propagation of light. Therefore, time-of-flight technique has to be engaged to measure such ultra-short time delay of light backreflected from the different depth of sample. OCT uses an optical interferometer illuminated by a low coherent light source to solve this problem.

This technique is conventionally implemented with the use of a dual-beam Michelson interferometer. A large number of schemes of coherent optical tomographs for the investigation of tissues have been described in the literature.[5,32,52-54,60-63,96-105] If the path length of light in the reference arm is changed with a constant linear speed v, then the signal arising from the interference between the light scattered in a backward direction (reflected) from a sample and light in the reference arm is modulated at the Doppler frequency $f_D = 2v/\lambda$. Owing to the small coherence length of a light source $l_c \sim \lambda^2/\Delta\lambda$, where $\Delta\lambda$ is the bandwidth of the light source, the Doppler signal is produced by backscattered light only within a very

small region (on the order of the coherence length l_c) corresponding to the current optical path length in the reference arm.

OCT performs cross sectional imaging by measuring the time delay and magnitude of optical echoes at different transverse positions. A cross sectional image is acquired by performing successive rapid axial measurements while transversely scanning the incident sample beam onto the sample. The result is a two-dimensional data set, which represents the optical reflection or backscattering strength in a cross sectional plane through a biological tissue.

9.11.2 *Conventional (Time-Domain) OCT*

Figure 9.13 presents one of the typical time-domain tomographic schemes based on a superluminescent diode (SLD) (λ = 830 nm, $\Delta\lambda$ = 30 nm) and a single-mode fiber optic Michelson interferometer.[102] The power of IR radiation on tissue surface is about 30 μW. The interference signal at the Doppler frequency, which is determined by the scanning rate of a mirror in the reference arm, is proportional to the coefficient of reflection of the nonscattered component from an optical inhomogeneity inside the tissue. One can localize an inhomogeneity in the longitudinal direction by equalizing the lengths of the signal and reference arms of the interferometer within the limits of the coherence length of the light source (~10 μm). Transverse resolution of beam scanning along the surface of a sample is determined by the radius w_0 of the focal spot of probing radiation (usually $w_0 \leq 20$ μm, which should be consistent with the required length of the probed area in the longitudinal direction, which is determined by the length of the beam waist, $2n\pi w_0^2 / \lambda_0$).

The scanning velocity of 50 cm/s, provided by a longitudinal-scanning system based on the fiber optical piezoelectric converter, allows one to acquire images with a size of 2.5×4 mm^2 (axial size × lateral size), resolution of 20×20 μm^2 and acquisition rate of 1 image/second. This OCT system was used for *in vitro* and *in vivo* studies of hard and soft oral cavity tissues.[97] Different types of healthy oral mucosa as well as normal and caries teeth were investigated. It was shown that OCT is able to differentiate various types of keratinized and non-keratinized mucosa

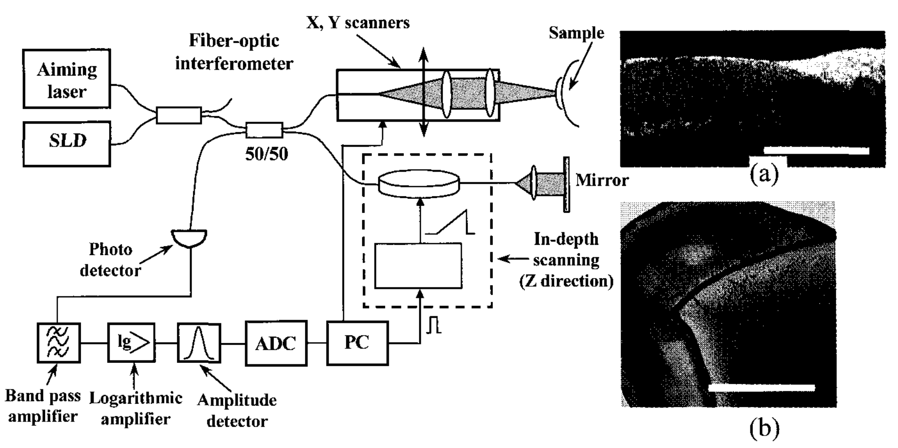


Fig. 9.13. Scheme of a fiber optic OCT system, and images (a) histology (b) dental tissues.[102]

with high resolution, and to give detailed structural information on caries and non-caries lesions in teeth.

In vivo OCT imaging of dental tissues showed that the effective penetration depth of probing radiation in teeth was 2–2.5 mm. The structure and content of dentin is known to be considerably different from those of enamel, thus, allowing differentiation between dentin and enamel and estimation of the state of the dentino-enamel junction (Fig. 9.13).[97] Therefore, due to different optical properties, OCT can differentiate tectorial and hard dental tissues revealing their regular layered structure. It can be used for oral soft tissues premalignancy and malignancy investigations[101] and for noninvasive imaging of tooth caries[96,97] and dental restorations on enamel.[104]

9.11.3 *En-Face* OCT

En-face OCT is a useful extending of the conventional OCT to image dental tissue structures which allows one to see image slices in a similar way as in a microscope.[103] To evaluate the demineralization of bovine teeth a dual imaging OCT/confocal system was used.[98,103] The teeth were painted with two coats of a non-fluorescent acid-resistant colorless nail varnish, except for an exposed window (2 mm × 2 mm) on the labial

surface of the teeth. Caries-like lesions were then produced on each window by 3-day demineralization of the teeth in acidic buffer solution. A pair of *en-face* OCT image and confocal image is displayed in Fig. 9.14. Both the C-scan and B-scan OCT images showed the caries lesion as volumes of reduced reflectivity. The caries appears bright in the confocal image. The confocal image displays an integral of the reflectivity over a large depth, 1 mm and therefore the high reflectivity of the superficial layer is expected to dominate any confocal variations in depth. Again, the confocal channel was instrumental in guiding the investigation.

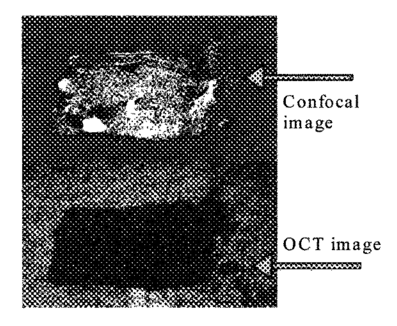


Fig. 9.14. Single frame of confocal and OCT images from a bovine tooth showing the demineralized part. Lateral size: 5 mm × 5 mm. Depth in the OCT image, 0.25 mm from the top of the tooth.[98]

The 3D OCT images of tooth are also possible,[98,103] they show the transversal appearance as well as longitudinal images. On examination of a tooth, the compounding information in rectangular directions, transversal and axial, allows better diagnosis than when using longitudinal OCT imaging only. Successive displays of transversal and longitudinal cuts at different positions in the 3D stack of *en-face* OCT images give a direct view of the caries volume.

9.11.4 *Doppler OCT*

Doppler OCT combines the Doppler principle with OCT to obtain high resolution tomographic images of static and moving constituents in

highly scattering biological tissues.[105] When light backscattered from a moving particle interferes with the reference beam, a Doppler frequency shift occurs in the interference fringe: $f_{Ds} = 2V_s n(\cos\theta)/\lambda_0$, where V_s is the velocity of a moving particle; n is the refractive index of the medium, which is surrounding the particles; θ is the angle between particle flow and sampling beam; and λ_0 is the vacuum center wavelength of the light source. Longitudinal flow velocity (velocity parallel to the probing beam) can be determined at discrete user-specified locations in a turbid sample by measurement of the Doppler shift. Transverse flow velocity can also be determined from the broadening of the spectral bandwidth due to the finite numeric aperture of the probing beam.[105] A fiber optic Doppler OCT was employed in investigations of oral tissue malignancy to quantify blood flow velocity in vessels related to tumor tissue.[101] This is a new approach to the investigation of directed blood flow in subsurface vessels under a layer of a tissue. Electronic data processing allows one to separate the signal characterizing the amplitude of backward scattering, which is necessary for the generation of a stationary tomogram of an object, from the Doppler signal, which characterizes the velocity of scatterers at a given point of an object.

9.11.5 *Polarization Sensitive OCT*

A new technique–polarization-sensitive optical coherence tomography (PS OCT), allows for the measurement of linear birefringence in turbid tissue with high precision.[52-54,60-64] The specificity of conventional OCT can be improved by providing measurements of polarization properties of probing radiation when it propagates through a tissue. Advanced PS OCT systems provide tissue imaging using Mueller-matrix elements[54] or Jones-matrix.[64] In the majority of studies on PS OCT, the criterion of pathological changes in tissue is a measured decrease in tissue macroscopic birefringence. However, there is difficult to provide correct measurements of birefringence on the depths of more than 300–500 μm. For deeper layers (up to 1.5 mm) a much simpler variant of PS OCT – the cross-polarization OCT can be employed.[102] Light depolarization caused by light scattering and tissue birefringence both lead to the appearance of cross-polarized component in the

backscattered light. Pathological processes are characterized by the changes of scattering, absorption and birefringence properties of tissues. In particular, the de- and reminiralization processes finally leading to carious lesion change the birefringence.[53] Therefore, a comparative analysis of cross-polarization backscattering properties of normal and pathological tissues may be used for early diagnosis of tooth caries or oral soft tissue neoplastic processes.

One of the first exploring of PS OCT facilities was its application to eliminate image artifacts caused by birefringence in conventional OCT tomograms, where a two-channel PS OCT system was used to record completely polarization-insensitive OCT images.[96] However, in this case the additional information contained in the polarization state of the light is lost. As it was already stated polarization-sensitive in-depth measurements might be a valuable tool for diagnosing and monitoring the processes related to caries development and growth. It was demonstrated that, in sound enamel, phase changes are small or absent at the enamel surface and at small depths below the surface.[53] These phase changes increase with increasing distance from the surface, at least over the first ~100–300 μm. A phase change of ~ 45° was observed within this optical distance for measurements at buccal and approximal surfaces, well away from the occlusal surface, with the beam orientation nearly perpendicular to the surface of the tooth.[53] Therefore, the beam direction was nearly parallel to the axes of the hydroxyapatite crystals, the deviation being probably less than 5–10°. Assuming an absolute birefringence value of $|\Delta n| \sim 2{\cdot}10^{-3}$, a phase change of 45° over a distance of ~ 500–1000 μm in enamel at a wavelength of 830 nm would be expected, if the beam orientation is 5–10° to the optical axis (which is parallel to the axes of the hydroxyapatite crystals). These estimations compare to the measured values indicate that additional processes, such as light scattering on irregular scatterers, might play a role.

In the area containing a brown spot lesion the observed phase changes are considerably larger than in the surrounding sound enamel. The larger amount of phase change in brown spot material could either be caused by a change of birefringence and/or crystal orientation since the de- and reminiralization processes associated with carious lesions are known to alter the birefringence of the material.[53] Another explanation would be

multiple scattering effects that may cause increase of polarization-sensitivity of tissue at increase of tissue absorption, as it was discussed early in section 9.5.2 (see Fig. 9.8).

Birefringence in enamel and an anisotropy effect of light propagation and scattering parallel and perpendicular to dentinal tubules have been observed by PS OCT.[52] Although dentin contains a considerable amount of collagen fibrils known to be birefringent, no features characteristic of birefringence were observed. Wang et al. explain this observation as caused by a structurally irregular network of the collagen fibrils in dentin extending over a wide spatial area and unlike the crystal prisms in the enamel region, which are arranged in a more orderly fashion parallel and perpendicular to the enamel surface.[52] The analysis of anisotropy of light propagation in dentin allowed authors of Ref. 52 to conclude that the observed variation in light propagation through dentinal tubules may be a combined effect that is due to both scattering anisotropy and light guiding (see discussion in section 9.4).

Using the concept of the measurements of the optical path length of the sample and the apparent displacement of the mirror image, the simultaneous determination of the group refractive index and the physical thickness of enamel and dentin was provided at λ_0 = 856 nm[52] (see Table 9.1). Recently the PS OCT technique was successfully applied for imaging and monitoring of the progression of artificially simulated caries lesions on occlusal surfaces and under composite sealants and restorations.[100] The artificial lesions can be detected under 750 μm of visible opaque sealant and up to 1000 μm of tooth colored sealant.

9.11.6 *Optical Coherence Microscopy*

Optical coherence microscopy (OCM) is a new biomedical modality for cross-sectional subsurface imaging of tissue combining ultimate sectioning abilities of optical coherence tomography (OCT) and confocal microscopy (CM).[99,106] In OCM spatial sectioning due to tight focusing of the probing beam and pinhole rejection provided by CM is enhanced by additional longitudinal sectioning provided by OCT coherence gating. A compact OCM with a flexible sample arm and a remote optical probe for laboratory and clinical environment was developed.[106] To achieve an

axial resolution of the cellular level a light source with an effective bandwidth of 100 nm was used. The light source comprised two SLDs based on one-layer quantum-dimensional (GaAl)As-heterostructures with shifted spectra. Radiations from both SLDs were coupled into polarization-maintaining (PM) fiber by means a multiplexer. The multiplexer was spectrally adjusted in order to achieve the minimum width of auto-correlation function. The dynamic focusing was provided by scanning the output lens of the objective located at the very end of the sample arm. The lens movement was controlled by the electronic system and aligning of the focal spot with the coherence gating during scanning up to depth of 0.5-0.8 mm into a tissue was provided. The spectral sidelobes, caused by non-uniformity of the light source spectrum, were suppressed.

In recent OCM studies of normal and neoplastic oral mucosa samples obtained from human oral biopsy[99] it was found that OCM consistently imaged more deeply compare to confocal microscopy. Extraction of scattering coefficients from reflected nuclear intensity was successful in nonhyperkeratotic layers and shown differentiation between scattering properties of normal and dysplastic epithelium and invasive cancer. The average scattering coefficients measured have shown increase from 27 (±11) cm^{-1} in normal tissue to 39 (±6) cm^{-1} in dysplastic tissue and to 60 (±9) cm^{-1} in squamous cell carcinoma. This increase of scattering in abnormal tissues is associated with the changes in cell nuclear morphology.

9.12 Concluding Remarks

The goal of this chapter was to summarize data on dental tissue optics and to overview different light scattering approaches successfully applied in tissue optics and that already applied or could be potential for designing of noninvasive technologies for tooth and oral soft tissue examination.

As highlighted from this overview, dental and oral tissue optics is mostly understood on the qualitative but not on the quantitative level. Dental tissues are very complex in structure and geometry and teeth have relatively small sizes, thus not all available in tissue optics approaches,

such as, for example, diffusion theory, could be applicable. More comprehensive theoretical approaches accounting tissue structural, scattering, and polarization anisotropy should be developed.

At present diffusion time- and spatially-resolved, polarization-sensitive, optothermal, speckle, and OCT approaches are seemed to be very prospective for designing of noninvasive diagnostic technologies based on dental and soft oral tissue structural and functional imaging and spectroscopy.

Acknowledgments

This work was supported by grant of Federal Agency of Education of RF № 1.4.06 (Optics-2), by Project grant RNP.2.1.1.4473 of the RF Program "The Development of Scientific Potential of the High School (2006–2008)," by CRDF BRHE Project grant RUXO-006-SR-06, and Palomar Medical Technologies Inc.

References

1. *Medical Optical Tomography: Functional Imaging and Monitoring*, vol. IS11, Eds. G. Müller, B. Chance, R. Alfano et al. (SPIE Press, Bellingham, WA, 1993).
2. *Laser–Induced Interstitial Thermotherapy*, vol. PM25, Eds. G. Müller and A. Roggan (SPIE Press, Bellingham, WA, 1995).
3. *Selected Papers on Tissue Optics: Applications in Medical Diagnostics and Therapy*, vol. MS102, Ed. V.V. Tuchin (SPIE Press, Bellingham, WA, 1994).
4. *Selected Papers on Optical Tomography, Fundamentals and Applications in Medicine*, vol. MS 147, Eds. O. Minet, G. Mueller, and J. Beuthan (SPIE Press, Bellingham, WA, 1998).
5. V.V. Tuchin, *Tissue Optics: Light Scattering Methods and Instruments for Medical Diagnosis*, SPIE Tutorial Texts in Optical Engineering **TT38** (SPIE Press Bellingham, WA, 2000).
6. *Handbook of Optical Biomedical Diagnostics*, vol. PM107, Ed. V.V. Tuchin (SPIE Press, Bellingham, WA, 2002).
7. D. Fried in *Biomedical Photonics Handbook*, Ed. Tuan Vo-Dinh (CRC Press, Boca Raton, 2003), p. 50-1.
8. G.B. Altshuler and V.N. Grisimov, *USSR Acad. Sci. Reports* **310**, 1245 (1990).
9. J.R. Zijp and J.J. ten Bosch, *Archs Oral Biol.* **36**, 283 (1991).
10. J.R. Zijp and J.J. ten Bosch, *Appl. Opt.* **32**, 411 (1993).

11. V.N. Grisimov, *Opt. Specrosc.* **77**, 272 (1994).
12. G.B. Altshuler, *J. Opt. Technol.* **62**, 516 (1995).
13. G.B. Altshuler and A.V. Erofeev in *Laser in Dentistry*, Eds. L.J. Miserendino and R.M. Pick (Quintessence Publ. Co, Inc, Chicago, et al., 1995) p. 283.
14. G. Levy and I.M. Rizoiu in *Laser in Dentistry*, Eds. L.J. Miserendino and R.M. Pick (Quintessence Publ. Co, Inc, Chicago, et al., 1995), p. 299.
15. D. Fried, J.D.B. Featherstone, R.E. Glena, and W. Seka, *Appl. Opt.* **34**,1278 (1995).
16. J.R. Zijp and J.J. ten Bosch, *Appl. Opt.* **36**, 1671 (1997).
17. A. Kienle, F.K. Forster, R. Diebolder, and R. Hibst, *Phys. Med. Biol.* **48**, N7 (2003).
18. *Biomedical Photonics Handbook*, Ed. Tuan Vo-Dinh (CRC Press, Boca Raton, 2003).
19. "Special Section on Tissue Polarimetry," Eds. L.V. Wang, G.L. Coté, and S.L. Jacques, *J. Biomed. Opt.* **7**, 278 (2002).
20. J.M. Schmitt and G. Kumar, *Opt. Lett.* **21**, 1310 (1996).
21. D.A. Zimnyakov, V.V. Tuchin, and A.A. Mishin, *Appl. Opt.* **36**, 5594 (1997).
22. J.M. Schmitt and G. Kumar, *Appl. Opt.* **37**, 2788, 1998.
23. C.F. Bohren and D.R. Huffman, *Absorption and Scattering of Light by Small Particles* (Wiley, New York, 1983).
24. *Light Scattering by Nonspherical Particles*, Eds. M.I. Mishchenko, J.W. Hovenier, and L.D. Travis (Academic Press, San Diego, 2000).
25. M.I. Mishchenko, L.D. Travis, A.A. Lacis, *Scattering, Absorption, and Emission of Light by Small Particles* (Cambridge Univ. Press, Cambridge, 2002).
26. V. Backman, R. Gurjar, K. Badizadegan, et al., *IEEE J. Sel. Top. Quant. Elect.* **5**, 1019 (1999).
27. H.C. van de Hulst, *Light Scattering by Small Particles* (Wiley, New York, 1957; reprint, Dover, New York, 1981).
28. H.C. van de Hulst, *Multiple Light Scattering. Tables, Formulas and Applications* (Academic Press, New York, 1980).
29. A. Ishimaru, *Wave Propagation and Scattering in Random Media* (IEEE Press, New York, 1997).
30. E.P. Zege, A.P. Ivanov, and I.L. Katsev, *Image Transfer through a Scattering Medium* (Springer-Verlag, New York, 1991).
31. V.V. Tuchin, L.V. Wang, and D.A. Zimnyakov, *Optical Polarization in Biomedical Applications* (Springer-Verlag, New York, 2006).
32. *Coherent-Domain Optical Methods: Biomedical Diagnostics, Environmental and Material Science*, vol 1 & 2, Ed. V.V. Tuchin (Kluwer Academic Publishers, Boston, 2004).
33. A. Ishimaru, *Appl. Opt.* **28**, 2210 (1989).
34. T.J. Farrell, M.S. Patterson, and B.C. Wilson, *Med. Phys.* **19**, 881 (1992).
35. M. Keijzer, W.M. Star, and P.R.M. Storchi, *Appl. Opt.* **27**, 1820 (1988).
36. G. Yoon, S.A. Prahl, and A.J. Welch, *Appl. Opt.* **28**, 2250 (1989).
37. L.V. Wang and S.L. Jacques, *Comput. Meth. Progr. Biomed.* **61**, 163 (2000).

38. T.J. Farrell and M.S. Patterson, *J. Biomed. Opt.* **6**, 468 (2001).
39. S.L. Jacques, in *Tissue Optics*, Eds. A.J. Welch and M.C.J. van Gemert (Academic Press, New York, 1992).
40. L.-H. Wang, S.L. Jacques, L.-Q. Zheng, *Comput. Meth. Progr. Biomed.* **47**, 131 (1995).
41. I.V. Meglinskii, *Quant. Electron.* **31**, 1101 (2001).
42. F.F.M. de Mul, in *Coherent-Domain Optical Methods: Biomedical Diagnostics, Environmental and Material Science*, vol. 1, Ed. V.V. Tuchin (Kluwer Academic Publishers, Boston, 2004), p. 465.
43. D. Hattery, B. Hattery, V. Chernomordik, et al., *J. Biomed. Opt.* **9**, 951 (2004).
44. M.S. Patterson, B. Chance, and B.C. Wilson, *Appl. Opt.* **28**, 2331 (1989).
45. S.L. Jacques, *IEEE Trans. Biomed. Eng.* **36**, 1155 (1989).
46. W.-F. Cheong, S.A. Prahl, and A.J. Welch, *IEEE J. Quantum Electr.* **26**, 2166 (1990).
47. B. Chance, M. Cope, E. Gratton, et al., *Rev. Sci. Instrum.* **69**, 3457 (1998).
48. D.A. Boas, M.A. O'Leary, B. Chance, and A.G. Yodh, *Phys. Rev. E.* **47**, R2999 (1993).
49. H. Rinneberg, in *The Inverse Problem*, Ed. H. Lübbig (Akademie Verlag, Berlin, 1995), p.107.
50. B.J. Tromberg, L.O. Svaasand, T.-T. Tsay, and R.C. Haskell, *Appl. Opt.* **32**, 607 (1993).
51. J.M. Schmitt, A. Knüttel, and J.R. Knutson, *J. Opt. Soc. Am. A.* **9**, 1832 (1999).
52. X.J. Wang, T.E. Milner, J.F. de Boer, et al., *Appl. Opt.* **38**, 2092 (1999).
53. A. Baumgartner, S. Dichtl, C. K. Hitzenberger, *et al.*, *Caries Res.* **34**, 59 (2000).
54. J.F. de Boer and T.E. Milner, *J. Biomed. Opt.* **7**, 359 (2002).
55. G. Khlebtsov, I.L. Maksimova, V.V. Tuchin, and L. Wang, in *Handbook of Optical Biomedical Diagnostics*, vol. PM107, Ed. V.V. Tuchin (SPIE Press, Bellingham, WA, 2002), p. 31.
56. R.P. Hemenger, *J. Biomed. Opt.* **1**, 268 (1996).
57. M. Born and E. Wolf, *Principles of Optics*, 7th ed. (Cambridge Univ., Cambridge, 1999).
58. D.J. Maitland and J.T. Walsh, *Laser Surg. Med.* **20**, 310 (1997).
59. G.V. Simonenko, V.V. Tuchin, N.A. Lakodina, *J. Opt. Technol.* **67**, 559 (2000).
60. M. R. Hee, D. Huang, E. A. Swanson, and J. G. Fujimoto, *J. Opt. Soc. Am. B.* **9**, 903 (1992).
61. J.F. de Boer, T.E. Milner, M.J.C. van Gemert, and J.S. Nelson, *Opt. Lett.* **22**, 934 (1997).
62. M.J. Everett, K. Schoenerberger, B.W. Colston, Jr., and L.B. Da Silva, *Opt. Lett.* **23**, 228 (1998).
63. J.F. de Boer, T.E. Milner, and J.S. Nelson, *Opt. Lett.* **24**, 300 (1999).
64. S. Jiao and L. V. Wang, *J. Biomed. Opt.* **7**, 350 (2002).
65. E.A. Kidd, *Br. Dent. J.* **155**, 196 (1983).

66. D.A. Zimnyakov and Yu. P. Sinichkin, *J. Opt. A: Pure Appl. Opt.* **2**, 200 (2000).
67. D.A. Zimnyakov, Yu. P. Sinichkin, P. V. Zakharov, and D. N. Agafonov, *Waves in Random Media* **11**, 395 (2001).
68. S.L. Jacques, J. C. Ramella-Roman, and K. Lee, "*J. Biomed. Opt.* **7**, 329 (2002).
69. D.A. Zimnyakov, Yu.P. Sinichkin, and V.V. Tuchin, *Izv. VUZ Radiphysics* **47**, 957 (2005).
70. L.T. Perelman, V. Backman, M. Wallace, *et al.*, *Phys. Rev. Lett.* **80**, 627 (1998).
71. K. Sokolov, R. Drezek, K. Gossagee, and R. Richards-Kortum, *Opt. Express* **5**, 302 (1999).
72. J.R. Mourant, T.M. Johnson, S. Carpenter, *et al.*, *J. Biomed. Opt.* **7**, 378 (2002).
73. A. Myakov, L. Nieman, L. Wicky, U. Utzinger, *et al.*, *J. Biomed. Opt.* **7**, 388 (2002).
74. T.T. Tower and R.T. Tranquillo, *Biophys. J.* **81**, 2954; 2964 (2001).
75. A. Asundi and A. Kishen, *J. Biomed. Opt.* **6**, 224 (2001).
76. A. Kishen and A. Asundi, *J. Biomed. Opt.* **7**, 262 (2002).
77. T.E. Milner, D.M. Goodman, B.S. Tanenbaum, *et al.*, *J. Biomed. Opt.* **1**, 92 (1996).
78. D. Fried, S.R. Visuri, J.D.B. Featherstone, *et al.*, *J. Biomed. Opt.* **1**, 455 (1996).
79. L. Nicolaides, A. Mandelis, and S.H. Abrams, *J. Biomed. Opt.* **5**, 31 (2000).
80. R.J. Jeon, A. Mandelis, V. Sanchez, and S.H. Abrams, *J. Biomed. Opt.* **9**, 804 (2004).
81. J.P. Gore and L.X. Xu in *Biomedical Photonics Handbook*, Ed. Tuan Vo-Dinh (CRC Press, Boca Raton, 2003), p.17-1.
82. J.D. Briers, *Physiol. Meas.* **22**, R35 (2001).
83. V.V. Tuchin, *J. Biomed. Opt.* **4**, 106 (1999).
84. D.A. Zimnyakov, J.D. Briers, V.V. Tuchin in *Handbook of Optical Biomedical Diagnostics*, vol. PM107, Ed. V.V. Tuchin (SPIE Press, Bellingham, WA, 2002), p. 987.
85. S.J. Kirkpatrick and D.D. Duncan in *Handbook of Optical Biomedical Diagnostics*, vol. PM107, Ed. V.V. Tuchin (SPIE Press, Bellingham, WA, 2002) p. 1037.
86. A. Kishen, V.M. Murukeshan, V. Krishnakumar, and A. Asundi, *J. of Dentistry*, **29**, 531 (2001).
87. P. Zaslansky, J.D. Currey, A.A. Friesem, and S. Weiner, *J. Biomed. Opt.* **10**, 024020 (2005).
88. E.I. Galanzha, G.E. Brill, Y. Aisu, et al. in *Handbook of Optical Biomedical Diagnostics*, vol. PM107, Ed. V.V. Tuchin (SPIE Press, Bellingham, WA, 2002), p. 881.
89. P. Starukhin, S. Ulyanov, E. Galanzha, and V. Tuchin, *Appl. Opt.* **39**, 2823 (2000).
90. M.H. Kao, A.G. Yodh, and D.J. Pine, *Phys. Rev. Lett.* **70**, 1993, 242 (1993).
91. E.R. Ingofsson, L. Tronstad, E.V. Hersh, and C.E. Riva, *Endod. Dent. Traumatol.* **10**, (1994).
92. D.Y. Zang, P. Wilder-Smith, J.E. Millerd, and A.M.A. Arrastia, *J. Biomed. Opt.* **2**, 304 (1997).

93. M.E. Fein, A.H. Gluskin, W.W.Y. Goon, et al., *J. Biomed. Opt.* **2**, 58 (1997).
94. A.V. Sedykh, N.A. Kharish, A. Karpovich, *et al.*, Proc. SPIE **4241**, 216 (2001).
95. K.M. Yoo, F. Liu, and R R. Alfano, *J. Opt. Soc. Am. B.* **7**, 1685 (1990).
96. B.W. Colston, Jr., M.J. Everett, L.B. DaSilva, et al., *Appl. Opt.* **37**, 3582 (1998).
97. F.I. Feldchtein, G.V. Gelikonov, V.M. Gelikonov, *et al.*, *Opt. Express* **3**, 239 (1998).
98. B. Amaechi, A. Podoleanu, G. Komarov, et al., *Laser Physics* **13**, 703 (2003).
99. A.L. Clark, A. Gillenwater, R. Alizadeh-Naderi, et al., *J. Biomed. Opt.* **9**, 1271 (2004).
100. R.S. Jones, M. Staninec, and D. Fried, *J. Biomed. Opt.* **9**, 1297 (2004).
101. P.Wilder-Smith, T. Krasieva, W.-G. Jung, et al., *J. Biomed. Opt.* **10**, 051601 (2005).
102. L.S. Dolin, F.I. Feldchtein, G.V. Gelikonov, *et al.* in *Coherent-Domain Optical Methods: Biomedical Diagnostics, Environmental and Material Science*, vol. 2, Ed. V.V. Tuchin (Kluwer Academic Publishers, Boston, 2004), p. 211.
103. A. Podoleanu in *Coherent-Domain Optical Methods: Biomedical Diagnostics, Environmental and Material Science*, vol. 2, Ed. V.V. Tuchin (Kluwer Academic Publishers, Boston, 2004), p. 163.
104. L.S.A. de Melo, R.E. de Araujo, A.Z. Freitas, *et al.*, *J. Biomed. Opt.* **10**, 064027 (2005).
105. Z. Chen in *Coherent-Domain Optical Methods: Biomedical Diagnostics, Environmental and Material Science*, vol. 2, Ed. V.V. Tuchin (Kluwer Academic Publishers, Boston, 2004), p. 315.
106. G.V. Gelikonov, V.M. Gelikonov, S.U. Ksenofontov, *et al.* in *Coherent-Domain Optical Methods: Biomedical Diagnostics, Environmental and Material Science*, vol. 2, Ed. V.V. Tuchin (Kluwer Academic Publishers, Boston, 2004), p. 345.
107. F.A. Duck, *Physical Properties of Tissue: a Comprehensive Reference Book* (Academic Press, London, 1990).
108. M. Ohmi, Y. Ohnishi, K. Yoden, and M. Haruna, *IEEE Trans. Biomed. Eng.* **47**, 1266 (2000).

CHAPTER 10

FIBER OPTIC DIAGNOSTIC SENSORS

Anil Kishen

Biophotonics Laboratory, Department of Restorative Dentistry,
National University of Singapore
Republic of Singapore 119074
E-mail: rsdak@nus.edu.sg

Fiber optic technology offers different advantages when applied for diagnosis in health care. This chapter provides an introduction to fiber optics and discusses different configurations and applications of fiber optic based, direct and indirect, diagnostic sensors. Relevant examples of fiber optic diagnostic sensors applied to dentistry are also presented.

10.1 Introduction

When light travels from air to glass a major portion of it is transmitted into glass, and this phenomenon is called refraction. Refraction also occur if light is transmitted nearly perpendicular to the interface from glass into air. Nevertheless, if a light beam is launched from glass to air at an angle of about 45° or more with respect to the normal to the interface, the light is totally reflected back into the glass. This phenomenon is called total internal refection. In 1870, John Tyndall used a jet of water that flowed from one container to another and a beam of light to demonstrate that light used total internal reflection to follow a specific path. The beam of light in this case made a zigzag path inside the water column without escaping into the air. Similarly, light can also travels from one side of a glass slab to the other side by a series of total internal reflection.

Optical fibers are thin, transparent, flexible rod of glass which can transmit light by total internal reflection, even if they are bent or flexed. The optical fiber primarily consists of two parts: (1) inner glass or core and (2) outer glass or polymer coating or cladding. The core is used to transmit the light, while the cladding prevented the light from leaking out of the core by reflecting the light back into the core. This principle is explained by Snell's Law, which states that the angle at which light is reflected at the core-cladding interface is dependent on the refractive index of the core and the cladding materials. The low refractive index of the cladding with respect to the core causes the light to be angled back into the core as illustrated in Fig. 10.1. Absence of cladding will allow light to leak out of the core.[1-4]

10.2 Fiber Optics in Diagnosis

Routinely diagnostic techniques are classified into two types: (1) Invasive and (2) non-invasive. The invasive methods require piercing the tissue, and they are often accurate and reliable. The non-invasive methods do not require penetration into the body. They do not cause pain to the patient and are potentially safe. Optical fibers are the basis for the family of minimally invasive diagnostic tools called fiber optic diagnostic sensors (FODS). A sensor is device in which changes in certain parameters called measurand produces corresponding changes in energy called signal. A thermocouple is a common example for a sensor. In a thermocouple, changes in temperature (measurand) produce changes in voltage (signal). In a sensor, the measurand can be (1) mechanical factors such as pressure, flow, weight, color, and light intensity, or (2) chemical factors such as chemical composition, pH, partial pressure of carbon dioxide and partial pressure of oxygen.[4]

The ideal requirements of a sensor system are the following. (1) Specificity: The ability to measure only a particular parameter without being effected by others. (2) Sensitivity: The ability to measure small changes of a given parameter. (3) Accuracy: The ability to give an accurate and stable measurement of a parameter. (4) Cost: Low cost would enable the sensor to be disposable. The fiber optic diagnostic

sensors have all these requirements, including the following advantages. (1) Miniaturization: They are based on very thin fibers and can easily be inserted into inaccessible locations in the body. This enables the clinicians to carry out real time in vivo measurements. (2) Biocompatibility: Materials used to fabricate fiber optics are non-toxic and biocompatible with tissues. (3) Accuracy: Fiber optic sensors are in principle fast, stable and accurate. (4) Immunity from Electromagnetic Radiation: Since fiber is made from dielectric (non-conductive) materials, it is unaffected by electromagnetic radiation. (5) Safety: Since no electrical power is involved they are potentially safe. (6) Versatility: Fiber optics serves analytical sciences in several ways. First they enable optical spectroscopy to be performed on locations inaccessible to conventional spectroscopy, over large distances, or even on several spots along the optical fiber. Secondly, fiber optic sensor enables detection of several analytes simultaneously. (7) Portability of the system: The system is lightweight and easy to get started.

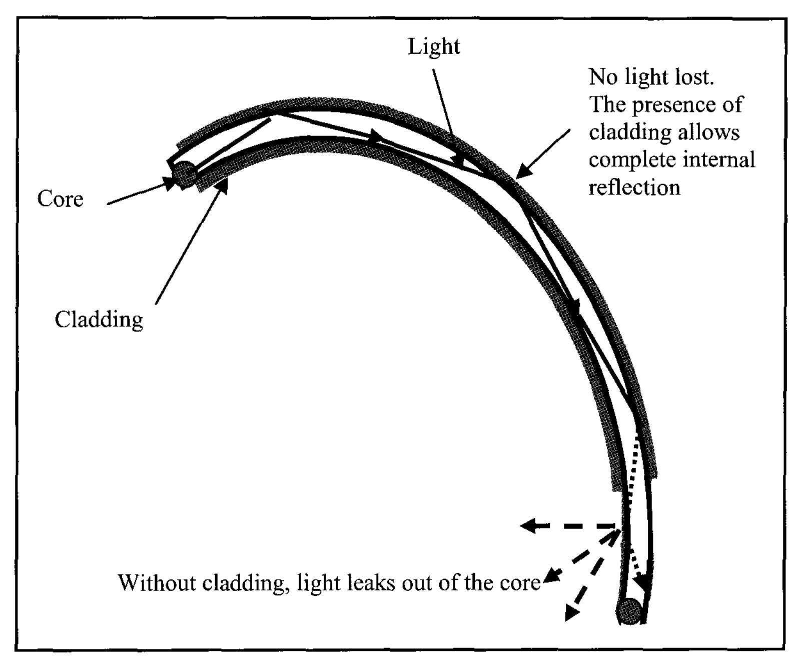


Fig.10.1. Propagation of light through an optical fiber with cladding.

10.3 Fiber Optic Diagnostic Sensors: Principles

Optical properties are intrinsic properties that characterize biological tissues and fluids. They do not depend on the geometry of the structure. Reflection, absorption, scattering, and fluorescence are some of the optical properties that are used to characterize biological tissues. Therefore a simple fiber optic sensor system can be designed by using two thin optical fibers. Light at a particular wavelength is transmitted through one of the fibers, while the reflected or scattered or absorbed light is collected and transmitted through the second optical fiber to a detector. The signal obtained from the detector is proportional to the optical spectrum of biological tissue. In some case the ends of the optical fibers are bare and diagnosis is made by direct interaction between light and tissue sample. This sensor is called direct fiber optic sensor (DFOS). DFOS is used to measure the intrinsic optical properties of the biological tissues. The indirect fiber optic sensor (IFOS) utilizes an optical transducer called an optrode for sensing. The optrode is usually attached to the end of the optical fibers. Light launched through the first optical fiber interacts with the optrode, which in turn interacts with the sample producing optically detectable signals. In both cases, the optical fibers are merely a medium for transmitting light into the sample and collecting light from the sample. The FODS allows investigation of tissues in the inaccessible areas without tissue removal or penetration (non-invasive). Schematic diagrams of general types of FODS are shown in Fig. 10.2 (A and B). FODS that measure physical parameters such as pressure and temperature are called physical sensors. While the FODS that measure chemical parameters such as pH, oxygen or glucose can be called as chemical sensors. Biosensors are a subtype of chemical sensors in which the sensing method utilizes a biological component such as antigen or antibody.[4]

10.4 Direct Fiber Optic Sensors: Principles

Different configurations of direct fiber optic sensors are shown in Figure 10.3. In direct fiber optic sensors, light is coupled into the proximal end of an optical fiber, and is transmitted to the distal end,

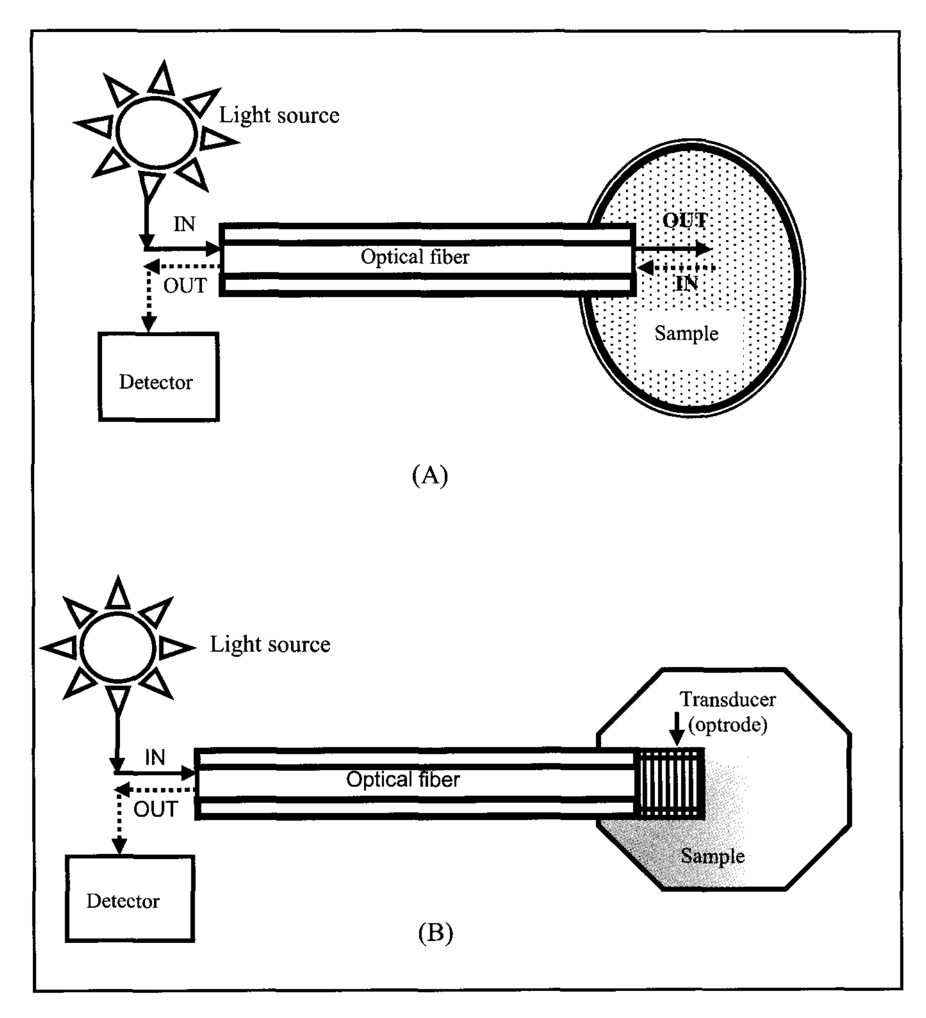


Fig.10.2. Fiber optic diagnostic sensors (A) direct fiber optic sensor (B) indirect fiber optic sensor.

where the sensing is carried out. The input light emerging from the optical fiber interacts directly with the sample, generating the output light. Most of the output light may be collected by a second optical fiber as shown in Fig. 10.3, and transmitted back to the proximal end. The proximal end of the second optical fiber is connected to a detector, spectrophotometer or an optical processing system. The information

obtained from the output light is used for sensing biological parameters. Alternative to the two optical fiber design, fiber optic bundle may also be used. When a fiber optic bundle is utilized, some fibers are used to deliver input light to the sample and some fibers are used to collect output light from the sample. This arrangement is called bifurcated fiber optic bundle, and is shown in Fig. 10.4. Optical properties such as reflectance, fluorescence and absorption of tissues can be measured by the direct fiber optic sensors. The absorption in a sample can also be directly measured by using the principles of evanescent wave absorption. As shown in Fig. 10.3 (D), the evanescent wave based sensor utilizes mostly a single optical fiber. The details about evanescent wave based fiber optic sensor are presented in the section on Biosensors. The direct fiber optic sensors are classified as: physical and chemical sensors, based on the nature of measurands.

10.4.1 *Direct Fiber Optic Physical Sensors*

Reflectance measurements using fiber optics is an example for direct physical sensor. Reflectance measurements are used to evaluate the superficial microcirculation of the skin. Light at 700 nm wavelength is observed to penetrate deep into the skin and is used for this purpose. Temperature is another parameter that is determined using direct fiber optic physical sensor. The fiber optic direct temperature sensor consists of an infrared (IR) detector and an IR optical fiber. The IR emission from a surface is collected by the optical fiber and is measured by the detector. They can be used to monitor tissue temperature during laser surgery.

10.4.2 *Direct Fiber Optic Chemical Sensors*

Fiber optic direct chemical sensors measures optical properties such as reflection, absorption and fluorescence from natural biological tissues or from some reagents, which are introduced into the tissue. Fiber optic oxygen sensor and fiber optic laser induced fluorescence sensor are some examples under this category. Optical methods used to monitor the

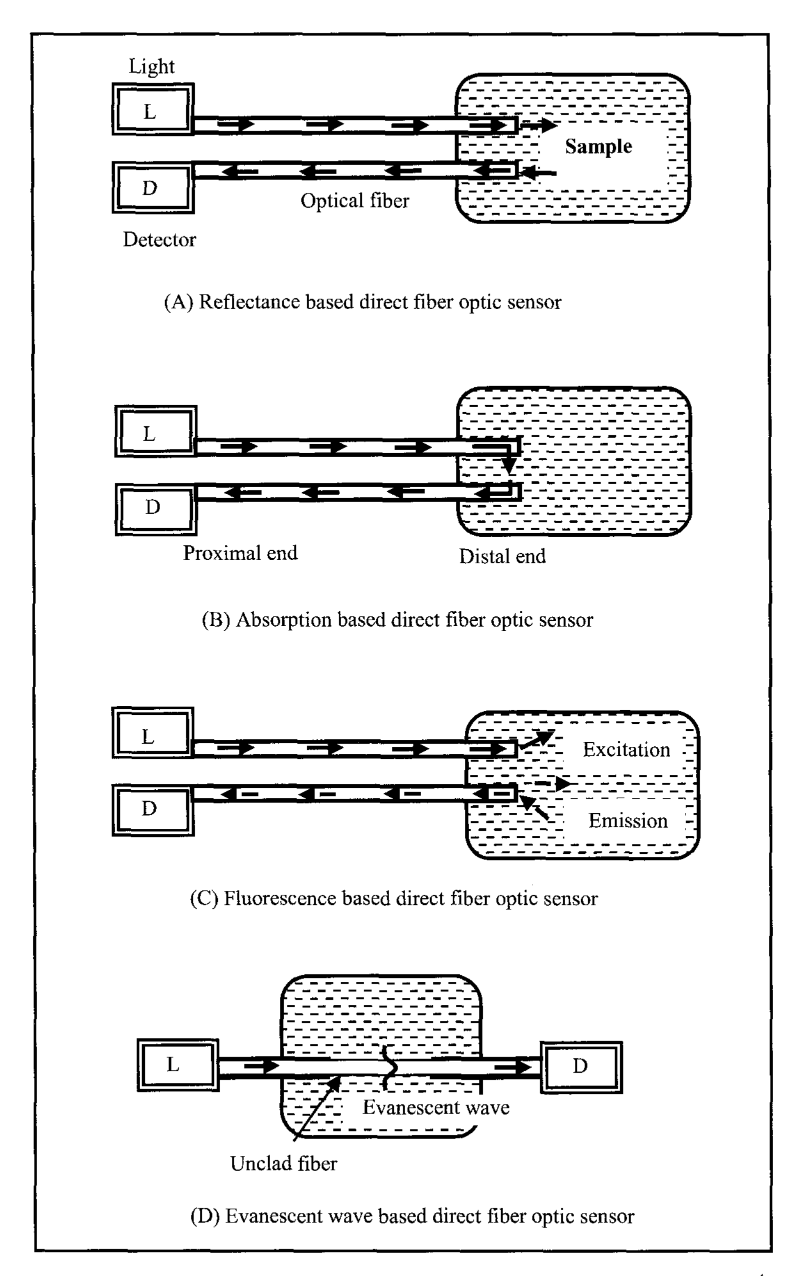


Fig.10.3. Different configurations of direct fiber optic diagnostic sensors.[4]

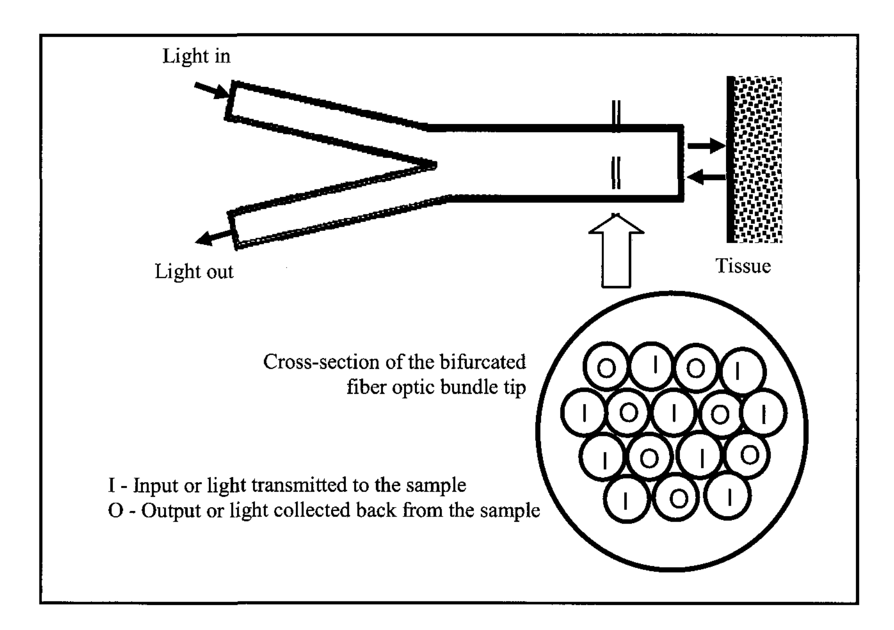


Fig.10.4. Bifurcated array of optical fibers for direct sensing.[4]

oxygen saturation are based on the different optical properties of saturated and reduced hemoglobin. The obvious difference between oxyhemoglobin and reduced hemoglobin is in the 620 nm (wavelength) region of the spectra.[4]

Laser induced fluorescence (LIF) techniques are well suited for systems that are based on lasers and optical fibers. LIF can be performed by both imaging method and non-imaging method. In an imaging based LIF technique fiber optic imaging bundles are used to acquire the fluorescence image of an area. In a non-imaging LIF technique, optical fibers are used to transmit the laser beam to excite the tissue and collect the light beam emitted from the tissue. There are two types of tissue fluorescence. (1) The natural, intrinsic fluorescence of the tissue, which is referred to as autofluorescence or endogenous fluorescence. Intrinsic fluorescence is produced by proteins, nucleic acids, and nucleotide coenzymes that are naturally present in biological tissues. The emission peak of collagen and elastin is at 380 nm, while melanin has a broad emission peak at 540 nm. (2) The extrinsic or exogenous fluorescence is produced by a reagent that is added to the tissue. Porphyrin compounds

are examples of exogenous fluorescence. These compounds when injected into the body show preferential accumulation in malignant tumor cells. The fluorescence of hematoporphyrin derivative is mostly in red. These non-toxic compounds are used for the detection of tumor cells.

Nicotinamide adenine dinucleotide (NAD) and reduced nicotinamide adenine dinucleotide (NADH) are used to measure alterations in the cell metabolism. In normally functioning cells, the ratio of NAD and NADH varies over a large range. Metabolic imbalance in the cell due to lack of oxygen (anoxia) or lack of blood supply (ischemia) will lead to 100% reduction of NAD to NADH, and this will lead to cell death. NADH absorbs UV light in the spectral range of 250 nm–400 nm, and emits visible light fluorescence which peaks in the spectral range 460 nm–480 nm. Since NAD does not fluoresce, the luminescence intensity is linearly proportional to the number of NADH molecules. Endogenous fluorescence from NADH is therefore directly correlated to the viability of the cell. Plasma emission from stones or calculus is also used for direct chemical sensing. When high energy laser impinge on urinary or biliary stones which are immersed in liquids, they generate plasma, which is accompanied by light emission.[5] The emitted light can be characterized using fiber optic spectroscopy to determine the concentrations of calcium in the stone. This sensor can be used for the diagnosis of pathological calcifications and for guidance during laser fragmentation of stones.

10.5 Indirect Fiber Optic Sensors: Principles

An indirect fiber optic sensor utilizes an optical transducer attached to the distal tip of the optic fibers (optrode). The input light passes through the optical fiber and activates the transducer, which in turn interact with the sample. The output light collected from the transducer is analyzed by an optical detection system. Different optical configurations used for indirect fiber optic sensor is shown in Fig. 10.5. In an indirect physical sensor, a physical optrode is used to measure physical parameters such as temperature or pressure. In an indirect chemical sensor, a chemical optrode is used to measure chemical parameters such as pH or protein.

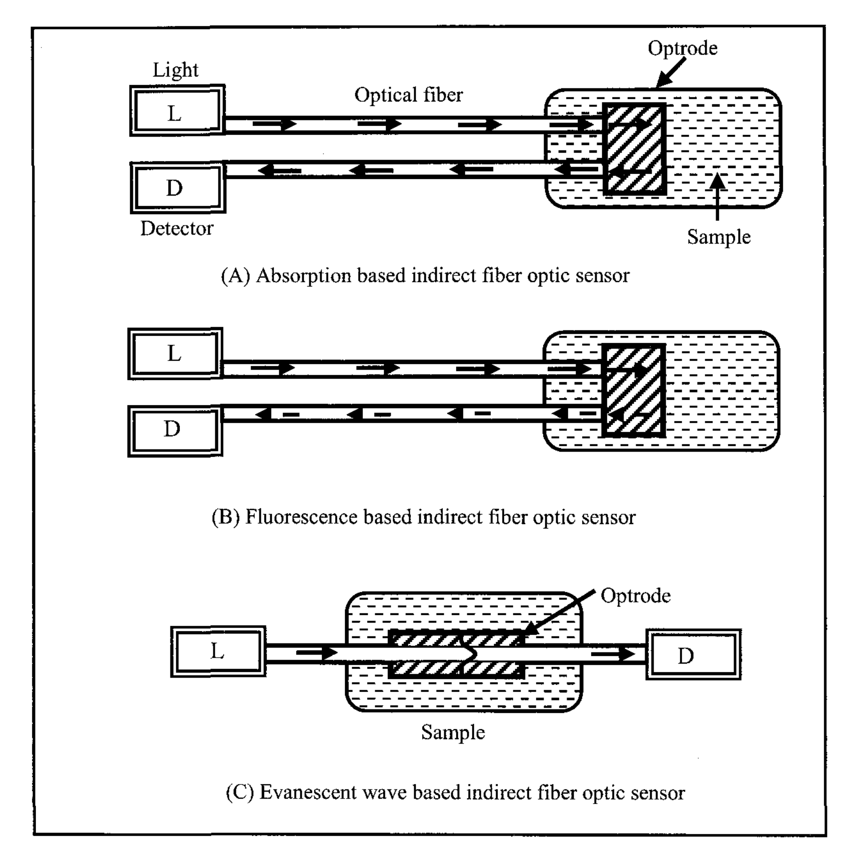


Fig.10.5. Indirect fiber optic diagnostic sensors.[4]

10.5.1 *Indirect Fiber Optic Physical Sensors*

Indirect physical sensors also utilize optical properties such as absorption, and fluorescence from the optrode for the measurements of physical parameters from samples. A schematic illustration of a fiber optic pressure sensor is shown in Fig. 10.6. Light is launched through an optical fiber and is reflected back from a thin diaphragm. The diagram will be pressure responsive. Under a particular pressure, the diaphragm is flat, and under these conditions, certain light is reflected from the diaphragm. When the optrode is exposed to higher pressure, the diaphragm is curved and a different amount of light is reflected back.

There is a correlation between the amount of light reflected through the optical fiber and the pressure of the liquid. The reflected light, which is related to the pressure, may be quantified by a photodetector. Pressure sensing optical transducers are also developed based on the displacement of a mirror and bending of a membrane. In vivo experiments using fiber optic pressure sensor have been conducted to monitor blood pressure as well as pressure in the bladder, urethra, and rectum.[6] Fiberoptic indirect temperature sensors have also been developed using optrodes in which the physical properties changes as a function of temperature. The property of liquid crystals to produce conspicuous color change in response to temperature, and the property of lanthanum oxysulfide activated with europium to produce increased luminescence emission intensity with temperature is utilized for temperature sensing.

Structural Health Monitoring (SHM) is a rapidly growing field in structural engineering and is a valuable technology to monitor structural defects such as cracks, interfacial failures, and variation of strains in mechanical structures non-destructively. This technology is useful to reduce life-cycle costs and to improve reliability in mechanical structures. Fiber optic based structural health monitoring sensors are based on the principle that physical bending has a significant effect on the light beam traveling in an optical fiber. In a straight fiber, the angle between the light ray and the normal to the plane of reflection is defined by an angle θ_o. However, when the fiber is bent, the plane of reflection and the reflective ray will rotate by an angle δ. Therefore, for a curved fiber, the angle between the reflected ray and the tangent will be θ_o-δ. In a straight fiber, when $\theta > \theta_c$ (critical angle), the rays will be total internally reflected. While, in a bent fiber, the effective critical angle is reduced by δ, and consequently the ray incident between θ_c and (θ_c-δ) will be lost through the cladding of the fiber.[7,8] The principle of fiber optic microbending (FOMB) is shown in Fig. 10.7. In a FOMB sensor, certain length of bare fiber optic cable is sandwiched between two undulated pieces of rigid metal or plastic padding to form the transducer element of the microbend sensor. Prior to testing, the fiber optic is straight within the transducer portion and the light, which is launched at one end of the fiber, is monitored at the other end without any loss. When an external load is applied on the transducer element of the FOMB

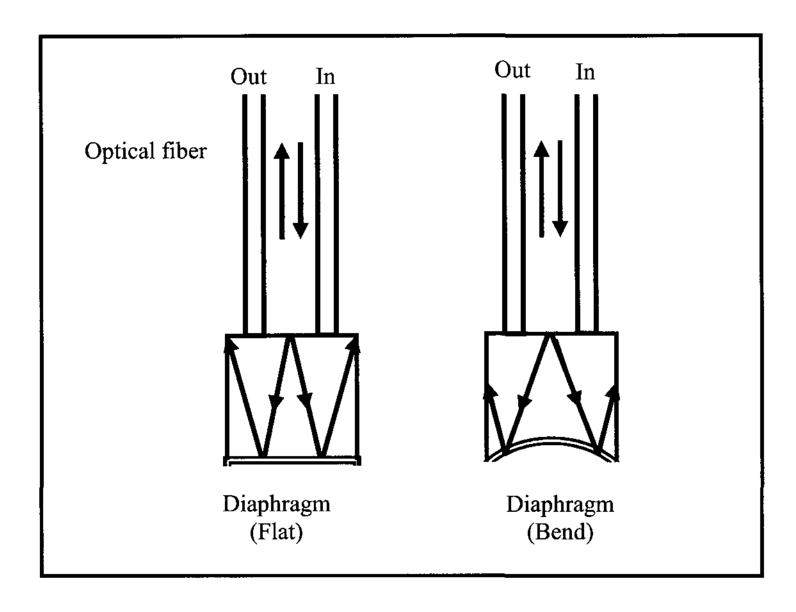


Fig.10.6. Indirect fiber optic pressure sensor.[4]

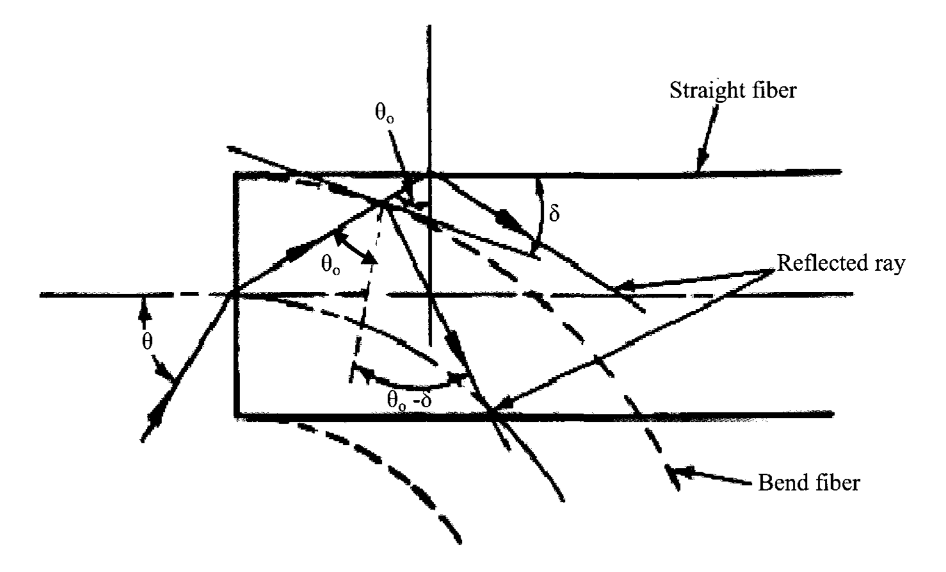


Fig.10.7. Illustrates the principle of the Fiber optic Microbend sensor.[7]

sensor, microbending and physical changes of the fiber optic cable occurs, resulting in the reduction of output light intensity.[7] The load versus output light intensity curve obtained from this sensor can be used to measure biting forces and to monitor tooth structural response to loads.

10.5.2 *Indirect Fiber Optic Chemical Sensors*

Indirect chemical sensors are used to determine pH, blood glucose content, and other chemical substances from biological samples. In a fiber optic pH sensor, an optrode is attached to the distal end of the optical fiber and is coated with a thin protective coating which permits only small ions such as hydrogen ions to permeate and interact with the optrode. When the fiber optic sensor tip is inserted into the sample, the interaction of the biological fluid with the optrode would give rise to optical changes. Routinely, indirect chemical sensors utilize optical properties such as absorption of an indicator or changes in the luminescence properties for sensing parameters in biological samples. Dye-immobilized polymer (matrix-entrapment) optrode, membrane-bound reagent (membrane-entrapment) and optical fiber bound regents (surface adsorption) are different optrode designs used in indirect chemical sensors. Some of the common optical configurations used for fiber optic indirect chemical sensors are shown in Fig. 10.8. Fiber optic indirect chemical sensors offer many advantages such as electrical safety, flexibility, low cost and disposability over the conventional microelectrodes.

A pH indicator is known to indicate the acidity or alkalinity of a solution by changing its color. Fiber optic pH sensors are commonly based on the color change produced by pH indicators. The color change produced by the pH indicator is quantified by measuring the optical absorption of the dye. In one fiber optic pH sensor, the dye is attached to polymeric microspheres and is packed near the tip of the optical fiber, and is later encapsulated by a thin membrane. The small sized microspheres has been found to assist the scattering of light in the optrode. Light from the input fiber is partly scattered by the

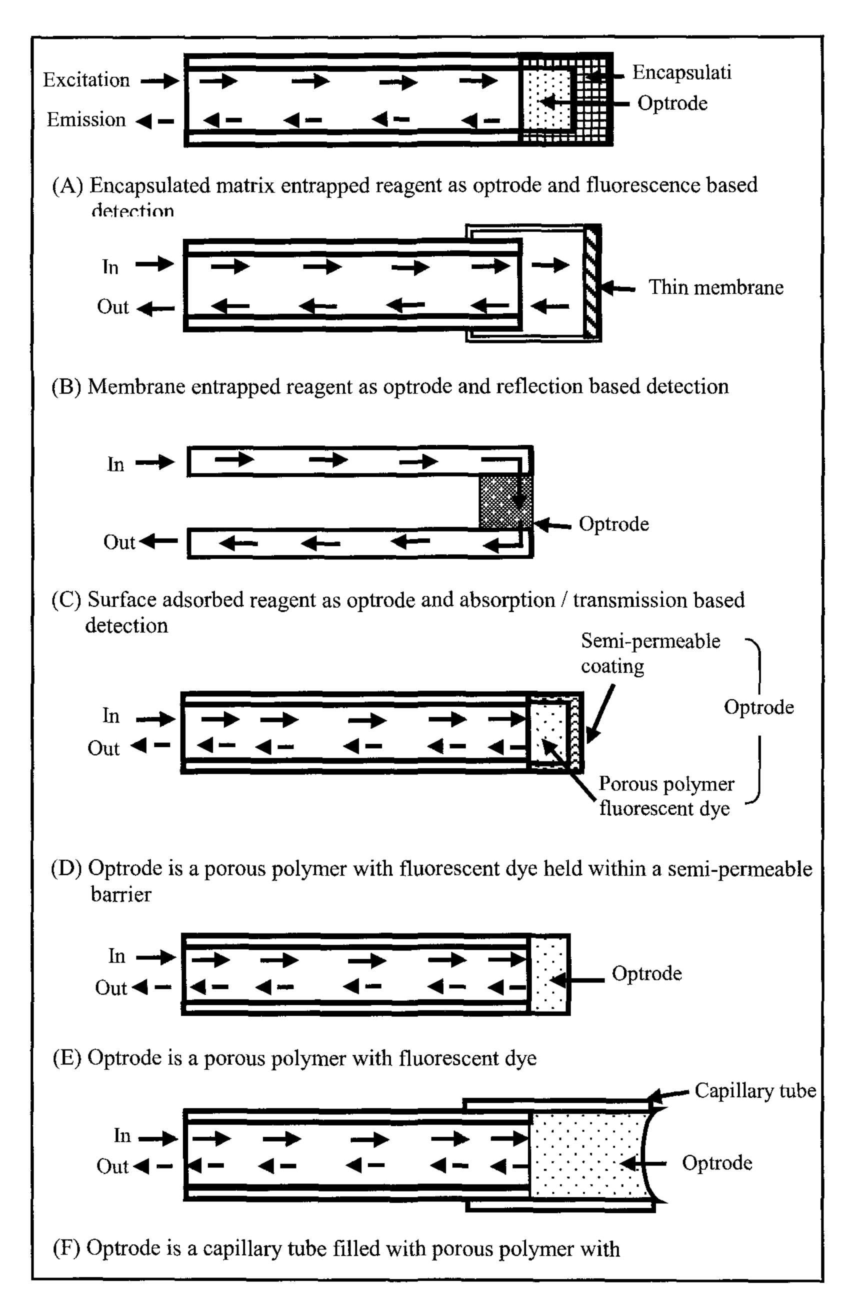


Fig. 10.8(A–F). Fiber optic indirect chemical sensor configurations showing optrodes prepared using matrix entrapment, membrane entrapment and surface adsorption methods.[4]

microspheres, partly absorbed by the dye and the rest is transmitted back through the output fiber. The amount of light collected from the optrode depends upon the absorption of the dye. Fiber optic pH sensors are also designed based on luminescent dyes whose luminescence is dependent on pH. One example is a water soluble dye (hydroxypyrene trisulfonic acid) that has two forms: acidic and basic. Both forms can be excited to emit a luminescence that peaks at 520 nm. There is a marked difference between the excitation spectra of the two forms. The excitation spectra, peak at 410 nm for the acidic form and at 460 nm for the basic form. Therefore the sample is excited once at 410 nm and again at 460 nm and the luminescence intensity at 520 nm is determined. The ratio of the two peaks gives the relative concentration of the basic and acidic forms of the dye, which is then related to the pH of the solution.[9]

The dyes used to measure pH can also be used indirectly to measure other biochemical reactions. For example: partial pressure of carbon dioxide in the blood. The pH of a bicarbonate solution depends on the partial pressure of carbon dioxide. Therefore, by measuring the pH of the solution, the partial pressure of carbon dioxide can be determined. Usually an increase in partial pressure of carbon dioxide will reduce the pH of the bicarbonate solution causing a decrease in the luminescence of the dye. The major difference between the optrode for partial pressure of carbon dioxide and that for pH is that in the former, ions are excluded from the probe and only gas molecules are allowed to enter. In some optrode this is achieved by encapsulating the bicarbonate solution in a matrix that provides necessary isolation from ions in the solution. Similar configuration is also used to design fiber optic oxygen sensors. Several dyes such as Cobalt II poryphyrins and Tetraphenyl porypyrins (TPP) are used to determine oxygen. The property of quenching of luminescence by oxygen is used to design the sensor. In this case the luminescence is inversely proportional to the oxygen concentration. High sensitive fiber optic sensor for oxygen sensing was also designed based on the quenching of the luminescence of a ruthenium diimine complex.

Glucose monitoring is another important application in health care. One of the earliest fiber optic glucose sensors is based on a competitive

binding method.[10] In this sensor, the optrode consist of a hollow tube plugged at one end, and its wall freely permeable to glucose. The tube is filled with a fluorescent dye called fluorescein, which was bound to a soluble glucose polymer. The inside of the hollow tube is coated with concanavalin A, a material which binds to glucose. A bifurcated fiber bundle is inserted into the open end of the hollow tube and is used to transmit and collect light from the optrode. In the absence of glucose, the binding compound binds the fluorescein polymer to the wall. The luminescence takes place in a geometric location that is away from the field of view of the fiber bundle. When the optrode is inserted into a glucose solution, the glucose penetrates the optrode and displaces the polymer from the walls. Consequently, the fluorescein concentration in the solution (away from the walls) increases. Under excitation, there is more luminescent light, which the fiber bundle can collect. Higher the concentration of glucose in the solution, greater will be the luminescent light intensity. Currently different types of indirect optical sensors have been tested for glucose monitoring.[11]

10.6 Biosensors

Biosensor is a subtype of chemical sensors that rely on biological components to sense a substance of interest (which by itself need not be a biological component). On the other hand, chemical sensors not using a biological component but placed in a biological matrix are not biosensors by definition.[12] The biological component utilized in a biosensor is called biorecognition element. The biorecognition element could be an enzyme, an antibody, a cell (bacterial or fungal), a tissue slice, a receptor, nucleic acid or an organelle. It is used to detect and interact specifically with the analyte of interest. Biosensors are used to determine genotoxicity, immunological effects, and endocrine effects. They are used to measure concentration of specific analyte that is difficult to detect normally. In a biosensor, optical fiber forms the transducing element that convert the biochemical recognition step into a quantifiable optical signal that has a direct relationship to the concentration of the analyte.

Generally, biosensors are divided into three types. (1) Catalytic biosensors: In this biosensor, biocatalyst such as enzymes and bacterial cells are used to recognize, bind and chemically convert a molecule. (2) Affinity biosensors: In this biosensor, receptor molecules such as antibodies, nucleic acids and hormone receptors are used to bind molecule irreversibly and non-catalytically. (3) Microorganism-based biosensors: This biosensor tends to use different bacterial biochemical characteristics to sense biologically relevant variables. For instance, microbial respiration and its inhibition by analytes have been measured optically. The advantages of microorganism-based biosensor over isolated enzymes are that: microorganism-based biosensors are relatively inexpensive to fabricate and can operate over a wide range of pH and temperature. Their general limitations involve the long assay times including the initial response and return to baseline. This sensor is mostly applied to detect toxic compound. Biosensors have also been developed using Genetically Engineered Microorganisms (GEMs) that recognize and report the presence of specific biochemical or toxic substances.

Different optical configurations used for indirect fiber optic chemical sensors are also applied to design biosensors. Nevertheless, Fiber Optic Evanescent wave spectroscopy (FOES) has been used extensively for biosensing. When light travels though a transparent core of the optical fiber (with higher refractive index) impinges the cladding (with lower refractive index), it is internally reflected back into the core. However, certain amount of light penetrates the cladding. In the cladding there is no flow of energy, but rather a non-propagating field called evanescent wave, which decays exponentially with distance from the surface of the core (see Fig. 10.9). Consequently, in an unclad optical fiber, which consists of glass core only, if the unclad portion is coated by a thin layer of polymer, which fluoresces when exposed to appropriate light.

It has been shown that under certain optical conditions, the visible light is coupled back into the core and is transmitted back through the same optical fiber, where it can be easily detected. A similar situation occurs when the unclad fiber is inserted into a dye solution or liquid that fluoresces when exposed to appropriate light. Thus evanescent wave can be used to detect the presence of luminescent species in a solution or luminescent signal from the polymer layer that coats the unclad portion

of the fiber. The luminescent intensity measured via an evanescent wave sensor can be used to determine the concentration of the analyte in the solution. Microorganisms, antigens-antibodies and toxins have been detected with fiber optic evanescent wave biosensors.

Biosensors used to detect antigen-antibody reactions are also called immunosensors. If the specific antibody that binds with an antigen is known, and if both the antigen and antibody are fluorescent, this combination can be used to design a immunosensor. First of all the antibody has to be covalently bonded to the surface of an unclad fiber. This step is called the immobilization of the antibody. When appropriate light is launched through the optical fiber, the evanescent wave excites the fluorescent antibody and fluorescent intensity is coupled back through the optical fiber. When the fiber tip is dipped into a solution containing the specific antigen, it will bind to the immobilized antibody. The evanescent wave will then excite the antigen and additional fluorescence will be determined. The intensity of the additional fluorescence is proportional to the concentration of antigen in the solution. The immunosensors combine the advantage of selectivity offered by an antigen-antibody reaction and the sensitivity offered by optical techniques. Recently, fluorescent quantum dots are being tested for immunosensing. Quantum dots are highly fluorescent molecular sized semiconductor crystals (nanocrystals). Fiber optic immunosensors have been developed using quantum dots as reporter labels for different antibodies with the aim to detect multiple pathogens with a single fiber. Different methods of immobilizing enzymes and/or biological components in a biosensor are shown in Table 10.1. The advantages of fiber optic biosensors are (1) availability of optical fibers with different characteristics (single-mode fibers, polarization preserving fibers and multimode fibers, single core fibers, dual core fibers, fiber bundles and Y-junction fiber), (2) ability to sense multiple analyte (3) enhanced sensitivity, (4) selectivity and (5) rapidity for biosensing. However, their disvantages are (1) difficulties associated with optrode construction (2) difficulties of calibration (3) deterioration of the optical transducer with time (ageing) (4) slow response time and (5) limited dynamic range.

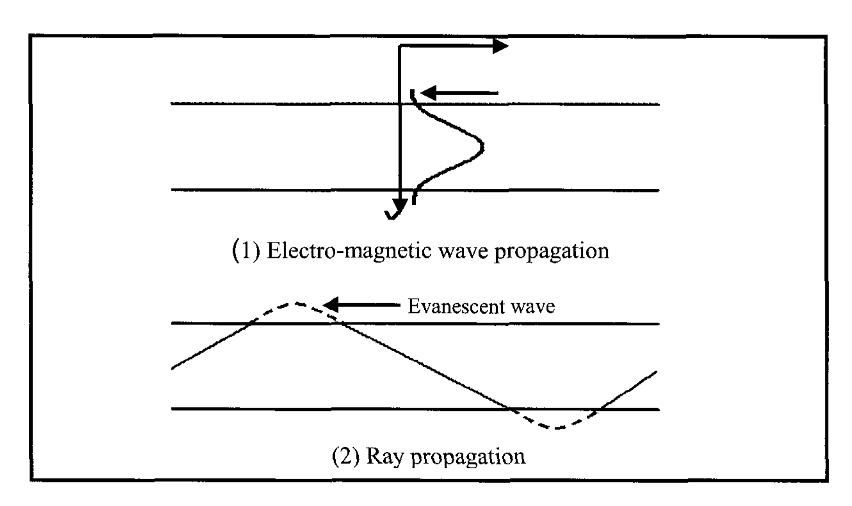
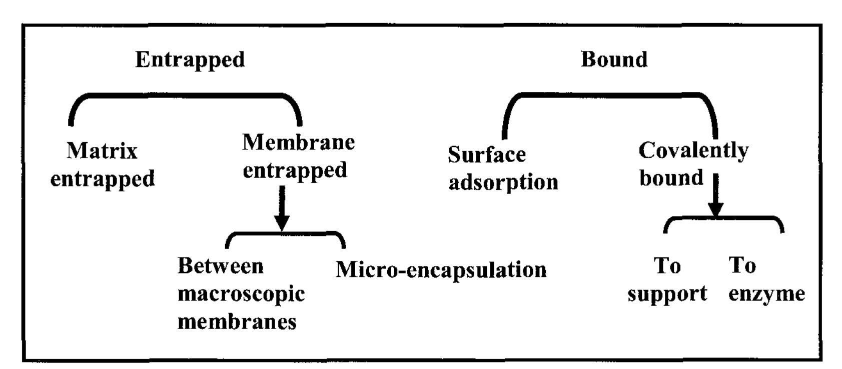


Fig. 10.9. Schematic illustration of evanescent waves based on (1) wave and (2) ray propagation of light.[4]

Table 10.1. Different immobilization methods used in biosensors.



10.7 Applications of Fiber Optic Diagnostic Sensors in Dentistry

Light based approaches have been used in dentistry to detect incipient dental caries. Some of these techniques are now commercially available, while some others are still being evaluated in the laboratories. DIAGNOdent uses red laser (at 655 nm) induced fluorescence from the enamel surface to detect early dental caries. This method identifies caries from its increased light induced fluorescence over sound tooth (see

Fig. 10.10). Nevertheless, the exact mechanism of their detection has not been fully understood. Apparently the system measures the fluorescence of the bacterial product such as porphyrins within the carious lesion rather than proper crystalline dissolution. It is also suggested that this method does not provide any other details about the caries lesion.

QLF is based on the ability of enamel to emit yellow light by autofluorescence when illuminated with blue light from an argon laser or from a xenon-arc source. Presence of caries is found to reduce the intensity of this autofluorescence. Fig. 10.11 shows the fluorescent images obtained from the enamel surface after different periods of demineralization in demineralization solution. A CCD micro-camera interfaced to a computer is used to acquire the digital image of the enamel, and a software program is used to detect the darker region in the image and model the fluorescence radiance of the sound enamel using a reconstruction algorithm. The software program will calculate the percentage radiance loss between actual and reconstructed enamel fluorescence. Many investigations have been conducted using QLF to quantify coronal dental caries, and acid erosion in enamel. Experiments were also conducted to study the effects of teeth whitening products and mouth rinses on enamel. Experience with the laser based caries detection system such as QLF demonstrated that deposits like plaque or calculus could give rise to false-positive reading.[13] The disadvantages of this system are (1) difficulty in reproducibly capturing images, (2) difficulty in determining the depth of the lesion and quantitatively analyze the detected lesion,[14] and (3) using this system necessitates significant learning curve for clinicians.

Dental caries is a multifactorial, bacterial disease affecting the hard tissues of the teeth. A quantitative measure of Mutans streptococci in saliva is said to be a reliable measure to predict true caries activity.[15] Early recognition of high caries activity enables dental professional to formulate and incorporate preventive treatment plan for such patients. A method used for the detection and the enumeration of mutans streptococci called Dentocult SM has been developed in 1989. The Dentocult SM (Orion Diagnostica, Espoo, Finland), consist of a special slide, coated with mitis salivarius agar medium containing 20% sucrose.



Fig. 10.10. A DIAGNOdent system.

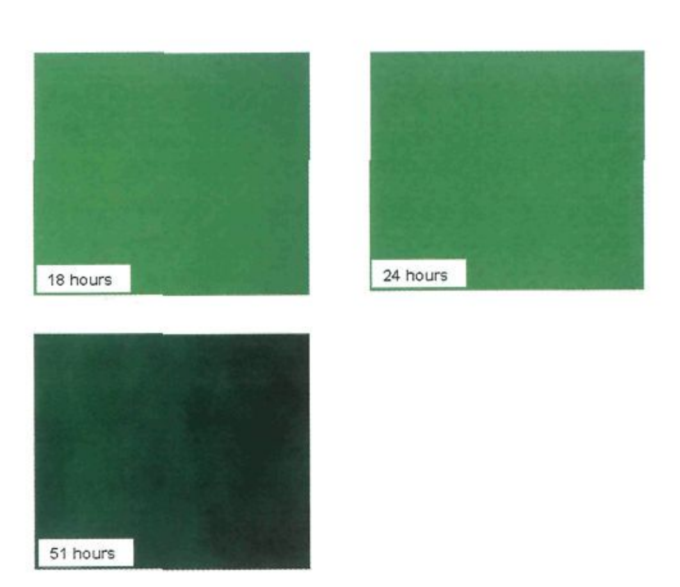


Fig. 10.11. Fluorescent image of the enamel surface after different periods of demineralization.

The slide is inoculated with saliva and the growth density of mutans streptococci are scored after incubation at 37C for 48 h. This type of slides has short shelf life because of the mitis salivarius-sucrose agar. Further, this technique is time consuming and is not a true quantitative method. Additional methods for the identification of mutans streptococci are based on Gram staining, distinctive cell shape on light microscopy, specific growth characteristics and enzymatic reactions. These techniques are also time consuming and needs laboratory support and trained personnel. A fiber optic evanescent wave spectroscopy (FOES) based biosensor was developed to monitor mutans streptococci mediated biochemical reaction in human saliva at real-time. This sensor utilized a photosensitive pH indicator that was immobilized within a porous glass coating on a cladding denude multi-mode optical fiber. It was observed that the intensity of the absorption peak increases conspicuously from the time of onset, through the entire period of test (120 min). A negative correlation was noted between the increase in absorption peak intensity and the decrease in pH of saliva with time. The experimental arrangement and the result obtained are shown in Fig. 10.12.[16] A similar FOEW sensor was also developed for the rapid and sensitive detection of total protein concentration. This fiber optic total protein sensor enabled single-step detection and quantification of microgram levels of total protein directly without destroying the sample. The sensor combined the advantage of highly sensitive Coomassie Brilliant Blue assay and fiber optic spectroscopy. The response time for this sensor was about 10 to 15 min, which was much faster than the conventional calorimetric methods. This sensor could be reused by submerging it in 40% (v/v) methanol for about 35 min.[17]

A fiber optic sensor was also developed to quantitatively monitor bacteria, *Enterococcus faecalis* in root canal infections. *E. faecalis* is a Gram-positive, facultative anaerobic bacteria that is capable of surviving in harsh environment. It has innate resistance to a variety of antibiotics and has been identified in 30% of teeth with unsuccessful endodontic treatment. It also is apparent from the dental literature that *E. faecalis* often is difficult to eradicate with current intracanal medications. Chromocult *Enterococci* broth (CEB) (MERCK, Darmstadt, Germany) is

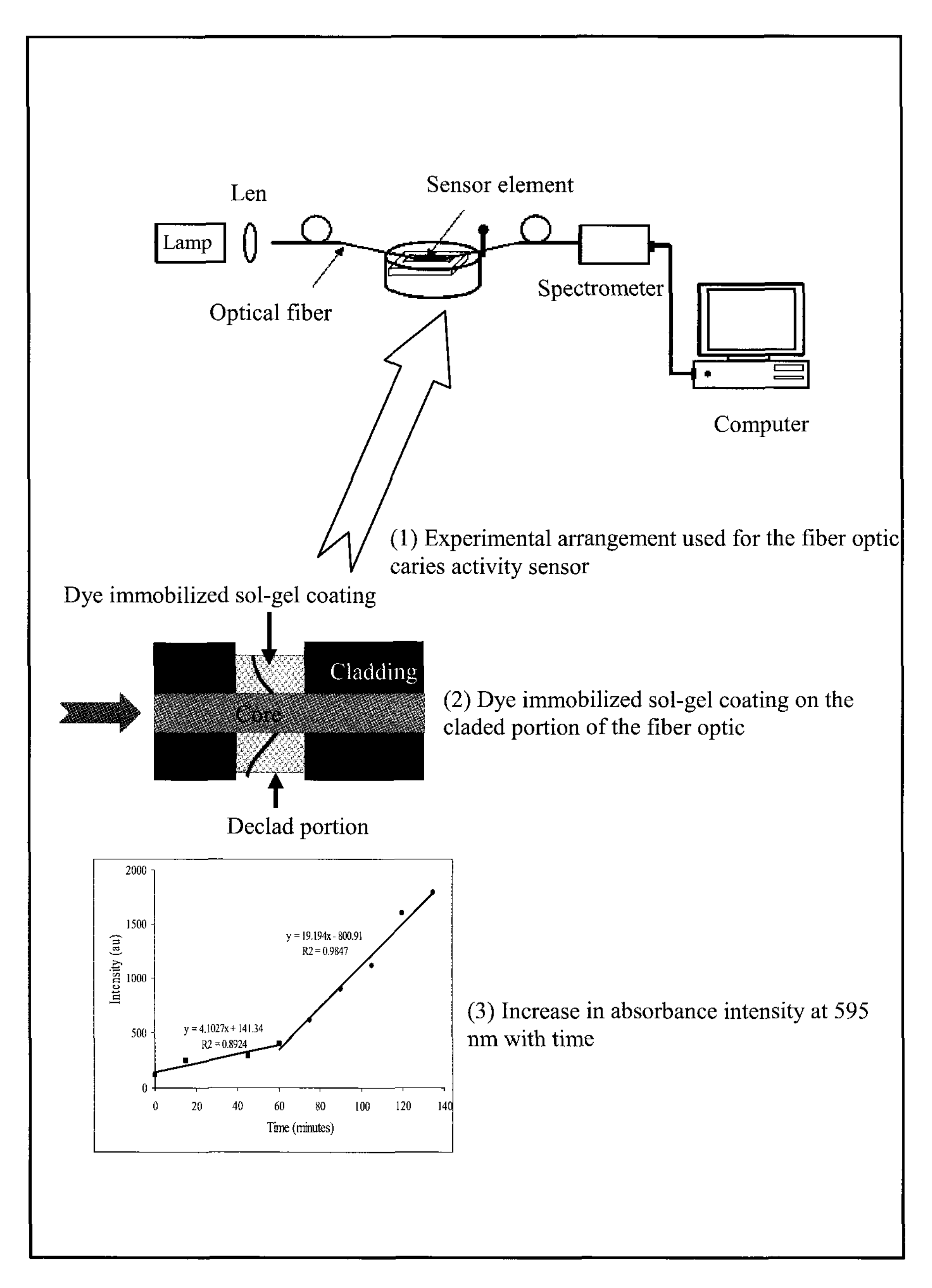


Fig.10.12. Fiber optic evanescent wave spectroscopic sensor to monitor caries activity.[16]

a new selective medium based on enzyme-substrate reaction specifically targeted for enterococci. The synthetic enzyme substrate, X-GLU (5-bromo-4-chloro-3-indolyl-β-D-glucopyranoside) in the medium is cleaved by the enzyme β -D glucosidase in the presence of selected peptones. This enzymatic reaction is characteristic for enterococci and results in an intensive blue-green color of the broth. The sodiumazide present in this medium prevents false-positive results by other β -D-glucosidase positive bacteria and inhibits the growth of accompanying Gram-negative microbial flora while sparing the enterococci. Hence, the color change of the CEB specifically confirms the presence of enterococci, and further isolation of pure culture or confirmatory tests are not recommended.[18] A Palm-SPEC Spectrophotometer (Ocean Optics, USA) that combines a handheld personal computer with a miniature spectrophotometer to create a complete system with a very small footprint. The visible light spectroscopic analysis of bacterial suspension in CEB showed a conspicuous increase in absorbance intensity at spectral range from 600 to 654 nm. This spectral change is attributed to the rapid oxidation of chromogenic substrate XGLU to bromo-chloro-indigo in the CEB. This increase in absorption intensity was most pronounced at 610 and 653 nm, 3.5 h and 4 h post incubation respectively. There was a significant correlation between the increase in CFU and the absorbance intensity at 610 and 653 nm. The experimental arrangement used for this experiment and the result is shown in Fig. 10.13. This method of applying fiber optic spectroscopy in conjunction with specific enzyme–synthetic chromogenic substrate-based medium allowed early detection of *E. faecalis* activity quantitatively and qualitatively.[19]

Fiber optic sensors are used to monitor the force and temperature of dental splints worn by patients suffering from sleep apnoea. Owing to the small size of the sensors they can be easily embedded within the splint in a way that does not affect the effectiveness of the splint, and at the same time are able to indicate whether the splint has been properly worn by the patient. The overall dimensions of the sensor are approximately 0.375 mm thickness, 1 cm length and 3 mm width. The force and

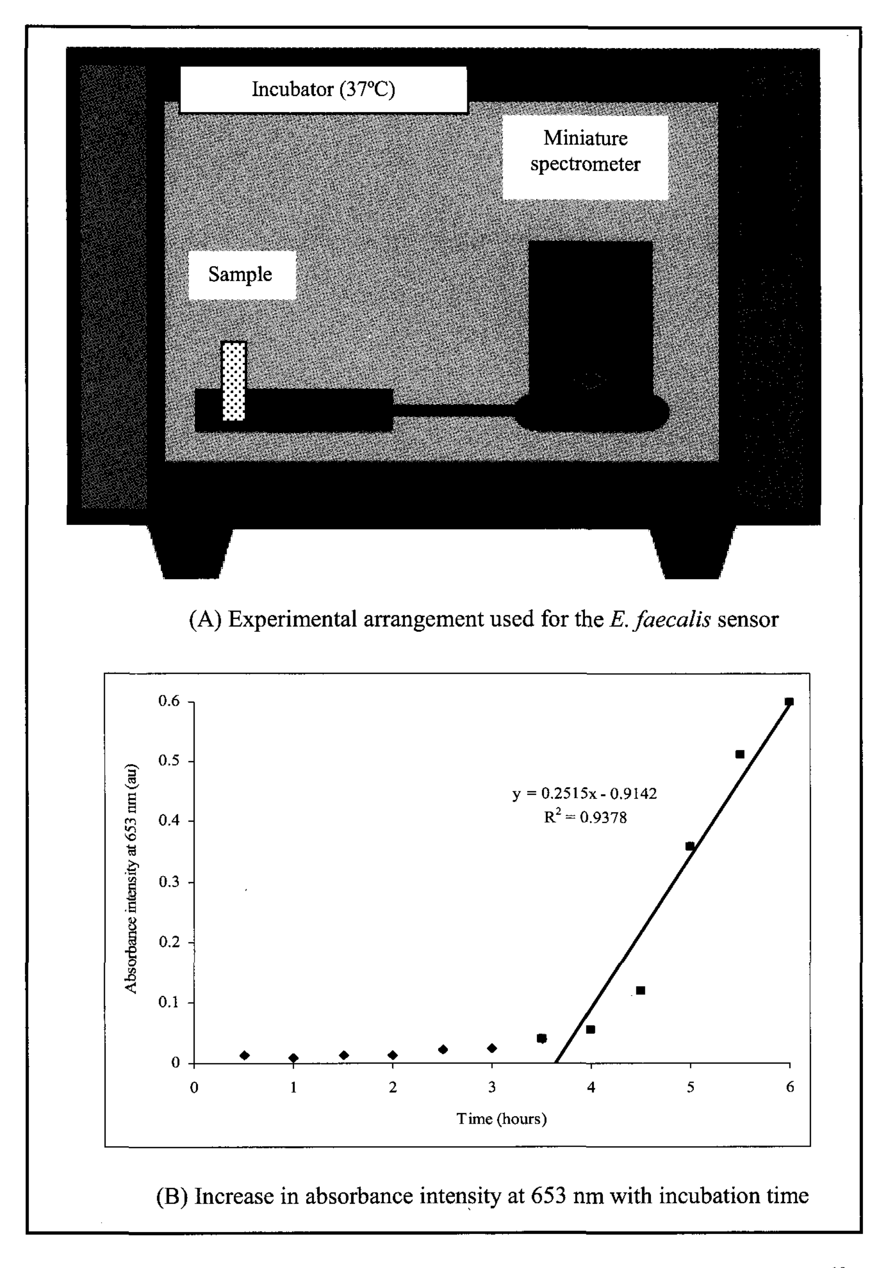


Fig. 10.13. Miniature spectrophotometer system used to detect *E. faecalis* activity.[19]

temperature sensors are calibrated and found to have sensitivity of better than 0.5 N and 0.1°C, respectively. Clinical trials on patients have shown that the measurements of pressure and temperature are an effective approach of monitoring the proper usage of the splint by the patients.[20]

10.8 Concluding Remarks

There have been many clinical cases in which premium technical standards of treatment was followed and yet resulted in failure. These failures have been attributed to factors related to the primary diagnosis. This observation highlights the need for rapid, chairside or bedside, diagnostic tools to achieve predictable success in clinical practice. Fiber optic technology offers distinct advantages when used for physical, chemical and bio-sensing. This chapter has focused on different types of fiber optic based direct and indirect, physical, chemical and biosensors configurations and examples of their applications.

References

1. D.W. Lubbers, N. Opitz, *Z Naturforsch [C]*, 30 (1975).
2. M.T. Wlodarczyk, *Proc SPIE 1067* (1989).
3. P.N. Prasad. Introduction to Biophotonics. Wiley Interscience Inc., New Jersy, (2003).
4. A. Katzir, *Lasers and optical fibers in medicine,* Elsevier: St Louis: USA (1993).
5. P. Teng, N.S. Nishioka, R.R. Anderson, T.F. Deutsch, *Appl Phys*. B42, 73 (1987).
6. M.T. Wlodarczyk, Proc SPIE 1067, 8 (1989).
7. D.A. Krohn, Fiber Optic Sensors–Fundamentals and Applications. *Instrument Society of America, International Research Triangle Park*: North Carolina 99 (1988).
8. J. Hecht, *Understanding Fiber Optics*, Prentice Hall: New Jersey (1999).
9. J.L. Gehrich, D.W. Lubbers, N. Opitz, D.R. Hansmann, W.W. Miller, J.K. Tusa, M. Yafuso, *IEEE Trans Biomed. Eng*. BME-33, 117 (1986)
10. J.S. Schultz, S. Mansouri, I.J. Goldstein, Diabetes Care 5 (1982).
11. T. Koschinsky, K. Jungheim, L. Heinemann, *Diabetes Technol Ther.* 5, 829 (2003).
12. O.S. Wolfbeis, Anal Chem. 76, 3269 (2004).
13. A. Lussi, S. Imwinkelried, N. Pitts, C. Longbottom, E. Reich, *Caries Res* 33 (1999).
14. G.K. Stookey, *J Dent Res* 83 (2004).
15. S. Kneist, R. Heinrich-Weltzien, W. Tietze, T. Fischer, L. Stosser, J Dent Res 75 (1998).

16. A Kishen, M.S. John, C.S. Lim. A. Asundi. *Biosensors & Bioelectronics* 18 (2003).
17. P.V. Preejith, CS Lim, A. Kishen MS John, A Asundi. *Biotechnology Letters* 25 (2003).
18. M. Manafi, R. Sommer, Wat Sci Tech. 27, 271 (1993).
19. A. Kishen, N.N. Chen, L. Tan, A. Asundi, *J Endod.* 30, 872 (2004).
20. S.C. Tjin, Y.K. Tan, M. Yow, Y.Z. Lam, J. Hao, *Med Biol Eng Comput.* 39, 182 (2001).

Biophotonics in dentistry is a rapidly growing area. Unlike other books, this *invaluable compendium* touches on the *fundamental* areas in biophotonics. Contributed by world-renowned authors, it provides a basic understanding on a range of topics for individuals of different backgrounds to acquire a minimum knowledge of research and development in biophotonics. The chapters are arranged in two major categories. The first describes the fundamental aspects of photonics, such as photomechanics, biomedical imaging, lasers and laser-tissue interaction, spectroscopy and photodynamic therapy.

Vol. 4

Series on Biomaterials and Bioengineering

Fundamentals and Applications of Biophotonics in Dentistry



The second details the applications of biophotonics, with special relevance to dentistry, including dental photobiomechanics, Raman spectroscopy and dental tissue optics.

Key Features

- A comprehensive textbook ideal for a course on photonics in dentistry
- Provides an in-depth introduction to light-tissue interactions

Imperial College Press

www.icpress.co.uk

P474 hc

ISBN 1-86094-704-2

9 781860 947049